THE MECHANICS OF ATHEROSCLEROTIC PLAQUE RUPTURE

by

Howard M. Loree II

M.S. Mechanical Engineering, Massachusetts Institute of Technology
(1988)

B.S. Mechanical Engineering, Massachusetts Institute of Technology
(1986)

Submitted to the Harvard - M. I. T.
Division of Health Sciences and Technology

in Partial Fulfillment of the
Requirements for the Degree of

DOCTOR OF PHILOSOPHY

at the

Massachusetts Institute of Technology

June 1992

Signature of Author _____
Harvard-M.I.T. Division of Health Sciences and Technology
May 15, 1992

Certified by _____
Roger D. Kamm
Professor, Department of Mechanical Engineering
Thesis Supervisor

Accepted by _____
Roger G. Mark
Co-Director, Harvard-M.I.T. Division of
Health Sciences and Technology

THE MECHANICS OF ATHEROSCLEROTIC PLAQUE RUPTURE

by

Howard M. Loree II

Submitted to the Harvard - M.I.T. Division of Health Sciences and Technology on May 15, 1992 in partial fulfillment of the requirements for the Degree of Doctor of Philosophy in Medical Engineering

ABSTRACT

The goal of this research is to characterize the mechanics of acute atherosclerotic plaque rupture, the major antecedent of transmural myocardial infarction (MI). There are three major objectives. First, fluid flow experiments have characterized the hydrodynamic forces on the surface of vascular stenoses, including turbulent pressure fluctuations. Second, the static anisotropic mechanical properties of plaque constituents in human post-mortem specimens were studied and compared to histological studies for cellular content, elastin, collagen, and calcium. Third, the effects of static mean pressure loads on the stress fields in plaques were studied using finite element computer models of idealized and real coronary artery plaques.

The conclusions of this research are fourfold: First, hemodynamic forces may play a role in plaque rupture. Turbulent pressure fluctuations are significant in severe (90%) asymmetric stenoses. However, many fatal MI's are caused by plaque ruptures in mild (50%) coronary stenoses where turbulence is insignificant. Second, the average static circumferential tensile stiffness was similar for cellular, hypocellular, and calcified plaques. Static tensile stiffness increased with applied circumferential stress, an effect that was statistically highly significant for cellular and hypocellular plaques. Cellular and hypocellular plaques exhibit strongly anisotropic properties in the physiologic range of loading, with circumferential tensile stiffness about 20 times greater than previously reported measurements of radial compressive stiffness. Third, reducing the fibrous cap thickness dramatically increases peak circumferential stress in the plaque, while increasing stenosis severity actually decreases peak stress in the plaque. Fourth, local circumferential stress concentrations are predicted to occur in the plaque cap under physiologic mean luminal pressure loads. These correspond to observed sites of coronary plaque rupture. However, the predicted magnitudes of peak stresses are often only 10 to 50% of the magnitude of experimentally measured plaque tensile fracture stresses. Other factors should be investigated as possible contributing causes of plaque rupture such as cyclic fatigue and local enzymatic degradation.

Thesis Supervisor:
Roger D. Kamm, Ph.D. Professor of Mechanical Engineering, M.I.T.

Thesis Committee:

Alan J. Grodzinsky, Ph.D.	Professor of Electrical Engineering, M.I.T.
Lorna J. Gibson, Ph.D.	Professor of Civil Engineering, M.I.T.
James E. Muller, M.D.	Associate Professor of Medicine, H.M.S.
Richard T. Lee, M.D.	Assistant Professor of Medicine, H.M.S.

ACKNOWLEDGEMENTS

I wish to thank the following people who have made this thesis possible:

Rich Lee has been a great friend and a superb mentor to me over these past three years. I look forward to working together with him for many years to come.

Roger Kamm, Al Grodzinsky , Lorna Gibson, and Jim Muller have all contributed their unique talents to the project and provided encouragement to me through the difficult problems I faced.

George Cheng contributed much of the work described in Chapter 5. He is an outstanding researcher and a valued friend.

Ann M. Black has provided the moral support that I needed in order to complete this project. She happily endured many lab dates and spent many hours assisting me. I love her with all my heart.

Roy Larson and Dean Farmer have called me to a high standard of excellence in my work, ministry, and relationship with God. They are the best friends I have ever had.

Elaine Lee, Eliot Frank, Dick Fenner, Bob Lang, Chris Atkinson, and Grace Timlin have all contributed invaluable technical support.

Peter Rothschild, Kristine Drobot, Mark Rawizza, Andrew Romaine, and Rob Grace played a key role in the timely completion of this document.

The entire M.I.T., Harvard, and Tufts ministry has been a constant source of encouragement to me. I am blessed to have such a terrific group of friends to depend on.

My family has always supported me in all of my efforts, and I look forward to celebrating my graduation with them.

TABLE OF CONTENTS

LIST OF FIGURES

LIST OF TABLES

CHAPTER 1

INTRODUCTION

The Atherosclerotic Plaque. An atherosclerotic lesion of the intimal layer of a blood vessel can range from a symptomless fatty streak to a raised fibrous plaque that can become a complicated lesion when altered by hemorrhage, calcification, cell necrosis, or mural thrombus (1). Atherosclerotic plaques in the coronary arteries interfere with perfusion to the heart in two important ways. Chronically, plaques result in stenoses of the arteries that limit flow and, during vasospasm or periods of exercise, result in angina. Acutely, they can fissure or rupture, presenting a thrombogenic subintimal surface to blood flowing through the artery and resulting in mural or occlusive thrombi (2,3,4), the most common cause of acute myocardial infarction (5,6). Plaque rupture may also be the initiating event in the pathogenesis of unstable angina and sudden cardiac death (7,8). In addition, injured carotid artery plaques may lead to embolic stroke (9,10).

Plaque Rupture. The mechanism of plaque rupture is disputed. Falk (6) proposed that rupture is a random incidental event in the evolution of the atherosclerotic plaque. Studies demonstrating a circadian variation in myocardial infarction (11), sudden death (12), stroke (9), and silent ischemia (13) argue against a purely random mechanism of plaque rupture, although it is possible that the circadian variation is due to factors other than plaque rupture. The peak in these ischemic events during the morning waking hours is similar to the variation in blood

pressure and heart rate (8). In addition, the Coronary Artery Surgery Study (CASS) identified left anterior descending arterial lesion length, severity, and roughness as predictive of anterior myocardial infarction in the next 3 yr; lesion eccentricity was predictive at borderline statistical significance (14,15). The CASS showed that risk of myocardial infarction increased 7.5 times for 90-98% stenoses relative to stenoses of <50% severity. In addition, the risk increased 1.9 times for eccentric relative to axisymmetric stenoses (P=0.06). The CASS also demonstrated that risk increased as 1.7 times the length of stenosis that is >50% narrowed (with stenosis length measured in units of lesion diameter).

Plaque rupture mechanisms that have been proposed include shear stress injury (16), transient collapse of the stenosis (17), turbulent plaque injury (18), and mechanical shear stress (19). Constantinides (20) has proposed that rupture occurs due to a "sudden explosion of pressure" in the lumen causing a fissure in the plaque surface. In contrast, Barger *et al.* (21) have reported that atherosclerotic plaques receive neovascularization from the vasa vasorum and have suggested that hemorrhage may occur from within the plaque due to static pressure differences between the vasa vasorum and arterial lumen. One mechanism that is strongly supported by pathologic data is fracture caused by increases in circumferential stress within the plaque. Because some components of the diseased vessel are stiffer than others, regions of "stress concentration" develop (19); Richardson *et al.* have identified stress concentration regions by finite element modeling that correlate with locations of plaque fracture in autopsy specimens (22,23).

It should be noted that hemodynamically induced plaque rupture may not be

the only cause of circadian variation in myocardial infarction (11). The Physicians' Health Study demonstrated that aspirin therapy caused a marked reduction in the morning peak of myocardial infarction (24). Thus at least a portion of the morning increase in myocardial infarction may be due to an increase in the tendency for thrombosis. However, because the aspirin group continued to show a slight morning peak of myocardial infarction, it is possible that the morning peak is a combination of increased rupture and a tendency for thrombosis in the morning.

A number of clinically successful strategies for limiting infarction size are directed at plaque rupture events, including thrombolytic therapy, acute mechanical intervention, and acute beta-adrenergic blockade. However, the ability to identify vulnerable atherosclerotic lesions and to intervene successfully *before* acute plaque rupture occurs has been an elusive goal. Although coronary angiography provides some prognostic information (11), factors other than stenosis severity predispose some atherosclerotic plaques to rupture (25). For example, Little *et al.* found that angiographic severity of coronary stenosis poorly predicted subsequent location of infarction (26). Based on a retrospective analysis of pre-infarction angiograms, Ambrose *et al.* also have suggested that myocardial infarction frequently develops from rupture of angiographically nonsevere coronary lesions (27).

A primary factor which may predispose a given plaque to rupture is the existence of tensile stress concentrations within the wall of the lesion. In a diseased artery, regions of high stress may be caused by variations in both luminal geometry and subintimal structure of the lesion; for example, since soft lipid pools in the diseased vessel are unable to bear significant stresses, regions with concentrations of

high stress develop near lipid pools. Using the method of finite element analysis to model the structure of coronary lesions, Richardson *et al.* have shown that high tensile stresses concentrate at the ends of plaque caps with underlying lipid pools (22,23). Their study of idealized plaque geometries supported by morphology studies of actual coronary lesions suggests that these stress concentrations may contribute to rupture vulnerability. However, fissures in plaque often extend longitudinally and no definitive data regarding initial location of fissuring of plaques are available.

It is likely that a variety of factors participate in setting the stage for rupture. As a coronary lesion gradually progresses, it is subjected to a number of steady and transient disturbances. Over time, pulsatile pressure fluctuations accentuate weaknesses in stress concentration regions by the process of fatigue, analogous to the way that a wire may eventually be broken by repetitive bending. Stresses resulting from shear over the plaque surface, turbulence, and coronary vasospasm may also serve to destabilize the plaque. Increases in arterial pressure during states of emotional stress or physical exertion may raise stress concentration levels further. When tensile stress reaches a critical level, rupture may ensue, followed by thrombosis; the consequences of thrombosis depend on a variety of factors, including the extent of injury to the vessel and the thrombotic state (28).

The "critical level" of stress required to rupture atheromatous tissue may not be of uniform value throughout a given lesion. Atherosclerotic materials are heterogeneous, one reason why biomechanical data on these tissues are limited. Since the plaque is also a biologically dynamic environment, with smooth muscle cells, macrophages, platelets, and other cells cooperating in the remodeling of its

extracellular matrix, a lesion's strength may vary with time. Regions of plaque tissue heavily populated with macrophages rupture at lower stresses than regions with few macrophages (29). Thus, the site where rupture occurs may depend on the relative locations of both stress concentrations and local defects in plaque strength.

The Effect of Blood Flow on Plaque. Both inertial and viscous effects determine the mean pressure distal to a stenosis. Mean pressure falls in the direction of flow both due to acceleration into the stenosis and due to turbulent dissipation. By analogy to an axisymmetric jet entering a large cavity, turbulence is expected to develop at a distance several stenosis diameters downstream of the narrowest point. The intensity of the turbulence falls both in the direction of flow and radially away from the center of the jet. Young and Tsai (30) demonstrated that the mean pressure falls sharply as flow enters a constriction and then rises slightly downstream due to gradual pressure recovery. Asymmetric constrictions typically produce higher mean pressure drops than do axisymmetric ones (30).

Previous studies by Dewey, Fredberg, and others (31,32,33) have characterized turbulent flow that develops when blood passes through a short, asymmetric stenosis. These studies suggest that when turbulent flow impinges on a vessel wall, the magnitude and frequency of the turbulent pressure fluctuations are related to the velocity of flow as well as stenosis geometry. Although vascular stenoses may rarely be very short relative to the diameter of the artery (diaphragm-like stenoses), the typical "long" stenosis has a length-to-diameter ratio >1 and some degree of taper both proximal and distal to its most severely stenotic portion. It is therefore possible that the interaction of turbulence with the distal surface of the atherosclerotic plaque

will lead to fluctuations in pressure or shear stress that may precipitate fissuring of the plaque. There is strong experimental evidence to believe that the effects of turbulent flow on the plaque surface are important in the pathogenesis of atherosclerosis. Turbulent shear stresses have already been demonstrated to affect normal vascular endothelium, causing cell retraction and cell loss. These effects were not observed after much longer exposures to laminar shear stresses, in which only cell alignment occurred (34).

The concept of similarity allows interpretation of experiments on scale models of a system by use of dimensional analysis. Flows are characterized by the dimensionless Reynolds number (Re):

$$Re = \rho UD/\mu \qquad (1.1)$$

where ρ is the fluid density, U is the upstream mean flow velocity, and μ is the fluid viscosity in a stenosis of specified geometry. Blood behaves like a Newtonian fluid (that is, the viscosity can be considered independent of shear rate) at the shear rates found in small arteries (30,35,36). Peak coronary artery flow at rest has $50<Re<150$ based on $D=0.40$ cm and $4.6<U<15$ cm/s (37,38) and peak carotid artery flow at rest has $250<Re<600$ based on $D=0.65$ cm and $15<U<31$ cm/s (39).

The effects of vessel wall compliance and pulsatility on the flow issuing from the stenosis are often neglected in model studies (32,40), because these effects scale with the ratio of vessel diameter fluctuations (ΔD), to mean vessel diameter (D) (35,36). In clinical studies, $\Delta D/D$ over the cardiac cycle in atherosclerotic coronary

artery segments is only 2-8% (41,42). Although flow in major arteries is unsteady and pulsatile with a typical ratio of mean flow to peak flow of 1:4, a steady-flow model of turbulent flow through stenoses is reasonable; previous studies have shown that the turbulent power spectra obtained at peak pulsatile flow are indistinguishable from spectra obtained in steady flow at the same flow rate (40).

what is this?

aren't you saying this is unimportant?

Plaque Mechanical Properties. There are few published data on the moduli, yield stress, or fracture properties of the material comprising the plaque fibrous cap; therefore the magnitude of pressure fluctuations on the surface of plaque that could cause rupture or microfissures is unknown. These data will be essential for understanding the effect of fluid dynamic loads on the stresses within a plaque and the role of fluid dynamics in plaque rupture. Experiments have demonstrated that plaques behave in a viscoelastic manner with radial compressive mechanical properties strongly affected by the underlying histological structure (43). The time-dependent behavior of plaque tissue suggests that the rate of change of pressure in the lumen may be an important factor in determining the stress field in the plaque.

Many studies of normal arterial mechanics have been performed by inflating arteries and measuring changes in radial, circumferential, and axial dimensions (44,45). Normal human abdominal aorta tested by inflation and measurement of circumferential dilation demonstrated static circumferential stiffness in the range of 500 to 1500 kPa for applied circumferential stresses of about 19 and 41 kPa, respectively (46). Other investigators have cut arteries into circumferentially or axially oriented strips and measured deformations under static and dynamic uniaxial

tensile loads (47,48). Previous work in the area of plaque mechanics includes study of radial moduli in static and dynamic compression (43,49) and circumferential moduli and fracture properties under static and dynamic tensile loads (50,51). Previous measurements of radial compressive stiffness of plaques classified by intravascular ultrasound gave average stiffnesses of nonfibrous, fibrous, and calcified plaques of 41.2 ± 18.8 kPa, 81.7 ± 33.2 kPa, and 354.4 ± 245.4 kPa, respectively (49). Lee found a significant relation between the mechanical properties of the specimen as measured by static radial stiffness and the composition as described by ultrasound class ($p=0.0002$).

Since plaque and artery tissues have similar properties in the circumferential (θ) and axial (z) directions which differ from the properties in the radial (r) direction, they belong to a class of orthotropic materials termed "transversely isotropic" with r-θ and θ-z as principal planes. Five material parameters therefore completely describe the mechanical properties of the material (52):

$$E_r,\ E_\theta,\ \nu_{r\,\theta},\ \nu_{\theta z},\ G_{r\,\theta}$$

E_r and E_θ are the Young's moduli in the radial and circumferential directions, respectively, where E_i is the ratio of normal stress in the i-direction (σ) to normal strain in the i-direction. $\nu_{r\,\theta}$ and $\nu_{\theta z}$ are the Poisson's ratios in the r- θ and θ-z planes, respectively, where ν_{ij} is the ratio of negative transverse strain in the i-direction to imposed normal strain in the j-direction:

$$\nu_{ij} = -\text{strain}_i/\text{strain}_j \qquad (1.2)$$

$G_{r\,\theta}$ is the shear modulus in the r- θ plane where G_{ij} is the ratio of the i-j component of shear stress to the i-j component of shear strain.

Purpose. The goal of this research is to characterize the mechanics of acute atherosclerotic plaque rupture, the major antecedent of transmural myocardial infarction. There are three major objectives. First, fluid flow experiments have characterized the hydrodynamic forces on the surface of vascular stenoses, including turbulent pressure fluctuations. Second, the static anisotropic mechanical properties of plaque constituents in human post-mortem specimens were studied and compared to histological studies for cellular content, elastin, collagen, and calcium. Third, the effects of static mean pressure loads on the stress fields in plaques were studied using finite element computer models of idealized and real coronary artery plaques. In addition, a preliminary model of the mechanical behavior of atherosclerotic arteries under angioplasty conditions was developed.

CHAPTER 2

THE ROLE OF TURBULENCE IN PLAQUE RUPTURE

ABSTRACT

Turbulence frequently develops when blood passes through a stenosis. To study the hypothesis that turbulence near a plaque surface can cause pressure fluctuations that may promote plaque rupture, models of intravascular stenoses were studied. Experimental conditions simulated peak flow in the coronary and carotid arteries through a stenosis of 80 or 90% diameter reduction into a region where the plaque had widened distally to a 50-75% stenosis. For symmetric stenoses under carotid artery flow conditions, peak pressure fluctuations were observed 1-1.5 upstream diameters distal to the stenosis, but there were no significant turbulent pressure fluctuations under coronary flow conditions. Stenosis asymmetry strongly increased the intensity of turbulent pressure fluctuations at flows simulating carotid flow and resulted in significant pressure fluctuations for coronary flow conditions. Increasing stenosis severity from 80 to 90% increased the root mean square pressure fluctuations 3.6-fold. These studies predict peak-to-peak pressure fluctuations of 15 mmHg in a 90% asymmetric coronary stenosis; it is possible that turbulence may play a role in acute damage of atherosclerotic plaques, particularly in asymmetric stenoses (18).

INTRODUCTION

This study was designed to test the hypothesis that under appropriate flow conditions an intense turbulent flow stream may impinge on the plaque itself distal to the most severe portion of the stenosis. A second goal of the study was to examine the influence of stenosis severity and asymmetry on the magnitude of turbulent pressure fluctuations at the wall of a long stenosis.

METHODS

Measurements of turbulent pressure fluctuations were made along the walls of rigid model vascular stenoses in steady flow. Four axisymmetric models and one asymmetric model were machined from acrylic according to the specifications given in Fig. 2.1, Table 2.1, and Fig. 2.2. The exit angle was kept constant at 59.5^{o}. Although at exit angles less than $\sim 10^{o}$ flow separation and turbulence may not occur, previous studies indicate that severity of the stenosis is the primary determinant of jet kinetic energy for a given flow rate (32, 53). Stenosis severity was characterized by percentage diameter reduction. The asymmetric stenosis had a proximal severity of 90% and a downstream area of 0.49 cm^2, representing an 84% distal reduction in area from the upstream area.

Pressure taps similar to those of Tobin and Chang (33) were installed at regular intervals distal to the most severe region of the stenosis. Distance downstream from the most severe region of the stenosis (x) is expressed in the dimensionless form by x/D, where D is the diameter upstream of the stenosis. For

each of the five stenosis models, pressure taps were located at x/D = 0.25, 0.5, 1.0, 1.5, 2.0, and 2.5. These ports were constructed by use of 1.6-cm-long, flat-tipped, 16-gauge (1.2-mm ID) stainless steel needles that were mounted radially into the side of the model with their tips communicating with the stenosis wall via 0.5-mm-long, 0.7-mm-diameter holes.

Pressure fluctuation measurements were made with a Kistler Instrument model 206 High Sensitivity Pressure Transducer with a sensitivity of 2.41 mV/mmHg, a nominal resolution of 0.037 mmHg root mean square (rms), and a noise level of 0.019 mmHg rms within the frequency range of interest. The transducer signal was amplified by a Kistler model 504E4 amplifier. An acrylic transducer housing was attached via a Luer-Lok adapter to the port to be monitored.

The model stenosis was connected proximally and distally to 2.5-cm internal diam flexible polyvinyl chloride tubing. Flow was controlled by varying the liquid level in the supply tank, which held 40 liters of room temperature normal saline, or with two parallel mounted valves (6- and 12-mm ID) located distal to the test section and flow probe. Flow rate was measured with an electromagnetic flowmeter (Carolina Medical Electronics model 501) and flow probe (model EP300A). The flow probe was positioned 30 cm downstream of the model stenosis, and the flowmeter was calibrated according to manufacturer's specifications by measurement of the time for 3 liters of saline to drain from the supply tank and comparison of this average flow rate with the average of the starting and ending flowmeter voltages. Calibration trials with various valve settings and initial tank heights demonstrated

that the flowmeter gave a linear response within the range of flow rates used in the experiment. A MASSCOMP model 5440 data acquisition system with Laboratory Workbench software and a Hewlett-Packard model 54200A/D digitizing oscilloscope were used to monitor the pressure fluctuations and flow rate. Flow conditions simulated peak coronary flow at rest of $50<Re<150$ and peak carotid flow at rest of $250<Re<600$. For calculations of Re, the kinematic viscosity (μ/ρ) for blood was taken to be 0.034 cm^2/s (54) and the kinematic viscosity for room temperature normal saline was taken to be 0.01 cm^2/s.

Pressure transducer signals were continuously averaged, and the variance about the mean was calculated. From the variance, P_{rms} was derived according to equation 2.1.

$$P_{rms} = \sqrt{\text{variance in P}} \qquad (2.1)$$

Pressure data were adjusted for no-flow noise by subtracting the no-flow P_{rms} from the measured P_{rms}. Only P_{rms} values greater than twice the noise level were considered to be significant. P_{rms} was expressed in dimensionless form as $P_{rms}/\rho U^2$.

Measurements of mean pressure drop across the stenosis (ΔP_{mean}) were made with Validyne model DP-15-20-NS54A and DP-45-26-2114 differential pressure transducers. ΔP_{mean} was defined as the pressure difference between points, one upstream vessel diameter ahead of and one upstream vessel diameter after the most

severe constriction. The pressure transducers were calibrated against water manometers.

RESULTS

P_{rms} on the surface of the stenosis was critically dependent on stenosis severity and distance downstream of the stenosis (Fig. 2.3a and 2.3b). For 90% axisymmetric stenoses with flow rates corresponding to $250<Re<600$ (in the carotid artery range), peak P_{rms} (P^*_{rms}) occurred at $0.5<x/D<1.5$. Pressure fluctuations were insignificant immediately distal of the point of minimum diameter. For $x/D>1.5$, pressure fluctuations gradually diminished due to the decay of turbulence so that at x/D of 2.5 they were below the noise level of the transducer. Decreasing stenosis severity from 90 to 80% decreased P^*_{rms} by a factor of 3.6 for Re = 600. There were no measurable turbulent pressure fluctuations for 90% axisymmetric stenoses with flow at Re = 60 (in the coronary arterial range).

The degree of diameter reduction in the distal portion of an axisymmetric model stenosis also influenced the magnitude and distribution of P_{rms}. As shown in Fig. 2.4a-2.4c, decreasing distal diameter caused P^*_{rms} to increase and the point of peak P_{rms} to move closer to the point of most severe constriction. This effect became more pronounced as Re increased. For $x/D>1$, P_{rms} was relatively insensitive to the degree of distal diameter reduction.

Stenosis asymmetry strongly increased the intensity of turbulent pressure fluctuations for both the coronary artery and carotid artery flow ranges (Fig. 2.5a-

2.5d). For Re as low as 60, P_{rms} was significant along the near wall (see Fig. 2.2) of the 90% asymmetric model stenosis with an 84% distal area reduction. At Re between 60 and 120, near-wall $P^*_{rms}/\rho U_2$ was 275 ± 50. Measurements of P_{rms} at Re = 60 were close to the limit of transducer resolution. On the near wall, P_{rms} peaked at $x/D<1.0$, indicating that the turbulent jet impinged on the wall very near to the most severe constriction. On the far wall, the profile of turbulent pressure fluctuations closely resembled that of a 90% axisymmetry stenosis model of 50% distal severity (75% distal area reduction) at the same Reynolds number.

The ratio of $P^*_{rms}/\Delta P_{mean}$ measured at $x/D=1.0$ was 0.01 for a 90% axisymmetric stenosis ($250<Re<600$, 50% distal diameter reduction). For a 90% asymmetric stenosis, $P^*_{rms}/\Delta P_{mean}$ measured at $x/D=1.0$ ranged from 0.03 to 0.06 ($60<Re<600$). Dimensional analysis using these model results and typical clinical measurements of mean pressure gradients across human arterial stenoses (55) gave $P^*_{rms}=2.4$ mmHg for a 90% asymmetric coronary stenosis (Re=60) and $P^*_{rms}=1.0$ mmHg for an axisymmetric carotid stenosis (Re=250) (see Table 2.2).

The ratio of maximum peak to peak turbulent pressure fluctuations to P^*_{rms} ranged from 4.5 to 7.0 for the 90% asymmetric stenosis model ($60<Re<600$), which indicated that high frequency (10-200 Hz) pressure excursions at least as large as 15 mmHg would be experienced along the luminal surface of an asymmetric coronary stenosis. The measured values of $P^*_{rms}/\rho U^2$ for the axisymmetric stenosis models were comparable with those measured in previous studies where the stenoses were modeled as short and axisymmetric (32,33).

DISCUSSION

Correlations have been found between coronary stenosis geometry and the risk of anterior myocardial infarction (14,15). The CASS showed that risk of myocardial infarction increased 7.5 times for 90-98% stenoses relative to stenoses of <50% severity. In addition, the risk increased 1.9 times for eccentric relative to axisymmetric stenoses (P = 0.06). In comparison, the model studies described here showed no significant turbulent pressure fluctuations for axisymmetric stenoses with flows in the coronary arterial range. However, stenosis asymmetry resulted in significant pressure fluctuations in the coronary arterial range. The CASS also demonstrated that risk increased as 1.7 times the length of stenosis that is >50% narrowed (with stenosis length measured in units of lesion diameter). The data from the current model studies showed that stenosis length has an important influence on turbulent pressure fluctuations at the stenosis surface; a stenosis shorter than one vessel diameter would show little effect of turbulence on its distal surface.

Our studies suggest that plaque rupture may initiate downstream of the most severe constriction in a stenosis. Fissures in plaque often extend longitudinally and no definitive data regarding initial location of fissuring of plaques are available. Therefore, it may be difficult to demonstrate turbulent plaque injury in humans. In fact, this study suggests that turbulence does not play a role in coronary plaque rupture when stenoses are axisymmetric or not severe.

When applied to asymmetric stenoses in human carotid and coronary arteries, the present model studies predict magnitudes of P^*_{rms} ranging between 1 and 6% of

the mean pressure drop across the stenosis (ΔP_{mean}; see Table 2.2) and peak to peak amplitude of turbulent pressure fluctuations as much as seven times P^*_{rms}. Although this study did not address frequency content of the turbulence, sampled spectra showed a character similar to previous reports; uniform energy content up to a certain frequency, then a sharp falloff for frequencies greater than this value (32). Based on this, the frequency of turbulent pressure fluctuations is most likely one to two orders of magnitude higher than that of the cardiac cycle (32). These may be important factors if plaques rupture either by reaching a critical yield stress or by reaching a fatigue limit after a certain number of load cycles.

The time-dependent behavior of plaque tissue suggests that the rate of change of pressure in the lumen may be an important factor in determining the stress field in the plaque. Richardson *et al.* (23) have used finite element computer modeling to propose that circumferential tensile stresses due to mean arterial pressure are important in plaque rupture. It is possible that turbulent fluctuations causing pressure excursions of >15 mmHg at frequencies 10-200 times higher than the heart rate could subject the plaque to significant additional mechanical stresses.

Limitations. There are several limitations to consider in this study. First, the model was rigid and not compliant. The rigid wall model neglects the effects of vessel wall compliance on the turbulent flow issuing from the stenosis, as have most previous model studies (32,40). Second, the flow was steady and not pulsatile. Therefore, the effects of unsteady velocity on wall pressure fluctuations were neglected (40). Third, the asymmetric stenosis represented an idealized stenosis

because the surface was flat. "Halfmoon" geometries have been seen in clinical stenoses, although the borders between plaque and normal lumen tend not to be sharp (56).

CONCLUSIONS

A turbulent jet may impinge on a stenosis surface distal to the most severe constriction. The amplitude of pressure fluctuations is dependent on Reynolds number, length of the stenosis, and severity of the stenosis but is especially elevated in stenoses with asymmetric geometry. For axisymmetric stenoses, turbulence is less likely to play a role in plaque injury, particularly in the coronary artery.

Table 2.1 Dimensions of axisymmetric stenosis models.

D_c (cm)	Proximal Dia. Reduction (%)	D_d (cm)	Distal Dia. Reduction (%)
0.4	80	1.0	50
0.2	90	1.0	50
0.2	90	0.75	62
0.2	90	0.50	75

Table 2.2 Pressure effects on wall of human arterial stenosis.

Pressure term (mmHg)	Frequency (Hz)	Coronary Stenosis (90%, asym., Re=60)	Carotid Stenosis (90%,axisym.,Re=250)
ΔP_{mean} (measured)	1	80	100
Peak P_{rms} (predicted)	10-200	2.4	1.0
Max. $P_{peak\text{-}peak}$ (predicted)	10-200	15	6.0

Given typical clinical measurements of mean pressure drop across human arterial stenoses (55), the model studies predict P_{rms}=2.4 mmHg on the surface of a coronary stenosis (90% stenosis, asymmetric, Re=60) and P_{rms}=1.0 mmHg on the surface of a carotid stenosis (90% stenosis, axisymmetric, Re=250). Peak to peak turbulent pressure fluctuations may be up to seven times greater.

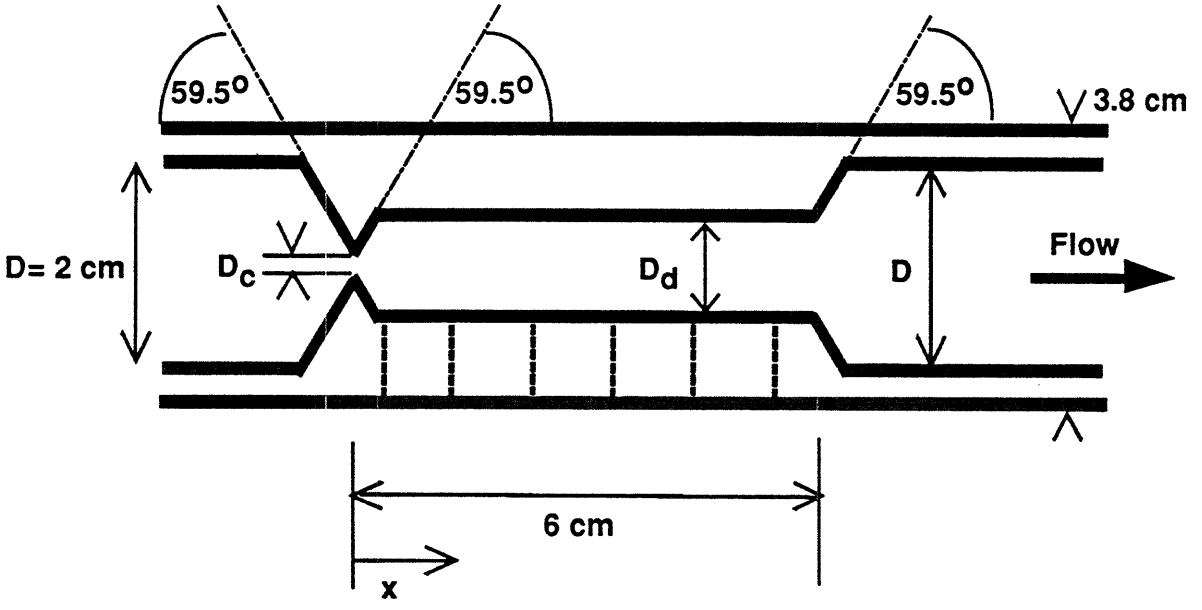

Fig. 2.1 Schematic of axisymmetric stenosis models. The rigid acrylic models simulated an artery with an atherosclerotic plaque of 80 or 90% proximal severity widening into a region of 50 to 75% distal severity. An axisymmetric turbulent jet from the most severe region of the stenosis impinges on the distal plaque surface.

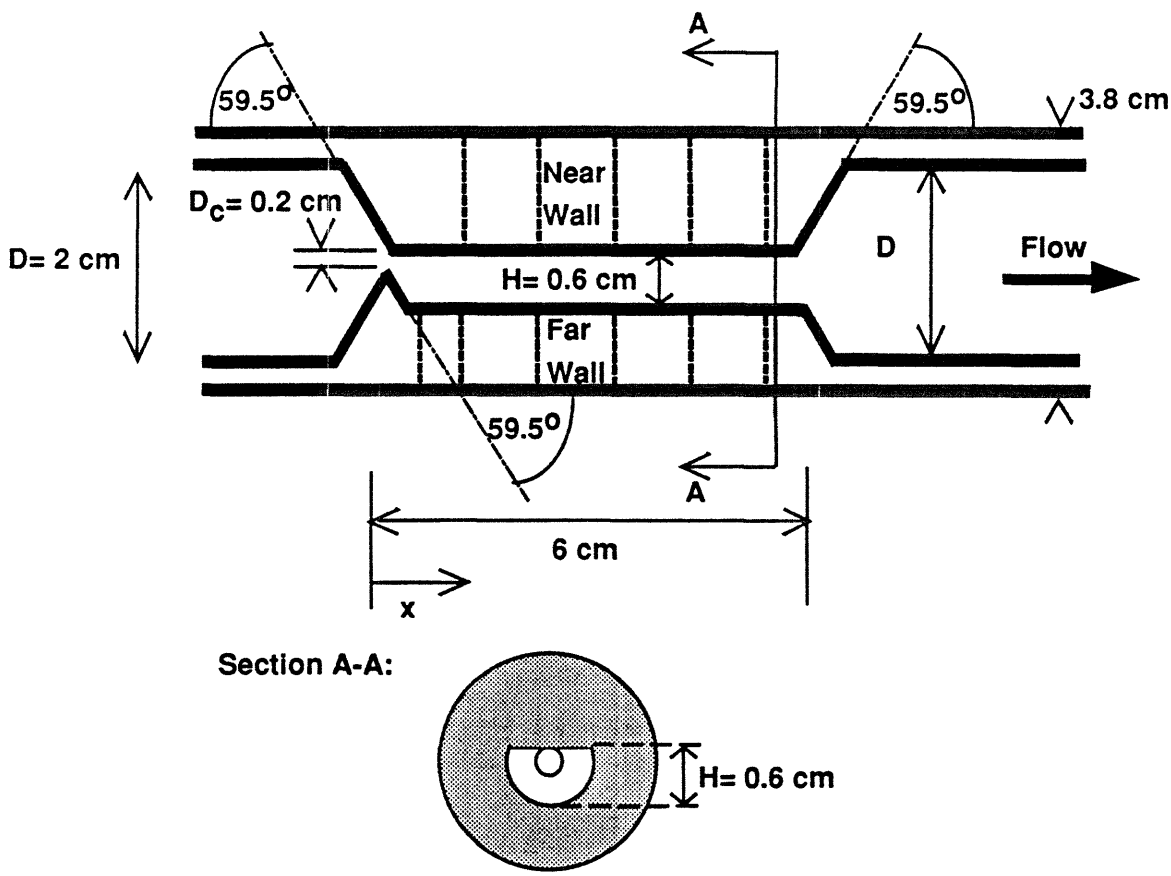

Fig. 2.2 Schematic of asymmetric stenosis model. The rigid acrylic section modeled an artery with an atherosclerotic plaque of 90% proximal severity widening distally to the asymmetric section A-A. A turbulent jet from the most severe region of the stenosis impinges directly on the near wall.

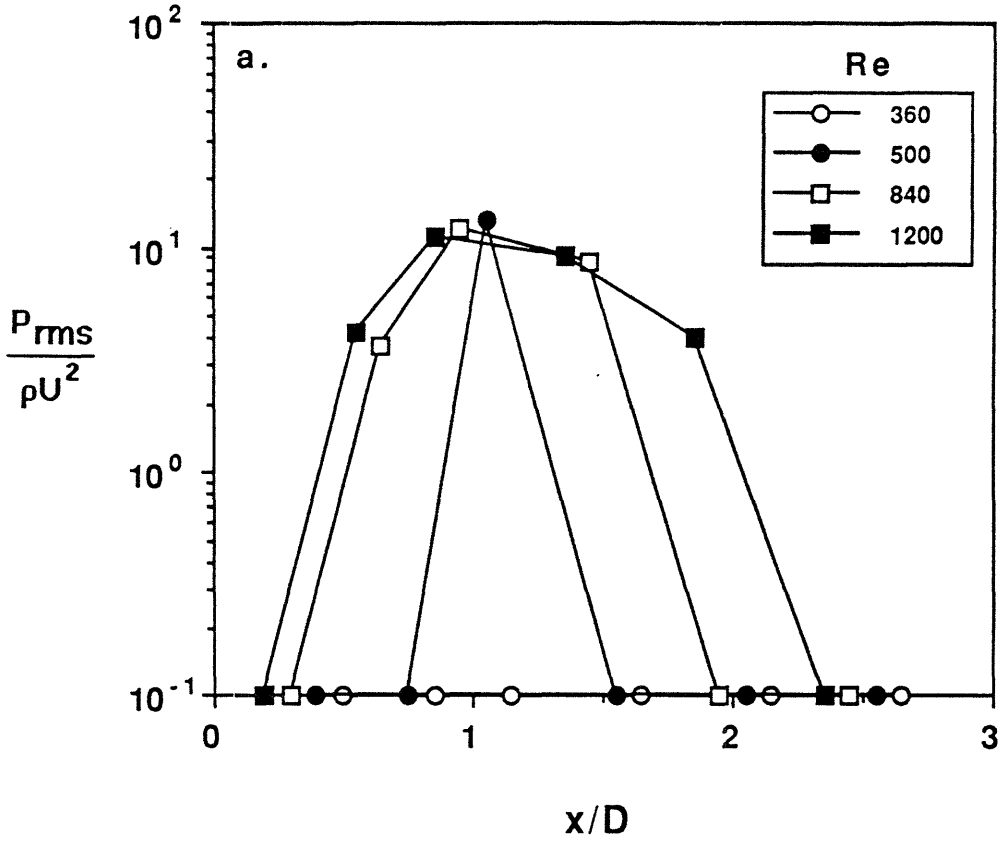

Fig. 2.3 Influence of stenosis severity and length P_{rms} for two axisymmetric stenosis models (50% distal diameter reduction): (a) a stenosis of 80% proximal diameter reduction and (b) a stenosis of 90% proximal diameter reduction. P_{rms} peaks at $1<x/D<1.5$. Increased stenosis severity increased peak P_{rms}. Turbulent pressure fluctuations were significant for flows in the carotid artery range but not for flows in the coronary artery range of Re. On the log scale of $P_{rms}/\rho U^2$, a value of 10^{-1} represents points where the pressure signal did not rise above the noise level.

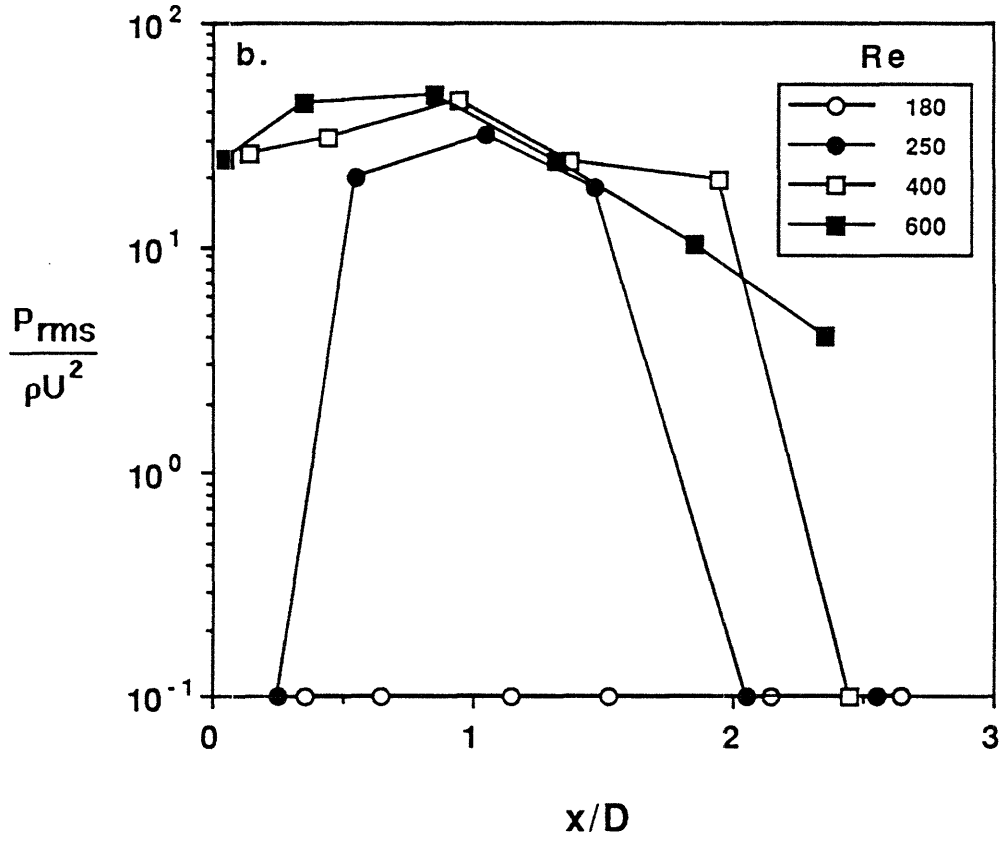

Fig. 2.3b 90% stenosis.

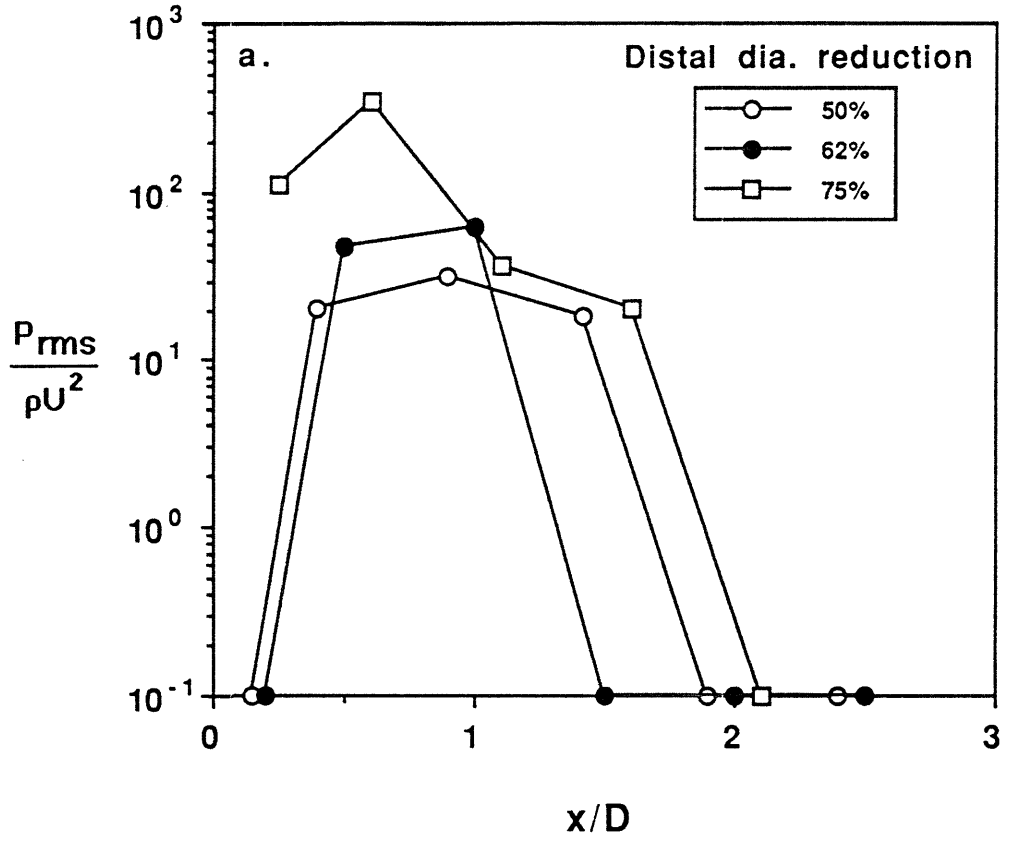

Fig. 2.4 Influence of distal diameter reduction on P_{rms} for three axisymmetric stenosis models (90% proximal diameter reduction) at three Reynolds numbers: (a) Re=250, (b) Re=400, and (c) Re=600. When distal diameter decreases, peak P_{rms} increases and occurs at a point closer to the region of most severe constriction, especially for higher Reynolds numbers. On the log scale of $P_{rms}/\rho U^2$, a value of 10^{-1} represents points where the pressure signal did not rise above the noise level.

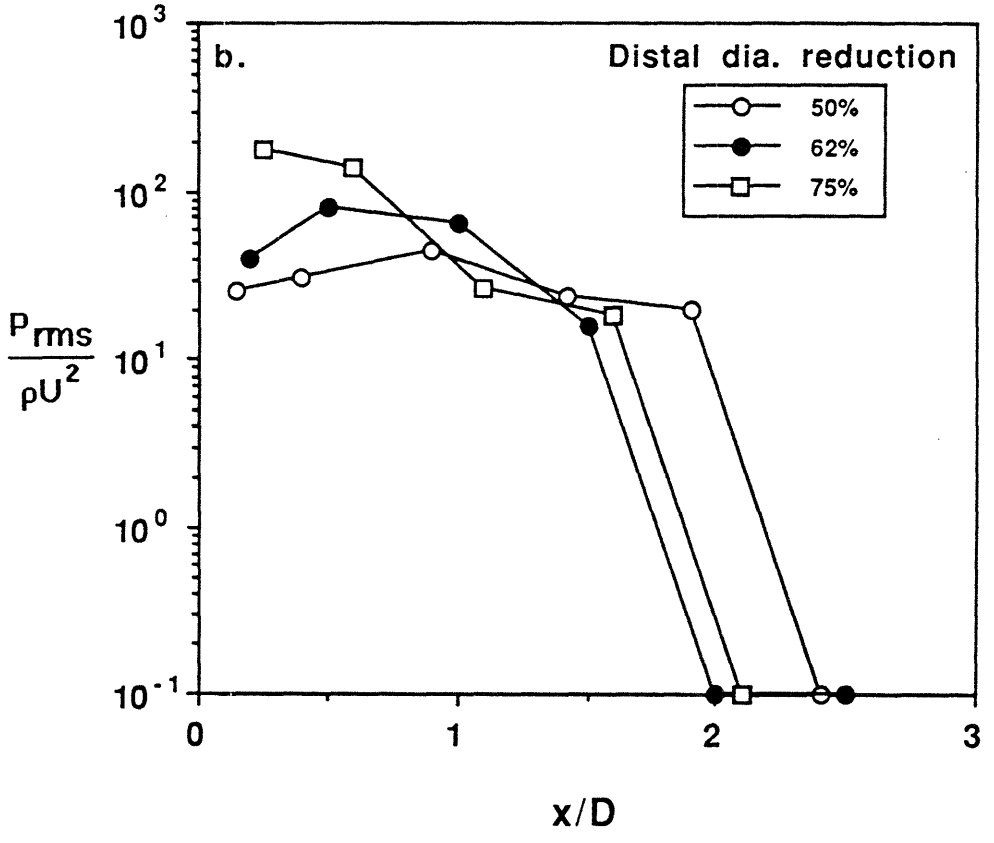

Fig. 2.4b Re=400.

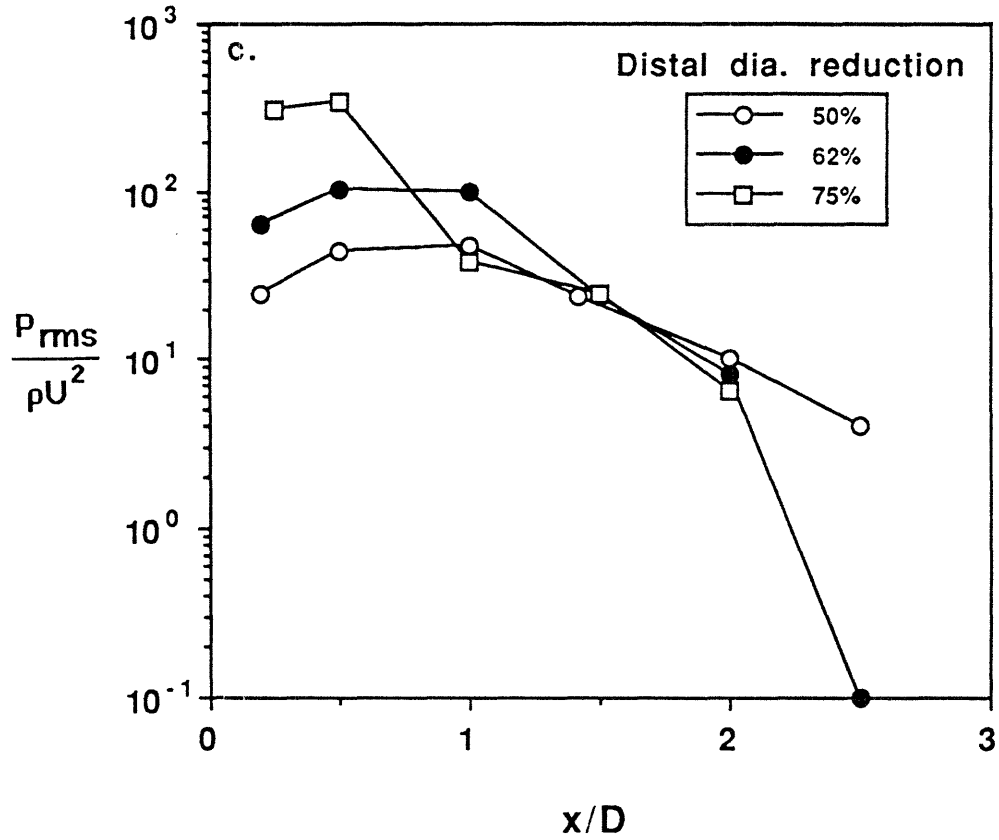

Fig. 2.4c Re=600.

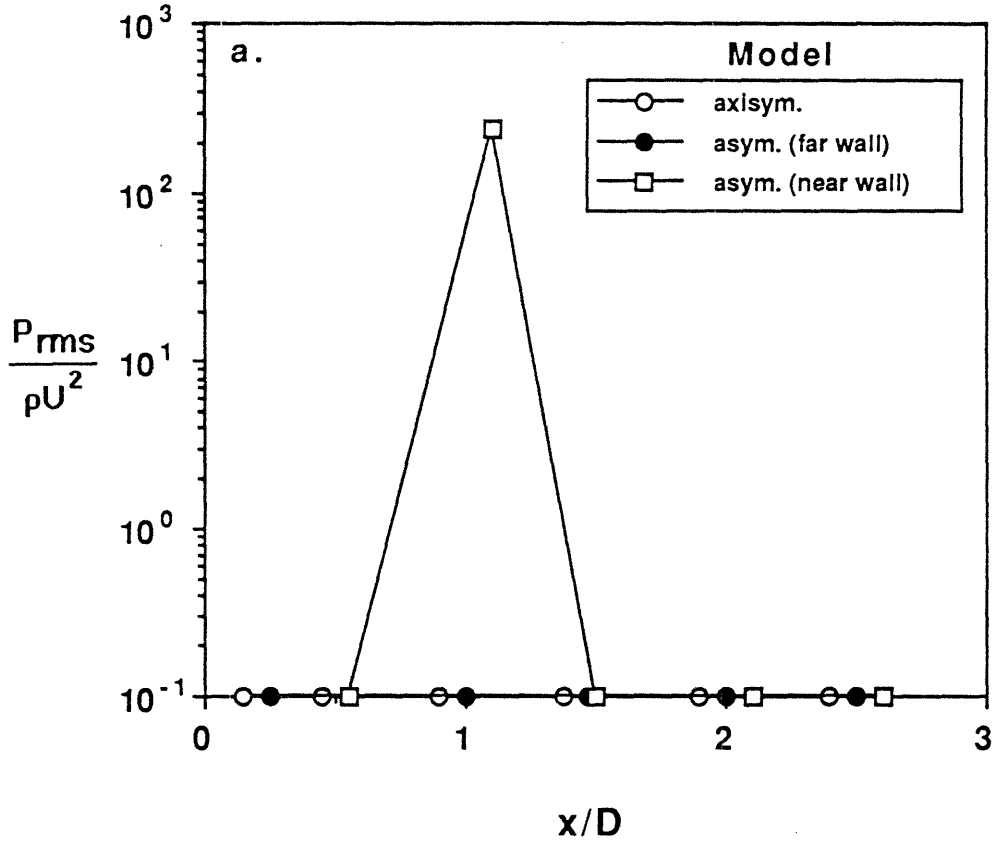

Fig. 2.5 Influence of asymmetry on P_{rms} for two stenosis models (90% proximal diameter reduction, 50% distal diameter reduction) at four Reynolds numbers: (a) Re=60, (b) Re=180, (c) Re=250, (d) Re=600. Asymmetry strongly increases P_{rms} for both coronary and carotid artery flow ranges. For Re as low as 60, P_{rms} was significant along the near wall and peaked at x/D<1.0. Profiles for the far wall resembled those of an axisymmetric stenosis. On the log scale of $P_{rms}/\rho U^2$, a value of 10^{-1} represents points where the pressure signal did not rise aboue the noise level.

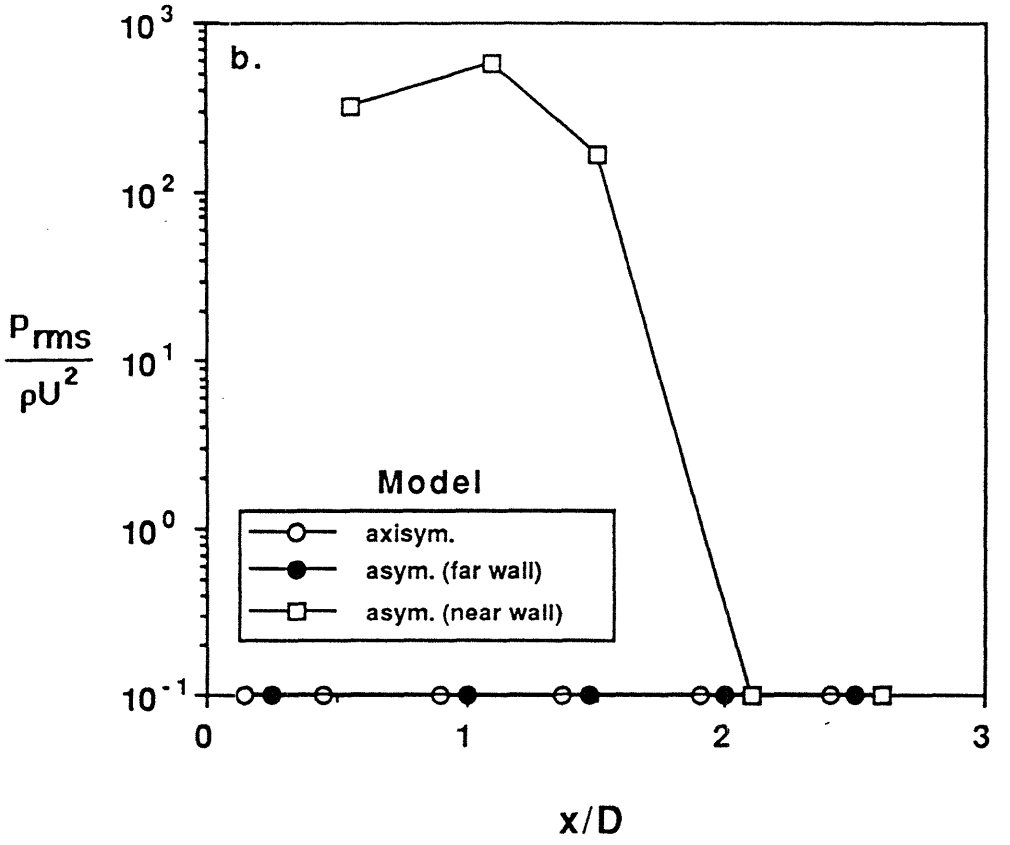

Fig. 2.5b Re=180.

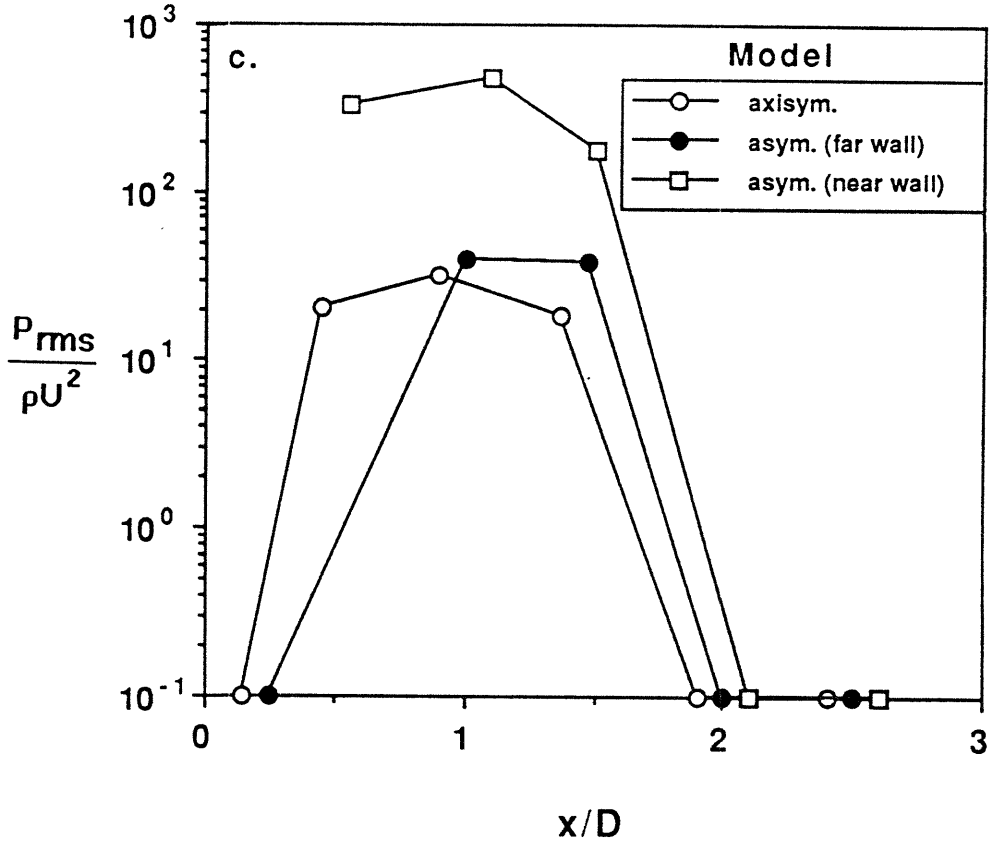

Fig. 2.5c Re=250.

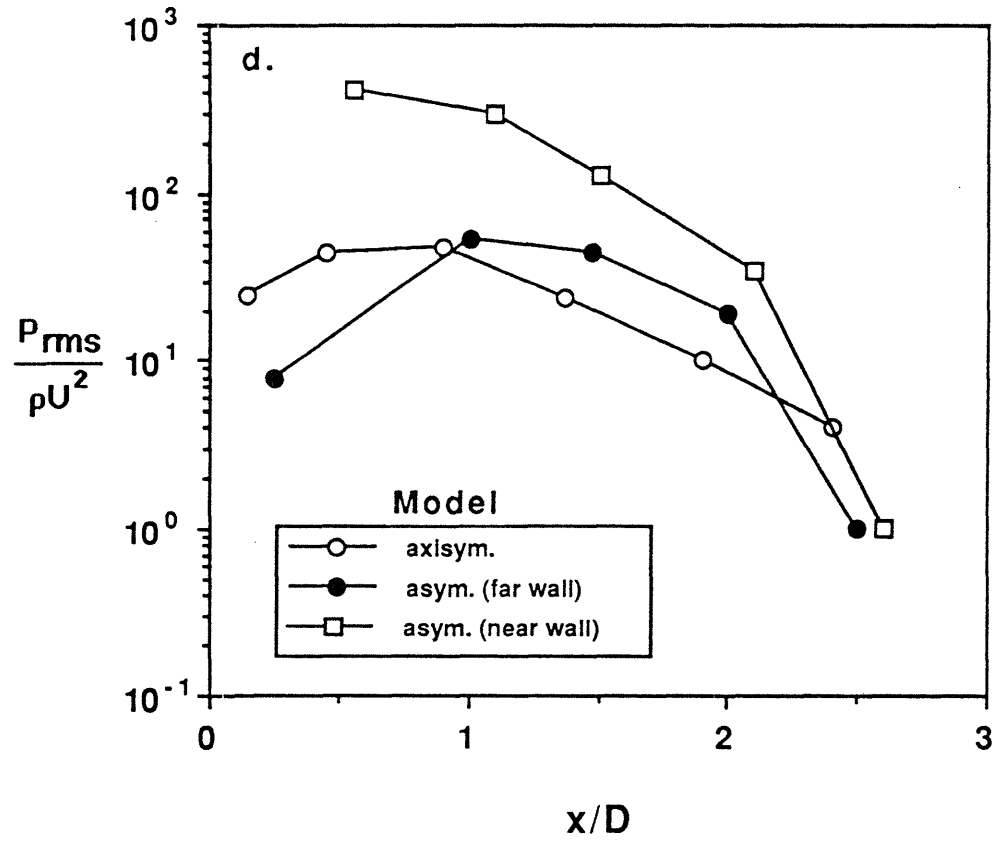

Fig. 2.5d Re=600.

CHAPTER 3

PROPERTIES OF PLAQUE IN CIRCUMFERENTIAL TENSION

ABSTRACT

The mechanical properties of atherosclerotic plaque may be of critical importance to the processes of plaque rupture, the most common antecedent of myocardial infarction. To investigate the effects of plaque structure and applied stress on the static circumferential tensile stiffness of atherosclerotic plaque, the stress-strain behavior of 26 human aortic intimal plaques was studied. Intimal plaques were collected during routine autopsies of 21 patients from the abdominal (n=19) and thoracic (n=2) aorta and were classified by histological analysis as cellular (n=12), hypocellular (n=9), and calcified (n=5). At a physiologic applied circumferential stress of 25 kPa, the stiffnesses of cellular, hypocellular, and calcified specimens were 927 ± 468 kPa, 2312 ± 2180 kPa, and 1466 ± 1284 kPa, respectively. In tension the average static circumferential stiffness for each histological class was similar (p=0.112). Hypocellular plaques were, on average, approximately twice as stiff as cellular plaques. Post hoc testing demonstrated a nonsignificant difference in stiffness at 25 kPa stress between specimens classified as cellular and hypocellular (p=0.098), cellular and calcified (p=0.410) and hypocellular and calcified (p=0.380). All 26 plaques tested demonstrated a change in stiffness throughout the range of applied stress used in this study. The increase in static tensile stiffness with applied circumferential stress was highly significant for specimens classed as cellular and

hypocellular ($p<0.001$) and significant for specimens classed as calcified ($p=0.015$). We conclude that the static circumferential tensile stiffness of atherosclerotic plaque is not significantly affected by the degree of cellularity and calcification determined by histological characterization. Static tensile stiffness increased with applied circumferential stress, an effect that was statistically highly significant for cellular and hypocellular plaques. Cellular and hypocellular plaques exhibit strongly anisotropic properties in the physiologic range of loading, with circumferential tensile stiffness about 20 times greater than previously reported measurements of radial compressive stiffness.

INTRODUCTION

The current study tested plaques at physiologic loads to obtain values of plaque stiffness. These may be useful as representative values for intrinsic material properties in numerical models of spontaneous plaque rupture. In addition, the study tested plaques at loads above the physiologic level, providing data that may allow modeling of plaque deformation and fracture during percutaneous transluminal coronary angioplasty (PTCA), a widely used clinical procedure for the treatment of coronary artery disease (57).

METHODS

Specimens. Aortic plaques were selected to provide large, flat specimens amenable to uniaxial mechanical tensile testing. Twenty-six fibrous caps from human atherosclerotic plaques were harvested from the aortas of 21 patients during routine autopsies at Brigham and Women's Hospital, the Beth Israel Hospital, and the New England Deaconess Hospital, Boston, MA. Eleven of the patients were male and the mean age of the patients was 68±12 years. In 17 patients, one specimen was obtained; in three patients, two specimens were obtained; and in one patient, three specimens were obtained. Specimens were visibly uncomplicated and at least 5 mm from a vessel ostium, with no overlying thrombus or surface fracture. In 19 patients, specimens were taken from 2 cm wide circumferential strips from the abdominal aorta between the renal arteries and the bifurcation. In two patients, the specimens were taken from circumferential strips from atherosclerotic thoracic aorta. A custom-designed die was used to cut tensile specimens from the strips, with the geometry shown in Fig. 3.1 (47). This geometry was chosen because it limited the effects of specimen clamping on the measured tensile behavior in the narrow gauge section. After cutting, the specimen was dissected free of adventitia, media, and necrotic plaque components. Specimens were placed in normal saline and refrigerated until use, within 36 hours of death.

Mechanical Testing Apparatus. Mechanical testing was performed using an ultrasensitive, servo-controlled mechanical spectrometer (Dynastat, IMASS, Hingham, MA) at room temperature. A continuous normal saline drip was used in an effort

to maintain normal tissue water saturation. A stainless steel tensile testing apparatus was fitted to the spectrometer which included an upper clamp with universal joint and saline drip line and a lower clamp with centering jaws and drip basin. The clamp jaws were sandblasted to provide a frictional surface. The spectrometer used a 10 kg load cell calibrated at zero and 1.000 kg (±0.002 kg error) and included a crosshead displacement gauge calibrated to 500 μm/volt. The voltage signal from the load cell was filtered through a 4.5 Hz low pass filter and the voltage signal from the displacement gauge was filtered through a 1.5 Hz low pass filter (model 1022F-01, Rockland, Tappan, NY). Both signals were displayed on a strip chart recorder (model 2007-2202, Gould, Cleveland, OH).

To measure specimen thickness in a noncompressed state, a micrometer gauge was developed that incorporated an electrical impedance measurement. A micrometer head (model 261L, L.S. Starrett Co., Athol, MA) was fit into a Delrin caliper body with a comparator circuit based on a 741 operational amplifier chip monitoring impedance across the caliper contracts. Before installing the tensile specimen in the spectrometer, a thickness measurement was made at the middle (gauge) section of each specimen. The average specimen thickness was 1.2±0.4 mm. The specimens were of nonuniform thickness throughout the gauge section; the standard error of estimates of thickness was 0.1 mm. Therefore, the changes in specimen thickness between equilibrium loading states could not be detected, and only the initial unloaded thickness measurement was used for stress calculations.

To isolate strains in the specimen gauge section, where a true uniaxial tensile stress field exists, an optical displacement measuring system was used (47). Under a dissecting microscope, four 300 μm fluorescent orange microspheres (58) were attached to the corners of each specimen gauge section with cyanoacrylate adhesive. A 9.5 mm thick lucite camera base rigidly supported a 35 mm camera (model N6000, Nikon, Japan) and was securely clamped to the spectrometer. The camera was fit with a Micro-Nikkor 60 mm f2.8 lens, a Nikon PK-13 27.5 mm extension, a +2 close up lens, a 62 mm orange filter, a 62 mm ultraviolet filter (Hoya, Japan) and a pneumatic shutter release. The camera was set to manual mode with an aperture of 5.6 and an exposure time of 1 sec, and used Kodak Ektachrome 100HC slide film. During the experiment, the room was darkened and the specimen was illuminated with a 250 W long wavelength ultraviolet lamp (model B-100A, Ultra-Violet Products, San Gabriel, CA) to provide maximum contrast between the fluorescent microspheres and plaque tissue background.

Testing Protocol. To determine the proper range of circumferential tensile loads to test, the plaques were modeled as the homogeneous wall of a symmetric, isotropic, linear elastic thick walled cylinder with outer radius equal to twice the inner radius. For this geometry, typical of coronary plaques, the physiologic peak circumferential stress is equal to 1.67 times the mean luminal pressure: 22 to 31 kPa for a mean pressure of 100-140mmHg. The specimens were preloaded at a 0.025 kg load (a tensile stress of about 50 kPa). The spectrometer was adjusted to a steady load of zero and a photograph taken. Next, the specimen was subjected to a series

of three preconditioning cycles (46). The first two preconditioning cycles each comprised a steady 0.015 kg load (a tensile stress of about 30 kPa) for 20 min, followed by a steady 0.025 kg load for 20 min. A photograph was taken at the end of each load increment. The third cycle was identical to the previous cycles, except that the specimens were allowed to equilibrate at each load, defined as when the spectrometer crosshead displacement at each load changed by no more than 2% over 5 minutes.

After preconditioning, the specimen was progressively loaded by increments of 0.025 kg, and photographed after reaching equilibrium at each load. After reaching 0.300 kg, the load was progressively increased by increments of 0.100 kg until fracture occurred. Only those specimens which fractured within the gauge section were considered valid fracture data points (six of the 26 specimens tested). Fracture usually occurred before an equilibrium strain was reached; from the known fracture stress, fracture strain was extrapolated from a curve fit to stress-strain data as described below.

Data Analysis. The optical measurements of displacement were performed by projecting slides on a screen and recording the vertical and horizontal distances between the four beads in gauge section (±0.25% error by ten measurements). Engineering strains were calculated as the ratio of displacement from the zero loaded position to the original zero loaded bead-to-bead distances. The averages of the strains in the circumferential (θ) direction (ϵ_θ) and in the axial (z) direction (ϵ_z) for

the two pairs of beads were recorded for each load increment. Engineering tensile stress (σ_θ) was calculated according to the following equation:

$$\sigma_\theta = mg/wt \qquad (3.1)$$

where m is applied mass, g is the acceleration of gravity (9.8 ms^{-2}), w is the original gauge section width (4.8 mm), and t is the original gauge section thickness.

The stress versus strain data points were plotted and a cubic function was fit to the data (Sigma Plot, Jandel Scientific, Corte Madera, CA):

$$\sigma_\theta = A\epsilon_\theta + B\epsilon_\theta^2 + C\epsilon_\theta^3 \qquad (3.2)$$

The restrictions $A>0$, $B>0$, and $C>0$ were placed on the equation to ensure a monotonic function through the origin. For $0<\sigma_\theta<1000$ kPa, the largest real root of equation 3.2 was found by a method previously described (59). The derivative of equation 3.2 with respect to ϵ_θ was calculated both as a continuous function of ϵ_θ and as a continuous function of σ_θ. This derivative was called the circumferential tensile stiffness of the plaque specimen. The data were analyzed by analysis of variance and post hoc testing between classes was performed with Student's t test (Minitab, Minitab, Inc., State College, PA). In all testing, a value of $p<0.05$ was considered to be statistically significant; results are presented as mean ± SD. Patient identification was not included in the analysis, since only four patients yielded multiple specimens for the study.

Histological Studies. After mechanical testing, the gauge sections of the tensile specimens were preserved in formalin and later embedded in paraffin, cut in cross-section at 5-6 μm, and stained with hematoxylin and eosin. As illustrated in

Fig. 3.2a-3.2c, specimens were classified as cellular, hypocellular, or calcified in the manner previously described (43) by a pathologist who had no knowledge of the results of mechanical testing.

RESULTS

Of the 26 specimens tested, 12 were classified as cellular; nine were hypocellular; and five were calcified. Figures 3.3a-3.3c illustrate the stress-strain data for all the specimens of each class. Note that the data for each class show a large scatter, but tend to have similar stiffnesses at the maximum strain states. The stress-strain curves for hypocellular plaques tend to have a shorter "toe region" than for either cellular or calcified plaques. In other words, they exhibit the largest changes in stiffness at low strain states. Figure 3.4a shows the average tensile stiffness of each class of plaques across a range of tensile stresses near physiologic levels. At a physiologic applied circumferential stress of 25 kPa, the average stiffnesses of cellular, hypocellular, and calcified specimens were 927 ± 468 kPa, 2312 ± 2180 kPa, and 1466 ± 1284 kPa, respectively. There was a nonsignificant relation between the mechanical properties of the specimen as measured by static circumferential stiffness and the composition as described by histological class ($F=2.42$, $p=0.112$). Hypocellular plaques were, on average, approximately twice as stiff as cellular plaques. Post hoc testing demonstrated a nonsignificant difference in stiffness at 25 kPa stress between specimens classified as cellular and hypocellular ($p=0.098$), cellular and calcified ($p=0.410$) and hypocellular and calcified ($p=0.380$).

The static circumferential tensile stiffnesses are recorded in Table 3.1 and Fig 3.4b for each class of plaques across a range of applied stresses. All 26 plaques tested demonstrated a change in stiffness throughout the range of applied stress used in this study. The effect of applied circumferential stress on static stiffness was highly significant for specimens classed as cellular and hypocellular ($p<0.001$) and significant for specimens classed as calcified ($p=0.015$).

Table 2 illustrates the change in static circumgerential tensile stiffnesses for each class fo plaques across a range of physiologic strain states. At a 1% strain state, the average stiffnesses of cellular, hypocellular, and calcified specimens were 184 ± 248 kPa, 1736 ± 2630 kPa, and 872 ± 1725 kPa, respectively. At this strain state, there was a nonsignificant relation between plaque static circumferential stiffness and the composition as described by histological class ($F=2.10$, $p=0.145$). Hypocellular plaques were, on average, approximately ten times stiffer than cellular plaques at 1% strains. All plaque classes demonstrated a wide variability in stiffness at the given strain states, with standard deviations on the order of the mean. Post hoc testing demonstrated a nonsignificant difference in stiffness at 1% strain between specimens classified as cellular and hypocellular ($p=0.120$), cellular and calcified ($p=0.420$), and hypocellular and calcified ($p=0.470$). There was a change in circumferential tensile stiffness throughout the range of strain states in this study. The effect of strain on static stiffness was significant for specimens classed as cellular ($F=4.01$, $p=0.001$), but not significant for specimens classed as hypocellular ($F=1.96$, $p=0.088$) and calcified ($F=0.55$, $p=0.766$).

Of the 26 specimens tested, six fractured within the gauge section, as shown in Fig. 5. Three of these specimens were classed as cellular, one was hypocellular, and two were calcified. The fracture stresses ranged from 149 to 701 kPa, with a mean of 484±216 kPa. The fracture strains extrapolated from the cubic curves fit to the data ranged from 0.15 to 0.60, with a mean fracture strain of 0.30±0.16.

DISCUSSION

The measurements of plaque circumferential tensile stiffnesses were comparable to measurements of normal artery and plaque stiffness obtained by other investigators. The fact that there is little statistically significant difference in the static tensile stiffness of histologically different groups of plaques suggests that in tension, the collagen network found in all plaques dominates mechanical behavior, rather than the cellular constituents or regions of calcification. In radial compression, other extracellular or cellular components may dominate and therefore lead to the significant differences between nonfibrous (cellular), fibrous (hypocellular), and calcified plaques found by Lee *et al* (49). It can be seen that cellular and hypocellular plaques exhibit strongly anisotropic properties in the physiologic range of loading, with circumferential tensile stiffness about 20 times greater than radial compressive stiffness.

The results of testing plaque tensile fracture stress were comparable to those obtained by other investigators. Using a similar apparatus, Mohan and Melvin measured a comparable average ultimate fracture stress of 1720 ± 890 kPa (47). In

another study of human coronary artery plaque specimens of different geometry, mean values of fracture stress were about 600 kPa for non-ulcerated plaques and about 200 kPa for ulcerated plaques (51). The plaque fracture stresses measured in this study are substantially higher than the expected peak physiologic circumferential stresses in circumferential coronary artery plaques of 20-30 kPa, based on homogeneous, linear elastic, isotropic thick walled cylinder theory. Finite element calculations of peak circumferential stresses in ruptured coronary lesions have demonstrated that a peak stress of 300 kPa may be associated with plaque rupture (Chapter 5). The measured fracture strains are much greater than the reported physiologic peak circumferential strains in coronary stenoses of 2-8% (41,42). Therefore, spontaneous plaque rupture must occur in the presence of local weakening of plaques, perhaps by cyclic fatigue or enzymatic degradation (29).

Limitations. There are three limitations in this study. First, true stress was not measured, even though the specimens underwent strains as large as 6%. Therefore, we draw a distinction between plaque stiffness (the local slope of the engineering stress-strain curve) and plaque modulus (an intrinsic material property). To calculate true stress the thickness (r-dimension) and width (z-dimension) of the specimen gauge section must be measured at each load increment. An attempt was made to measure gauge section thickness at each load increment, but the non-uniform thickness of the plaque made it impossible to distinguish any change in thickness with the instruments used. The same problem was encountered in previous investigations of this type using more sophisticated optical techniques of thickness

measurement (47). To predict the effects of specimen geometry change on calculated tensile stress, estimates were made for the Poisson's ratios $\nu_{z\theta}$ and $\nu_{r\theta}$ which relate imposed ϵ_θ to resulting strains in the z and r dimensions (ϵ_z and ϵ_r) where:

$$\nu_{z\theta} = -\epsilon_z/\epsilon_\theta \quad \text{and} \quad \nu_{r\theta} = -\epsilon_r/\epsilon_\theta \tag{3.3}$$

Using measurements of ϵ_θ and ϵ_z from cellular plaques, $\nu_{z\theta}$ was calculated and found to range from 0.1 to 2.5, with no apparent relation to applied stress or measured stiffness. Assuming that $\nu_{r\theta}=\nu_{z\theta}$, the predicted true stress ($\sigma_{\theta t}$) was calculated according to the modified form of equation 3.1:

$$\sigma_{\theta t}=mg/[wt(1-\nu_{z\theta}\epsilon_\theta)^2] \tag{3.4}$$

as a function of $\nu_{z\theta}$. Figure 3.6 shows $\sigma_{\theta t}$ plotted against circumferential extension ratio ($\lambda_\theta=1+\epsilon_\theta$) for a range of $\nu_{z\theta}$. The plot is based on engineering stress-strain data for a typical cellular plaque. For the maximum physiologic state of strain $\epsilon_\theta=8\%$ the true stress is no more than 18% greater than engineering stress for both Poisson's ratios equal to 1.0 and only 55% greater for $\nu_{r\theta}$ and $\nu_{z\theta}$ as great as 2.5. Compared to the effects of specimen to specimen variability, even a 55% error in stress may not have a significant effect on the slope of the average stress-strain curves for each class of plaques. Therefore, the plaque circumferential stiffnesses described in this study can be considered a good approximation to the intrinsic plaque circumferential moduli (E_θ) for the physiologic range of loading. Caution should be used when applying the data in this study to models of plaque deformation and fracture under super-physiologic loads, as in the case of PTCA.

The second limitation of this study is the assumption that all deformation of the plaque is due to strain of the solid constituents, neglecting the role of water loss from the plaque. Because specimens were loaded over time scales large enough for the specimen to reach an equilibrium state, changes in specimen thickness and width are probably due more to water flow out of the specimen than to transverse strains of solid components. For example, the value of $\nu_{r\theta}$ for normal artery has been calculated using assumptions of linear elasticity and incompressibility to be in the range of .71 to .80 (44). Using the assumption of a linear elastic transversely isotropic material with E_θ= 1000 kPa, E_r= 50 kPa (49), and $\nu_{z\theta}$= 0.27 (44), the physical requirements of a positive definite compliance matrix (52) dictate $\nu_{r\theta} < 0.20$. The higher values of $\nu_{r\theta}$ calculated by Patel may be due to equilibrium water loss. Thus, the elastic moduli and Poisson's rations alone may not adequately describe plaque mechanical behavior. A poroelastic material model accounting for hydraulic permeability, fluid volume fraction, and matrix stiffness would probably be more applicable (60).

The third limitation was the small amount of fracture data in the study. This was probably due to inhomogeneities in the specimens and may have been increased if the gauge section was made narrower. However, the specimen geometry was chosen because it allowed comparison of data with that of a previous study (47). Because of the small number of valid fracture data, it was not possible to correlate plaque fracture strength to histologic structure.

CONCLUSIONS

We conclude that the static circumferential tensile stiffness of atherosclerotic plaque is not significantly affected by the degree of cellularity and calcification as determined by histological characterization. Although hypocellular plaques are on average about twice as stiff as cellular plaques at physiologic ranges of tensile stress, the large variability in tensile properties within cellular and hypocellular histologic classes makes the difference statistically nonsignificant. Static tensile stiffness increased with applied circumferential stress, an effect that was statistically highly significant for cellular and hypocellular plaques. This is in marked contrast to static radial compressive stiffness, where it was previously observed that cellularity decreased stiffness and calcification increased stiffness (49). Cellular and hypocellular plaques exhibit strongly anisotropic properties in the physiologic range of loading, with circumferential tensile stiffness about 20 times greater than previously reported measurements of radial compressive stiffness. Plaques fracture at tensile stresses comparable to those found in previous studies, at stresses well above those caused by physiologic mean arterial pressure.

Table 3.1 Static circumferential tensile stiffness (in kPascals) of 26 human aortic plaque specimens classified by histological analysis as cellular, hypocellular, or calcified. Stiffness values are the slope of the cubic curve fit to stress-strain data at stresses of 25, 50, 100, 200, and 400 kPa. Values are mean ± SD.

	Average Stiffness for Histologic Class		
Applied Stress (kPa)	Cellular (n=12) (kPa)	Hypocellular (n=9) (kPa)	Calcified (n=5) (kPa)
25	927±468	2312±2180	1466±1284
50	1397±761	2908±2118	2136±1687
100	2160±1215	3955±2251	3224±2353
200	3385±1915	5784±2954	5228±3173
400	5527±2820	8908±4658	7970±4874

Table 3.2 Static circumferential tensile stiffness (in kPascals) of 26 human aortic plaque specimens classified by histological analysis as cellular, hypocellular, or calcified. Stiffness values are the slope of the cubic curve fit to stress-strain data at strains of .01, .02, .04, .06, and .08. Values are mean ± SD.

Strain	Average Stiffness for Histologic Class		
	Cellular (n=12) (kPa)	Hypocellular (n=9) (kPa)	Calcified (n=5) (kPa)
.01	183±248	1736±2630	872±1725
.02	282±328	2280±3098	1411±2785
.04	594±658	4107±5144	2858±5504
.06	1059±1173	6896±8691	4793±9013
.08	1679±1869	10653±13793	7213±13319

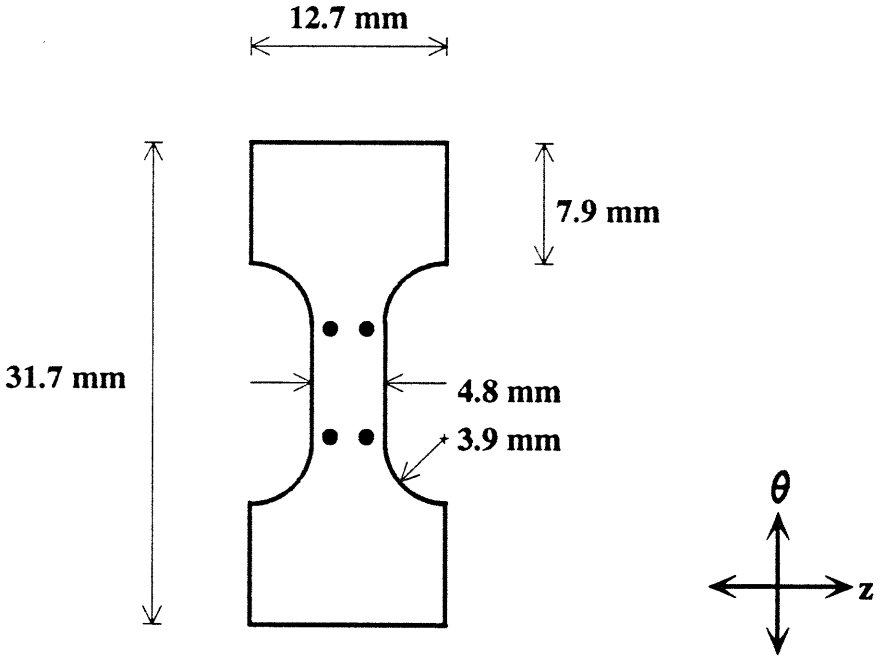

Fig. 3.1 Schematic of tensile test specimen.

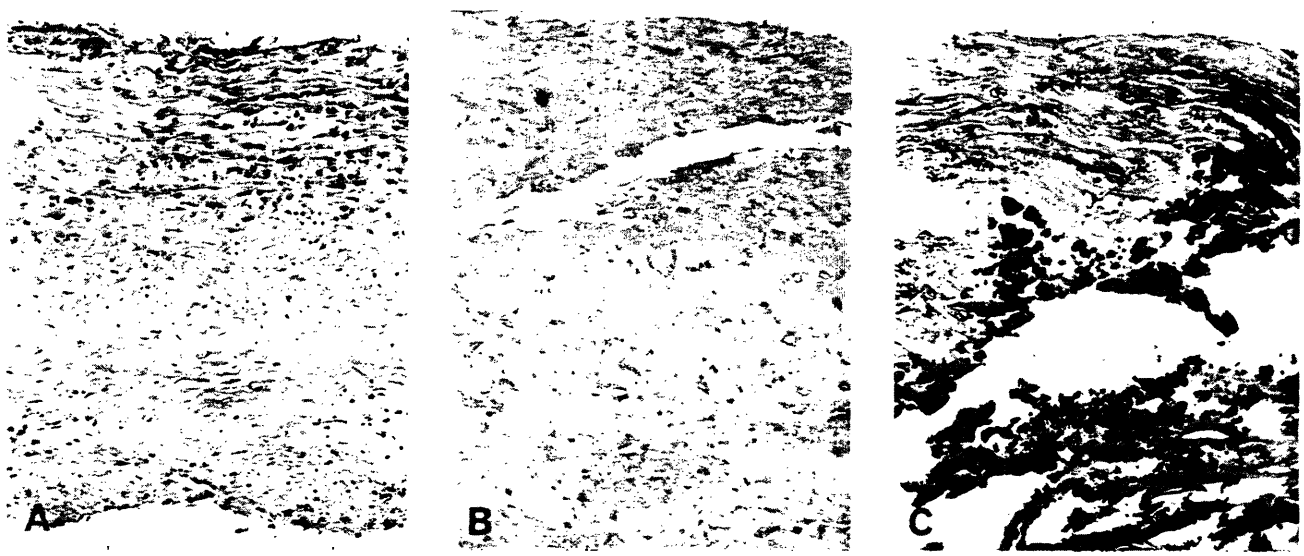

Fig. 3.2 Histology photomicrograph of a.) cellular, b.) hypocellular, and c.) calcified aortic intimal plaque.

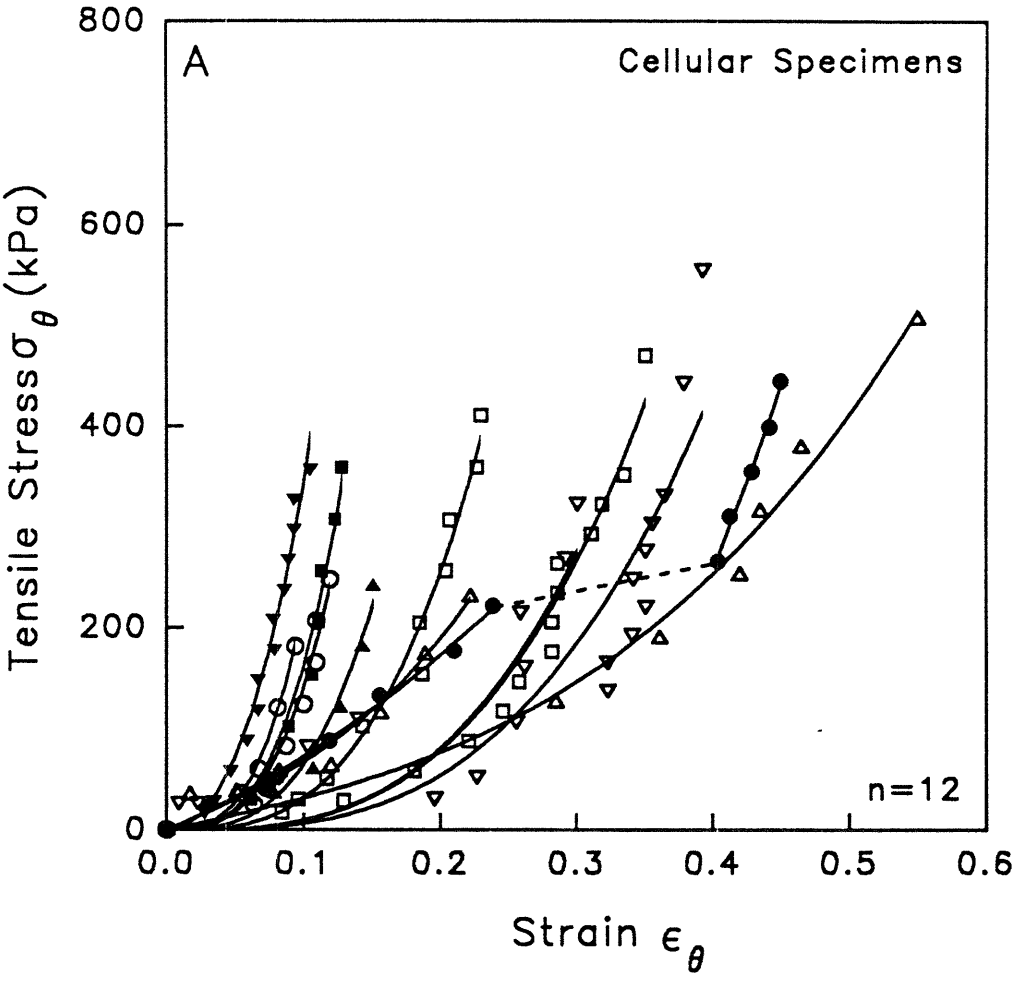

Fig. 3.3 Tensile stress-strain relation for a.) cellular, b.) hypocellular, and c.) calcified specimens.

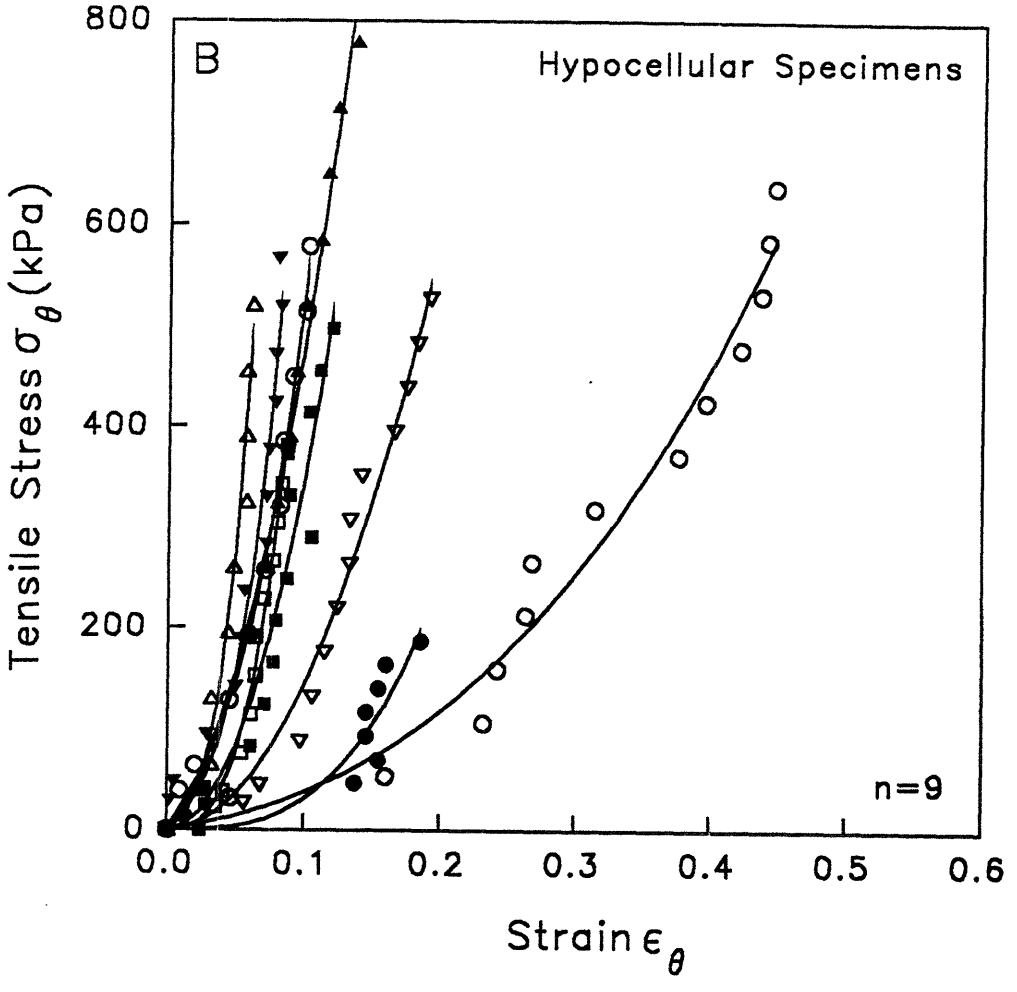

Fig. 3.3b Hypocellular specimens.

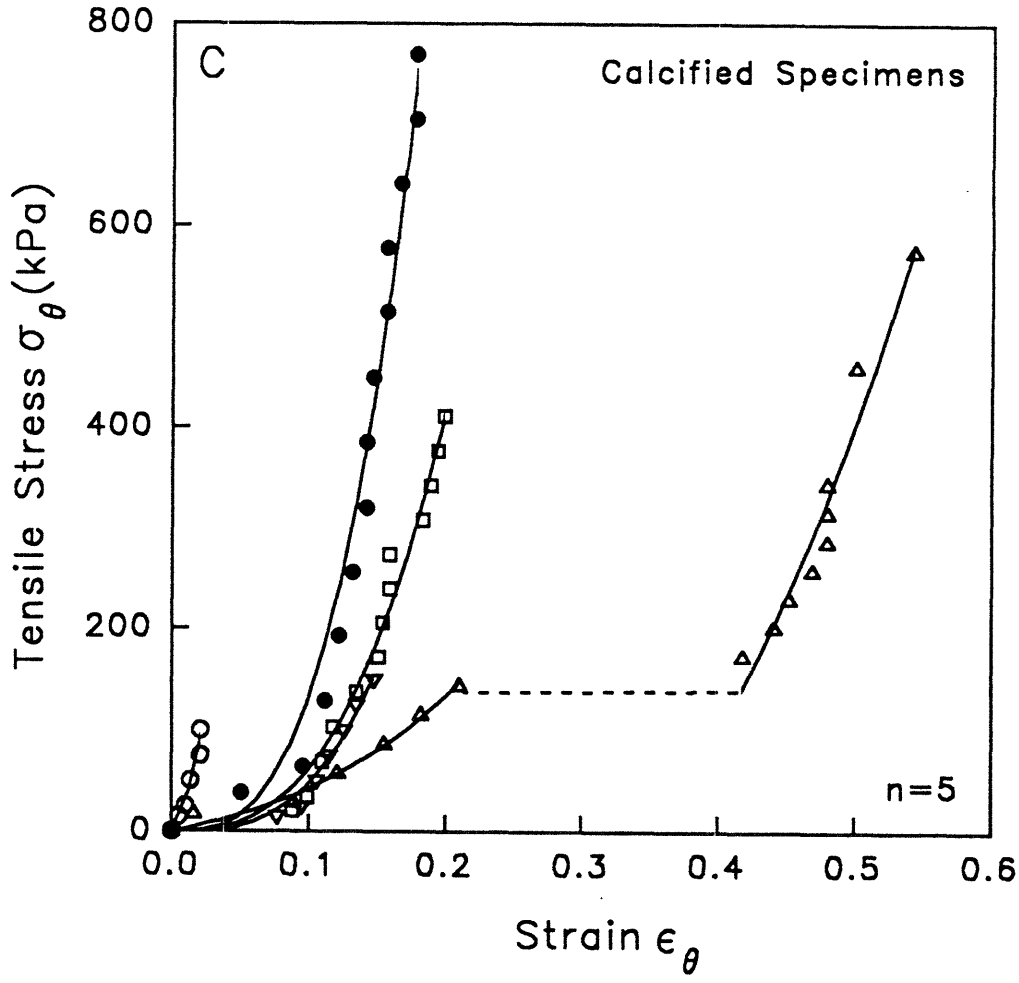

Fig. 3.3c Calcified specimens.

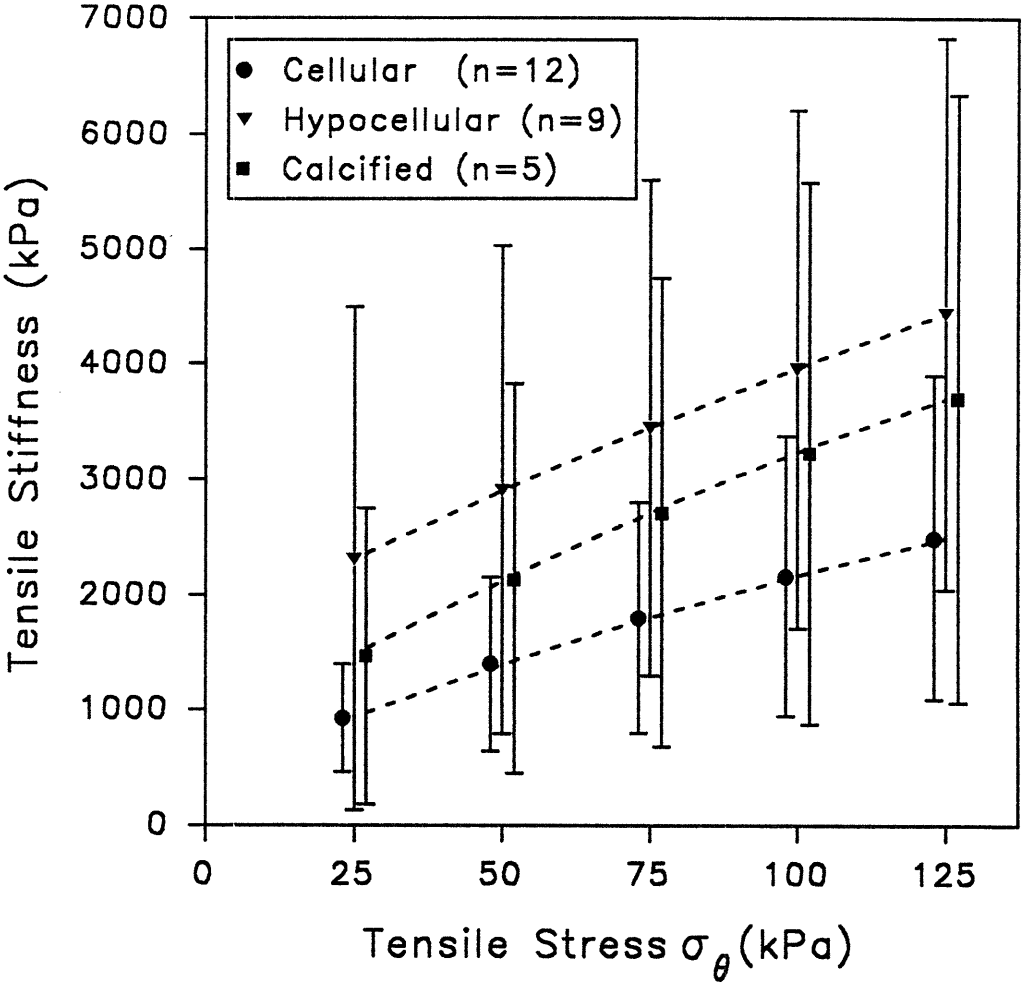

Fig. 3.4 Tensile stiffness .vs. stress relation, averaged for three histologic classes in a.) low stress and b.) high stress ranges.

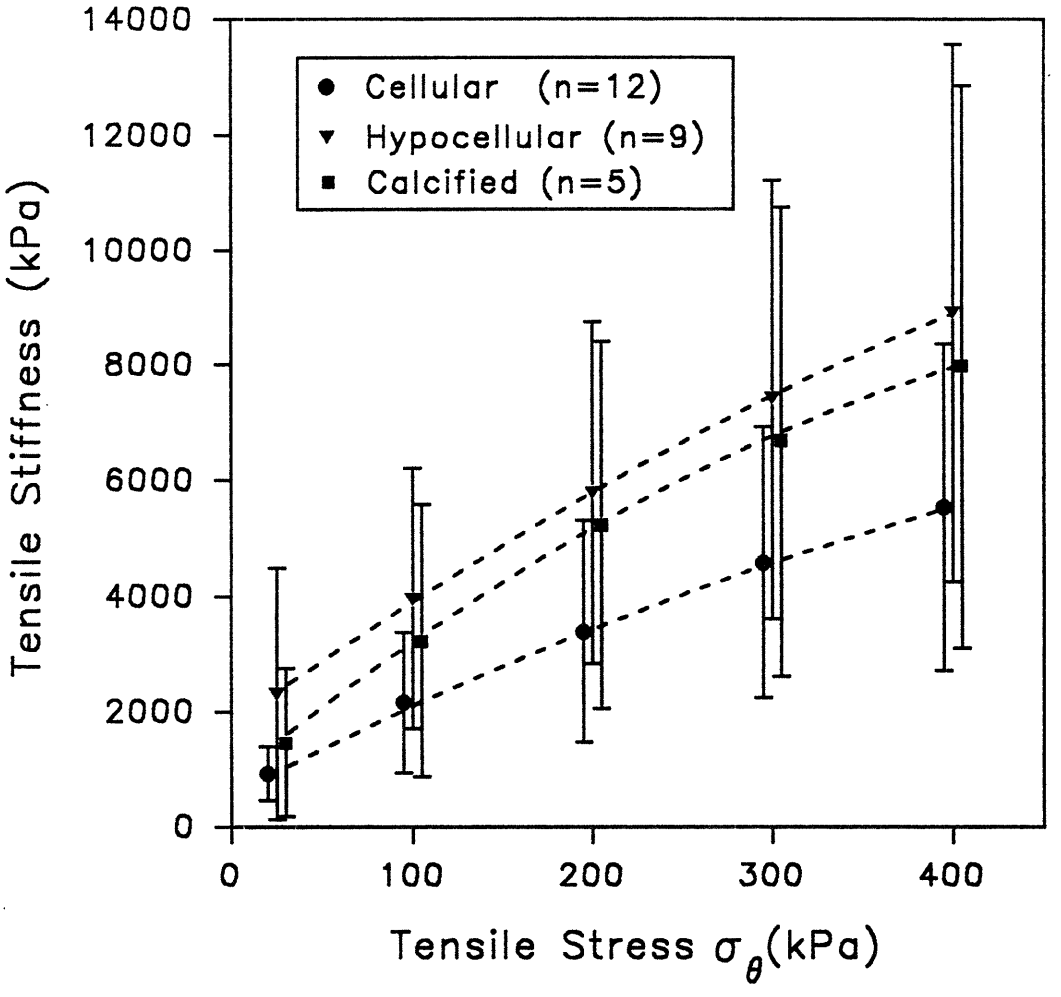

Fig. 3.4b High stress range.

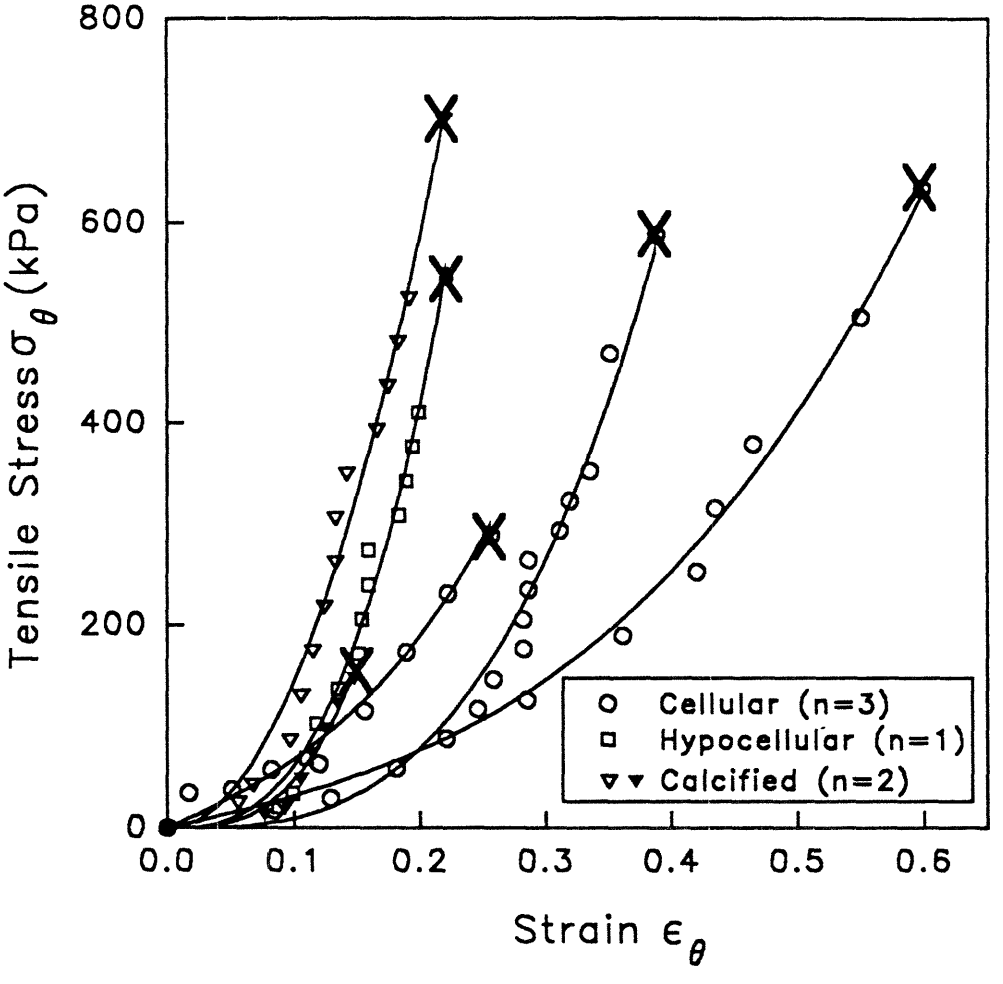

Fig. 3.5 Tensile stress-strain relation for five fractured specimens.

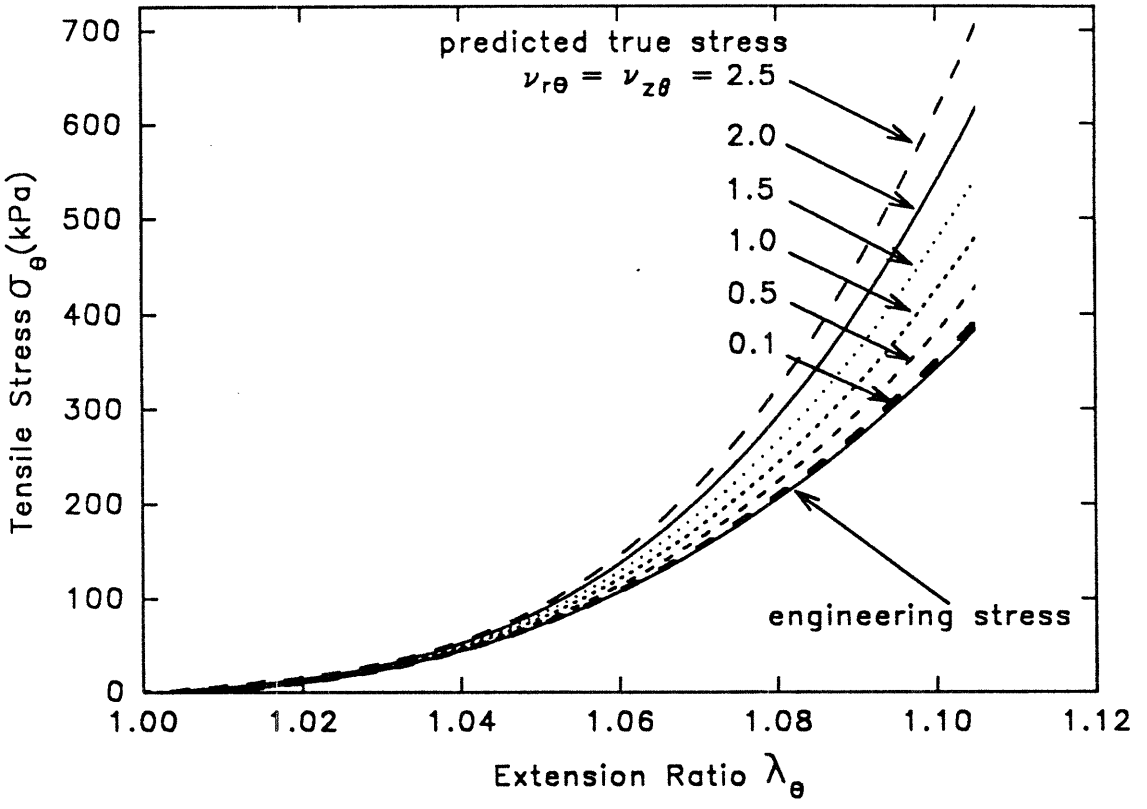

Fig. 3.6 Predicted true tensile stress .vs. extension ratio for a typical cellular plaque specimen.

CHAPTER 4

MODELING STRESS FIELDS IN IDEALIZED PLAQUE GEOMETRIES

ABSTRACT

It is likely that factors other than stenosis severity predispose some atherosclerotic plaques to rupture. Because focal increases in circumferential stress may be an important mechanism of plaque rupture, we examined peak circumferential stress of atherosclerotic lesions using finite element analysis based on idealized two-dimensional cross-sections of diseased vessels similar to intravascular ultrasound images. The study was designed to test the hypothesis that subintimal plaque structural features such as thickness of the fibrous cap are more important factors in the distribution of stress in the plaque than stenosis severity. The analysis incorporated equilibrium biomechanical parameters from normal and diseased vessels and determined the stress distribution within the plaque at a mean luminal internal pressure (P) of 110 mmHg. With a constant luminal area reduction of 70%, maximum circumferential stress (σ_{max}) normalized to luminal pressure (σ_{max}/P) increased from 6.0 to 24.8 as the thickness of the lipid pool was increased from 38 to 54% of the plaque thickness due to the thinner fibrous cap over the lipid pool. Holding the lipid pool thickness constant, increasing stenosis severity from 70 to 91% by increasing fibrous cap thickness decreased σ_{max}/P from 24.8 to 4.7. When no lipid pool was present and the stenosis severity was increased from 70 to 99%, σ_{max}/P decreased from 5.3 to 4.7. Thus, reducing the fibrous cap thickness

dramatically increases peak circumferential stress in the plaque, while increasing stenosis severity actually decreases peak stress in the plaque. The critical dependence of peak circumferential stress on subintimal structure may explain why some atherosclerotic plaques that rupture and cause myocardial infarction are not angiographically severe (61).

INTRODUCTION

Subintimal structure, rather than stenosis severity, may be critical in determining overall plaque stability, explaining why coronary angiography has not been a reliable method for predicting future myocardial infarction. This study was designed to test the hypothesis that subintimal plaque structural features such as thickness of the fibrous cap and size of lipid pools are more important factors in the distribution of circumferential stress in the plaque than stenosis severity.

METHODS

Design of Models. Ten idealized models were designed to test the effects of plaque geometry on circumferential stress fields in the diseased vessel. All models represented cross-sections of typical atherosclerotic human coronary arteries with eccentric intimal plaques. As illustrated in Fig. 4.1, the artery is modeled as a thick-walled cylinder with inner radius 1.8 mm and outer radius 2.0 mm. The lumen is modeled as a circular hole of varying radius (R) with an eccentricity of 0.5 mm with respect to the artery center. Fibrous plaque occupies the region between the luminal wall and the inner wall of the artery. The assumption was made in these idealized

models that the fibrous cap was continuous with the fibrous plaque and had the same material properties as the fibrous plaque. In some models, a subintimal lipid pool exists as a 140^{o} crescent with inner radius (a) and outer radius 1.75 mm with respect to the lumen center. Only (R) and (a) varied in the ten models described below.

The ends of the lipid pool are hemicircular. The portion of plaque between the lumen and the lipid pool is the fibrous cap. A static pressure (P) of 110 mmHg (14.6 kPa) acts along the luminal wall, representing mean physiologic blood pressure in the coronary arteries. Table 4.1 gives the dimensions of the models. In Models A to D, fibrous cap thickness is varied by changing lipid pool size (changing a) at a constant stenosis severity; the outer radius of the lipid pool remained constant, so that the lipid pool increased in size by thinning of the fibrous cap. In Models E to G, stenosis severity is varied with no lipid pool present. In Models A,H,I, and J, fibrous cap thickness is varied by changing stenosis severity (changing R) with a constant lipid pool size (as in model A).

Material Properties. Both the plaque and artery are modeled as orthotropic materials with linear elastic properties. Although finite element codes can accommodate nonlinear incremental solutions, little nonlinear biomechanical testing data from atherosclerotic plaque tissue are available. In the absence of reliable nonlinear parameters, the estimates of linear elastic parameters were used. The selection of z-θ transversely isotropic material properties for the models is described in Table 4.2; although these parameters vary from specimen to specimen, estimations of typical values were made. Note that these are estimates for static, not dynamic,

parameters, because the finite element solutions in this study evaluate stresses caused by mean arterial pressure. E_r for fibrous aortic plaque and E_r for normal artery were measured in static uniaxial compression between a radial stress of 30 mmHg (-4.0 kPa) and 90 mmHg (-12.0 kPa) as previously reported (49). E_θ for fibrous plaque was estimated from previous reports of static tensile properties of human aortic atherosclerotic plaque (50). E_θ for coronary artery was based on previously published studies of normal arteries using inflation or ultrasound techniques (44,63) as well as additional previous reports (45). The Poisson's ratios for plaque and artery were based on a previously measured value of $\nu_{\theta z}$=0.27 in canine aorta (44). $\nu_{r\theta}$ was then chosen to satisfy the requirements for positive diagonal entries in a positive definite material stiffness matrix, as illustrated in Fig. 4.2 (52). To evaluate the effects of potential errors in parameter estimation, a sensitivity analysis of the effects of varying plaque E_z , $\nu_{r\theta}$, $\nu_{\theta z}$ and other parameters on maximum circumferential stresses was performed (Table 4.3).

The $G_{r\theta}$ shear moduli for plaque and artery were estimated based on a limit argument (64). The upper bound for $G_{r\theta}$ was chosen to be the larger of the elastic moduli E_θ. If $G_{r\theta}$ were greater than E_θ, then the layers of fibers within plaque or artery would more easily stretch than slide over one another; in the plaque, this is unlikely since the bonds between collagen fibers form a highly rigid structure. The artery wall is less rigid than the plaque, so that higher $G_{r\theta}$ relative to E_θ may be possible. However, sensitivity analysis demonstrated little effect of increases in $G_{r\theta}$ for artery on circumferential tensile stress. The lower bound for $G_{r\theta}$ was

established by modeling plaque and artery as incompressible isotropic materials with $E=E_r$ and then solving for $G_{r\,\theta}=E/3$. For plaque the predicted range was 17 kPa$<G_{r\,\theta}<$1000 kPa and for artery the predicted range was 3 kPa$<G_{r\,\theta}<$100 kPa. The lipid pool was modeled as a nearly incompressible isotropic material with Young's modulus one hundredth that of the arterial circumferential Young's modulus, as previously described (22,65).

Mesh Generation and Model Solution. All finite element meshes were designed using SDRC I-DEAS software on a DEC Microvax II computer. Regions were defined and then automatically meshed with 8-noded quadrilateral plane strain elements using a free meshing algorithm designed to minimize element distortion. The assumption of plane strain was made because the axial dimension of atherosclerotic lesions is on the order of the vessel diameter. Plane stress models would be more appropriate if axial dimensions were very small relative to the vessel diameter. Models A and E were also analyzed with plane stress elements (data not shown); these results were not significantly different from those of the plane strain models. The average element dimension was 0.1 mm. Because of symmetry, only half of the artery and plaque system was analyzed, with nodes along the centerline restrained to move only in the radial direction and one node on the outer wall of the artery completely restrained. The origin of the r- θ coordinate system was defined as the center of the lumen.

To improve accuracy of the finite element stress analysis, each mesh was refined using an adaptive remeshing algorithm. This remeshing algorithm increases

the number of elements in regions of high strain energy, providing a more accurate finite element solution. A simplified isotropic shell element model with artery assigned E=100 kPa, ν=0.27 and plaque assigned E=1000 kPa, ν=0.27 was solved for strain energy in each element. The elements with the top 15% strain energy gradients were then divided into smaller triangular or quadrilateral elements. Examples of finite element meshes following the adaptive remeshing process are illustrated in Fig 4.3a-4.6a. The refined finite element models with orthotropic linearly elastic material properties and plane strain elements were then solved using HKS ABAQUS 4.9 software on a CRAY-2 or CRAY X-MP supercomputer. Contour plots of circumferential stress (Figures 4.3b-4.6b) were displayed using ABAQUS POST on a Tektronics 4107A graphics terminal.

RESULTS

The results of the finite element analyses for several of the plaque models are shown in Figures 4.3b-4.6b. Circumferential stress σ_θ is plotted linearly with respect to the color scale. The regions of maximum circumferential stress lie either in the plaque cap over the subintimal lipid pool or on the luminal wall near the thinnest plaque section. Small compressive circumferential stresses occur in the subintimal lipid pool (range, 0.3 to 2.0 kPa; mean 0.8 ± 0.6 kPa). Peak compressive circumferential stresses were found in the plaque at the lipid pool tip (shown as the largest negative stress in Figures 4.3b-4.6b). Results for the remaining six models can be found in Appendix Fig A.1-A.6.

The maximal circumferential stress (σ_{max}) in each model was normalized by luminal pressure (P). By adjusting plaque cap thickness and stenosis severity across the range of geometries studied, σ_{max}/P varied from 4.7 to 24.8. As shown in Fig. 4.7, for a constant stenosis severity, σ_{max}/P decreased from 24.8 to 5.3 as cap thickness increased from 0.05 mm to 0.5 mm due to the decreasing lipid pool size. When plaque cap thickness was increased by increasing stenosis severity with constant lipid pool geometry, slightly lower values of σ_{max}/P resulted. As shown in Fig. 4.8, for a constant lipid pool geometry, σ_{max}/P decreased from 24.8 to 4.7 as stenosis severity increased from 69% to 91%; this effect is due to the increase in fibrous cap thickness as the stenosis becomes more severe. For models without a lipid pool, σ_{max}/P decreased from 5.3 to 4.7 as stenosis severity increased from 70% to 99%. Additional analyses of the effect of increasing lipid pool size toward the adventitia (with constant fibrous cap thickness of 0.15 mm) were performed (data not shown); this caused very little increase in circumferential stress.

Sensitivity Analysis. An analysis of sensitivity of maximum circumferential stress to changes in plaque orthotropic properties is shown in Table 4.3. The range of E_θ tested corresponds to typical values obtained through experimentation. The ranges of $\nu_{r\theta}$ and $\nu_{\theta z}$ tested correspond to values satisfying the necessary condition of a positive definite stiffness matrix. Thus, reasonable errors in estimation of these material parameters would not significantly influence the primary conclusions of this study.

DISCUSSION

Although many questions about the initiating events of myocardial infarction remain unanswered, it is likely that the increases in circumferential stress within the plaque proposed by Richardson et al. play an important role (23). In this study of idealized atherosclerotic vessels, increasing stenosis severity actually decreased circumferential stresses in the absence of a lipid pool, but the effect was small and may be biologically insignificant. On the other hand, decreasing the thickness of the fibrous cap over a subintimal lipid pool (either by decreasing stenosis severity or increasing lipid pool size toward the lumen) dramatically increased peak circumferential stresses.

Limitations. Coronary atherosclerotic lesions are often exceedingly complex, with irregular geometries and heterogeneous subintimal structure. The idealized geometries in this study assumed a constant plaque eccentricity, a smooth and round luminal surface, and a smooth boundary between plaque and lipid pool. This was necessary to isolate the effects of fibrous cap thickness and stenosis severity on stresses in the plaque. It is likely that small cracks or irregularities in the plaque surface as well as local variations of moduli (19) could result in much greater stress concentrations than those described in this study. Further studies of specific fatal coronary lesions may demonstrate the importance of lesion geometric irregularities; these studies are complicated by the assumptions made during reconstruction of prerupture geometries. In addition, due to the complexity of atherosclerotic lesions, three-dimensional modeling may be essential in some cases; preliminary evidence

suggests that intravascular ultrasound may be a feasible approach for obtaining three-dimensional structure (66).

Plaque and artery were modeled as transversely isotropic linearly elastic biomaterials for the range of stresses encountered in this study. Atherosclerotic changes are likely to influence the distribution and orientation of fibers; thus, transverse isotropy is an approximation. Biomaterials typically are not linearly elastic in the physiologic range, and it is unlikely that any component of the plaque behaves in a linearly elastic fashion or has the same properties in ression as in tension. Very limited experimental data regarding nonlinearity of plaque within the physiologic range are available (50), so that nonlinear orthotropic modeling was not performed in this study. It is also likely, given the range of moduli found within a histologic class of plaque, that non-uniformities within the fibrous cap or variabilities between different fibrous caps will affect stress concentrations. However, the sensitivity analyses performed in this study indicate that relatively minor changes in stress result from major changes in material properties. In addition, the lipid pool was modeled as a soft, nearly incompressible material. Because necrotic core components of the lipid pool are variable (65), the stiffness of the lipid pool is probably also different from lesion to lesion. However, the lipid pool will bear very little circumferential stress under any conditions due to its semifluid nature, so that the precise choice of material parameters for this region will not significantly affect the distribution of stress in the plaque. Thus, the results of this study indicate important increases in circumferential stress due to variations in fibrous cap thickness. It is important to

note that major changes in material properties may affect the shear stresses between layers and also contribute to high stress concentrations (19).

This study addressed circumferential stresses resulting from the static load of mean luminal pressure. The plaque and artery have dynamic characteristics related to tissue viscoelasticity and poroelasticity that will determine the stresses related to pulsatile flow. These dynamic parameters are variable within the range of physiologic heart rate (43), so that modeling these time-dependent effects is a formidable task.

CONCLUSIONS

This study demonstrated that the maximum stresses in the plaque are critically dependent on subintimal structure of the lesion. Thus, reducing the fibrous cap thickness dramatically increases peak circumferential stress in the plaque, while increasing stenosis severity actually decreases peak stress in the plaque. This suggests that angiography alone will not provide sufficient information to determine the structural stability of atherosclerotic lesions. By understanding the importance of plaque structural features, particularly subintimal structure, and with improved coronary imaging modalities, identification of unstable lesions prior to rupture may become feasible.

Table 4.1 Geometry of 10 finite element models based on schematic of idealized atherosclerotic coronary artery cross-section in Fig. 4.1.

Model	R (mm)	a (mm)	stenosis severity % area reduction	fibrous cap thickness (mm)	max. lipid pool thickness as % max plaque thickness	Peak stress σ_{max}/P
A	1.00	1.05	70	0.05	54	24.8
B	1.00	1.15	70	0.15	46	9.2
C	1.00	1.25	70	0.25	38	6.0
D	1.00	1.50	70	0.50	19	5.3
E	1.00	–	70	–	–	5.3
F	0.45	–	94	–	–	4.6
G	0.18	–	99	–	–	4.7
H	0.90	1.05	75	0.15	41	8.8
I	0.80	1.05	80	0.25	38	5.6
J	0.55	1.05	91	0.50	19	4.7

Table 4.2 Orthotropic material parameters for plaque and artery used in finite element models.

Parameter	Plaque	Artery
E_r (kPa)	50	10
E_θ (kPa)	1000	100
$G_{r\theta}$ (kPa)	500	50
$\nu_{r\theta}$	0.01	0.01
$\nu_{\theta z}$	0.27	0.27

Table 4.3 Sensitivity of maximum circumferential stress σ_{max}/P in Model D to changes in various orthotropic material parameters.

Parameter	Change in Parameter (%)	Change in σ_{max}/P from baseline (%)
E_r plaque	-40.0	+20.6
E_r plaque	+100.0	-17.6
E_θ plaque	-50.0	-20.8
E_θ plaque	+50.0	+16.7
$\nu_{r\theta}$ plaque	-90.0	+0.2
$\nu_{r\theta}$ plaque	+900.0	-4.7
$\nu_{\theta z}$ plaque	-63.0	-2.2
$\nu_{\theta z}$ plaque	+85.0	+8.4
$G_{r\theta}$ plaque	-90.0	+0.2
$G_{r\theta}$ plaque	+100.0	-4.7
E_r artery	+400.0	-0.2
E_θ artery	+900.0	-4.9
$G_{r\theta}$ artery	+100.0	+0.2

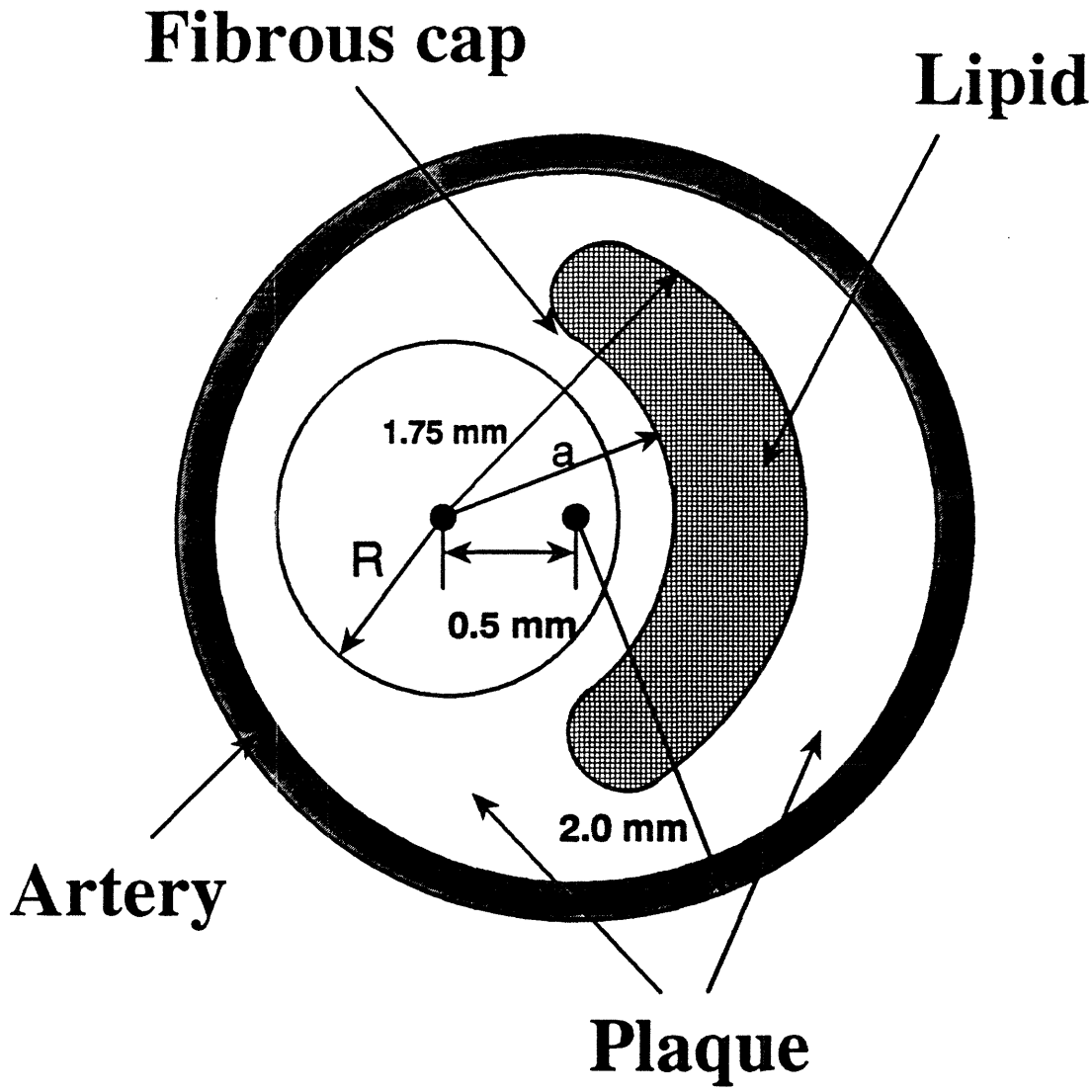

Fig. 4.1 Geometry of idealized atherosclerotic coronary artery cross section. Eccentric plaque has lumen of radius R and subintimal crescent-shaped lipid pool with inner radius a.

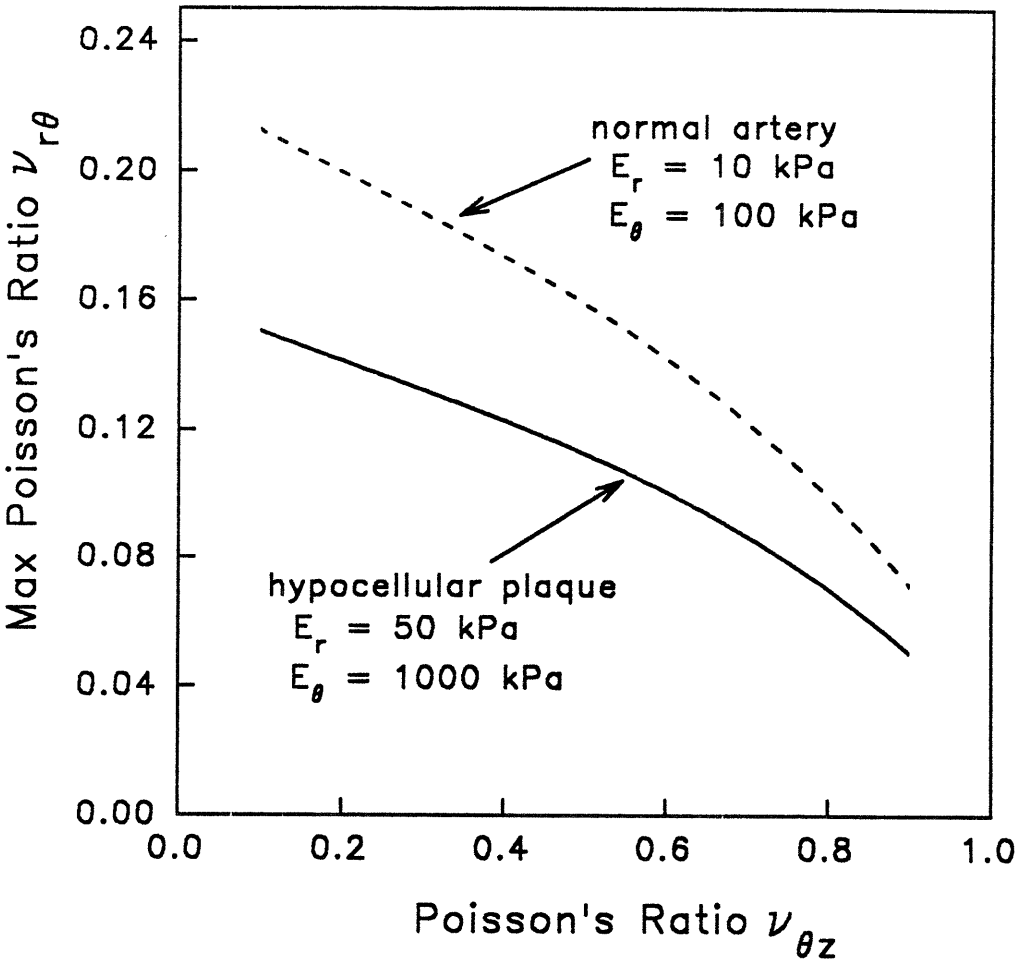

Fig. 4.2 Range of allowable Poisson's ratios for hypocellular plaque and normal artery.

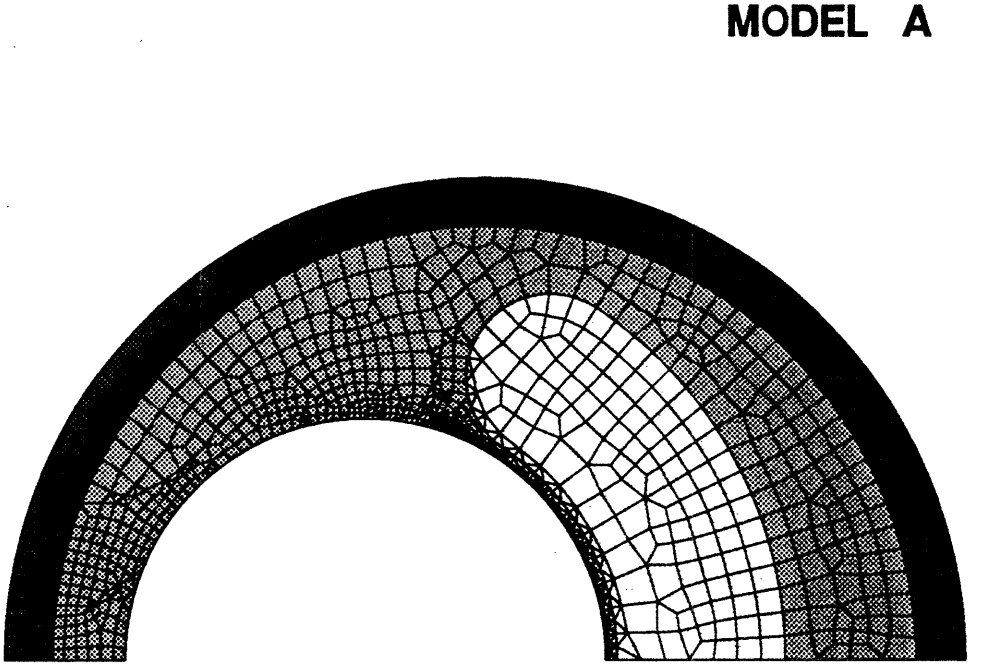

Fig. 4.3 (a) Geometry of Model A: 70% stenosis severity, 0.05 mm fibrous cap thickness, maximum lipid pool thickness 54% of maximum plaque thickness. 1283 plane strain elements: 957 plaque, 166 artery, 160 lipid. (b) Contour map of circumferential stress (σ_θ) in model A (in pascals). Maximum normalized circumferential stress $\sigma_{max}/P = 24.8$ at arrowhead. P = 110 mmHg.

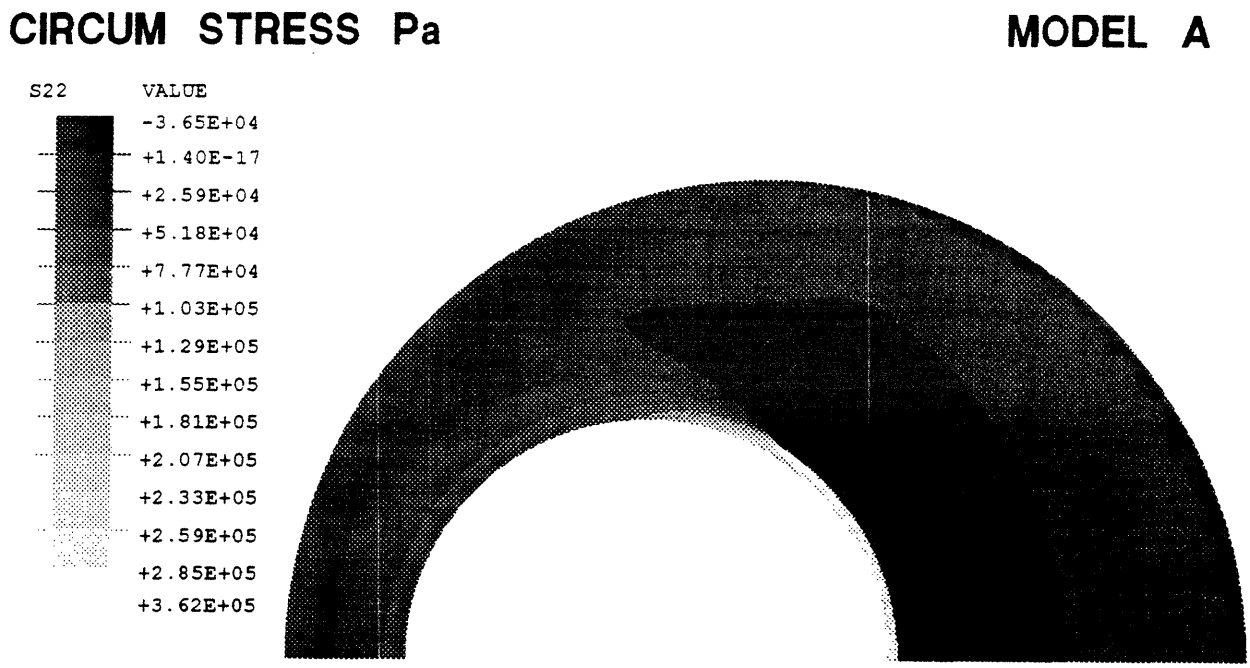

Fig. 4.3b Contour map of circumferential stress (Model A).

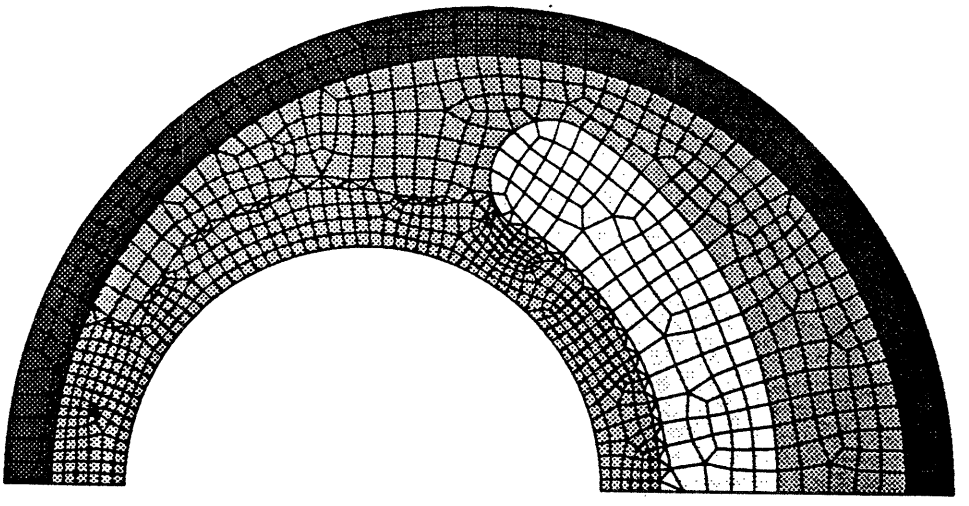

Fig. 4.4 (a) Geometry of model C: 70% stenosis severity, 0.25 mm plaque cap thickness, maximum lipid pool thickness 38% of maximum plaque thickness. 962 plane strain elements: 663 plaque, 166 artery, 133 lipid. (b) Contour map of circumferential stress (σ_θ) in model C (in pascals). Maximum normalized circumferential stress $\sigma_{max}/P = 6.0$ at arrowhead. P = 110 mmHg.

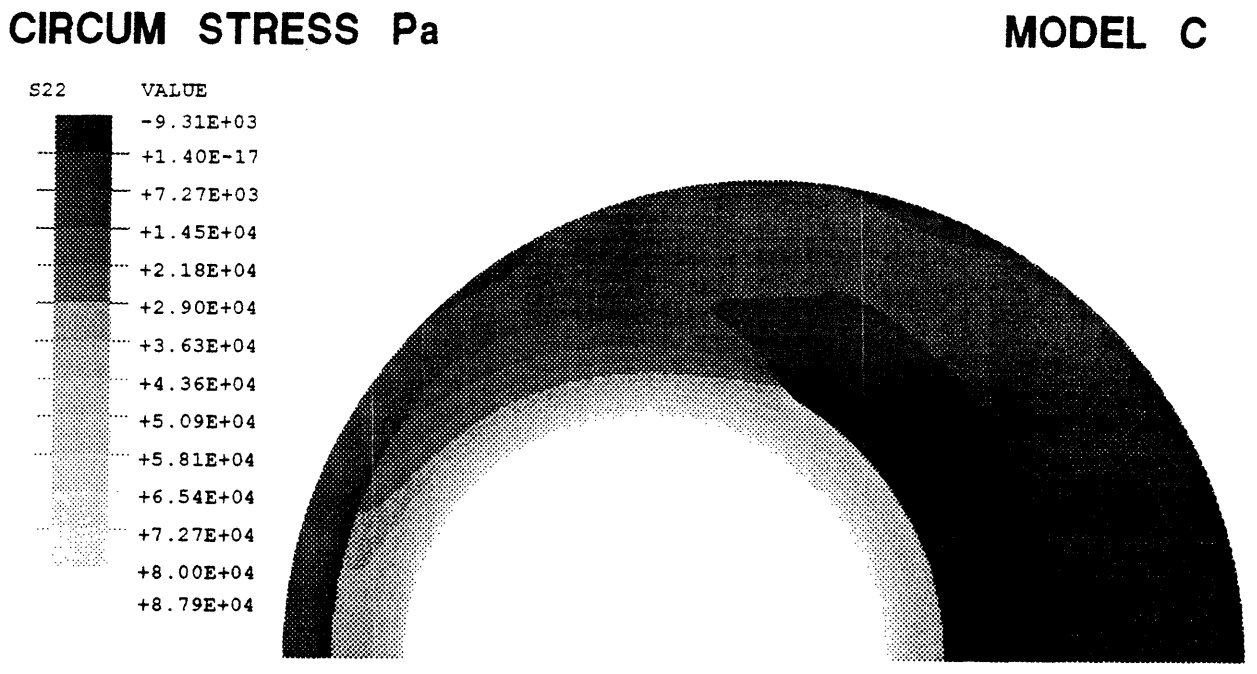

Fig. 4.4b Contour map of circumferential stress (Model C).

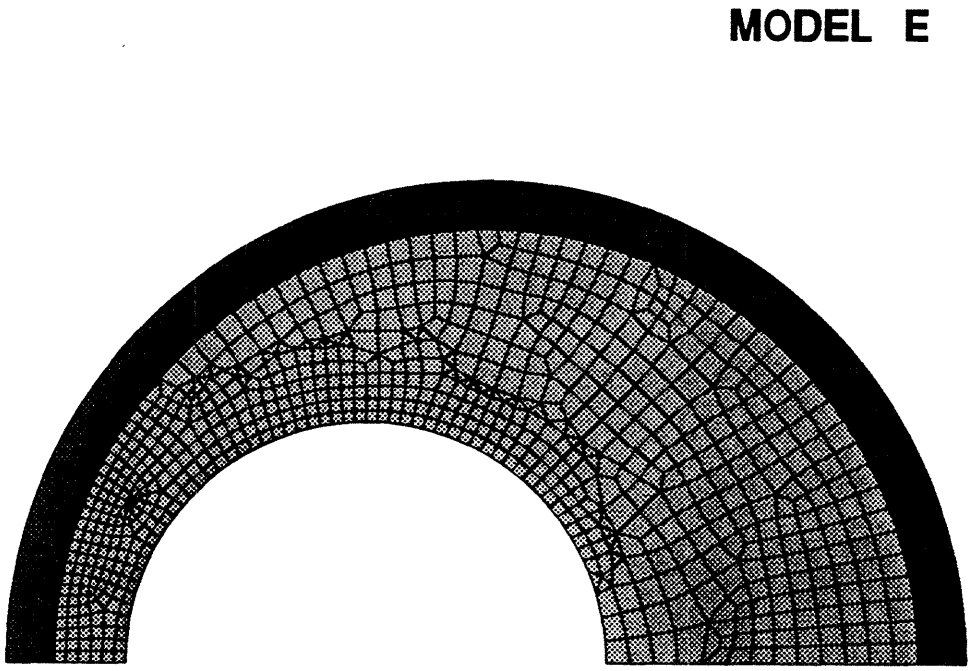

Fig. 4.5 (a) Geometry of model E: 70% stenosis severity, no lipid pool. 874 plane strain elements: 696 plaque, 178 artery. (b) Contour map of circumferential stress (σ_θ); in model E (in pascals). Maximum normalized circumferential stress, σ_{max}/P = 5.3 at arrowhead. P = 110 mmHg.

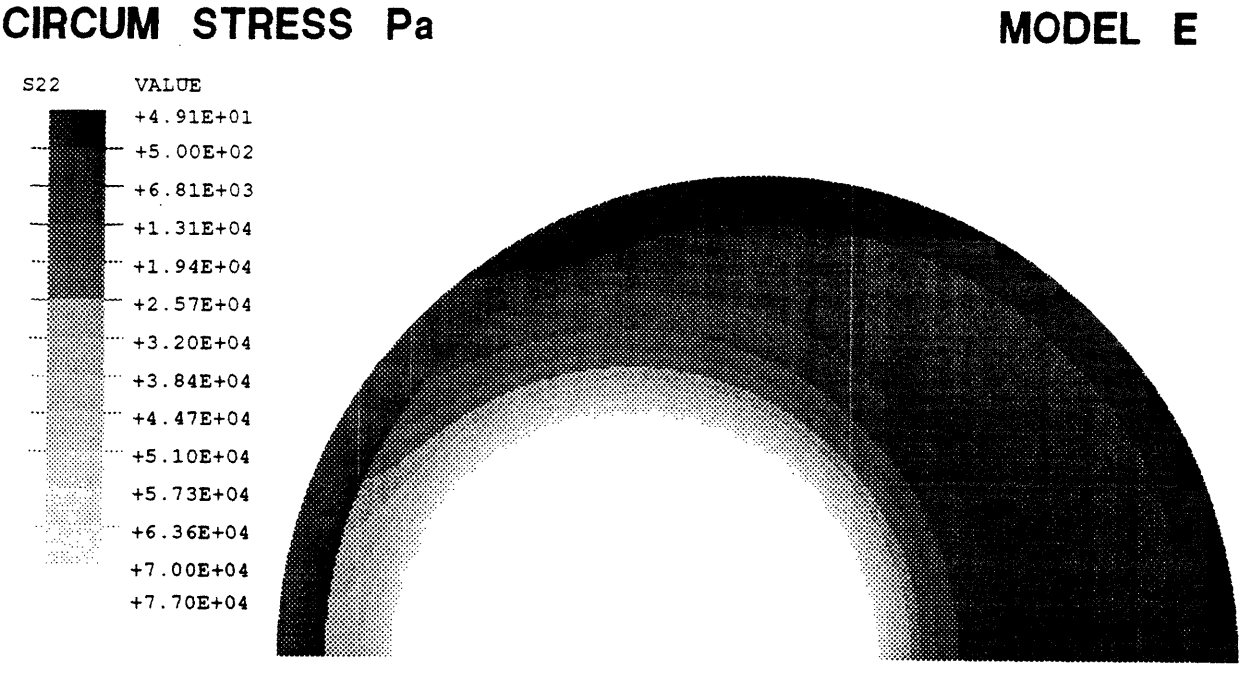

Fig. 4.5b Contour map of circumferential stress (Model E).

MODEL G

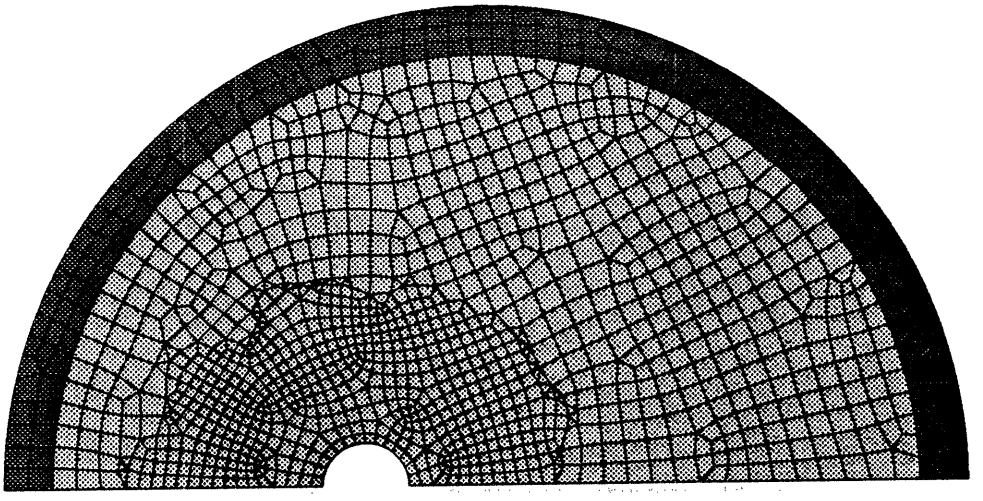

Fig. 4.6 (a) Geometry of model G: 99% stenosis severity, no lipid pool. 1228 plane strain elements: 1075 plaque, 153 artery. (b) Contour map of circumferential stress (σ_θ) in model G (in pascals). Maximum normalized circumferential stress σ_{max}/P = 4.7 at arrowhead. P = 110 mmHg.

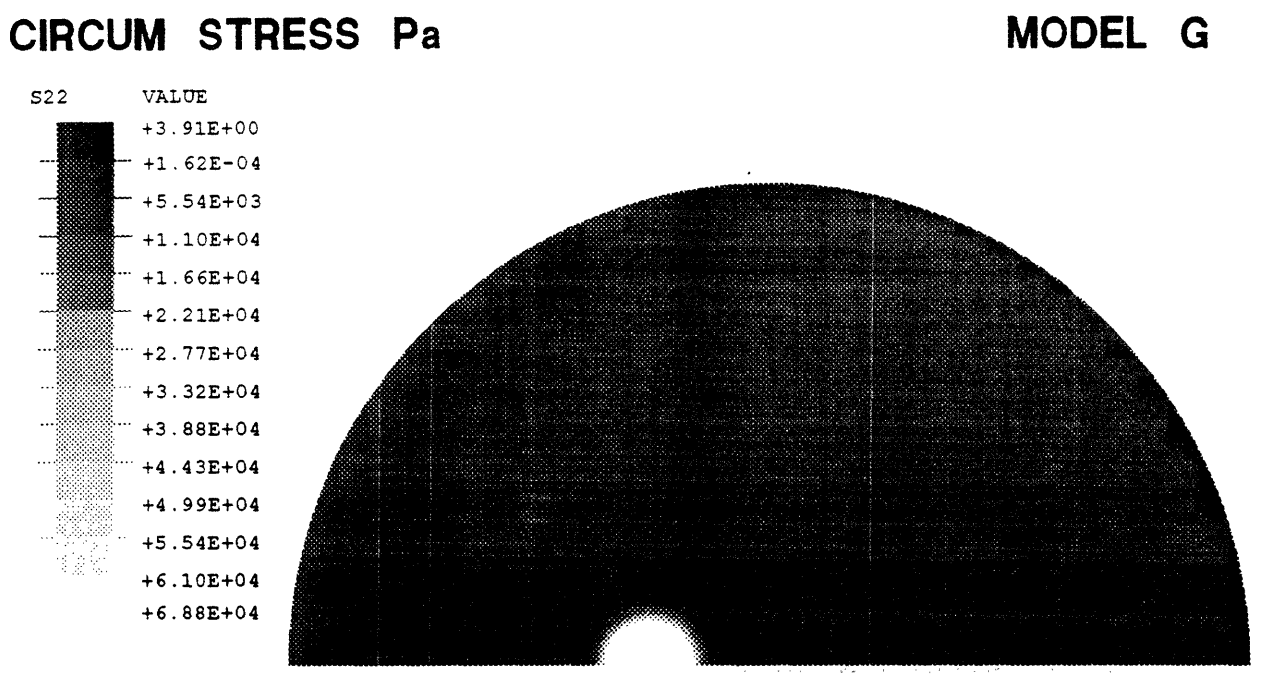

Fig. 4.6b Contour map of circumferential stress (Model G).

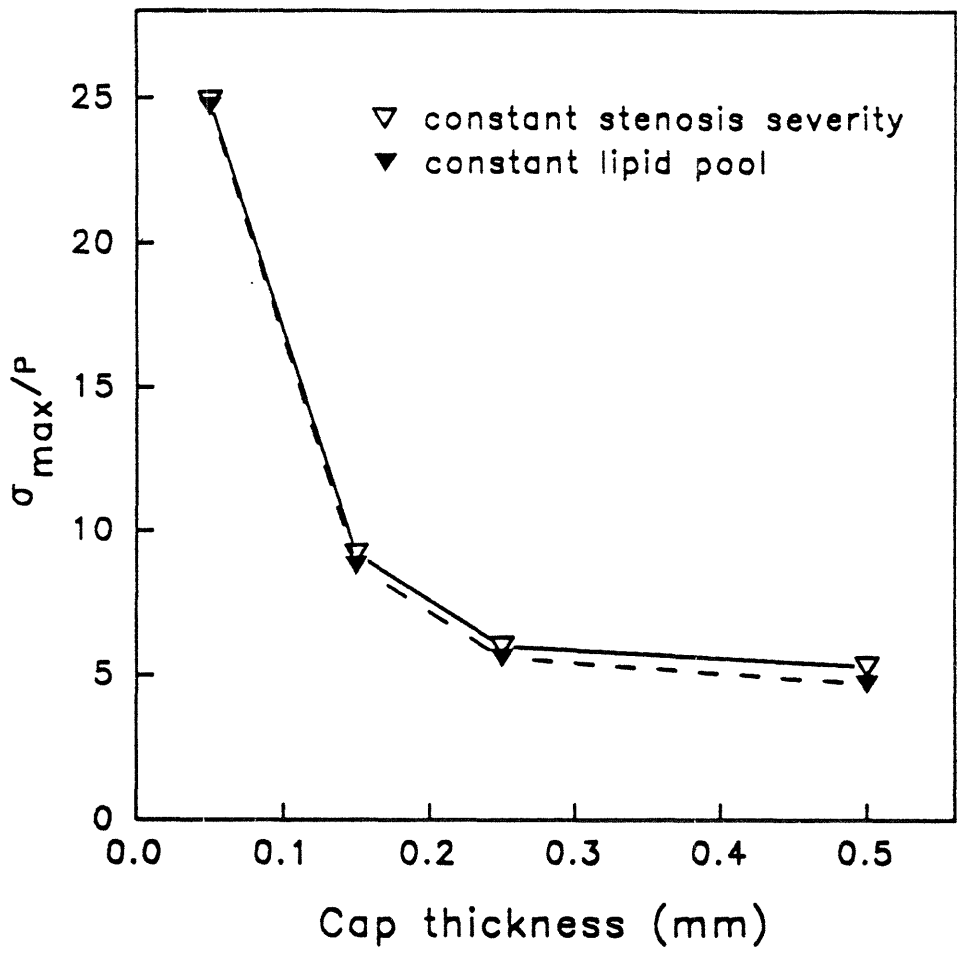

Fig. 4.7 Effect of plaque cap thickness (x-axis) on maximum circumferential stress normalized to luminal pressure (y-axis). Cap thickness was varied by changing lipid pool thickness with a constant stenosis severity (open triangles) and by changing stenosis severity with a constant lipid pool thickness (solid triangles). Decreasing cap thickness dramatically increases maximum circumferential stress.

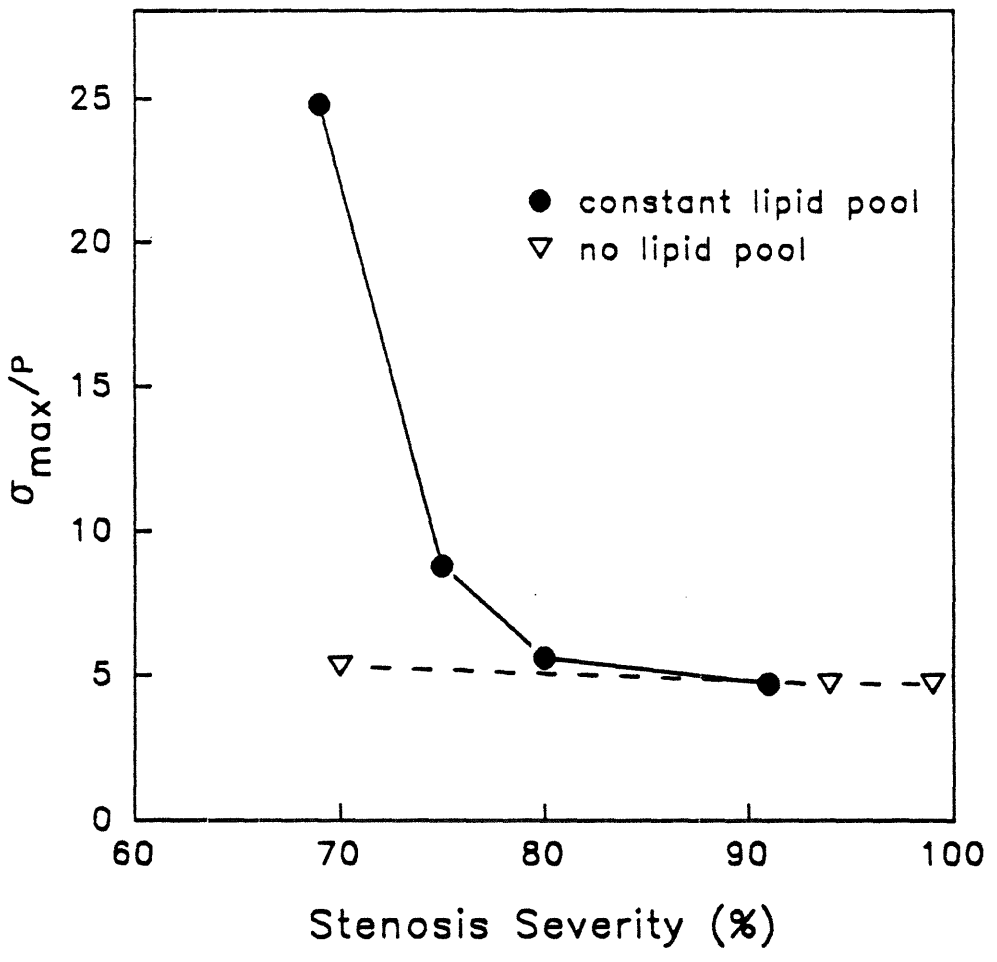

Fig. 4.8 Effect of stenosis severity (% area reduction, x-axis) on maximum circumferential stress normalized to luminal pressure (y-axis) with and without a constant lipid pool. Increasing stenosis severity decreases maximum circumferential stress slightly when no lipid pool is present (triangles). When a lipid pool is present, increasing stenosis severity dramatically decreases maximum stress by increasing fibrous cap thickness (circles).

CHAPTER 5

MODELING STRESS FIELDS IN ACTUAL PLAQUE GEOMETRIES

(IN COLLABORATION WITH GEORGE C. CHENG)

ABSTRACT

Although rupture of atherosclerotic plaque is considered to be the cause of most acute coronary syndromes, the mechanism of plaque rupture is controversial. To test the hypothesis that locations of plaque rupture occur at regions of high circumferential stress in the diseased vessel, analysis of the distribution of stress was performed on 24 coronary artery lesions using the finite element method. The stress distributions based on histologic specimens from 12 coronary artery lesions that caused lethal myocardial infarction were compared to those of 12 stable control lesions. Finite element modeling at a mean intraluminal pressure of 110 mmHg was performed using plane strain parabolic elements and a linearly elastic, transversely isotropic material law. The maximum circumferential stress in plaques that ruptured was significantly higher than maximal stress in stable specimens (543 ± 166 kPa vs 192 ± 68 kPa, $p<0.0001$). Twelve of 12 ruptured lesions had a total of 31 regions of stress concentration greater than 300 kPa, (mean, 2.6 ± 1.4 high stress regions per lesion); only 1 of 12 control lesions had a stress concentration region greater than 300 kPa. In 7 of 12 lethal lesions (58%), rupture occurred at the maximum circumferential stress concentration region; in ten of the 12 lethal lesions, rupture occurred at a stress concentration region greater than 300 kPa. These data support the hypothesis that concentrations of circumferential tensile stress in the

atherosclerotic plaque play an important role in plaque rupture and myocardial infarction. However, plaque rupture does not always occur at the region of highest stress, suggesting that local variations in plaque integrity contribute to plaque rupture.

INTRODUCTION

Atherosclerotic lesions are complex, and detailed data regarding stresses based on specific coronary lesions are limited. The possible association between locations of rupture and locations of high stress concentration regions in individual diseased vessels would provide a strong explanation as to why luminal geometry based on coronary angiography has been a poor predictor of plaque rupture (26,27). Thus, this study was designed to test the hypotheses that 1) plaques rupture near regions of high tensile circumferential stress, and 2) these stresses are higher than those found in stable lesions.

METHODS

Specimens. All specimen selection and processing was performed by investigators uninvolved in the finite element analysis. Twenty histologic specimens were randomly selected from previously described specimens from patients who died of acute plaque rupture complicated by coronary thrombosis and myocardial infarction at Cedars Sinai Hospital (67). Eight of these specimens were determined to have undergone too much disruption for reconstruction of the prerupture morphology and were rejected from the study. Twelve "stable" control specimens

were then randomly chosen from a group of unruptured coronary lesions with no evidence of coronary thrombosis from the same time period from Cedars Sinai Hospital. Tracings of the cross-sectional geometries of the specimens were made, identifying regions of normal vessel, fibrous plaque, calcified plaque, and necrotic lipid pool. Control specimens were reproduced completely while tracings of test specimens were reconstructed to represent their probable pre-rupture geometries. An approximate center of the lumen was identified, and a randomly oriented radial coordinate axis was drawn on each tracing. The rupture location relative to this coordinate system was recorded, but was not drawn on the tracing. A radial coordinate system was also drawn on each control specimen tracing so that it was not possible to identify which lesions were ruptured and which lesions were control specimens. Two experienced cardiac pathologists independently reviewed the accuracy of these tracings, including rupture locations; one cardiac pathologist was uninvolved with the study and served as an external reviewer. In five of 24 cases, the reviewers made minor changes in shapes of lipid pools or calcified plaque regions. In the 12 ruptured lesions, the mean stenosis area reduction (by digitizing the tracings) was 87 ± 10%; in the 12 stable lesions, the mean area reduction was 86 ± 14% (p=NS by Student's t test). Of the ruptured lesions, six were from the right coronary artery, four from the left anterior descending artery, one from the circumflex artery, and one from a ramus branch. Of the stable lesions, four were from the right coronary artery, four from the left anterior descending artery, and four from the circumflex artery.

Finite Element Analysis. Investigators responsible for the finite element analysis were uninvolved in the acquisition of specimens or in subsequent production of tracings either of the ruptured or control lesions, and thus had no knowledge of the rupture status of any of the specimens.

While variations in biomechanical behavior probably exist both between lesions and within any given plaque, characteristics regarding lesion components were generalized to facilitate analysis. All components were approximated by linearly elastic material parameters (Table 4.2); although finite element codes can perform solutions based on nonlinear material properties, little data regarding the nonlinear mechanical behavior of atherosclerotic plaque tissue in the physiologic range have been described. Because stress analysis was performed for a static pressure load, no parameters associated with time-varying viscoelastic and poroelastic effects were used. In addition, the general structures of plaque and artery tissue were each assumed to have similar mechanical properties in the circumferential (θ) and axial (z) directions which differ from properties in the radial (r) direction, an assumption termed "transverse isotropy". Selection of material properties for the finite element models is described in Chapter 4. Lipid and calcified plaque were each assumed to be nearly incompressible ($\nu = 0.48$) and isotropic, indicating that their mechanical properties are independent of direction. Lipid E was estimated to be one hundredth of the stiffness of normal artery, as previously described (22,23). The Young's modulus of calcified plaque was estimated as ten times that of plaque E_θ. To evaluate the effects of potential errors in parameter estimation, a sensitivity analysis

of the effects of varying plaque E_θ, $\nu_{r\theta}$, $\nu_{\theta z}$ and other parameters on maximum circumferential stresses was performed.

Finite element meshes were designed using SDRC I-DEAS software on a DEC Microvax II computer. Geometric and compositional information from each tracing was entered into the computer with a digitizing pad. Meshes were generated with a global element size of 0.1mm and local element sizes of between 0.02 to 0.05mm to improve solution accuracy near regions adjacent to the lumen. The finite element models with orthotropic material properties and plane strain elements were then solved using HKS ABAQUS 4.9 software on a CRAY X-MP supercomputer for an intraluminal pressure load of 110 mmHg (14.6 kPa). Contour plots of circumferential stress were displayed using ABAQUS POST on a Tektronics 4209B graphics terminal. In vitro testing of human atherosclerotic materials indicate that nonulcerated atheromatous tissue usually fractures at stresses greater than 300 kPa (29). Therefore, in each specimen peak circumferential stress and all other stress concentrations greater than 300 kPa were identified with respect to the radial coordinate system of the tracing. When the angle between the rupture site and a stress concentration was less than 15 degrees, rupture was assumed to have occurred at the stress concentration location. Comparison of peak stresses in ruptured and stable plaques was performed with Student's t test; a p value < 0.05 was considered statistically significant. All data are presented as mean $\pm$ one standard deviation.

RESULTS

Peak Stresses in Ruptured and Unruptured Plaques. Peak stress in the ruptured lesions averaged 543 ± 166 kPa, significantly higher than the peak stress of 197 ± 68 kPa found in control lesions ($p<.0001$) (Fig. 5.1). The 12 ruptured lesions had a total of 31 regions of high stress concentration, defined as stress greater than 300 kPa. All ruptured lesions had at least one region of high circumferential stress (mean, 2.6 ± 1.4 high stress region per specimen); only one control lesion had a single region of peak stress greater than 300 kPa. Examples of analyses for a ruptured lesion (number 1) and a control lesion (number 6) are shown in Figures 5.2a-5.2c and Figures 5.3a-5.3c, respectively.

Locations of Rupture and Stress Concentration Regions. The angle between the location of peak circumferential stress and the rupture site in each of the test lesions was calculated (Fig. 5.4). The angle between the highest circumferential stress concentration and rupture location ranged from -137 to 90 degrees. Seven of 12 plaques (58%) ruptured within 15 degrees of the highest stress region. The 95% confidence interval for the angle between the rupture site and peak stress location was (-27 to +42 degrees).

Although not all plaques ruptured at the peak circumferential stress region, most plaque ruptures occurred very close to a region of high circumferential stress. Ten of 12 ruptures occurred within 15 degrees of a high stress region; the angle between the nearest stress concentration region and rupture site ranged from -14 to

+37 deg. The 95% confidence interval for the angle between rupture site and the nearest stress concentration region was (-3 to +16 degrees).

Sensitivity Analysis. A model (number 19) with both calcium and lipid pools was selected to evaluate the sensitivity of peak stress estimates by finite element analysis to wide variations in material parameters (Table 5.2). Calculations of peak circumferential stress were not changed by even large changes in estimates of most of the material parameters. For example, large changes in artery material properties had no effect on peak circumferential stress since almost all stress was borne by the plaque. Large changes in plaque or lipid stiffness, on the other hand, led to significant changes in peak stress; this was expected since the different material properties of lipid and plaque are important factors in determining where stress is concentrated.

DISCUSSION

Based on morphologic data and structural analysis of idealized plaque configurations, Richardson *et al.* (23) and Vito *et al.* (19) have suggested the potential importance of subintimal structure in creating stress concentration regions prone to rupture. The present study using finite element analysis specific for individual coronary lesions was performed to examine the relationship between circumferential stress distributions and potential rupture vulnerability in diseased vessels. These data demonstrate that locations of stress concentration coincide closely with actual rupture sites. Moreover, the magnitudes of these stresses significantly exceeded those found

in stable lesions. The stresses at rupture locations were also in reasonable agreement with failure stresses of atherosclerotic plaque measured in mechanical tests by Lendon *et al.* (29) and in our laboratory (See Chapter 3).

Limitations. The finite element analysis of preruptured coronary lesion structure was necessarily performed on geometric reconstructions of post-rupture specimens. Several measures were taken to minimize potential errors in the reconstruction process and biases which could enter into the finite element analysis. The tracings were performed by an investigator who did not participate in the structural analysis; the accuracy of the tracings was reviewed by additional investigators uninvolved in the finite element analysis. In turn, the investigators performing the finite element analysis did not have access to the original specimens, and neither the identities of control and ruptured test lesions nor the locations of rupture were available during the analysis. We believe that a prospective clinical study of prerupture configurations and subsequent rupture will only be possible if current coronary imaging modalities (such as intravascular ultrasound) dramatically improve.

Because the structural analysis in this study was performed on the coronary artery cross-section, luminal and subintimal geometry was assumed to be essentially uniform in the axial direction of the lesion. However, in particular cases, irregularities along the length of the lesion may be significant determinants of stress concentrations. Moreover, strains in the axial direction were assumed to be negligible, an assumption called "plane-strain". This assumption would be valid for

long stenotic regions or longitudinally tethered regions in which longitudinal deformations would be small compared to radial and circumferential deformations. On the other hand, a lesion whose longitudinal dimension is small relative to the diameter of the artery might undergo significant longitudinal deformations; such behavior is not considered by plane-strain analysis.

Assumptions concerning the plaque structural orientation that were made to allow this analysis may not reflect local heterogeneities and inter-specimen variation. For example, in lesions where fiber orientation has been sufficiently altered by the atherosclerotic process, transverse isotropy may be a poor assumption. In addition, the material components were approximated by linear elastic properties and assigned fixed sets of material parameters. Given that most biomaterials exhibit nonlinear elastic behavior (especially at high stresses or strains), the linearly elastic assumption is only approximate. Unfortunately, limited data concerning plaque nonlinear biomechanical behavior are available. By fixing material parameter sets, local material variabilities also were not considered in this study; these may have the effect of creating new regions of high stress or increasing magnitudes of pre-existing stress concentrations. Errors in calculating tensile stresses arising from inaccurate parameter estimation were probably small, since the sensitivity analysis yielded relatively narrow ranges of stress concentration magnitudes computed over a wide range of most material parameters. Note, however, that shear stresses at boundaries between materials of markedly different stiffnesses were not addressed and may be extremely sensitive to parameter selection (19).

This study examined the tensile stress distribution due to a static load of mean arterial pressure. It is tempting to extrapolate stress in a linear fashion with respect to the pressure load. However, in light of the probable nonlinear behavior of plaque, estimates obtained in this manner are likely to be inaccurate at high physiologic pressures and would certainly be inaccurate at the pressures of balloon angioplasty. Moreover, time-varying effects due to tissue viscoelasticity and poroelasticity may be important and can only be considered in a complete dynamic analysis.

CONCLUSIONS

Peak stress in the ruptured lesions averaged 543 ± 166 kPa, significantly higher than the peak stress of 192 ± 68 kPa found in control lesions. The angle between the highest circumferential stress concentration and rupture location ranged from -137 to 90 degrees. Seven of 12 plaques (58%) ruptured within 15 degrees of the highest stress region. The 95% confidence interval for the angle between the rupture site and peak stress location was (-27 to +42 degrees). Although not all plaques ruptured at the peak circumferential stress region, most plaque ruptures occurred very close to a region of high circumferential stress. Ten of 12 ruptures occurred within 15 degrees of a high stress region; the angle between the nearest stress concentration region and rupture site ranged from -14 to +37 deg. Large changes in plaque or lipid stiffness, on the other hand, led to significant changes in peak stress; this was expected since the different material properties of lipid and plaque are important factors in determining where stress is concentrated.

Table 5.1 Sensitivity of maximum circumferential stress in one model to changes in various orthotropic material parameters.

Parameter	Change in Parameter (%)	Change in peak stress from baseline (%)
E_r plaque	-40	+11.3
E_r plaque	+100	-8.1
E_θ plaque	-50	-21.7
E_θ plaque	+50	+17.9
$\nu_{r\theta}$ plaque	-90	-0.6
$\nu_{r\theta}$ plaque	+900	+6.0
$\nu_{\theta z}$ plaque	-63	-2.3
$\nu_{\theta z}$ plaque	+85	+8.1
$G_{r\theta}$ plaque	-90	+36.7
$G_{r\theta}$ plaque	+100	+0.3
E_r artery	+400	0
E_θ artery	+900	0
$G_{r\theta}$ artery	+100	0
E lipid	-90	+26.2
E lipid	+900	-46.3
E calcium	-90	+0.3
E calcium	+900	-0.1

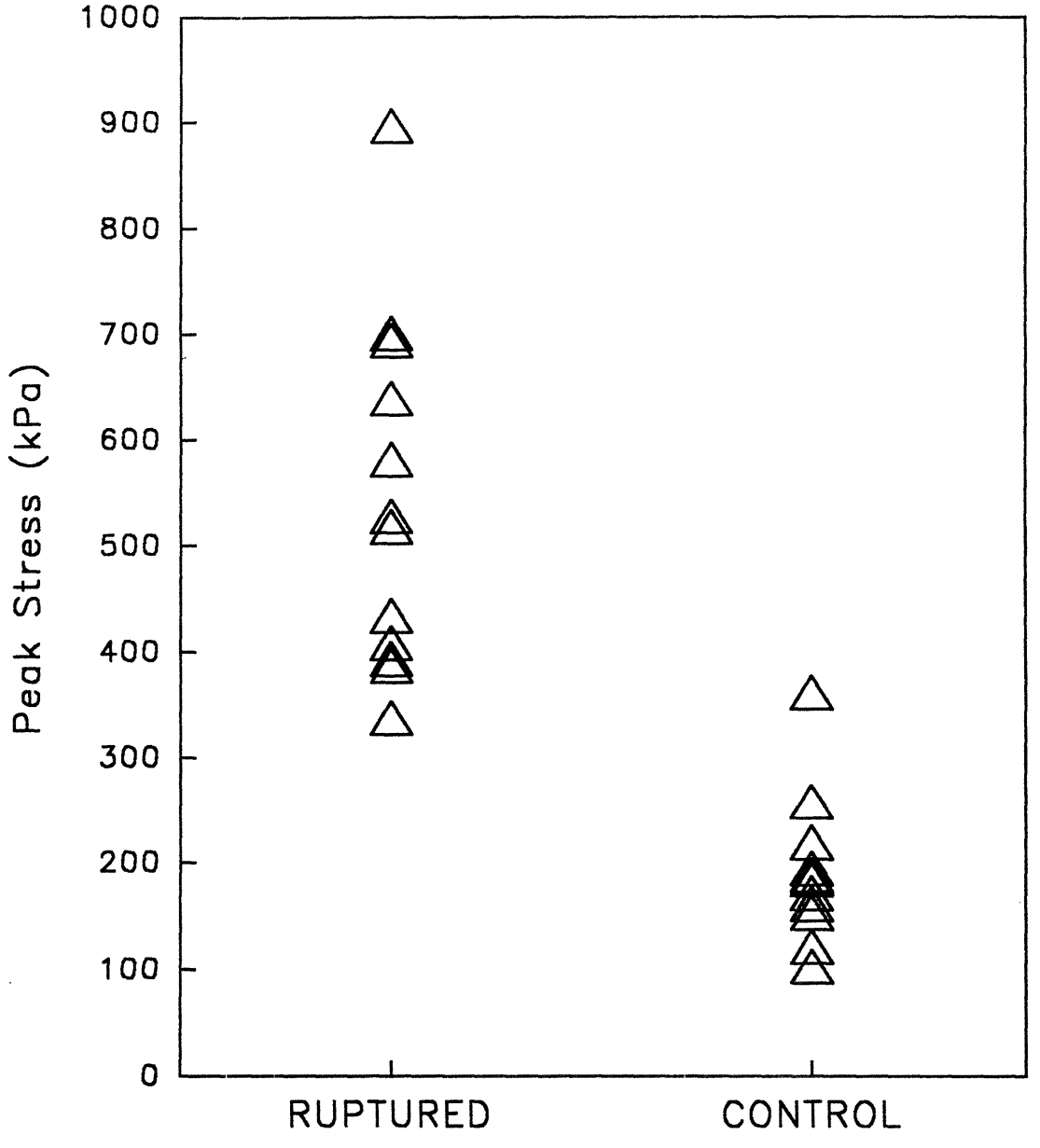

Fig. 5.1 Peak circumferential tensile stress in 12 ruptured and 12 stable coronary lesions. Peak stresses are significantly increased in ruptured lesions ($p < 0.0001$).

Fig. 5.2 (a) Hematoxylin and eosin stain of ruptured coronary lesion from a circumflex coronary artery associated with myocardial infarction. The arrow designates the rupture location. (b) Finite element mesh with regions with different material properties. Dark blue is calcium, red is fibrous plaque, yellow is lipid pool, and light blue is artery. (c) Color contour map of circumferential stress from finite element solution. The color scale is linear (by pascal values). The peak circumferential stress in this specimen was 325 kPa.

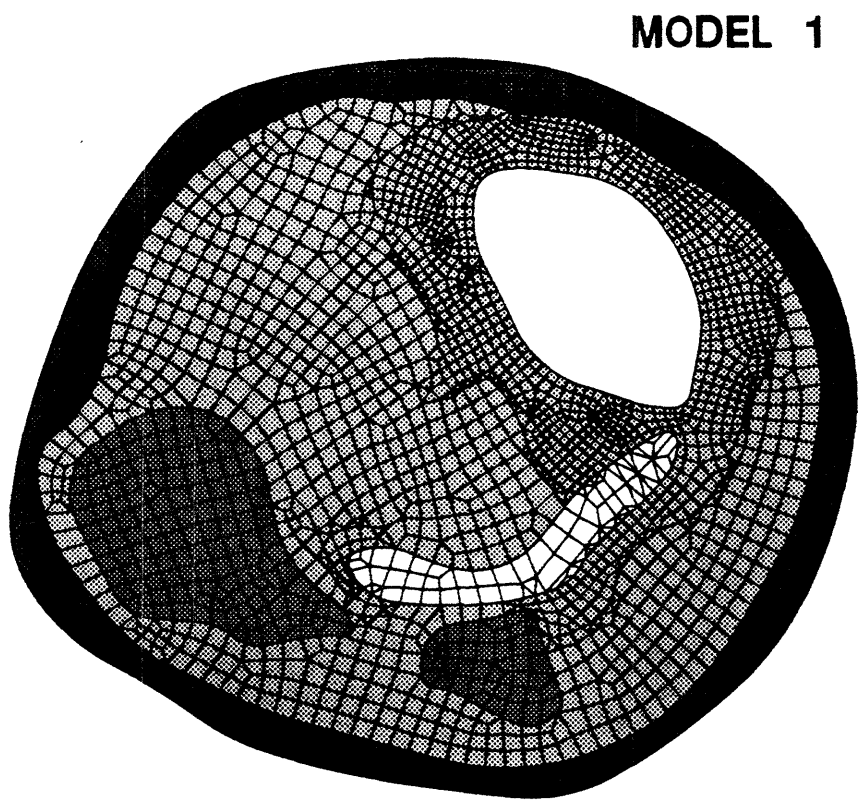

Fig. 5.2b Finite element mesh of ruptured lesion.

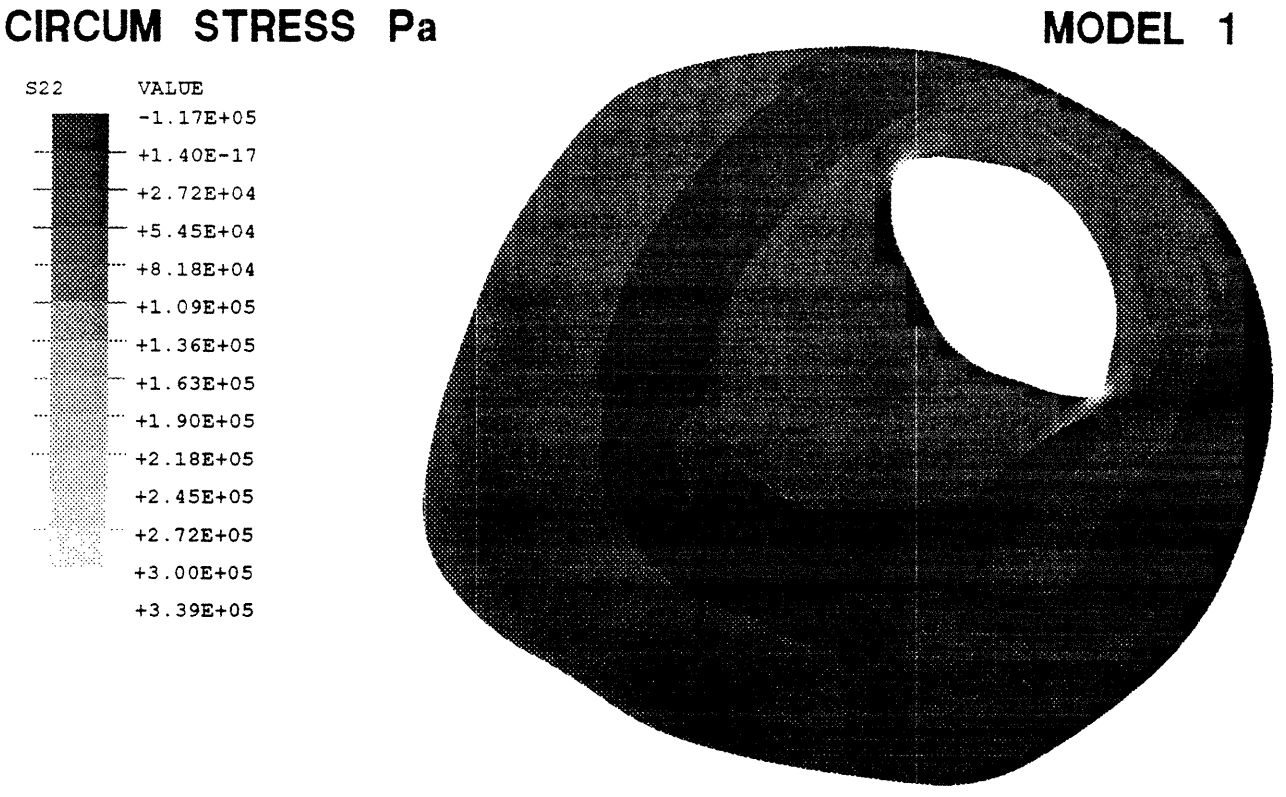

Fig. 5.2c Contour map of circumferential stress in ruptured lesion.

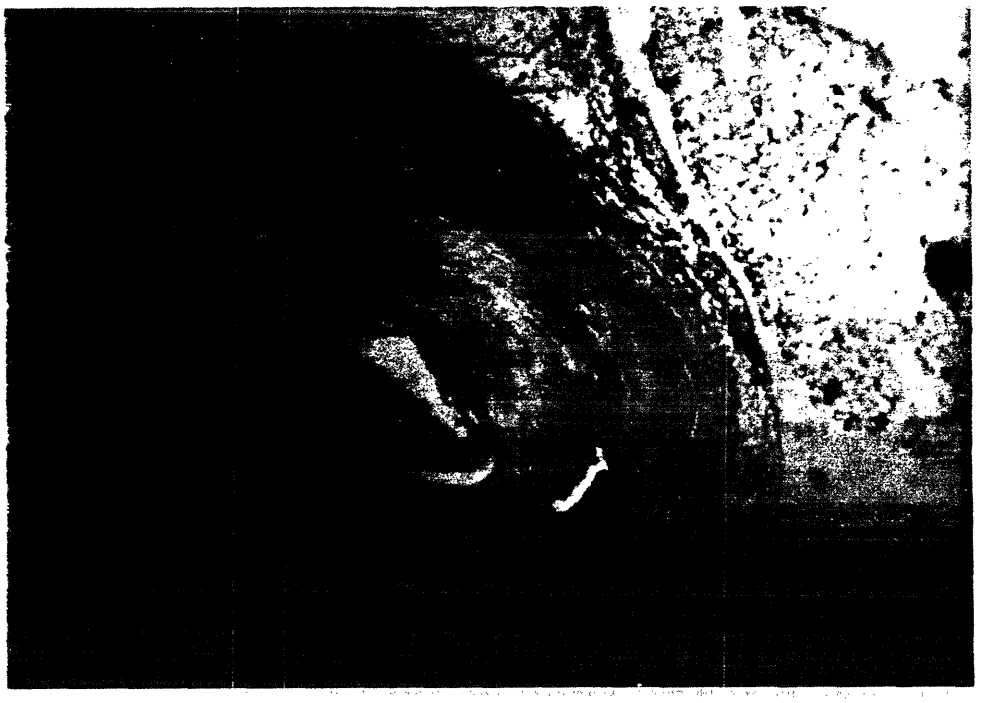

Fig. 5.3 (a) Hematoxylin and eosin stain of stable coronary lesion from a left anterior descending coronary artery. (b) Finite element mesh with regions with different material properties. Dark blue is calcium, red is fibrous plaque, and light blue is artery. (c) Color contour map of circumferential stress from finite element solution. The color scale is linear (by pascal values). The peak circumferential stress in this specimen was 102 kPa.

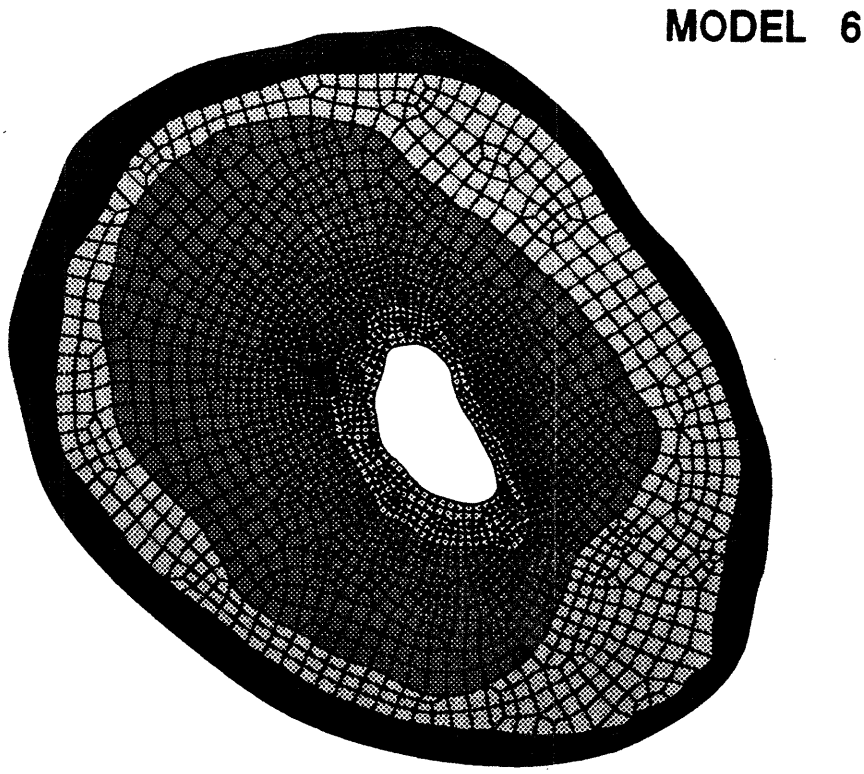

Fig. 5.3b Finite element mesh of stable lesion.

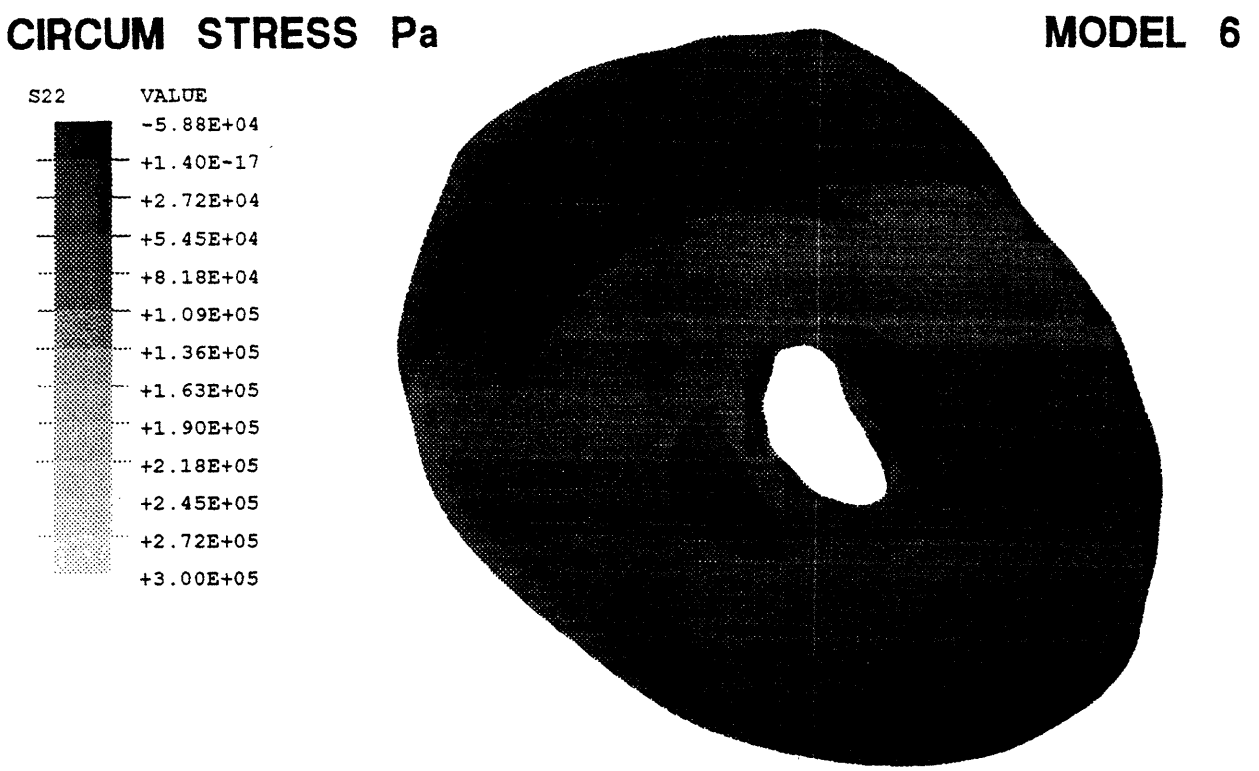

Fig. 5.3c Contour map of circumferential stress in stable lesion.

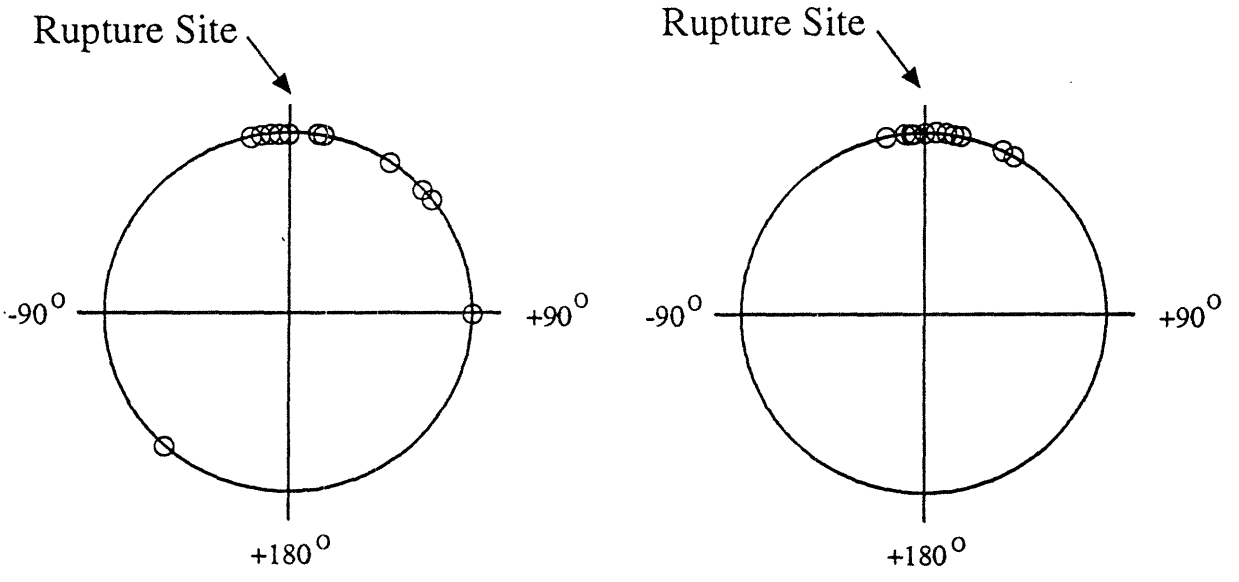

Fig. 5.4 Angles between regions of stress concentration and rupture sites in 12 specimens. **Left,** angle between rupture site and peak stress concentration. **Right,** angle between rupture site and nearest high (>300 kPa) stress concentration.

CHAPTER 6

MODELING STRESS FIELDS IN ATHEROSCLEROTIC ARTERIES UNDER ANGIOPLASTY CONDITIONS

ABSTRACT

Intravascular ultrasound imaging prior to interventional procedures has potential for providing information useful for guiding therapeutic strategies. This in vitro study was designed to test the hypothesis that a structural analysis based on intravascular ultrasound images of atherosclerotic vessels prior to angioplasty can be used to predict plaque fracture locations and balloon pressures required to cause plaque fracture. Intravascular imaging was performed on 16 atherosclerotic human iliac vessel segments obtained freshly at autopsy; balloon angioplasty was then performed with one minute inflations at 2 atmosphere increasing increments until fracture of the luminal surface occurred. Fracture locations were confirmed by histopathologic examination. Structural analysis of intravascular ultrasound images was performed with a large strain finite element analysis of the image which calculated the distribution of stress in the vessel with 2 atmospheres of luminal pressure. Structural analysis demonstrated a total of 30 high (>3 megapascal) circumferential stress regions in the vessels (mean, 1.9 high stress regions per vessel). A total of 18 plaque fractures occurred in the 16 vessel segments. Of the 17 fractures that occurred in the 15 specimens with regions of high circumferential stress, 14 (82%) occurred at a high stress region. However, there was no significant

relationship between the peak stresses estimated by structural analysis and the ultimate balloon inflation pressure required to cause fracture.

Therefore, structural analysis based on intravascular ultrasound imaging prior to in vitro balloon angioplasty can predict the locations of plaque fracture that usually accompany angioplasty. However, these data suggest that intravascular ultrasound may not be useful for predicting the ultimate balloon inflation pressure necessary to cause fracture, possibly due to the variable fracture properties of atherosclerotic tissues, and limiting vessel injury by this approach may not be feasible.

INTRODUCTION

Although the clinical effectiveness of percutaneous transluminal coronary angioplasty has led to widespread utilization of this technique, late restenosis following angioplasty continues to be an important clinical problem (68-71). Because residual post-angioplasty lesion morphology may be a critical factor in determining outcome, understanding more about the consequences of interventional procedures may improve strategies to prevent excessive injury to the vessel that may lead to complications (72). Recent studies have documented that intravascular ultrasound imaging provides a more complete description of the effects of coronary interventional procedures than coronary angiography (73,74). For example, Honye *et al* found that intravascular ultrasound could identify a subset of patients with lesions more likely to develop clinical restenosis (73). Isner *et al* have performed imaging of peripheral vascular stenoses prior to and during angioplasty using a

combined imaging-angioplasty catheter, which improved monitoring of the effects of balloon angioplasty on the vessel (75).

Although current intravascular ultrasound imaging catheters are too large to allow imaging of most coronary stenoses prior to angioplasty, further miniaturization of transducers may allow visualization of preangioplasty morphology. It is possible that these cross-sectional images could provide structural detail–particularly subintimal detail–that could guide strategies *before* any interventional procedures begin. Angioscopy may also be a useful technique for characterizing lesions before PTCA (76). For example, although high balloon inflation pressures may lead to improved immediate hemodynamic results, some evidence suggests that high inflation pressures are related to late restenosis (77-79). Identification of highly stable lesions--that is, lesions that would require unusually high balloon inflation pressures to cause fracture of the intimal surface–could influence the choice of interventional technique. This in vitro study was designed to test the hypothesis that a structural analysis based on intravascular ultrasound images of atherosclerotic vessels prior to angioplasty can be used to predict plaque fracture locations and balloon pressures required to cause fracture.

METHODS

Specimens. Segments of diseased iliac vessel were obtained freshly at autopsy from Brigham and Women's Hospital and the Beth Israel Hospital, Boston, MA. At autopsy, specimens were immediately transferred to normal saline and washed free of blood. The specimens were then cut into 1 cm long cross-sectional segments; each

segment was visually inspected to exclude intimal fractures made by cutting the vessel. The most severely diseased segment was selected for the study. The internal lumen area was traced using the intravascular ultrasound imaging device, and the area of the "normal" vessel was estimated from a visual estimate of the vessel. Only lesions with 50% or more area reduction were used; the mean area reduction was 57 ± 5%. All experimentation was completed within 6 hours of autopsy.

Imaging Protocol. Sutures were placed in the adventitia at 90 degree intervals to suspend the vessel in a 37 degree Centigrade waterbath filled with normal saline. The sutures were color encoded so that orientation of the vessel could be recorded; an arbitrary "zero degree" reference point was chosen with respect to the colored sutures. Intravascular ultrasound images were then obtained using a commercially available imaging system with a 30 Mhz transducer with a rotating mirror assembly on a 5 Fr catheter. Axial resolution on the video display of this system is approximately 150 μm and lateral resolution is approximately 250 μm. Gain and other imaging settings were adjusted by the operator to achieve optimal gray scale appearance. The supporting stent on the imaging catheter was used to align with the "zero degree" reference point, and the imaging catheter was then rotated 90 degrees to allow imaging of the area previously obscured by the stent. Only the approximate center of the 1 cm vessel segment was imaged, and the images were recorded on standard 0.5 inch videotape.

Angioplasty. Following ultrasound imaging, angioplasty was performed using polyethylene terephthalate balloon catheters. Initially, the balloon size was chosen

to be 1.3 times the diameter of the artery without plaque, as previously described by Tobis *et al* (80). However, if a visible waist was not apparent during serial inflations, the balloon size was increased to maximize the delivery of internal balloon pressure to the vessel intimal surface. The initial inflation was 2 atmospheres (atm) for 1 minute; inflations were then increased at 2 atm increments. Following each inflation, the balloon was deflated and removed allowing visual inspection of the vessel for fracture of the luminal surface. The balloon was then reinserted and inflated directly to pressure 2 atm greater than in the previous inflation. Intravascular ultrasound was not used as an endpoint for fracture because we and others have found that intravascular ultrasound images may not reveal small fractures (76). When fracture of the surface was apparent, the experiment was terminated and the vessel was immediately placed in 10% formalin for histopathologic examination.

Structural Analysis. Structural analysis was performed using the finite element method (61). Ultrasound images prior to angioplasty were traced on to transparencies by an investigator who was uninvolved with the angioplasty experiments and therefore had no knowledge of fracture locations or final balloon pressures at fracture. The stent of the imaging catheter was used to identify the "zero degree" reference point. The approximate center of the lumen was used as the origin of the cylindrical coordinate system. The image was traced, identifying internal lumen border, "normal" vessel border, regions of plaque, and regions of dystrophic calcification. These tracings were then used to build finite element meshes using SDRC I-DEAS IV software on a DEC Vaxstation 3100 computer with

a graphics tablet. A finite element mesh is comprised of small elements, with each element representing a small region of material with a defined material law. The average element dimension was 0.15 to 0.2 mm; in regions near the junction of plaque and more normal artery, the element dimension was reduced to 0.05 mm to improve accuracy of the model. Elements were plane strain, 8-noded, quadrilateral elements using mixed formulation. The range of number of elements was 1,100-3,300 and the range of number of nodes was 3,500-10,200.

The material laws for the models were based on the static circumferential tensile data described in Chapter 3 and several important assumptions. A second order fit was performed on the stress-strain relations for the six stiffest hypocellular plaques tested (Fig. 3.3b). The non-equilibrium stiffness of plaque under angioplasty was first assumed to be 100 times the static stiffness. This non-equilibrium stiffness was used as the modulus of a non-linear, isotropic, incompressible plaque material law. The material law for normal artery was similar to that of plaque, but with a stiffness one-fifth that of plaque. Model number 1 was run with these material laws at a luminal pressure of 2 atm. The results of the analysis gave the approximate operating point on the nonlinear stress-strain curves. To adapt the model for stable performance at the large strains expected in angioplasty, the plaque and artery material laws were next assumed to be linear, with moduli taken to be one tenth that of the operating point stiffnesses found in the pilot run (81). Fig. 6.1 illustrates the final choice of linear plaque and artery material laws used in all 17 iliac artery models. The elastic modulus for plaque at 2 atm was estimated to be approximately

30 megapascals (MPa), for artery 15 MPa, and for areas of dystrophic calcification 1000 MPa.

Finite element models were then solved using HKS ABAQUS 4.9 software on a CRAY X-MP supercomputer for an intraluminal pressure load of 2 atm. A large strain model based on strain energy potential, typically used to describe elastomeric materials, was used with Newton's method and residual nodal force tolerance of 0.1 newton. Contour plots of circumferential and shear stresses (tangent to the lumen surface in the circumferential direction) were displayed using a Tektronics 4209B graphics terminal. Regions with concentrations of circumferential tensile stress greater than 3 MPa were identified and angles with respect to the coordinate system were recorded.

Specimens were sectioned and stained with hematoxylin and eosin. Rupture locations were recorded by an experienced cardiac pathologist on the tracings made from the ultrasound images (using the color-encoded sutures as a guide), and locations were recorded using the same cylindrical coordinate system. When the angle between the rupture site (as determined by histopathologic examination) and a circumferential stress concentration was less than or equal to 15 degrees, rupture was assumed to have occurred at the stress concentration location. Comparisons of peak circumferential and shear stresses estimated by structural analysis to balloon pressure at rupture were performed with linear regression analysis. All data are presented as mean ± one standard deviation, and a p value < 0.05 was considered statistically significant.

RESULTS

Structural Analysis. The results of two typical analyses are illustrated in Fig. 6.2 and 6.3. The calculated peak circumferential tensile stress in the vessels using the finite element model was 8.2 ± 2.7 MPa (range, 1.4 to 12 MPa). In the 16 of the 17 specimens, a total of 30 high stress regions of circumferential stress greater than 3 MPa were seen (mean, 1.9 high stress regions per lesion). In one lesion, no high stress region was found; in two lesions, one high stress region was found; in 11 lesions, two high stress regions were found; and in two lesions, three high stress regions were found. Generally, these high stress regions were located near the junctions of plaque with more normal vessel, explaining why the most common configuration was two high stress regions per lesion. Results for the additional 15 models can be found in Appendix Figures A.7-A.22.

Angioplasty. The balloon pressure used to cause fracture was 6.4 ± 3.7 atm (range, 2-14 atm). Two of the 16 specimens had two different intimal fracture locations, giving a total of 18 fracture locations. Of the 17 fracture locations that occurred in the 15 specimens with regions of high circumferential stress (greater than 3 MPa), 14 (82%) occurred within 15 degrees of a high circumferential stress region (Fig. 6.4). The angle between the high stress region identified by structural analysis of intravascular ultrasound images and the fracture location was 3 ± 37 degrees (95% confidence interval, -16 to +22 degrees). Thus, the majority of fracture locations caused by angioplasty occurred at or very near a region of high circumferential stress.

Relation of Predicted Stresses to Balloon Pressures. If atherosclerotic materials behaved in a linearly elastic or nearly linearly elastic manner, and plaque materials had a characteristic fracture stress, it is possible that the circumferential tensile stresses predicted in the vessel wall at two atmospheres luminal pressure by finite element analysis could predict the balloon pressure required to cause fracture of the plaque. In this in vitro study, there was no significant relationship between the peak stresses estimated by structural analysis and the ultimate balloon pressure used to cause fracture (R=0.03, p=NS) (Fig. 6.5).

In addition, shear stresses in the circumferential direction were calculated at two atmospheres luminal pressure in the finite element analysis. Shear stresses were 2.0 ± 0.9 MPa and were maximum in the same areas as the maximal circumferential tensile stresses. There was no significant relationship of peak shear stresses estimated by finite element analysis of the ultrasound images and the ultimate balloon pressure used to cause plaque fracture (R=0.09, p=NS) (Fig. 6.6).

DISCUSSION

In this in vitro study investigating the potential for using intravascular ultrasound to predict the results of angioplasty, a large strain finite element analysis based on vascular mechanics was used. This approach predicted regions of high circumferential stress where fracture of the intimal surface occurred. Previous investigators have proposed that the predominant mechanism of balloon angioplasty is rupture of the surface (often near the junction of plaque with more normal vessel)

which then allows "stretching" of the lumen (82,83). It is likely that this stretching includes both a nonlinear viscoelastic component that results in some "recoil" of the vessel and a component of plasticity, where breaking of molecular bonds leads to a more permanent deformation.

Although fracture sites were accurately identified in this study, there was no significant relationship between computed stresses from the simulation of a two atmosphere balloon inflation and the ultimate balloon inflation pressure used to fracture the intima. There are a number of potential explanations for the failure of this structural analysis to predict ultimate balloon inflation pressure. First, the biomechanical behavior of human atherosclerotic tissue is variable even when the tissues are histologically similar, so that a single plaque material law is probably inadequate (43,49). Second, current intravascular imaging catheter technology provides relatively primitive "tissue characterization" information, so that variations of mechanical properties within the plaque could not be considered. Third, these studies only considered stresses in two dimensional images. It is possible that mechanical behavior in the third dimension, the longitudinal direction, was important. In addition, the linearly elastic finite element simulation of stresses and strains during a two atmosphere inflation may simply be inadequate for modeling the complex phenomena of angioplasty, which probably include viscoelastic and viscoplastic effects (84). Lastly, and perhaps most important, little is known about the fracture properties of human atherosclerotic tissues. It is likely that peak stress

alone is not sufficient to predict fracture and that fracture is actually a complex function of stress and strain that varies between individual specimens.

The clinical literature regarding the relationship between inflation pressure and outcome of balloon angioplasty is not conclusive, with some studies reporting improved long-term results with higher inflation pressures and other studies reporting an increased restenosis rate (77,78,85,86). However, data from experimental studies suggests that smooth muscle injury and intimal hyperplasia are greater at high balloon inflation pressures (79). The data from this study on chronic non-ruptured iliac artery lesions suggest that intravascular ultrasound may not be useful for predicting balloon inflation pressure necessary to cause intimal fracture, the most common mechanism of successful angioplasty. However, the outcome of the study may have been different if acute (already ruptured) coronary lesions were dilated. Such lesions can cause unstable angina, stable angina, and myocardial infarction: conditions treated with PTCA.

Limitations. An important limitation in this study concerns the material laws used in the finite element analysis. By assuming that plaque, calcium, and normal arterial wall were each characterized by a single set of material parameters, spatial variation or variations between specimens were not considered. In addition, since the investigators performing the finite element analyses did not know the actual balloon pressures at rupture, all modeling was performed at a relatively low (two atmosphere) pressure. Because biologic materials are nonlinear, particularly at high strains, it is likely that distribution of stresses in the diseased vessel changes at higher

balloon pressures. However, since one would not know the balloon pressure at plaque fracture prior to performing the procedure, we selected one single luminal pressure for the structural analysis.

In this study, balloon size was selected to insure that a "waist" appeared with each inflation to maximize delivery of balloon pressure to the intimal surface. In clinical practice, delivery of balloon pressure to the intimal surface will be a function of lesion geometry as well as compliance of the balloon. Therefore, the strains of angioplasty will depend on balloon material properties, lesion geometry, balloon pressure, and duration of inflation. In addition, we used moduli for the normal artery estimated from mechanical testing of human aortic tissues. Because the aorta and iliac vessels are elastic arteries rather than muscular arteries like the coronary arteries, different material parameters may be necessary for considering coronary angioplasty.

Clinical Implications. This in vitro study suggests that structural information from imaging atherosclerotic lesions prior to angioplasty or other interventions could be useful, although it may not be possible to predict balloon inflation pressures necessary to fracture the lesion. It is currently not feasible to perform finite element computational models in the catheterization laboratory, but structural analysis could be used to develop a "catalog" of configurations with particular features that could guide therapeutic decisions. However, before this approach could be applied clinically, more must be learned about the biomechanical behavior of diseased vessels, and intravascular ultrasound imaging technology will need to improve.

CONCLUSIONS

Although fracture sites were accurately identified in this study, there was no significant relationship between computed stresses from the simulation of a two atmosphere balloon inflation and the ultimate balloon inflation pressure used to fracture the intima. The linearly elastic finite element simulation of stresses and strains during a two atmosphere inflation is simply inadequate for modeling the complex phenomena of angioplasty. More sophisticated models of plaque deformation and fracture are needed to predict minimal inflation pressures for balloon angioplasty.

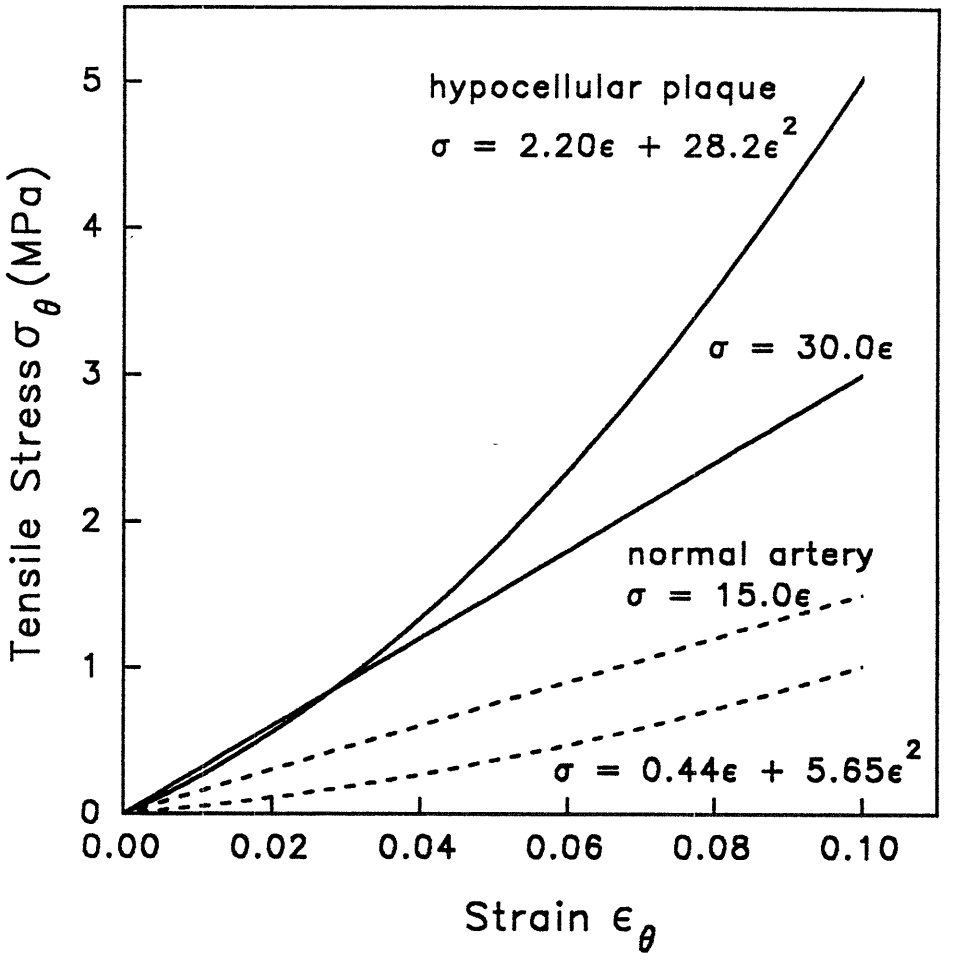

Fig. 6.1 Tensile stress-strain relations used in iliac artery models for hypocellular plaque and normal artery.

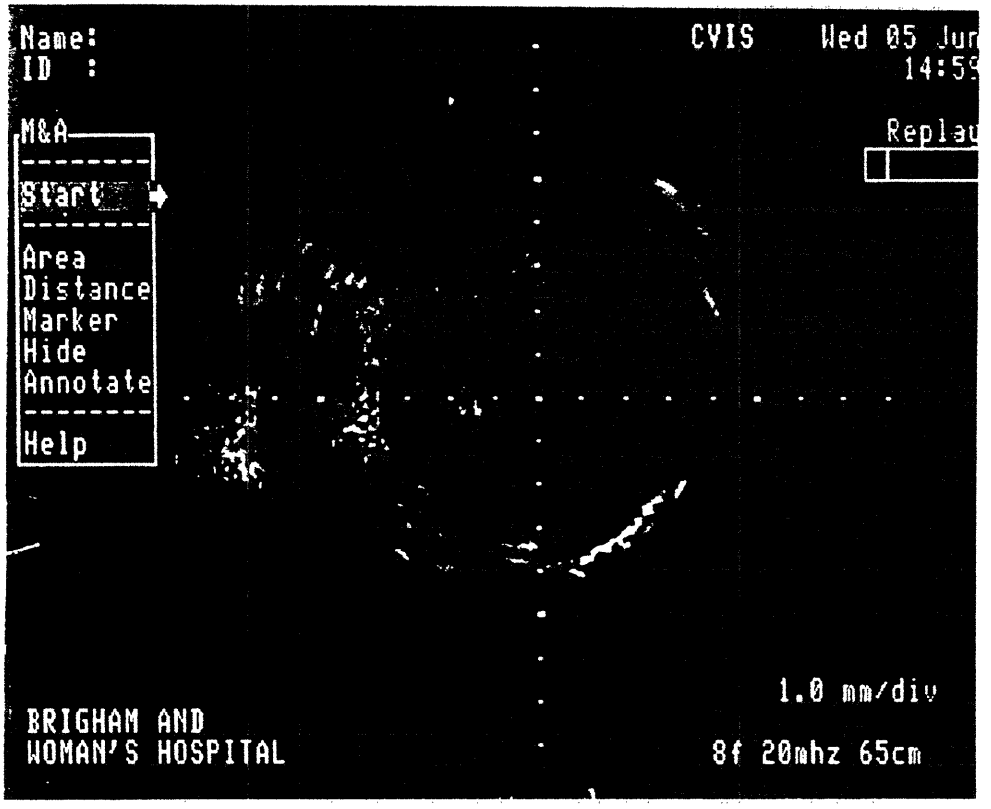

Fig. 6.2 (a) Intravascular ultrasound image of atherosclerotic iliac artery Model 1. (b) Finite element mesh of ultrasound image. The dark elements are more normal vessel, while the lighter elements are fibrous plaque with a region of calcium included. (c) Finite element solution at 2 atm pressure demonstrating high circumferential stress locations. (d) Deformed mesh.

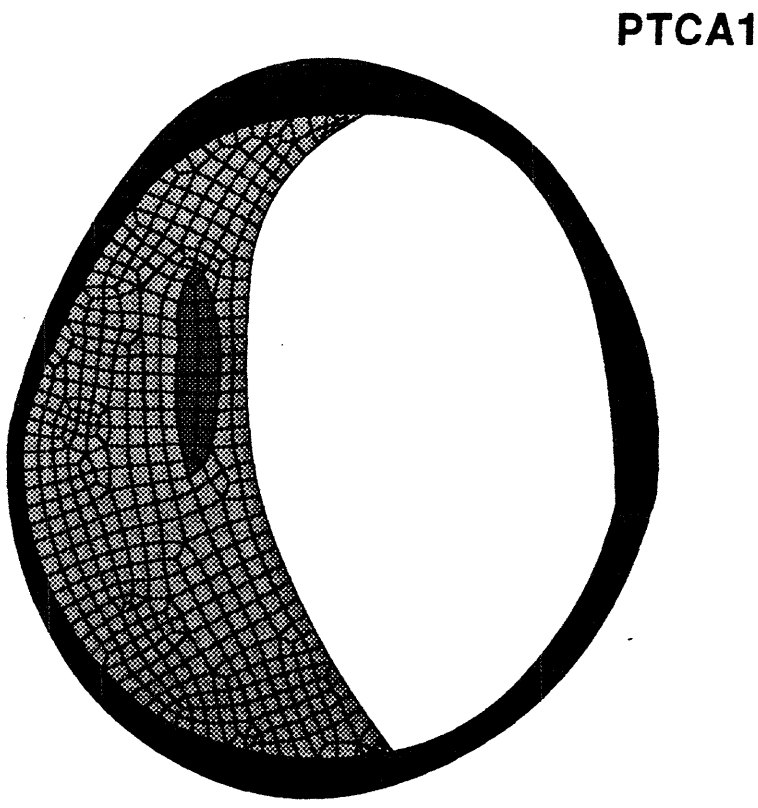

Fig. 6.2b Finite element mesh of ultrasound image (Model 1).

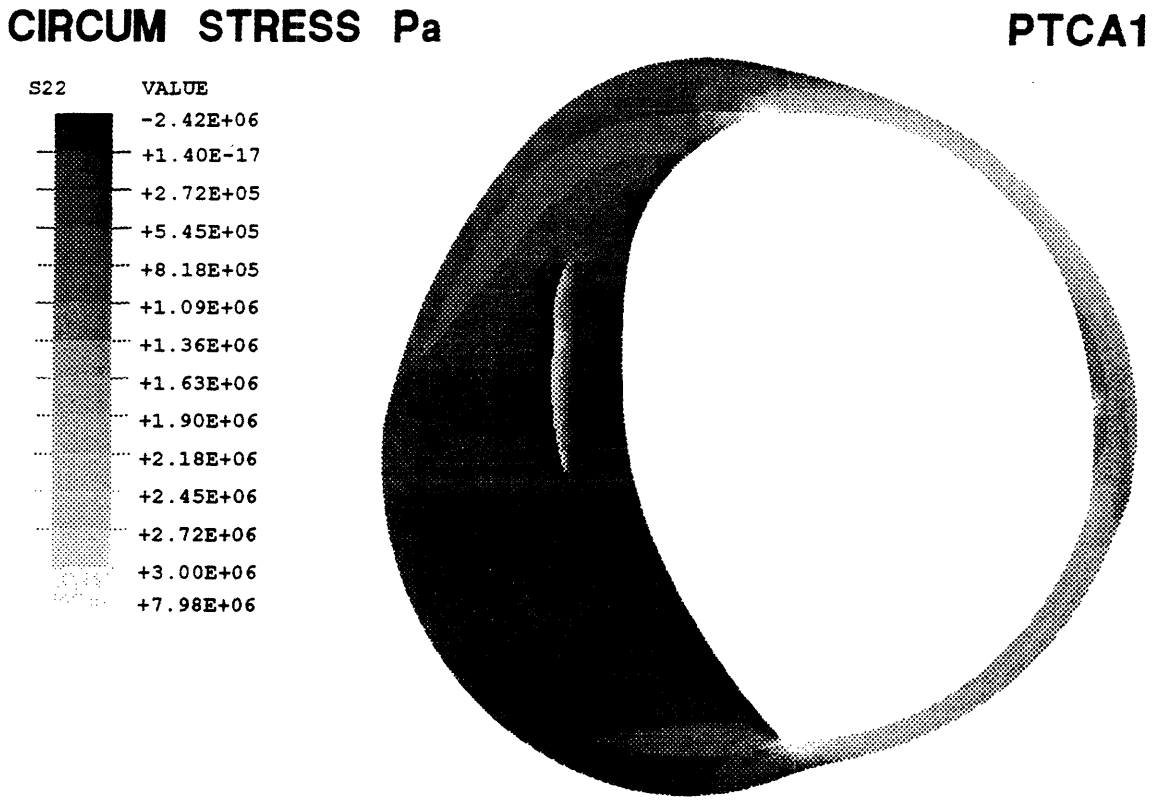

Fig. 6.2c Contour map of circumferential stress (Model 1).

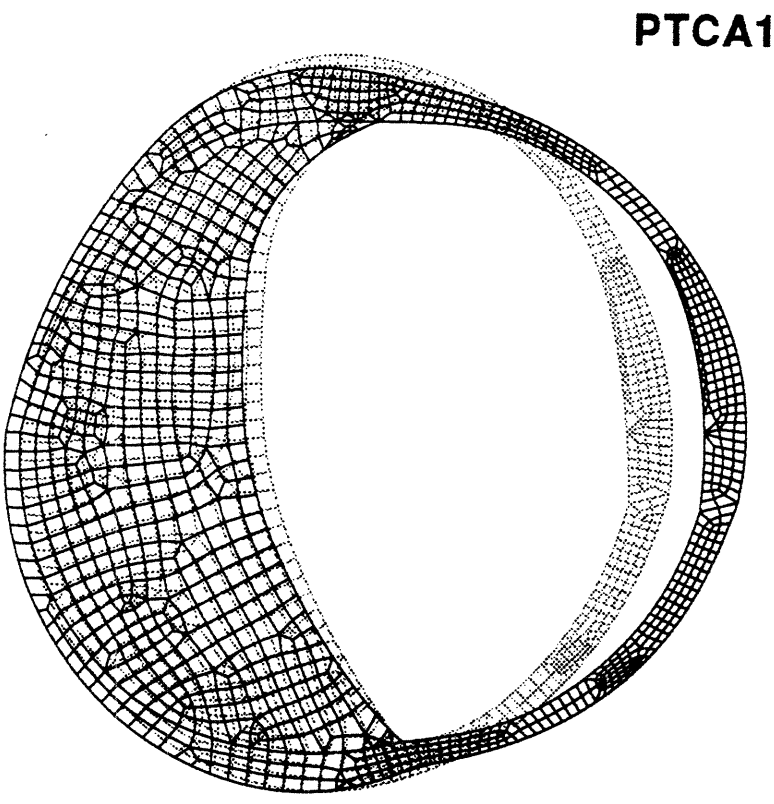

Fig. 6.2d Deformed finite element mesh (Model 1).

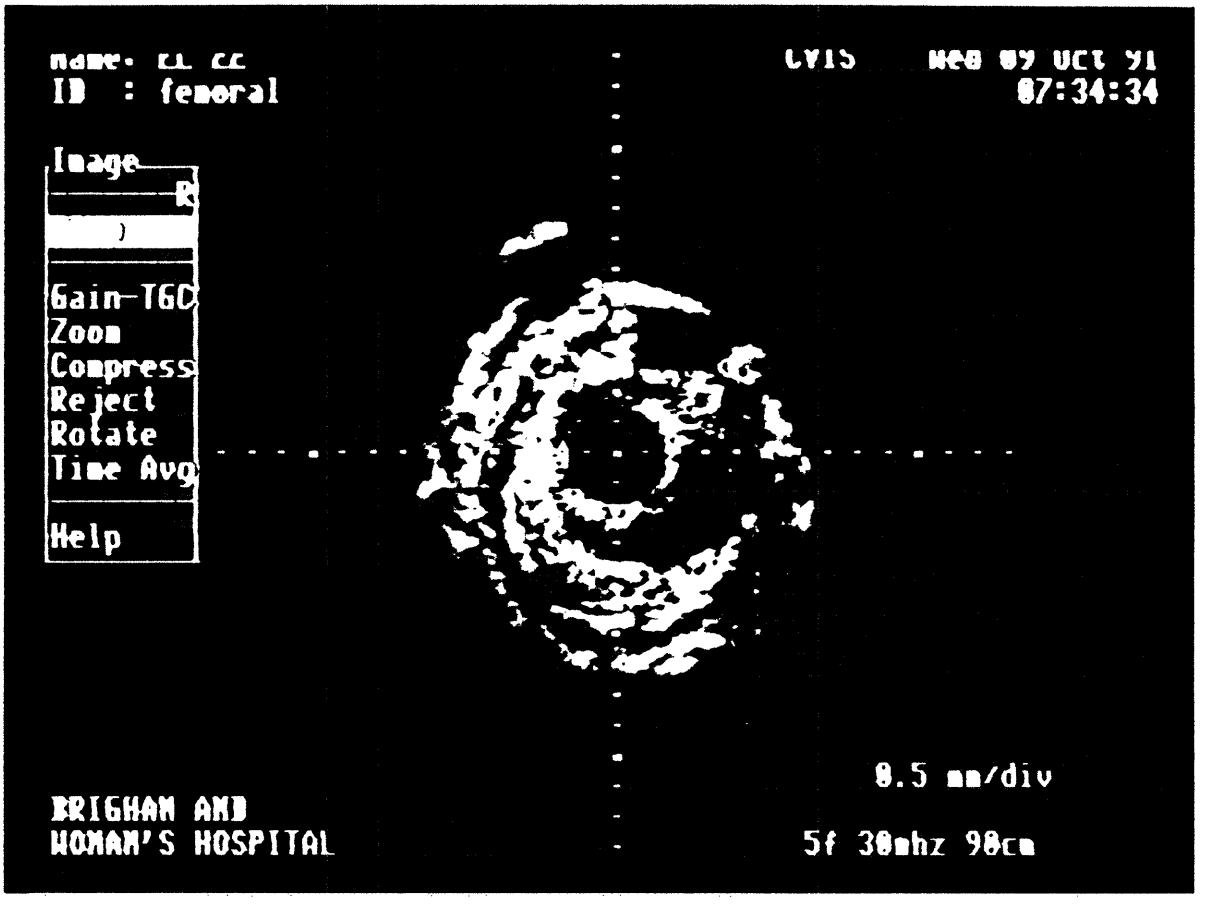

Fig. 6.3 (a) Intravascular ultrasound image of atherosclerotic iliac artery Model 22. (b) Finite element mesh of ultrasound image. The dark elements are more normal vessel, while the lighter elements are fibrous plaque. (c) Finite element solution at 2 atm pressure demonstrating high circumferential stress locations. (d) Deformed mesh.

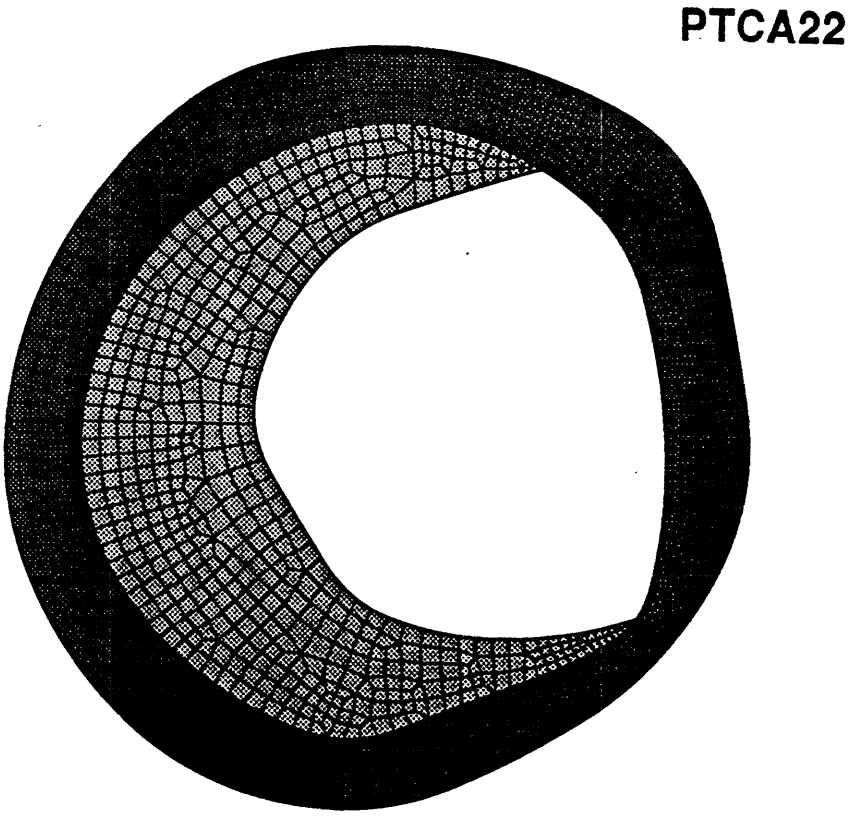

Fig. 6.3b Finite element mesh of ultrasound image (Model 22).

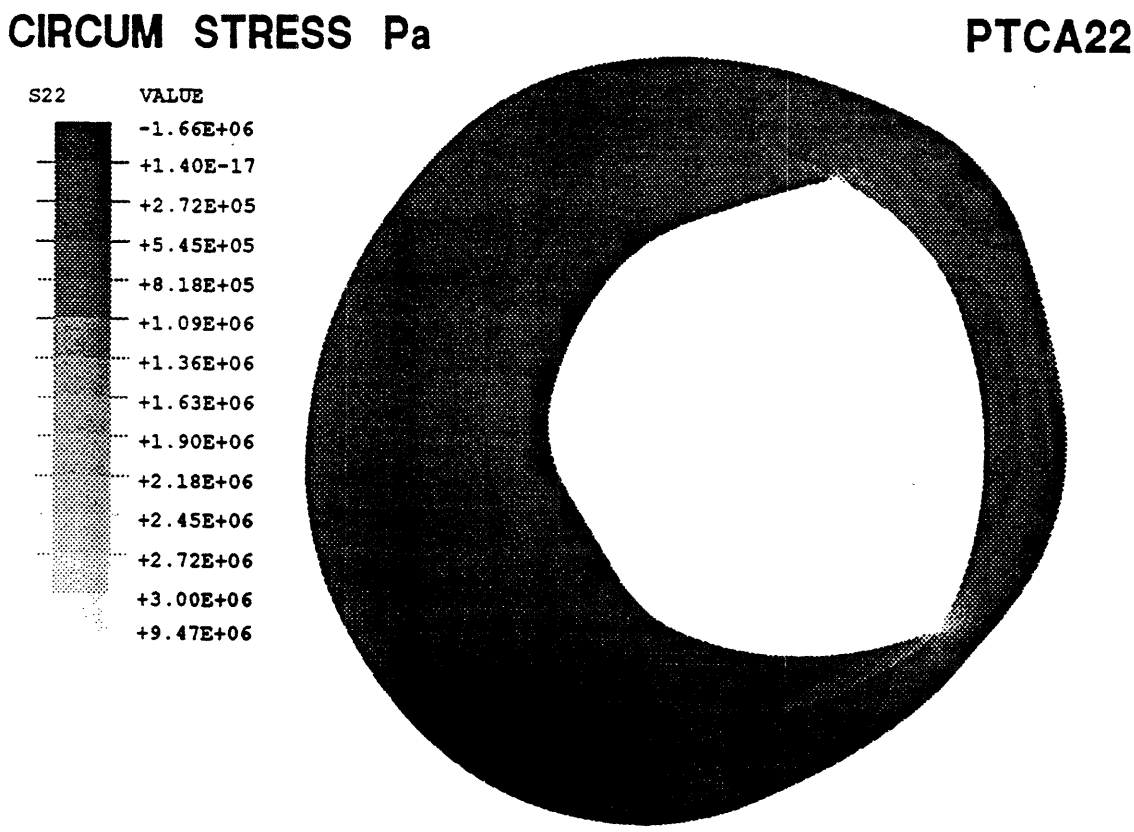

Fig. 6.3c Contour map of circumferential stress (Model 22).

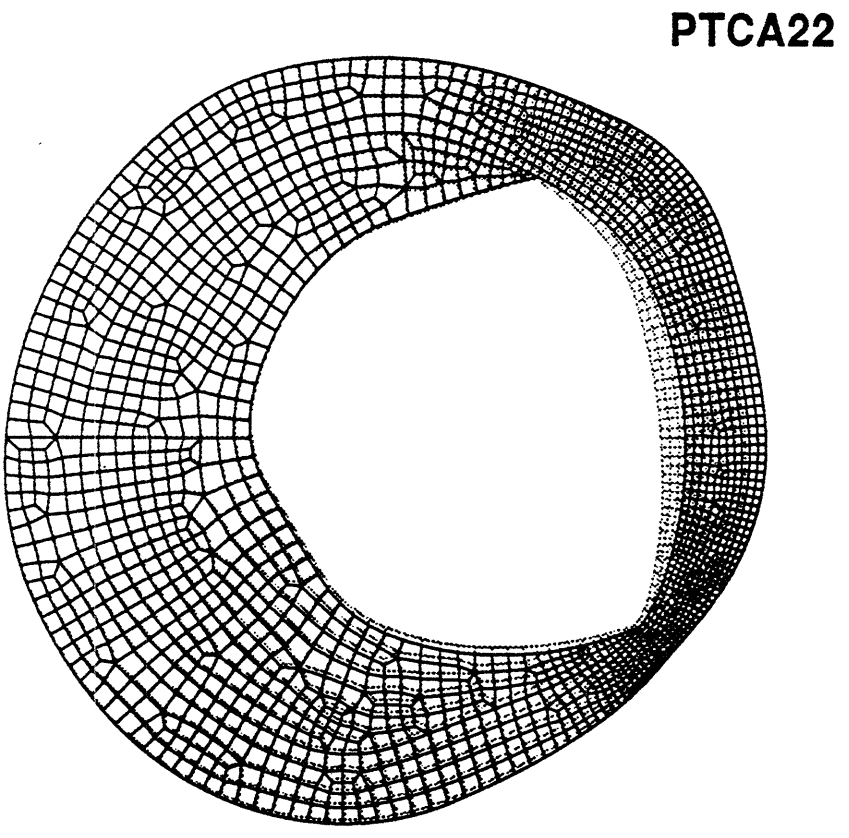

Fig. 6.3d Deformed finite element mesh (Model 22).

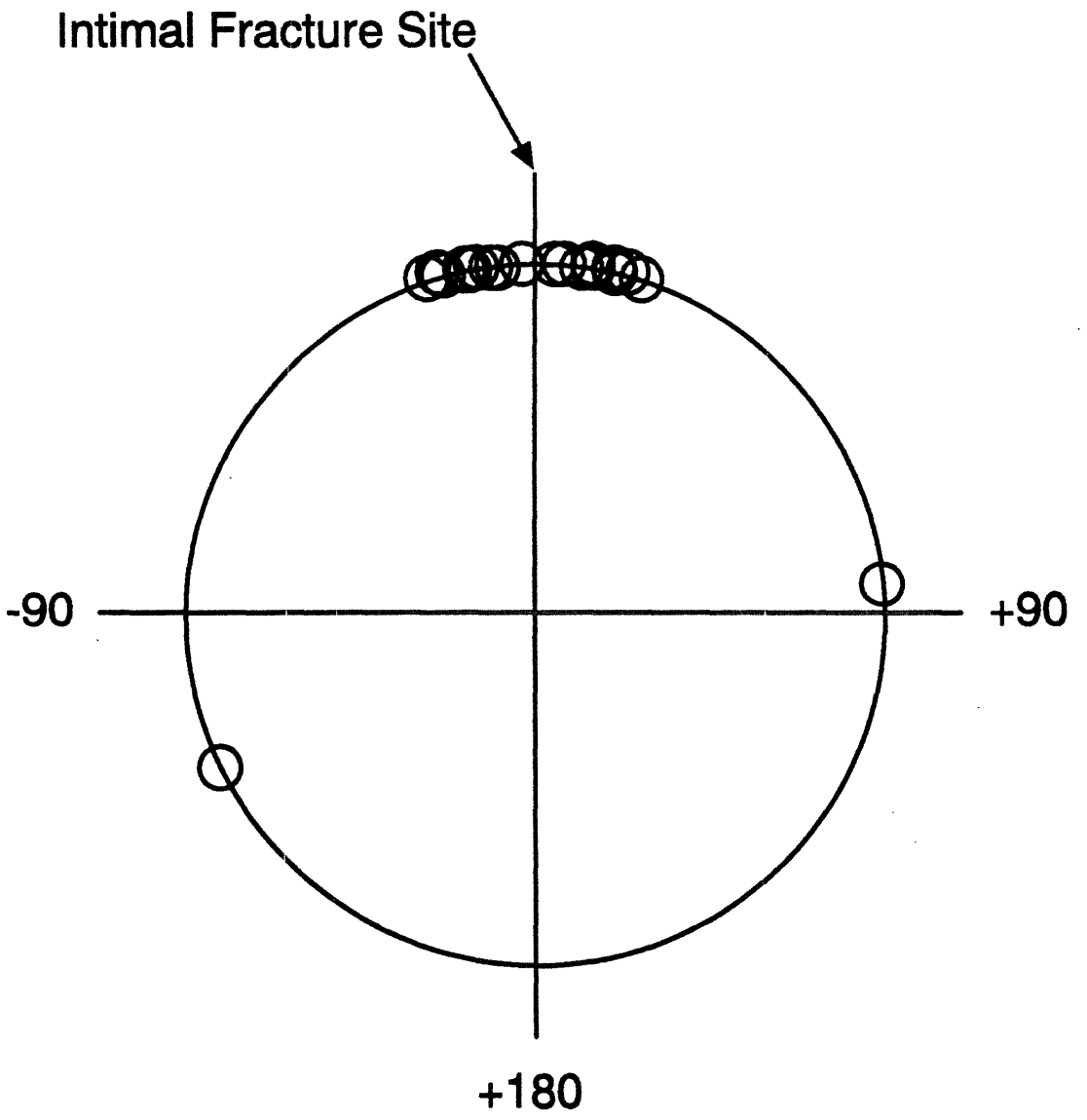

○ One lesion had no high stress regions

Fig. 6.4 Angle between location of 18 intimal fracture sites as described by histopathologic examination and nearest high (>3 megapascal) circumferential stress region in the 16 vessels determined by structural analysis. One fracture occurred in a vessel with no high stress region. Fourteen of the remaining 17 (82%) fractures occurred within 15 degrees of high stress regions.

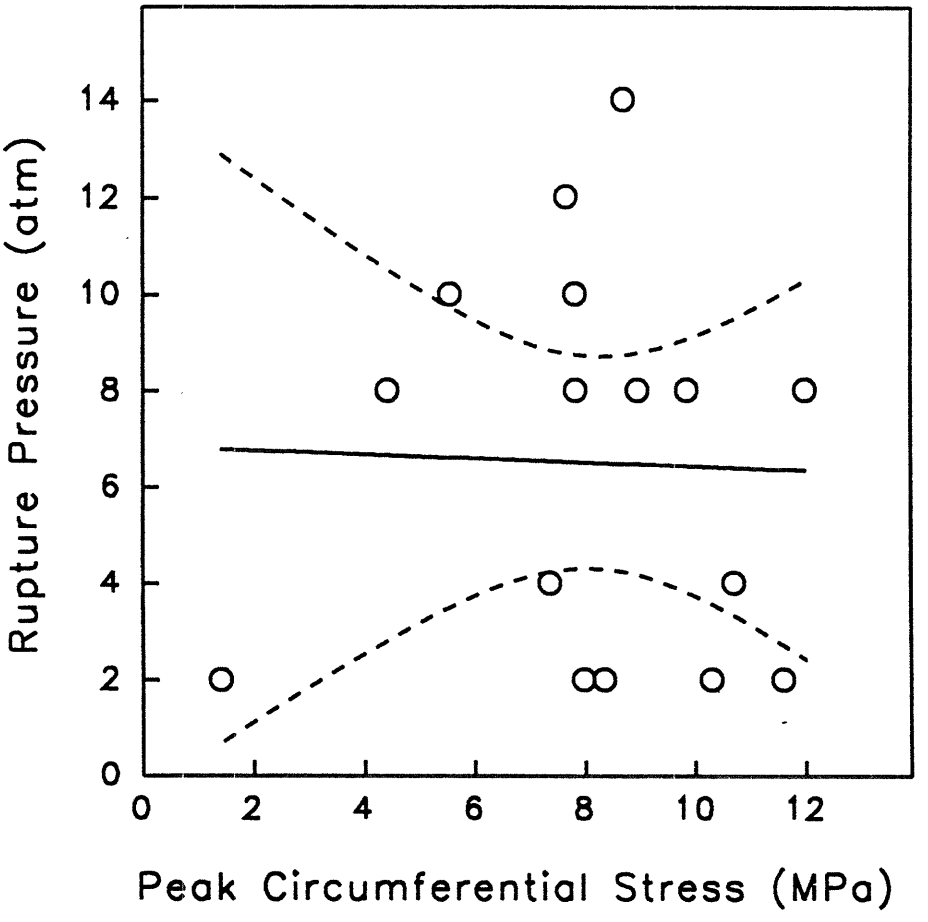

Fig. 6.5 Relationship of peak circumferential tensile stress (x axis, in megapascals) to ultimate balloon inflation pressure used to fracture the intimal surface (y axis, in atmospheres). The solid line is the linear regression (R=0.03, p=NS) and the dotted lines are 95% confidence lines. There is no significant relationship between estimated peak tensile stress and ultimate balloon inflation pressure.

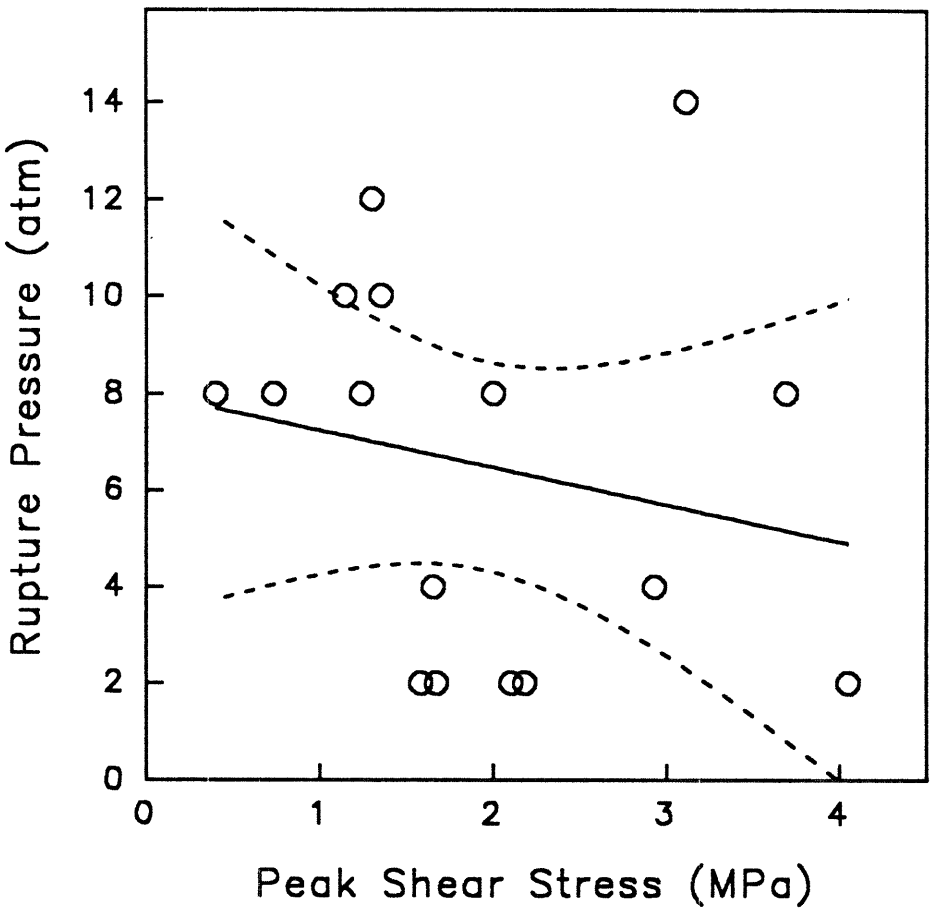

Fig. 6.6 Relationship of peak circumferential shear stress (x axis, in megapascals) to ultimate balloon inflation pressure used to fracture the intimal surface (y axis, in atmospheres). The solid line is the linear regression (R=0.09, p=NS) and the dotted lines are 95% confidence lines. There is no significant relationship between estimated peak circumferential shear stress and ultimate balloon inflation pressure.

CHAPTER 7

CONCLUSIONS

An Understanding of Plaque Rupture. The conclusions of this research are fourfold: First, hemodynamic forces may play a role in plaque rupture. A turbulent jet may impinge on a stenosis surface distal to the most severe constriction. The amplitude of pressure fluctuations is dependent on Reynolds number, length of the stenosis, and severity of the stenosis but is especially elevated in (90%) stenoses with asymmetric geometry. For axisymmetric stenoses, turbulence is less likely to play a role in plaque injury, particularly in the coronary artery. However, many fatal myocardial infarctions are caused by plaque ruptures in mild (50%) coronary stenoses where turbulence is insignificant.

Second, the average static circumferential tensile stiffness of atherosclerotic plaque is similar between the groups of cellular, hypocellular, and calcified plaques tested. Although hypocellular plaques are on average about twice as stiff as cellular plaques at physiologic ranges of tensile stress, the large variability in properties within cellular and hypocellular histologic classes makes the difference statistically nonsignificant. Static tensile stiffness increased with applied circumferential stress, an effect that was statistically highly significant for cellular and hypocellular plaques. Cellular and hypocellular plaques exhibit strongly anisotropic properties in the physiologic range of loading, with circumferential tensile stiffness about 20 times

greater than previously reported measurements of radial compressive stiffness. Plaques fracture at tensile stresses comparable to those found in previous studies.

Third, reducing the fibrous cap thickness dramatically increases peak circumferential stress in the plaque, while increasing stenosis severity actually decreases peak stress in the plaque. The maximum stresses in the plaque are critically dependent on subintimal structure of the lesion, suggesting that angiography alone will not provide sufficient information to identify vulnerable plaques. By understanding the importance of plaque structural features, particularly subintimal structure, and with improved coronary imaging modalities, identification of vulnerable lesions prior to rupture may become feasible. Fourth, local circumferential stress concentrations are predicted to occur in the plaque cap under physiologic luminal mean pressure loads. These correspond to observed sites of coronary plaque rupture. However, predicted peak stresses at a luminal mean pressure of 110 mmHg are often less than experimentally measured plaque tensile fracture stresses. Preliminary investigations (29) and this study indicate that the fracture stresses of stable human fibrous caps have a broad range that is generally 2-10 times peak static stresses predicted by finite element analysis (depending on geometry and subintimal structure). Nonulcerated aortic plaques generally do not fracture at tensile circumferential stresses lower than 600 kPa (29). Three important factors may explain why fracture stresses are higher than predicted stresses. First, myocardial infarctions do not occur randomly throughout the day, and it is likely that at least some infarctions are "triggered" by significant elevations in blood pressures, which

will increase circumferential stresses (8). In the linearly elastic model used in this study, increases in mean blood pressure would lead to directly proportional increases in circumferential stress; it is conceivable that large sustained increases in blood pressure could raise stresses into the fracture range. Second, repetitive dynamic stresses will be caused by pulsatile pressure; these dynamic stresses may cause "fatigue" of the plaque. It is also possible that fatigue through repetitive bending of the artery during the cardiac cycle occurs; this mechanism cannot be studied with the plane strain model. Third, the plaque is a biologically active environment, where macrophages, smooth muscle cells, platelets, and other cells participate in secretion and remodeling of the extracellular matrix. Richardson *et al.* have demonstrated that macrophage-rich regions of plaque will fracture at lower stresses than macrophage-poor plaques (29). In addition, evidence for stromelysin mRNA has been found in human atherosclerotic plaques; this protease may be one of the macrophage proteases causing plaque weakening (87).

Clinical Applications. Although acute plaque rupture is a major cause of death in developed countries, no therapeutic strategies have been developed specifically to prevent plaque rupture. Instead, most therapies for myocardial infarction are directed at the events that follow acute plaque rupture by thrombolysis or limiting myocardial oxygen demands. An approach that may allow identification of vulnerable plaques with thin fibrous caps overlying lipid pools is intravascular ultrasound and possibly angioscopy if the plaque cap is thin enough to show a yellow lipid pool underneath. Catheter-tipped ultrasound imaging transducers provide

information about subintimal structure that has previously been unavailable antemortem (76). These images can provide information that can be used to predict plaque biomechanical behavior (49,74,76,89). It may be possible through a combination of intravascular ultrasound imaging and finite element modeling to obtain much more information during cardiac catheterization than that provided by coronary angiography. Unfortunately, no currently available clinical method provides the antemortem subintimal structural detail required for the type of finite element analysis used in this study.

The results of this study may support a rationale for cholesterol-lowering therapy beyond its inhibitory effects on atherogenesis. Investigators involved in the FATS study found that cholesterol-lowering therapy dramatically reduced the incidence of acute events in hypercholesterolemic men, but had minimal effect on stenosis severity (88). A potential explanation for this is that cholesterol-lowering therapy may stabilize plaque structure through regression of underlying lipid pools and replacement by fibrous tissue. In addition, changing the mechanical properties of the lipid pool can lead to significant changes in stress in the plaque.

Future Work. One potential scenario of the events leading to plaque rupture is raised by these studies. The plaque grows with a necrotic lipid pool so that it is structurally unstable. Macrophage infiltration, perhaps promoted by activation of endothelial cells (90,91), leads to a focal weakening of the plaque structure. Pulsatile and mean circumferential stresses further weaken this area until rupture occurs. If the balance of thrombosis and thrombolysis favors thrombus formation, an occlusive

thrombus may ensue; however, if the thrombus is not severe enough to occlude the lumen, relief of the peak circumferential stress may allow the plaque to remodel, perhaps with lower levels of stress concentration than before rupture occurred (2).

Stresses reflect only one component of rupture vulnerability. Further progress in understanding plaque fracture strength is essential. For example, interactions among smooth muscle cells, platelets, and macrophages in the remodeling of plaque structure may contribute to focal weakening of the extracellular matrix. Studies focused on the fatigue properties and dynamic failure modes of plaque tissue under pulsatile loads may also lend insight to the rupture process. Unfortunately, fracture and fatigue studies of human atherosclerotic tissues are difficult due to the heterogenous nature of human plaque. Therefore, the development of an in vitro model of plaque based on a vascular smooth muscle cell gel culture system may be useful for providing homogenous test specimens. Animal atherosclerosis models may also offer improved homogeneity over human specimens. If more is understood about how plaques actually rupture, it may be possible to identify and treat vulnerable plaques in patients before rupture occurs, preventing myocardial infarction and sudden cardiac death.

REFERENCES

1. R Russell, JA Glomset. The pathogenesis of atherosclerosis. *N. Engl. J. Med.* 295:369-377, 1976.

2. MJ Davies. A macro and micro view of coronary vascular insult in ischemic heart disease. *Circulation* 82, Suppl. II: II-38-II-46, 1990.

3. V Fuster, L Badimon, M Cohen, JA Ambrose, JJ Badimon, J Chesebro. Insights into the pathogenesis of acute ischemic syndromes. *Circulation* 77:1213-1220, 1988.

4. E Falk. Coronary thrombosis: pathogenesis and clinical manifestations. *Am. J. Cardiol.* 68:28B-35B, 1991.

5. M DeWood, J Spores, R Notske, LT Mouser, R Burroughs, MS Golden, HT Lang. Prevalence of total coronary occlusion during the early hours of transmural myocardial infarction. *N. Engl. J. Med.* 303:897-902, 1980.

6. E Falk. Plaque rupture with severe pre-existing stenosis precipitating coronary thrombosis: characteristics of coronary atherosclerotic plaques underlying fatal occlusive thrombi. *Br. Heart J.* 50:127-134, 1983.

7. MJ Davies, AC Thomas. Plaque fissuring: the cause of acute myocardial infarction, sudden ischemic death, and crescendo angina. *Br. Heart J.* 53:363-373, 1985.

8. JE Muller, GH Tofler, PH Stone. Circadian variation and triggers of onset of acute cardiovascular disease. *Circulation* 79:733-743, 1989.

9. SA Tsementzis, JS Gill, ER Hitchcock, SK Gill, DG Beevers. Diurnal variation of activity during the onset of stroke. *Neurosurgery* 17:901-904, 1985.

10. LR Wechsler. Ulceration and carotid artery disease. *Stroke* 19:650-653, 1988.

11. JE Muller, PH Stone, ZG Turi, JD Rutherford, CA Czeisler, C Parker, WK Poole, E Passamani, R Roberts, T Robertson, BE Sobel, JT Willerson, E Braunwald, and the MILIS Study Group. Circadian variation in the frequency of acute myocardial infarction. *N. Engl. J. Med.* 313:1315-1322, 1985.

12. JE Muller, PL Ludmer, SN Willich, GH Tofler, G Aylmer, I Klangos, PH Stone. Circadian variation in the frequency of sudden cardiac death. *Circulation* 75:131-138, 1987.

13. MB Rocco, J Barry, S Campbell, E Nabel, EF Cook, L Goldman, AP Selwyn. Circadian variation of transient myocardial ischemia in patients with coronary artery disease. *Circulation* 75:395-400, 1987.

14. S Ellis, EL Alderman, K Cain, L Fisher, W Sanders, M Bourassa. Prediction of risk of anterior myocardial infarction by lesion severity and measurement method of stenoses in the left anterior descending coronary distribution: a CASS Registry Study. *J. Am. Coll. Cardiol.* 11:908-916, 1988.

15. S Ellis, EL Alderman, K Cain, A Wright, M Bourassa, L Fisher, and the Participants of the Coronary Artery Surgery Study. Morphology of left anterior descending coronary territory lesions as a predictor of anterior myocardial infarction: a CASS Registry Study. *J. Am. Coll. Cardiol.* 13:1481-1491, 1989.

16. SD Gertz, WC Roberts. Hemodynamic shear force in rupture of coronary arterial atherosclerotic plaques. *Am. J. Cardiol.* 66:1368-1372, 1990.

17. RL Binns, DN Ku. Effect of stenosis on wall motion: a possible mechanism of stroke and transient ischemic attack. *Arteriosclerosis* 9:842-847, 1989.

18. HM Loree, RD Kamm, CM Atkinson, RT Lee. Turbulent pressure fluctuations on surface of model vascular stenoses. *Am. J. Physiol.* 261:H644-H650, 1991.

19. RP Vito, MC Whang, DP Giddens, CK Zarins, S Glagov. Stress analysis of the diseased arterial cross-section. *ASME Advances in Bioengineering Proceedings* 273-276, 1990.

20. P Constantinides. Plaque fissures in human coronary thrombosis. *J. Atheroscler. Res.* 6:1-17, 1966.

21. AC Barger, R Beeuwkes, LL Lainey, KJ Siverman. Hypothesis: vasa vasorum and neovascularization of human coronary arteries: a possible role in the pathophysiology of atherosclerosis. *N. Engl. J. Med.* 310:175-177, 1984.

22. SM Keeny, PD Richardson. Stress analysis of atherosclerotic arteries. *IEEE/EMBS Proceedings* 1484-1485, 1987.

23. PD Richardson, MJ Davies, GVR Born. Influence of plaque configuration and stress distribution on fissuring of coronary atherosclerotic plaques. *Lancet* 2:941-944, 1989.

24. PM Ridker, JE Manson, JE Buring, JE Muller, CH Hennekens. Circadian variation of acute myocardial infarction and the effect of low-dose aspirin in a randomized trial of physicians. *Circulation* 82:897-902, 1990.

25. DJ Kereiakes, EJ Topol, BS George, RS Stack, CW Abbottsmith, S Ellis, RJ Candela, L Harrelson, LH Martin, RM Califf. Myocardial infarction with minimal coronary atherosclerosis in the era of thrombolytic reperfusion. *J. Am. Coll. Cardiol.* 17:304-312, 1991.

26. WC Little, M Constantinescu, RJ Applegate, MA Kutcher, MT Burrows, FR Kahl, WP Santamore. Can coronary angiography predict the site of subsequent myocardial infarction in patients with mild-to-moderate coronary artery disease? *Circulation* 78:1157-1166, 1988.

27. JA Ambrose, MA Tannenbaum, D Alexopoulos, H Hjemdahl-Monsen, J Leavy, M Weiss, S Borrico, R Gorlin, V Fuster. Angiographic progression of coronary artery disease and the development of myocardial infarction. *J. Am. Coll. Cardiol.* 12:56-62, 1988.

28. V Fuster, L Badimon, JJ Badimon, JH Chesebro. The pathogenesis of coronary artery disease and the acute coronary syndromes. *N. Engl. J. Med.* 326:242-250, 1992.

29. CL Lendon, MJ Davies, GV Born, PD Richardson. Atherosclerotic plaque caps are locally weakened when macrophage density is increased. *Atherosclerosis* 87:87-90, 1991.

30. DF Young, FY Tsai. Flow characteristics in models of arterial stenoses-1. steady flow. *J. Biomech.* 6:395-410, 1973.

31. RS Lees, CF Dewey. Phonoangiography: a new noninvasive diagnostic method for studying arterial disease. *Proc. Natl. Acad. Sci. USA* 67:935-942, 1970.

32. JF Fredberg. Origin and character of vascular murmurs: model studies. *J. Acoust. Soc. Am.* 61:1077-1085, 1977.

33. RJ Tobin, JD Chang. Wall pressure spectra scaling downstream of stenoses in steady tube flow. *J. Biomech.* 9:633-640, 1976.

34. PF Davies, A Remuzzi, EJ Gordon, CF Dewey, MA Gimbrone. Turbulent fluid shear stress induces vascular endothelial cell turnover in vitro. *Proc. Natl. Acad. Sci. USA* 83:2114-2117, 1986.

35. TJ Benson, RM Nerem, TJ Pedley. Assessment of wall shear stress in arteries, applied to coronary circulation. *Cardiovasc. Res.* 14:568-576, 1980.

36. CF Dewey. Fluid mechanics of arterial flow. *Adv. Exp. Med. Biol.* 115:55-103, 1976.

37. RM Fuchs, JA Brinker, PA Guzman, DE Kross, FCP Yin. Regional coronary blood flow during relief of pacing-induced angina by Nitroglycerin. Implications for mechanism of action. *J. Am. Coll. Cardiol.* 51:19-23, 1983.

38. CJ Pepine, J Mehta, WW Webster, WW Nichols. In vivo validation of a thermodilution method to determine regional left ventricular blood flow in patients with coronary disease. *Circulation* 58:795-802, 1978.

39. A Benetos, A Simon, J Levenson, P Lagneau, J Bouthier, M Safar. Pulsed Doppler: an evaluation of diameter, blood velocity and blood flow of the common carotid artery in patients with isolated unilateral stenosis of the internal carotid artery. *Stroke* 16:969-972, 1985.

40. WH Pitts, CF Dewey. Spectral and temporal characteristics of post stenotic turbulent wall pressure fluctuations. *J. Biomech. Eng.* 101:89-95, 1979.

41. M Hori, M Inoue, T Shimazu, M Mishima, H Kusuoka, H Abe, K Kodama, S Nanto. Clinical assessment of coronary artery elastic properties by image processing of coronary arteriograms. *Comput. Cardiol.* 393-395, 1983.

42. JA Vita, CB Treasure, P Ganz, DA Cox, RD Fish, AP Selwyn. Control of shear stress in the epicardial coronary arteries of humans: impairment by atherosclerosis. *J. Am. Coll. Cardiol.* 14:1193-1199, 1989.

43. RT Lee, AJ Grodzinsky, EH Frank, RD Kamm, FJ Schoen. Structure-dependent dynamic mechanical behavior of fibrous caps from human atherosclerotic plaques. *Circulation* 83:1764-1770, 1991.

44. DJ Patel, JS Janicki, TE Carew. Static anisotropic elastic properties of the aorta in living dogs. *Circ. Res.* 22:765-779, 1969.

45. WW Nichols, MF O'Rourke. Properties of the arterial wall. In *Blood Flow in Arteries*. Lea & Febiger, Philadelphia, pp77-114, 1990.

46. DH Bergel. The static elastic properties of the arterial wall. *J. Physiol.* 156:445-457, 1961.

47. D Mohan, JW Melvin. Failure properties of passive human aortic tissue I-uniaxial tension tests. *J. Biomech.* 15:887-902, 1982.

48. MH Sherebrin, HA Bernans, MR Roach. Extensibility changes of calcified soft tissue strips from human aorta. *Can. J. Physiol. Pharmacol.* 65:1878-1883, 1987.

49. RT Lee, G Richardson, HM Loree, AJ Grodzinsky, SA Gharib, FJ Schoen, N Pandian. Prediction of mechanical properties of human atherosclerotic tissue by high-frequency intravascular ultrasound imaging. *Arteriosclerosis and Thrombosis* 12:1-5, 1992.

50. GVR Born, PD Richardson. Mechanical properties of human atherosclerotic lesions. In *Pathophysiology of the Human Atherosclerotic Plaque* (Edited by S Glagov, WP Newman, SA Schaffa). Springer-Verlag, New York. pp413-423, 1990.

51. CL Lendon, MJ Davies, GV Born, PD Richardson. Atherosclerotic plaque caps are locally weakened when macrophage density is increased. *Atherosclerosis* 87:87-90, 1991.

52. RM Jones. Macromechanical behavior of lamina. In *Mechanics of Composite Materials*. McGraw-Hill Book Co., New York. pp31-57, 1975.

53. G Golia, NA Evans. Flow separation through annular constrictions in tubes. *Experimental Mechanics* 13:157-162, 1973.

54. TJ Pedley. *The Fluid Mechanics of Large Blood Vessels.* Cambridge University Press, Cambridge, UK. pp301-368, 1980.

55. P Ganz, DP Harrington, J Gaspar, WH Barry. Phasic pressure gradients across coronary and renal artery stenoses in humans. *Am. Heart J.* 106:1399-1406, 1983.

56. BF Waller. The eccentric coronary atherosclerotic plaque: morphometric observations and clinical relevance. *Clin. Cardiol.* 12:14-20, 1989.

57. BF Waller. Pathology of coronary balloon angioplasty and related topics. In *Textbook of Interventional Cardiology* (Edited by EB Topol). W. B. Saunders, New York. pp395-442, 1990.

58. DL Jan, AH Shapiro, RD Kamm. Some features of oscillatory flow in a model bifurcation. *Journal of Applied Physiology* 67:147-159, 1989.

59. WH Press, BP Flannery, SA Teulkolsky, WT Vetterling. *Numerical Recipes: the Art of Scientific Computing.* Cambridge University Press, New York. pp145-146, 1986.

60. SLY Woo, P Lubock, MA Gomez, GF Jemmott, SC Kuei, WK Akeson. Large deformation nonhomogeneous and directional properties of articular cartilage in uniaxial tension. *J. Biomech.* 12:437-446, 1979.

61. HM Loree, RD Kamm, RG Stringfellow, RT Lee. Effects of fibrous cap thickness on peak circumferential stress in model atherosclerotic vessels. *Circ. Res.* (in press), 1992.

62. DJ Patel, JS Janicki. Static elastic properties of the left coronary circumflex artery and the common carotid artery in dogs. *Circ. Res.* 27:149-158, 1970.

63. CM Buntin, FH Silver. Noninvasive assessment of mechanical properties of peripheral arteries. *Ann. Biomed. Eng.* 18:549-566, 1990.

64. MS Goodin. Aqueous vein collapse and its effect on outflow resistance. Masters thesis, Mechanical Engineering, Massachusetts Institute of Technology. pp50-51, 1986.

65. B Lundberg. Chemical composition and physical state of lipid deposits in atherosclerosis. *Atherosclerosis* 56:93-110, 1985.

66. K Rosenfield, DW Losordo, K Ramaswamy, JO Pastore, RE Langevin, S Razvi, BD Kosowsky, JM Isner. Three-dimensional reconstruction of human coronary and peripheral arteries from images recorded during two-dimensional intravascular ultrasound examination. *Circulation* 84:1938-1956, 1991.

67. JH Qiao, MC Fishbein. The severity of coronary atherosclerosis at sites of plaque rupture with occlusive thrombosis. *J. Am. Coll. Cardiol.* 17:1138-1142, 1991.

68. JS Forrester, M Fishbein, R Helfant, J Fagin. A paradigm for restenosis on cell biology: clues for the development of new preventive therapies. *J. Am. Coll. Cardiol.* 17:758-769, 1991.

69. KJ Beatt, PW Serruys, HE Luijten *et al.* Restenosis after coronary angioplasty: the paradox of increased lumen diameter and restenosis. *J. Am. Coll. Cardiol.* 19:258-266, 1992.

70. JJ Popma, RM Califf, EJ Topol. Clinical trials of restenosis after coronary angioplasty. *Circulation* 84:1426-1436, 1991.

71. JW Hirshfeld, JS Schwartz, R Jugo *et al.* Restenosis after coronary angioplasty: a multivariate statistical model to relate lesion and procedure variables to restenosis. *J. Am. Coll. Cardiol.* 18:647-656, 1991.

72. G Keren, MB Leon. Characterization of atherosclerotic lesions by intravascular ultrasound: possible role in unstable coronary syndromes and in interventional therapeutic procedures. *Am. J. Cardiol.* 68:85B-91B, 1991.

73. J Honye, DJ Mahon, A Jain *et al.* Morphological effects of coronary balloon angioplasty in vivo assessed by intravascular ultrasound imaging. *Circulation* 85:1012-1025, 1992.

74. JM Tobis, J Mallery, D Mahon, K Lehmann, P Zalesky, J Griffith, J Gessert, M Moriuchi, M McRae, ML Dwyer, N Greep, WL Henry. Intravascular ultrasound imaging of human coronary arteries in vivo. *Circulation* 83:913-926, 1991.

75. JM Isner, K Rosenfield, DW Losordo *et al.* Combination balloon-ultrasound imaging catheter for percutaneous transluminal angioplasty - validation of imaging, analysis of recoil, and identification of plaque fracture. *Circulation* 84:739-754, 1991.

76. RJ Siegel, M Ariani, MC Fishbein, JS Chae, JC Park, G Maurer, JS Forrester. Histopathologic validation of angioscopy and intravascular ultrasound. *Circulation* 84:109-117, 1991.

77. T Marantz, DO Williams, S Reinert, H Gewirtz, AS Most. Predictors of restenosis after successful angioplasty. *Circulation* 70(suppl II):II-176, 1984.

78. RE Shaw, RK Myler, J Fishman-Rosen, MC Murphy, SH Stertzer, EJ Topol. Clinical and morphologic factors in prediction of restenosis after multiple vessel angioplasty. *J. Am. Coll. Cardiol.* 7:63A, 1986.

79. IJ Sarembock, PJ LaVeau, SL Sigal *et al.* Influence of inflation pressure and balloon size on the development of intimal hyperplasia after balloon angioplasty - a study in the atherosclerotic rabbit. *Circulation* 80:1029-1040, 1989.

80. JM Tobis, JA Mallery, J Gessert *et al.* Intravascular ultrasound cross-sectional arterial imaging before and after balloon angioplasty in vitro. *Circulation* 80:873-882, 1989.

81. DH Bergel. The dynamic elastic properties of the arterial wall. *J. Physiol.* 156:458-469, 1961.

82. A Farb, R Virmani, JB Atkinson, FD Kolodgie. Plaque morphology and pathologic changes in arteries from patients dying after coronary balloon angioplasty. *J. Am. Coll. Cardiol.* 16:1421-1429, 1990.

83. RT Lyon, CK Zarins, CT Lu, CF Yang, S Glagov. Vessel, plaque, and lumen morphology after transluminal balloon angioplasty. *Arteriosclerosis* 7:306-314, 1987.

84. RN Vaishnav, J Vossoughi. Incremental formulations in vascular mechanics. *J. Biomech. Eng.* 106:105-111, 1984.

85. B Meier, AR Bruentzig, SB King *et al.* Higher balloon dilatation pressure in coronary angioplasty. *Am. Heart J.* 107:619-622, 1984.

86. E Levine, CJ Ewels, DR Rosing, KM Kent. Coronary angioplasty: clinical and angiographic follow-up. *Am. J. Cardiol.* 55:673-676, 1985.

87. AM Henney, PR Wakeley, MJ Davies, K Foster, R Hembry, G Murphy, S Humphries. Localization of stromelysin gene expression in atherosclerotic plaques by in situ hybridization. *Proc. Natl. Acad. Sci. USA* 88:8154-8158, 1991.

88. G Brown, JJ Albers, LD Fisher, SM Schaefer, JT Lin, C Kaplan, XQ Zhao, BS Bisson, VF Fitzpatrick, HT Dodge. Regression of coronary artery disease as a result of intensive lipid-lowering therapy in men with high levels of apolipoprotein B. *N. Engl. J. Med.* 323:1289-1298, 1990.

89. B. Barzilai, JE Saffitz, JG Miller, BE Sobel. Quantitative ultrasonic characterization of the nature of atherosclerotic plaques in human aorta. *Circ. Res.* 60:459-463, 1987.

90. MJ Davies, N Woolf, PM Rowles, J Pepper. Morphology of the endothelium over atherosclerotic plaques in human coronary arteries. *Br. Heart J.* 60:459-464, 1988.

91. EG Nabel. Biology of the impaired endothelium. *Am. J. Cardiol.* 68:6c-8c, 1991.

APPENDIX A

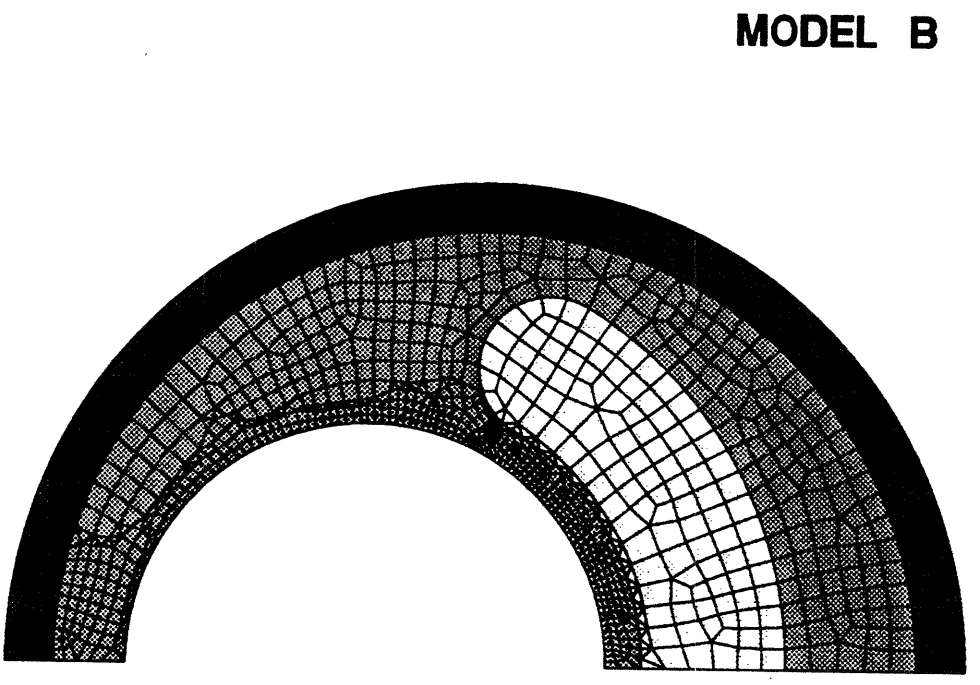

Fig. A.1 Idealized coronary plaque Model B: a.) FEA mesh and b.) contour map of circumferential stress.

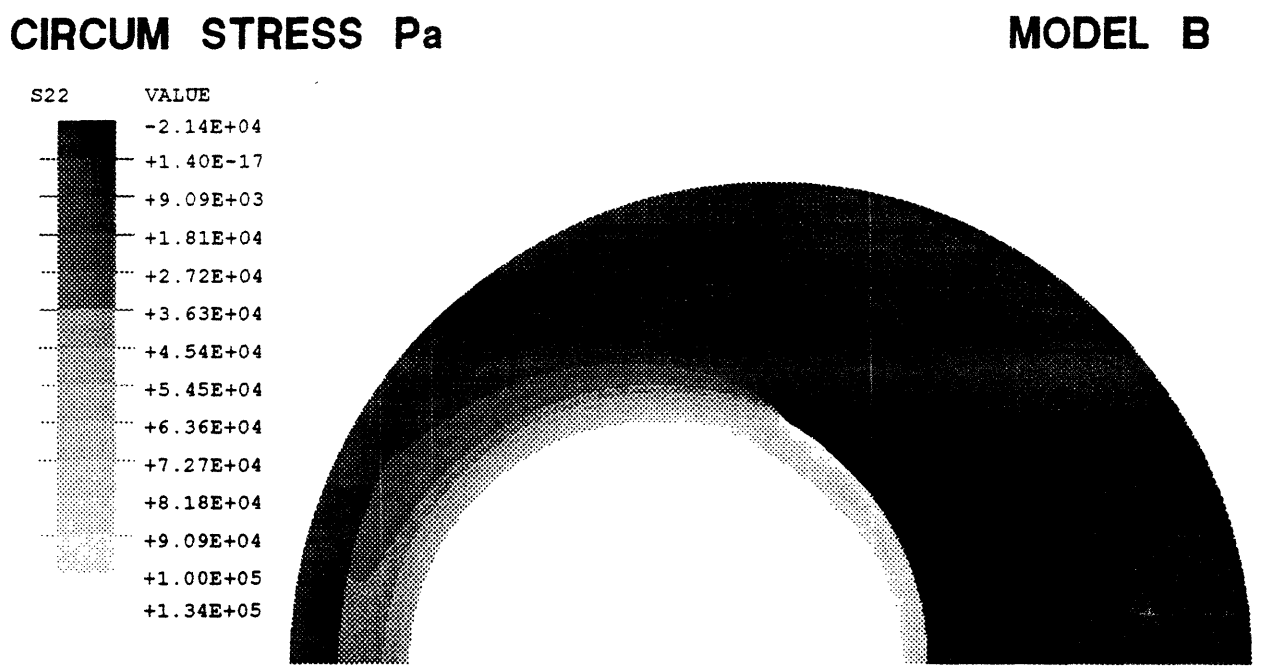

Fig. A.1b Contour map of circumferential stress (Model B).

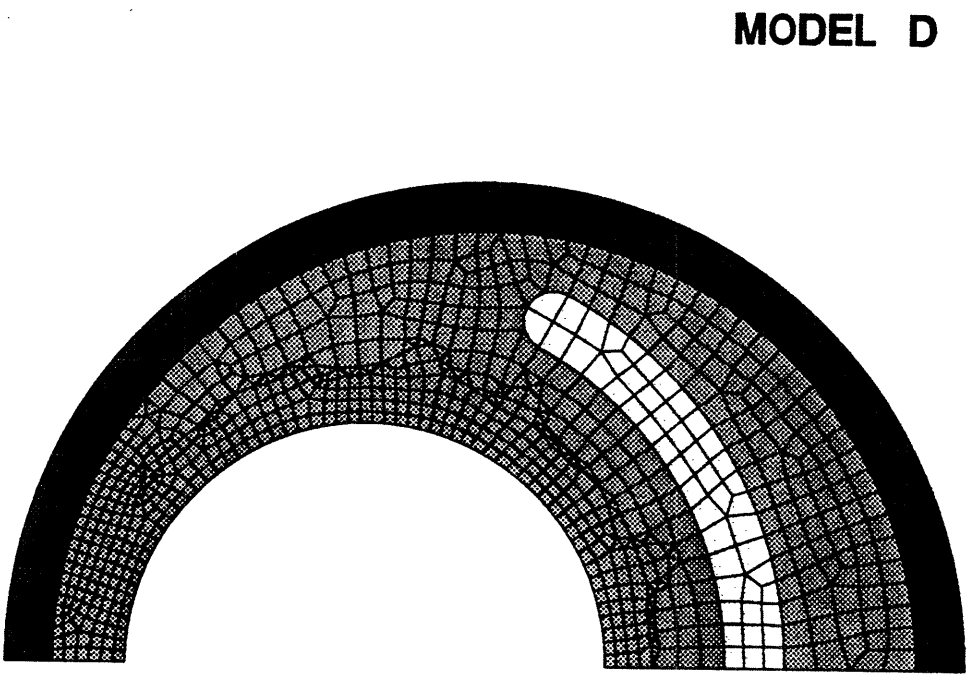

Fig. A.2 Idealized coronary plaque Model D: a.) FEA mesh and b.) contour map of circumferential stress.

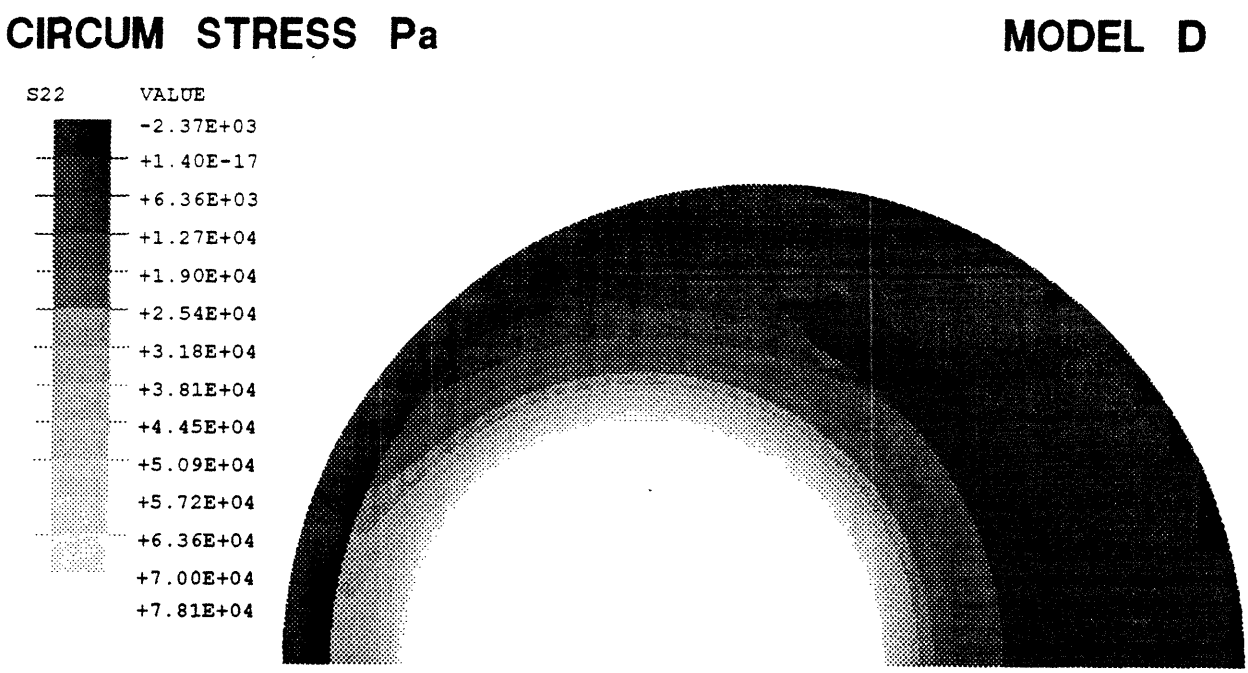

Fig. A.2b Contour map of circumferential stress (Model D).

MODEL F

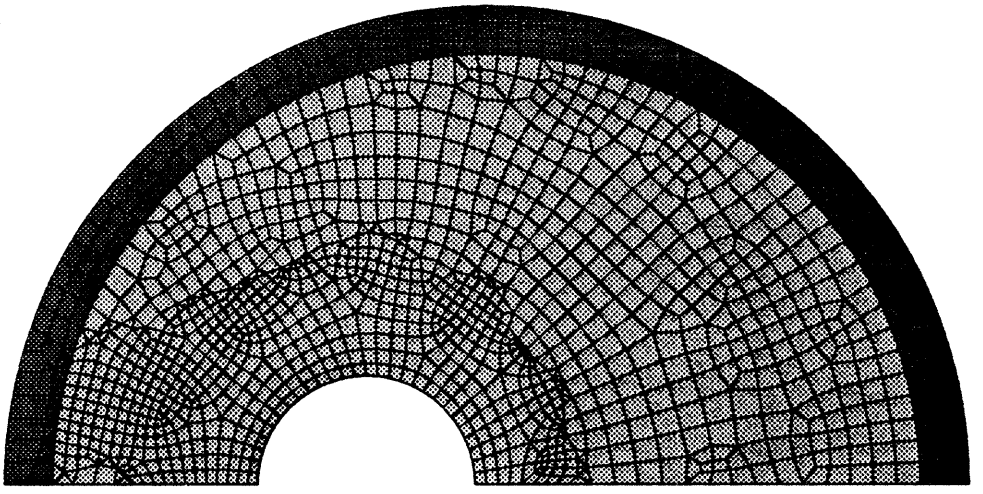

Fig. A.3 Idealized coronary plaque Model F: a.) FEA mesh and b.) contour map of circumferential stress.

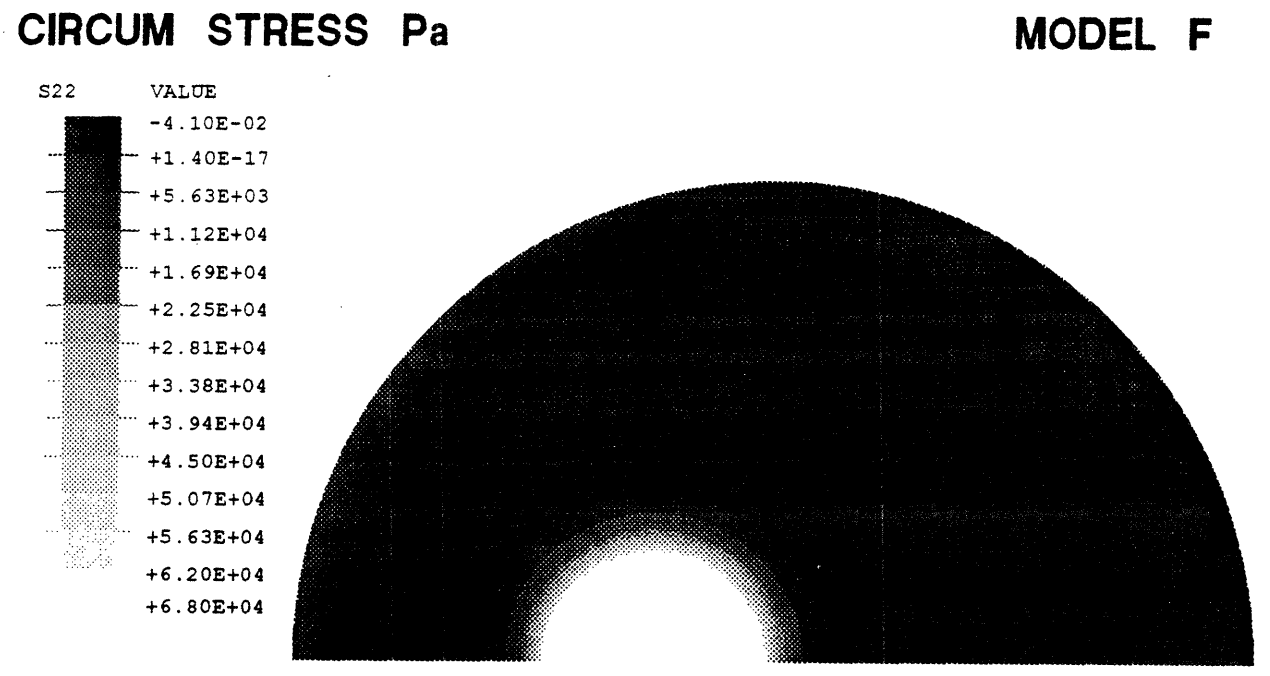

Fig. A.3b Contour map of circumferential stress (Model F).

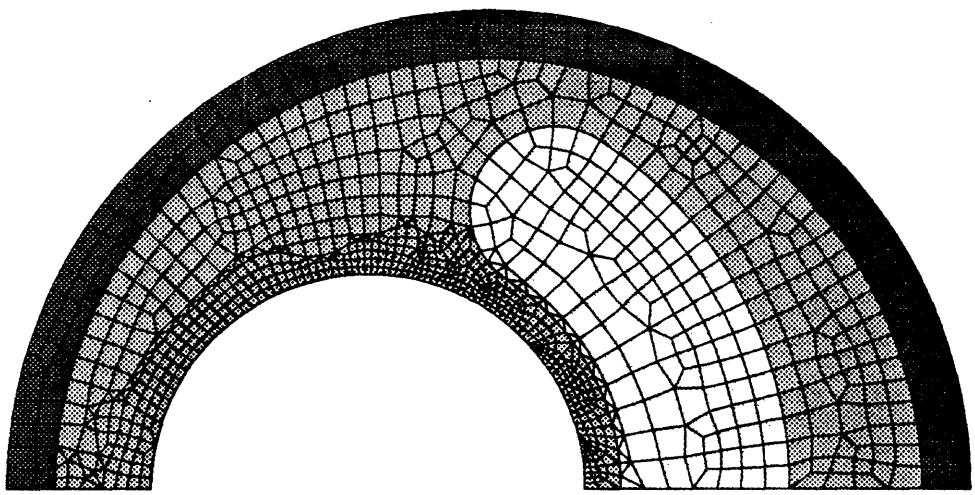

Fig. A.4 Idealized coronary plaque Model H: a.) FEA mesh and b.) contour map of circumferential stress.

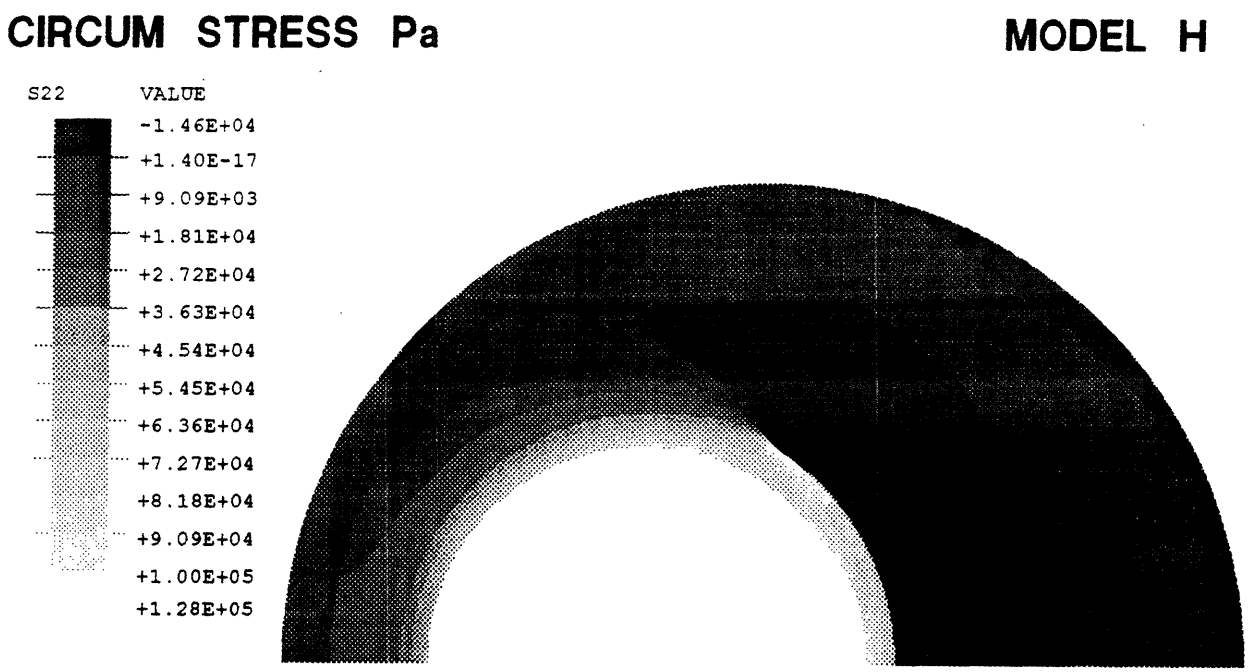

Fig. A.4b Contour map of circumferential stress (Model H).

MODEL I

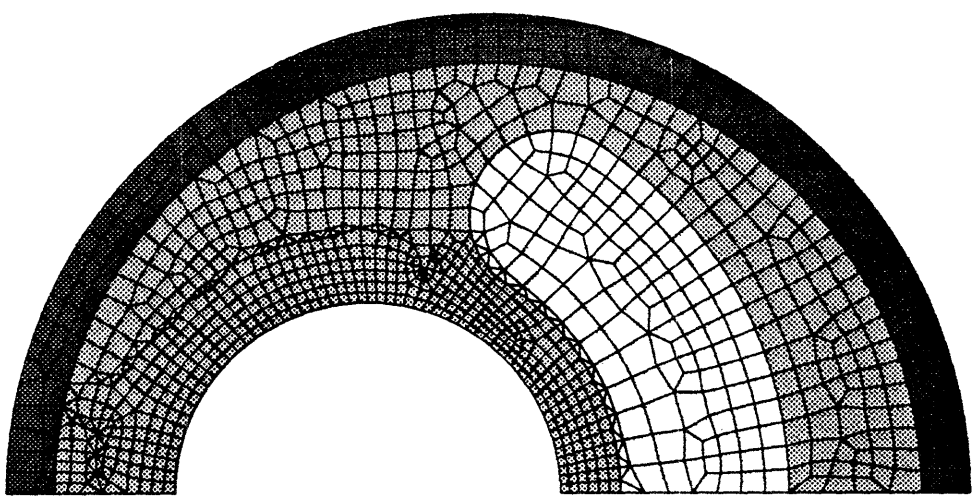

Fig. A.5 Idealized coronary plaque Model I: a.) FEA mesh and b.) contour map of circumferential stress.

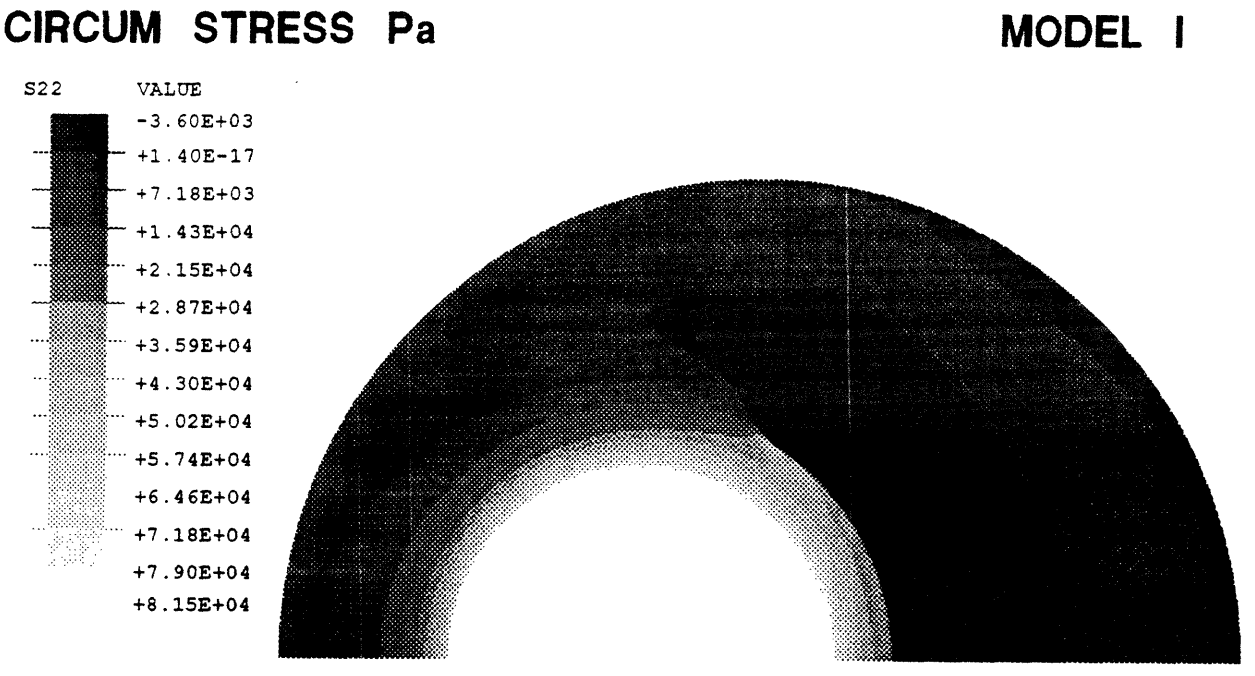

Fig. A.5b Contour map of circumferential stress (Model I).

MODEL J

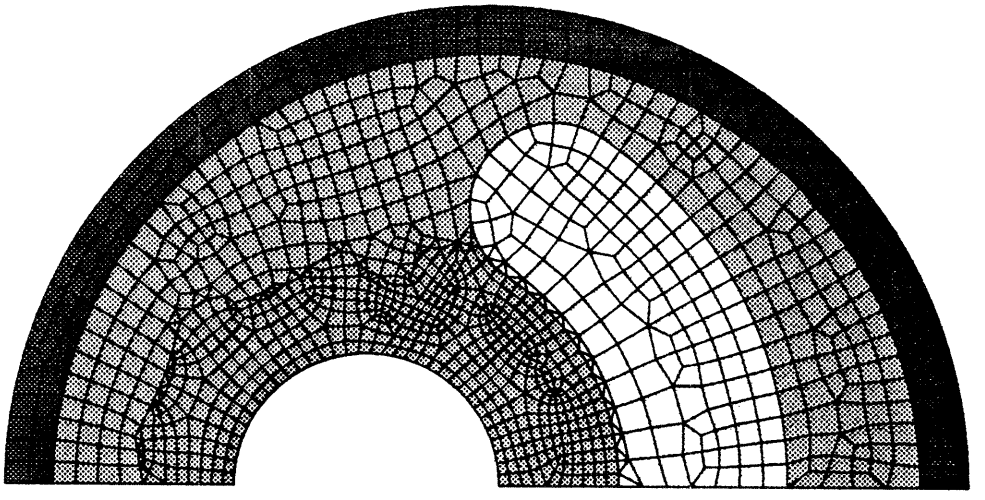

Fig. A.6 Idealized coronary plaque Model J: a.) FEA mesh and b.) contour map of circumferential stress.

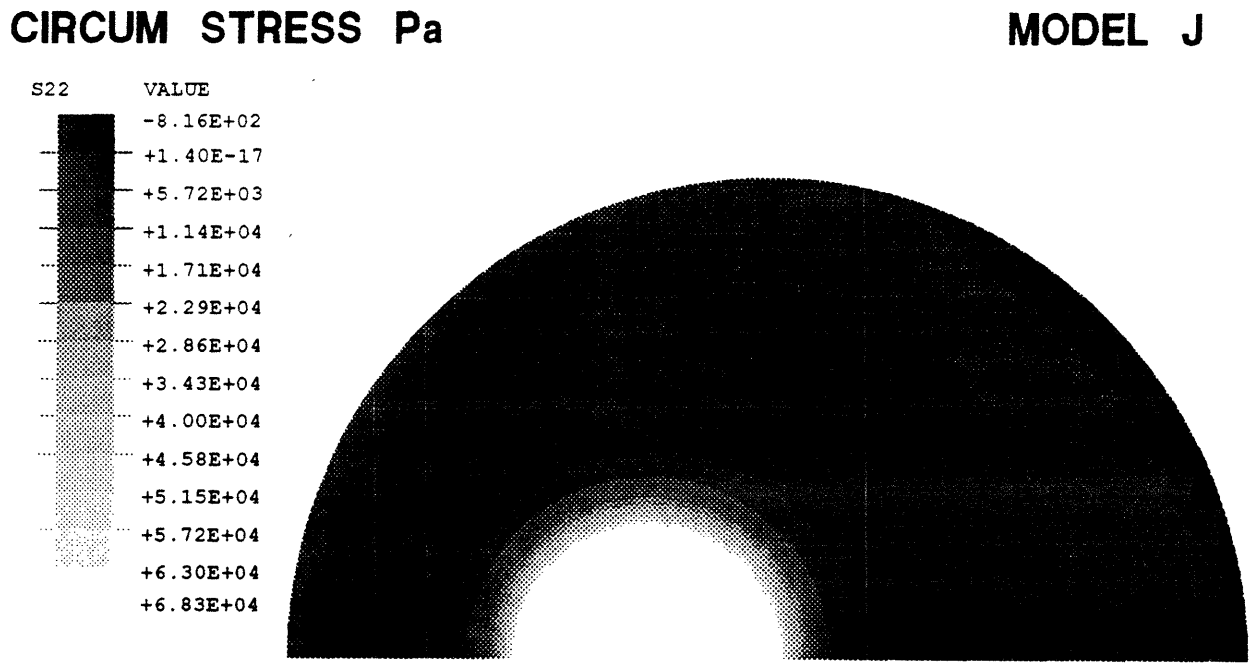

Fig. A.6b Contour map of circumferential stress (Model J).

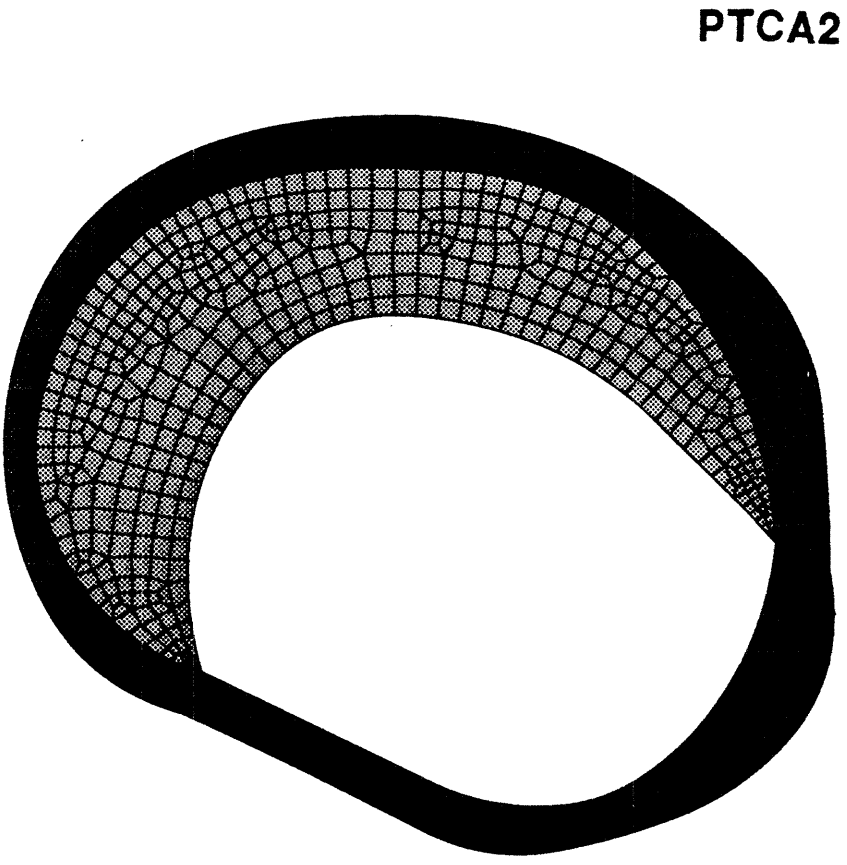

Fig. A.7 Iliac artery Model 2: a.) FEA mesh and b.) contour map of circumferential stress, and c.) deformed mesh.

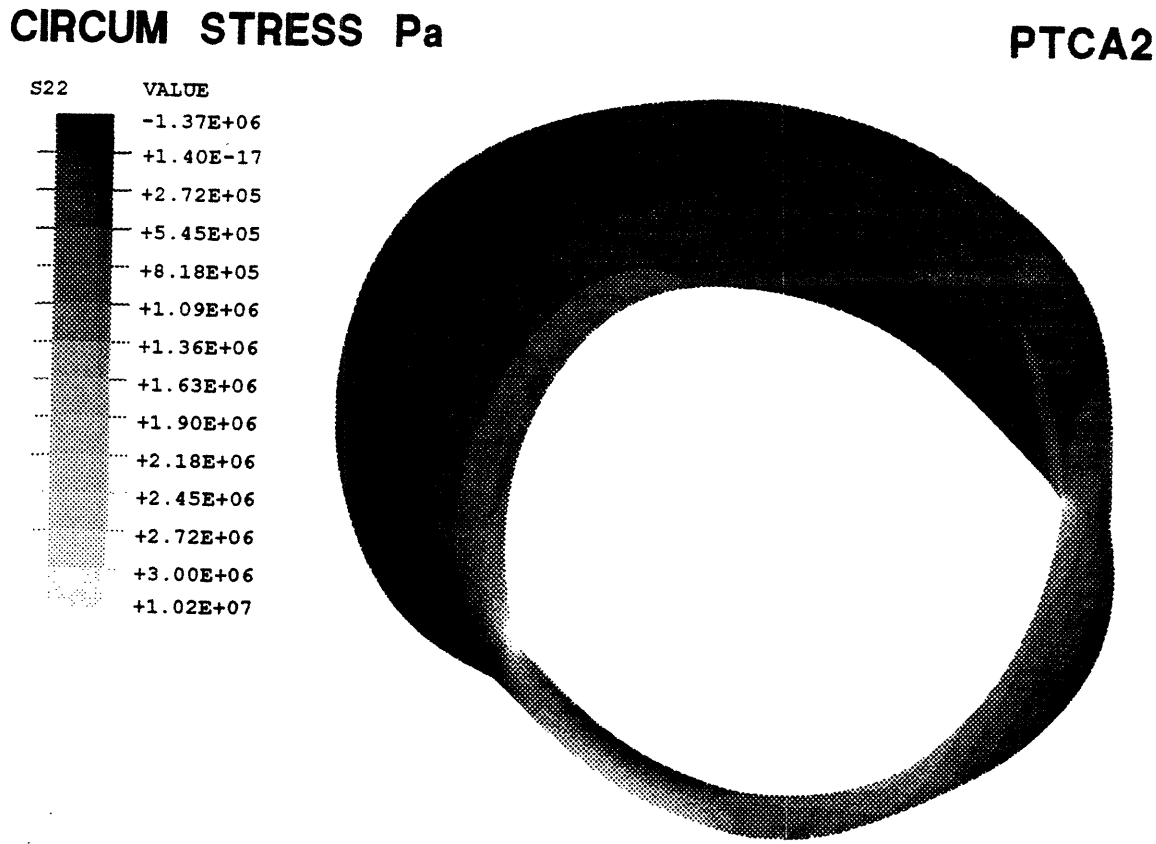

Fig. A.7b Contour map of circumferential stress (Model 2).

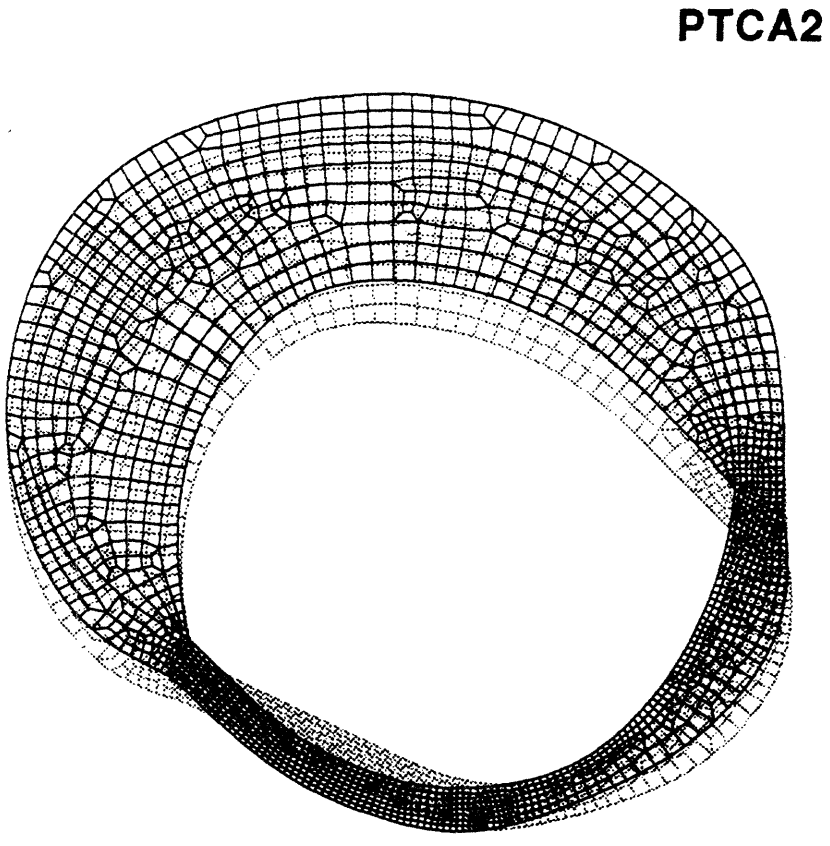

Fig. A.7c Deformed mesh (Model 2).

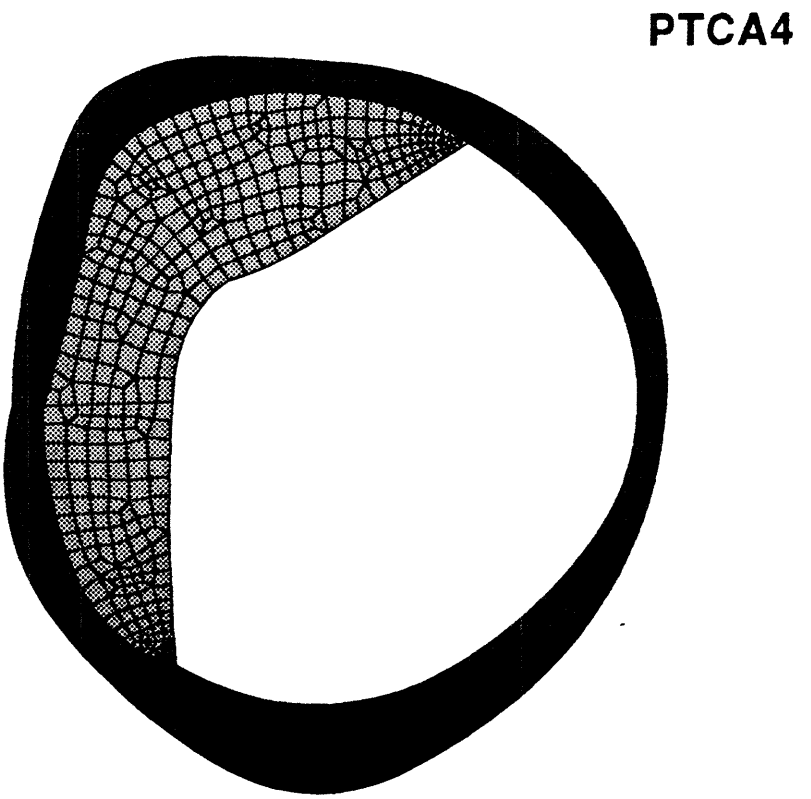

Fig. A.8 Iliac artery Model 4: a.) FEA mesh and b.) contour map of circumferential stress, and c.) deformed mesh.

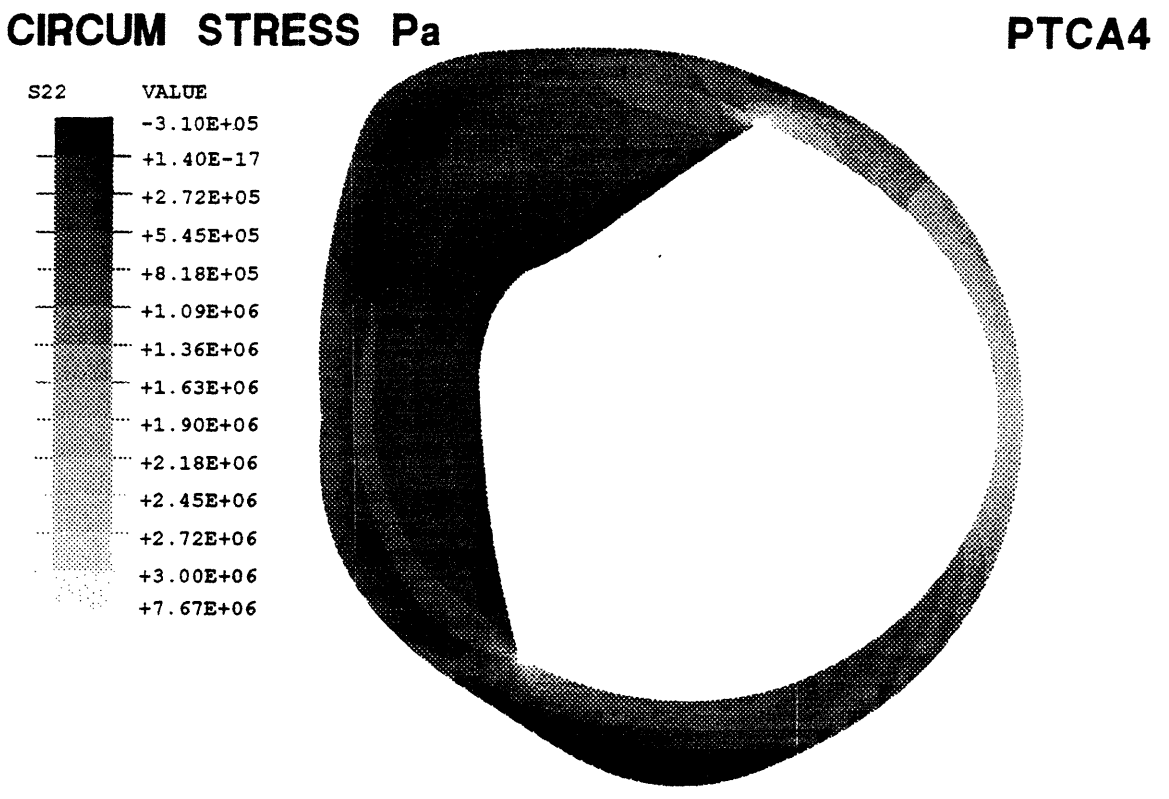

Fig. A.8b Contour map of circumferential stress (Model 4).

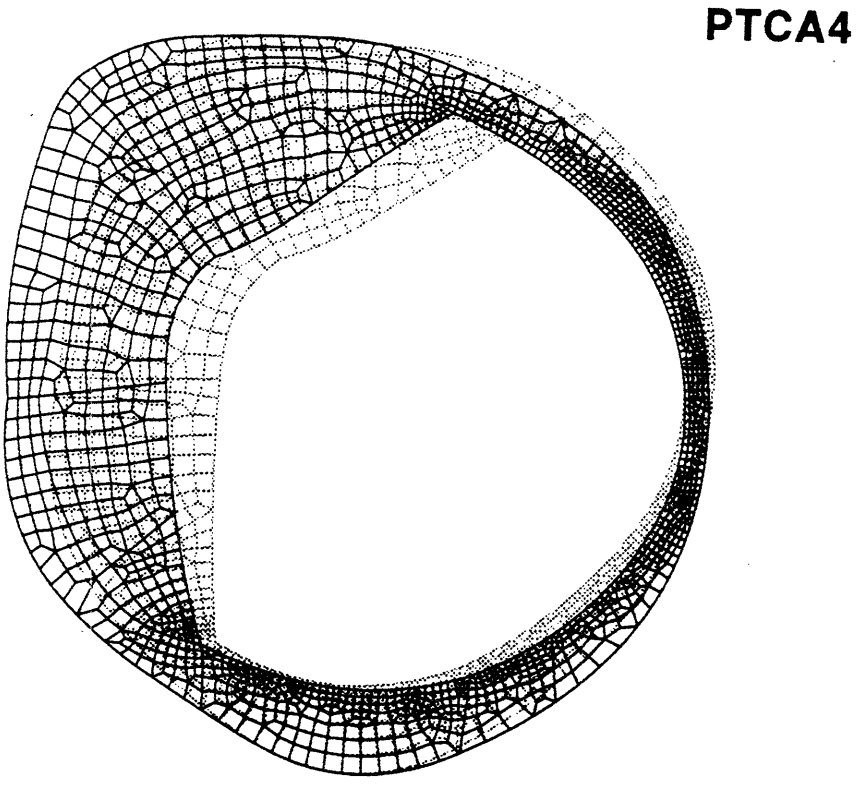

Fig. A.8c Deformed mesh (Model 4).

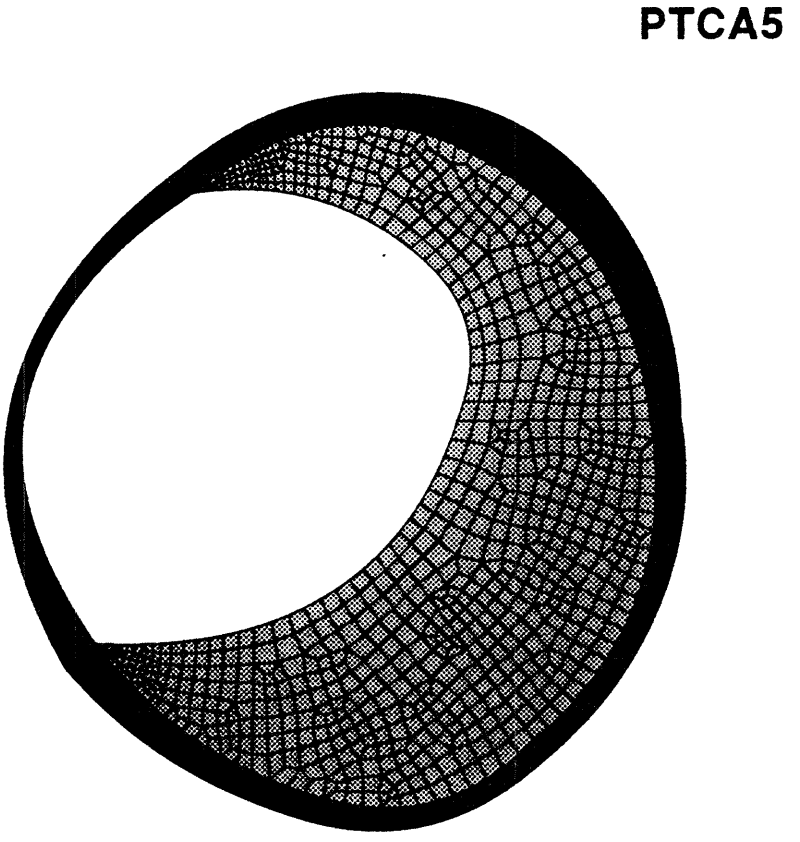

Fig. A.9 Iliac artery Model 5: a.) FEA mesh and b.) contour map of circumferential stress, and c.) deformed mesh.

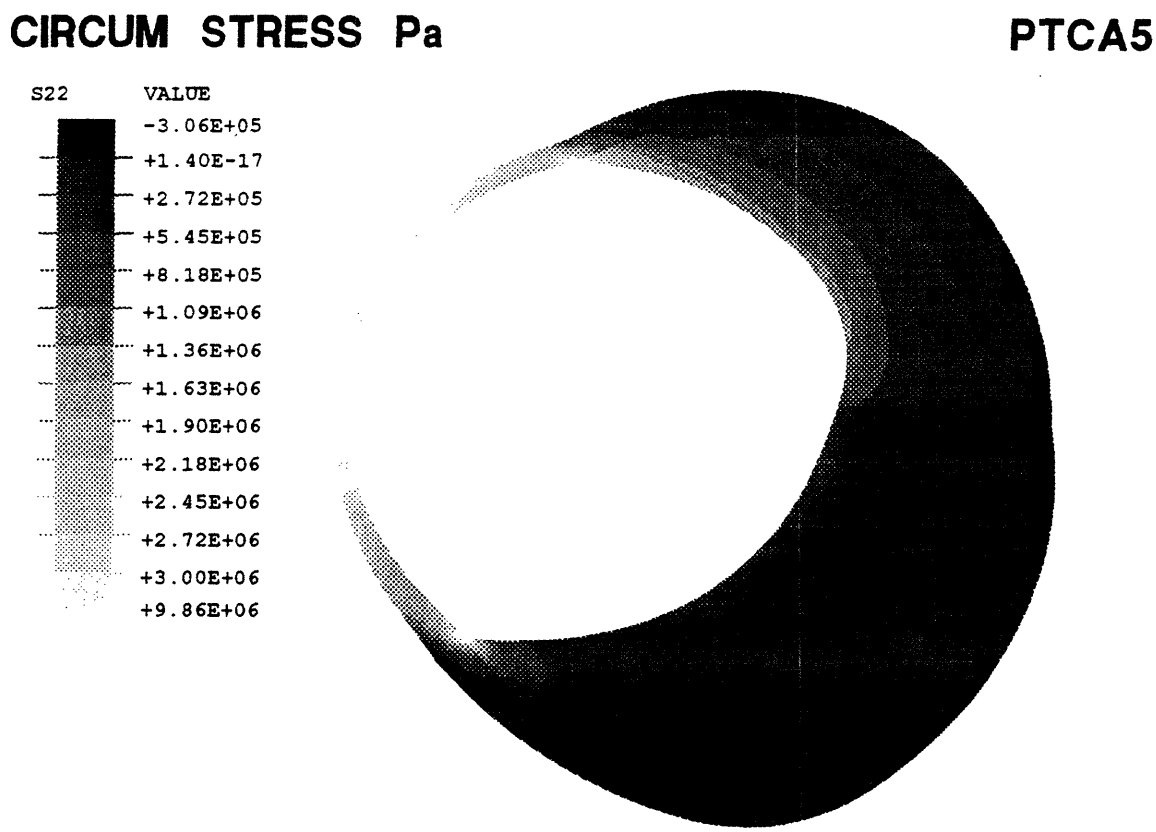

Fig. A.9b Contour map of circumferential stress (Model 5).

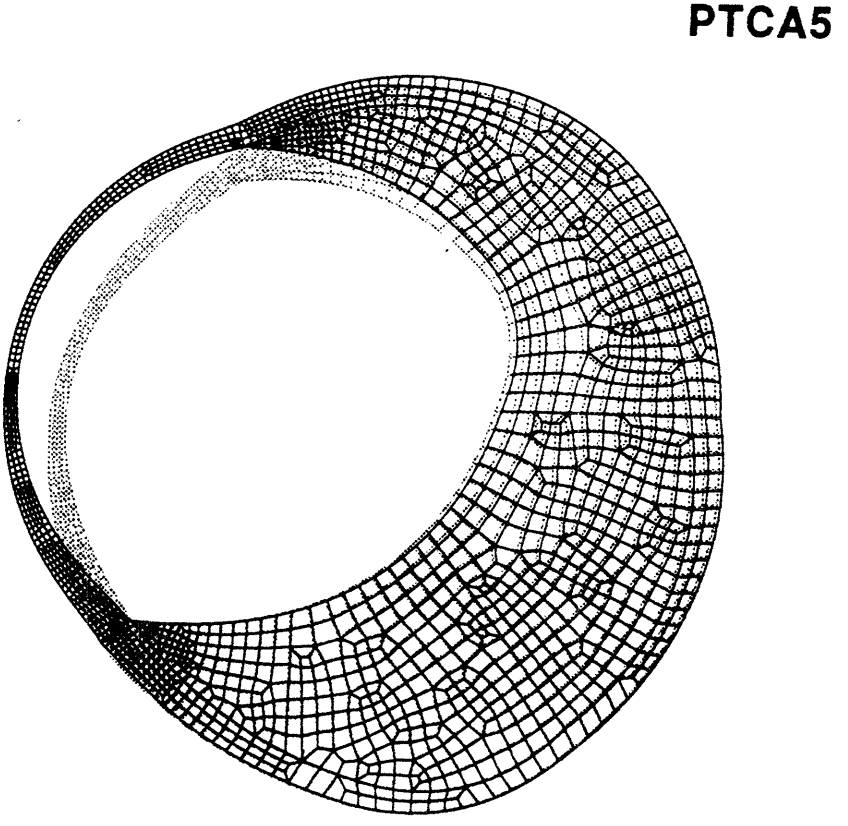

Fig. A.9c Deformed mesh (Model 5).

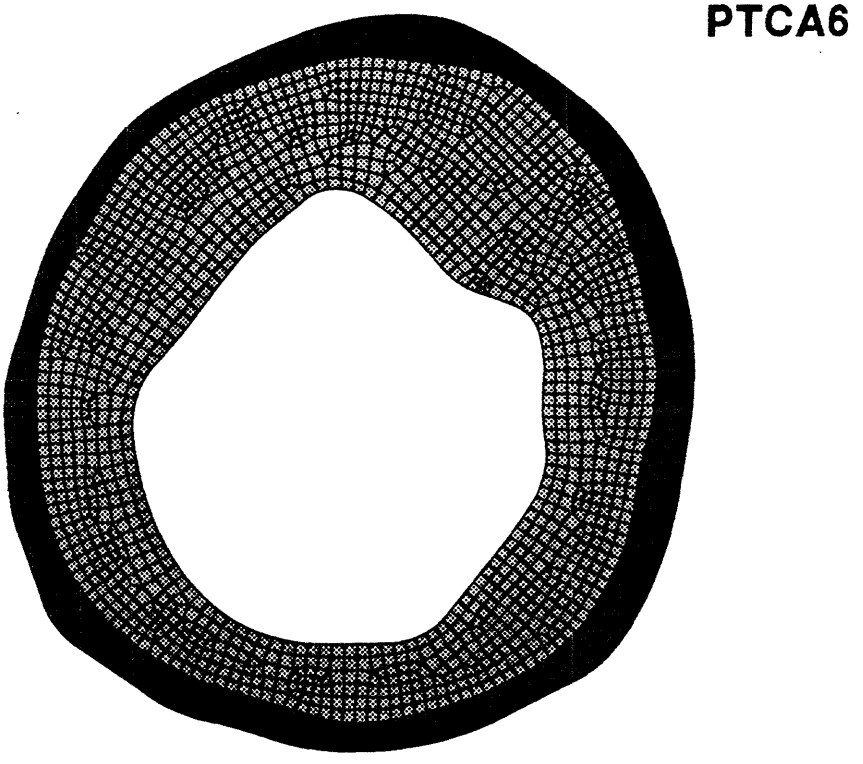

Fig. A.10 Iliac artery Model 6: a.) FEA mesh and b.) contour map of circumferential stress, and c.) deformed mesh.

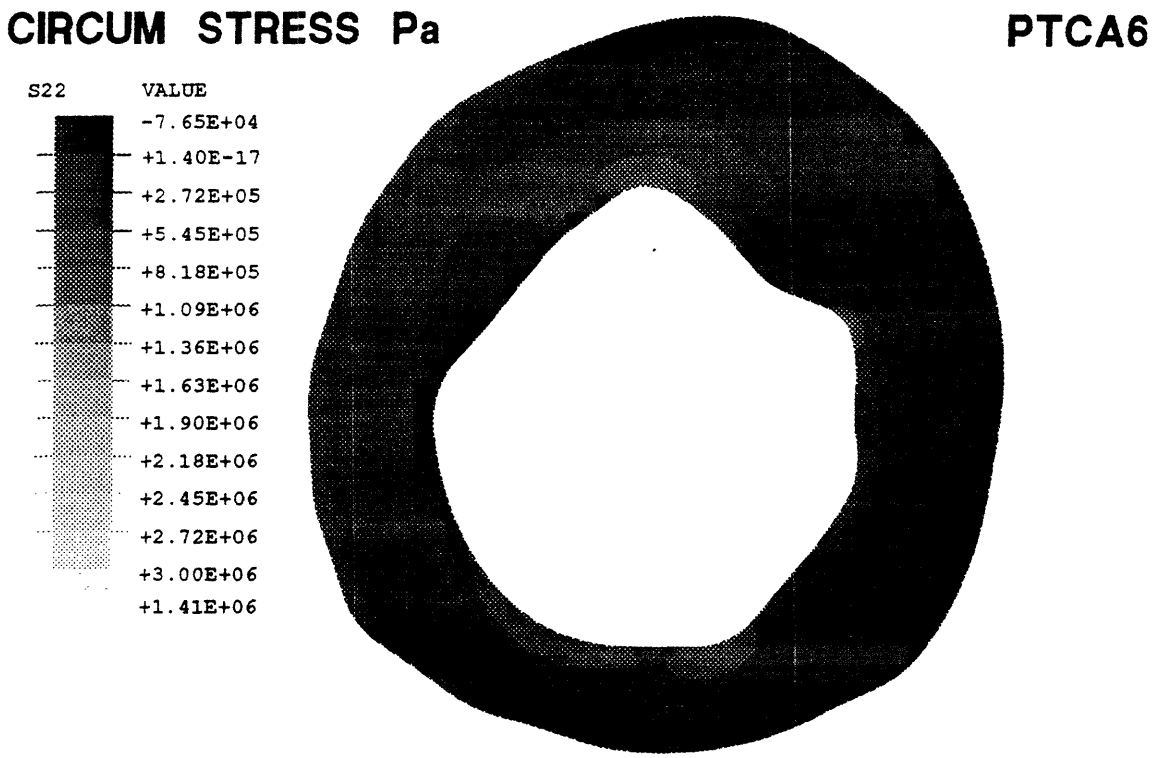

Fig. A.10b Contour map of circumferential stress (Model 6).

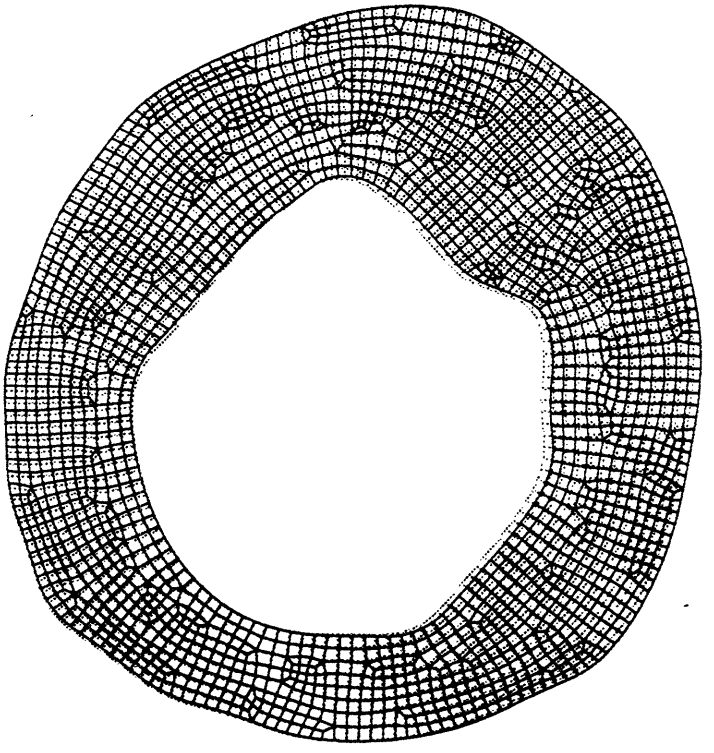

Fig. A.10c Deformed mesh (Model 6).

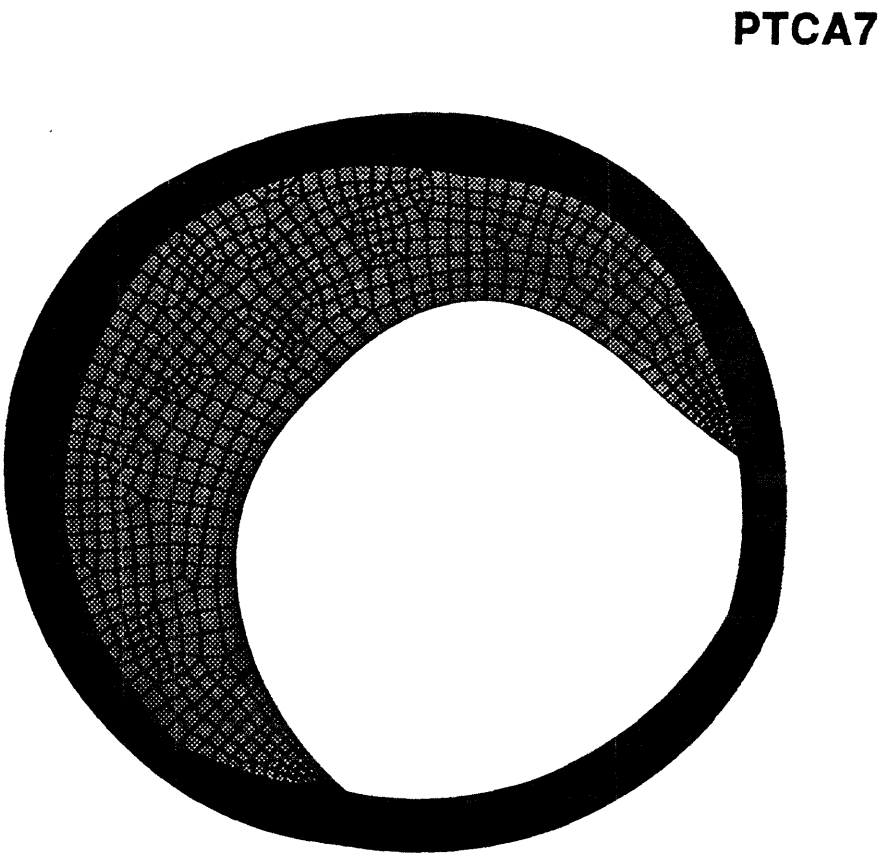

Fig. A.11 Iliac artery Model 7: a.) FEA mesh and b.) contour map of circumferential stress, and c.) deformed mesh.

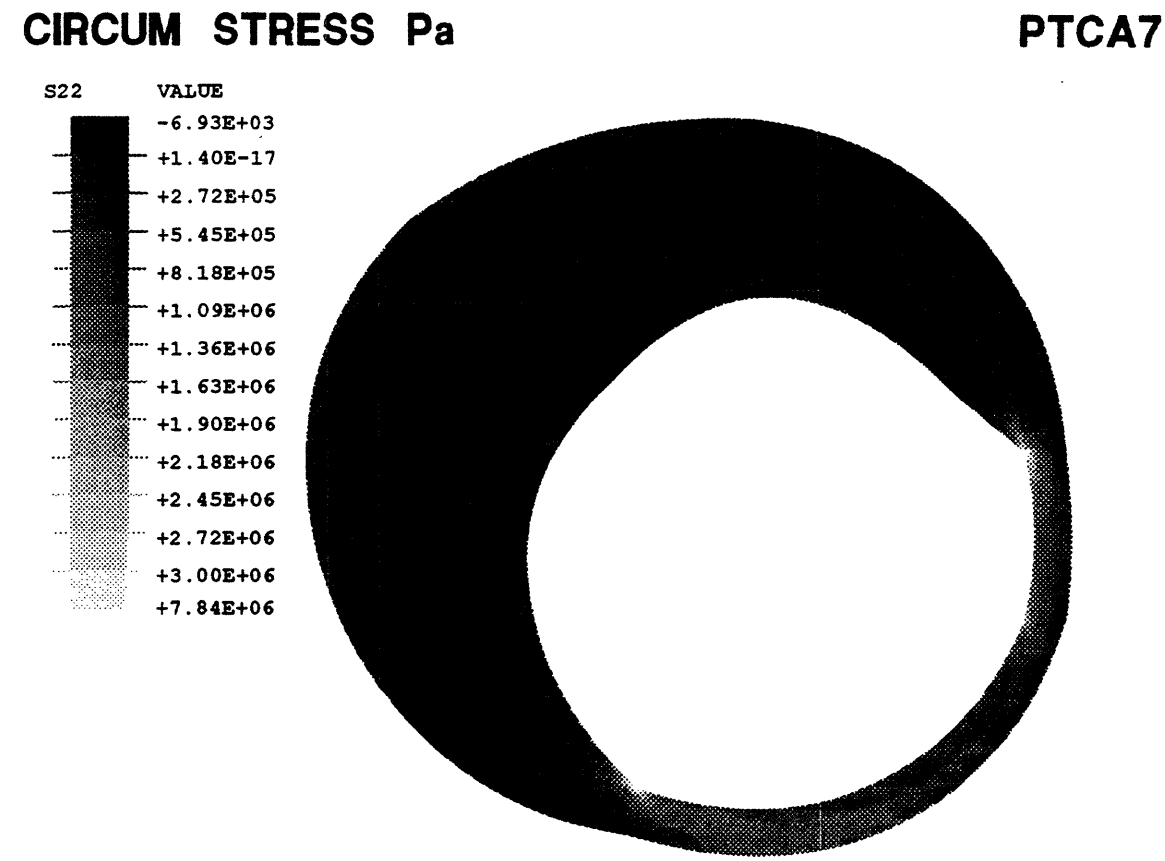

Fig. A.11b Contour map of circumferential stress (Model 7).

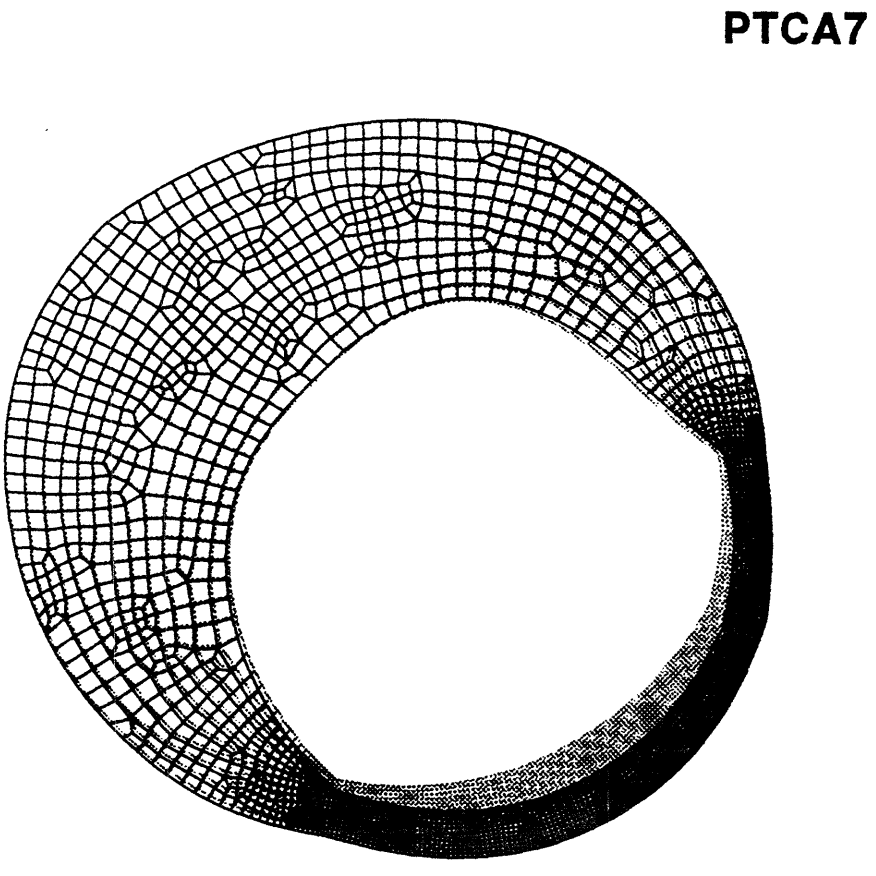

Fig. A.11c Deformed mesh (Model 7).

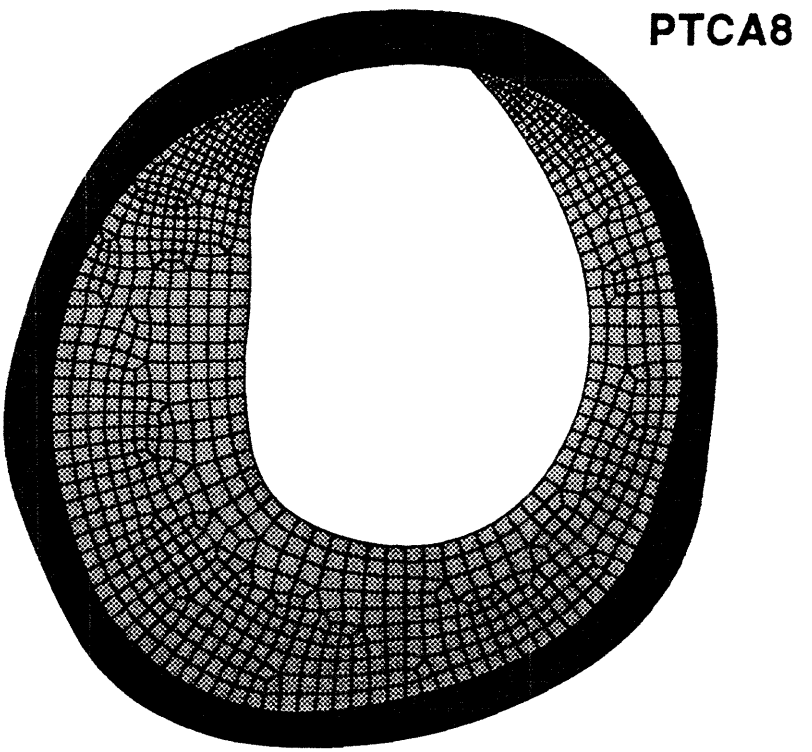

Fig. A.12 Iliac artery Model 8: a.) FEA mesh and b.) contour map of circumferential stress, and c.) deformed mesh.

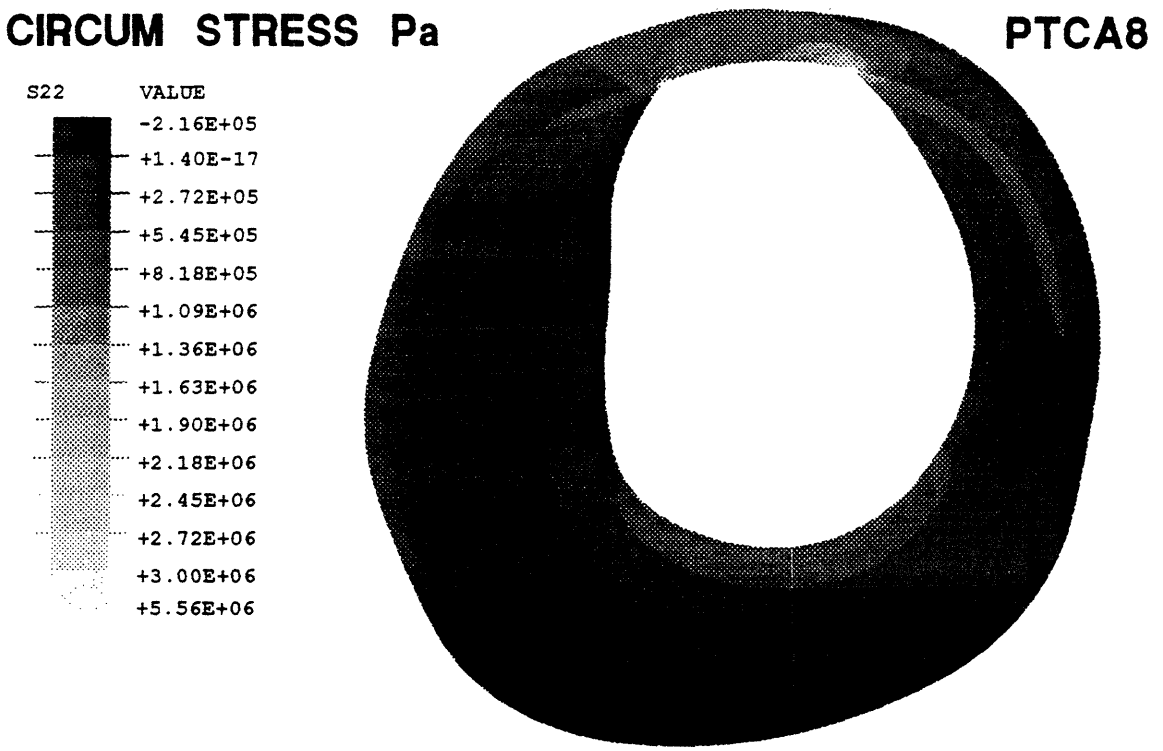

Fig. A.12b Contour map of circumferential stress (Model 8).

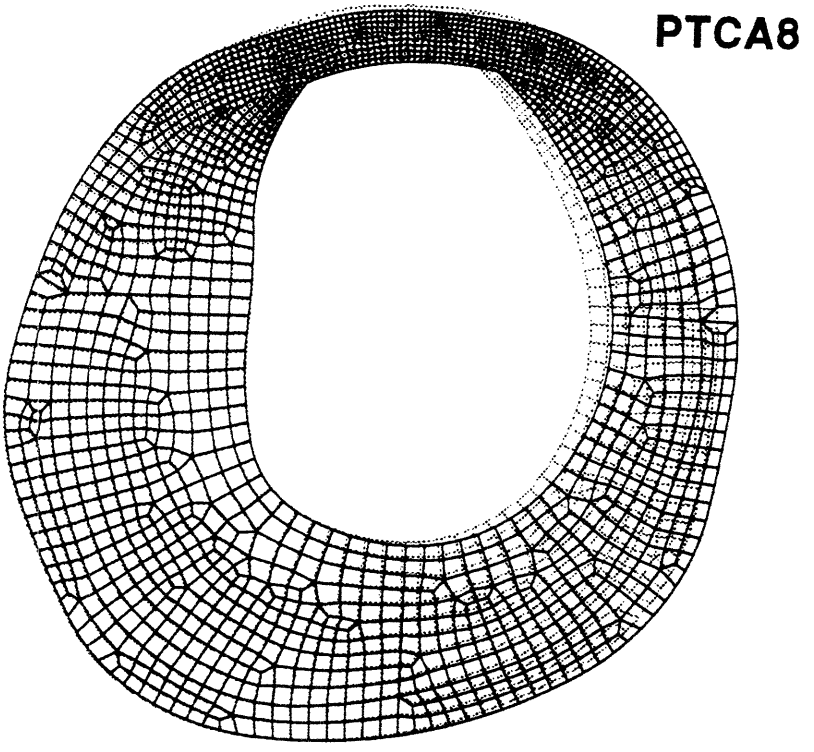

Fig. A.12c Deformed mesh (Model 8).

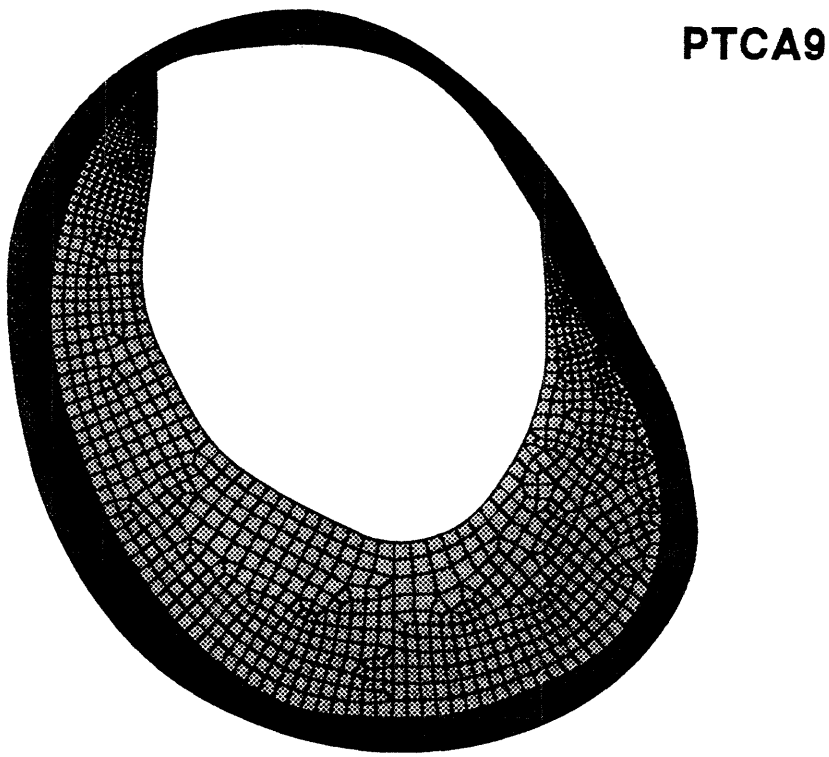

Fig. A.13 Iliac artery Model 9: a.) FEA mesh and b.) contour map of circumferential stress, and c.) deformed mesh.

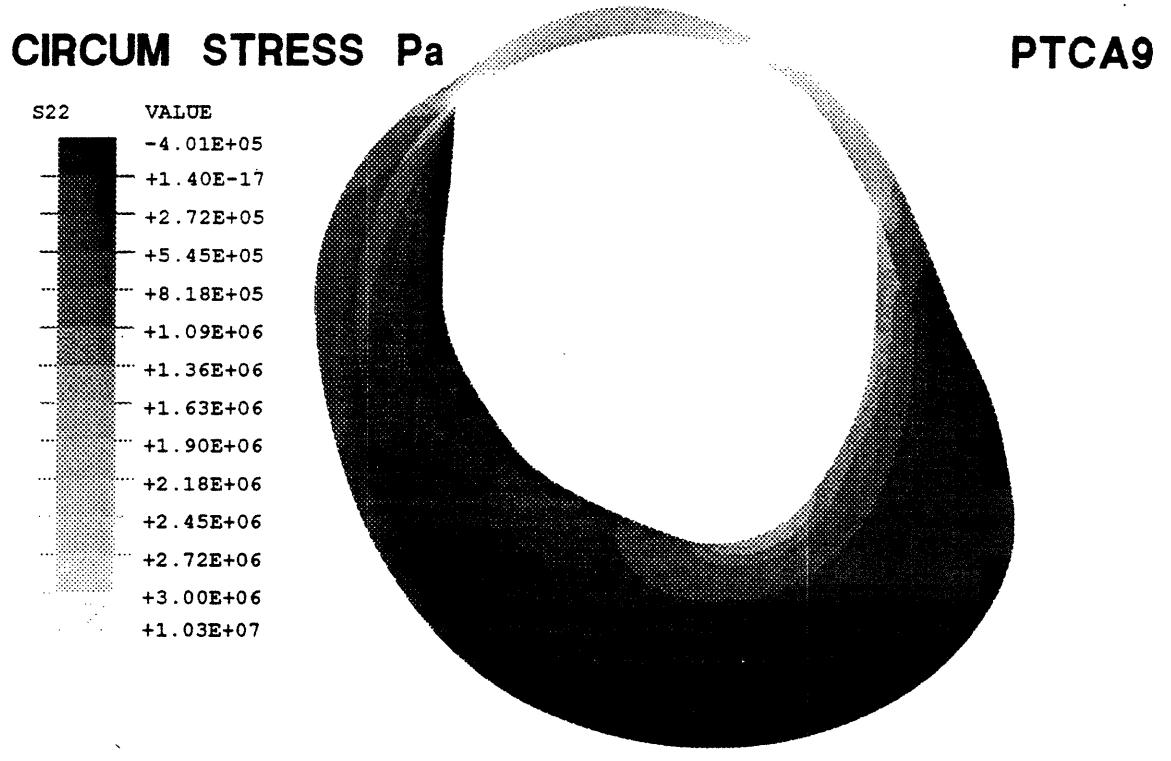

Fig. A.13b Contour map of circumferential stress (Model 9).

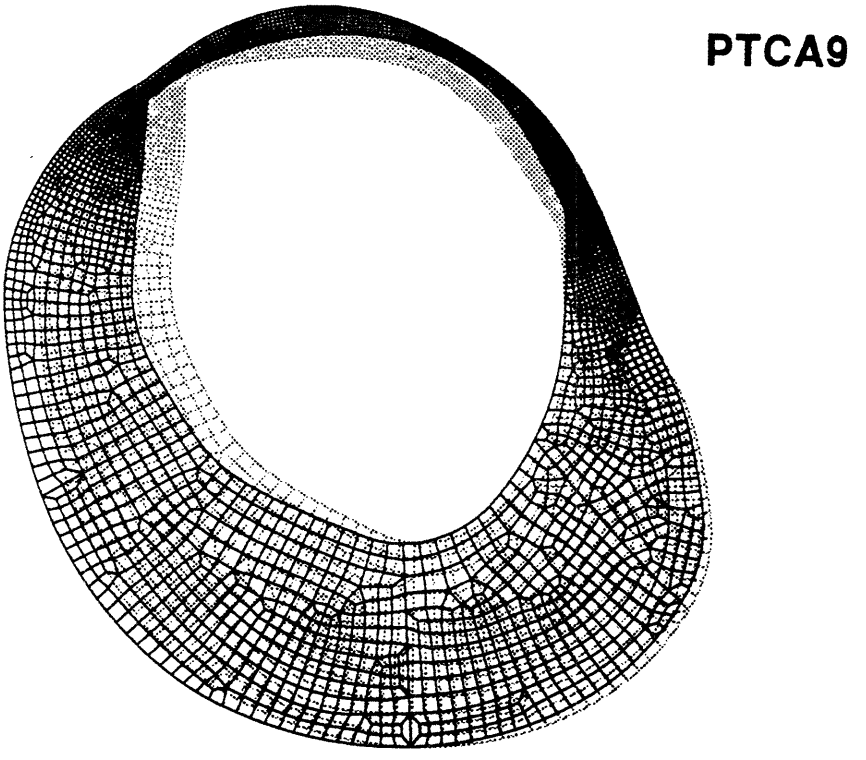

Fig. A.13c Deformed mesh (Model 9).

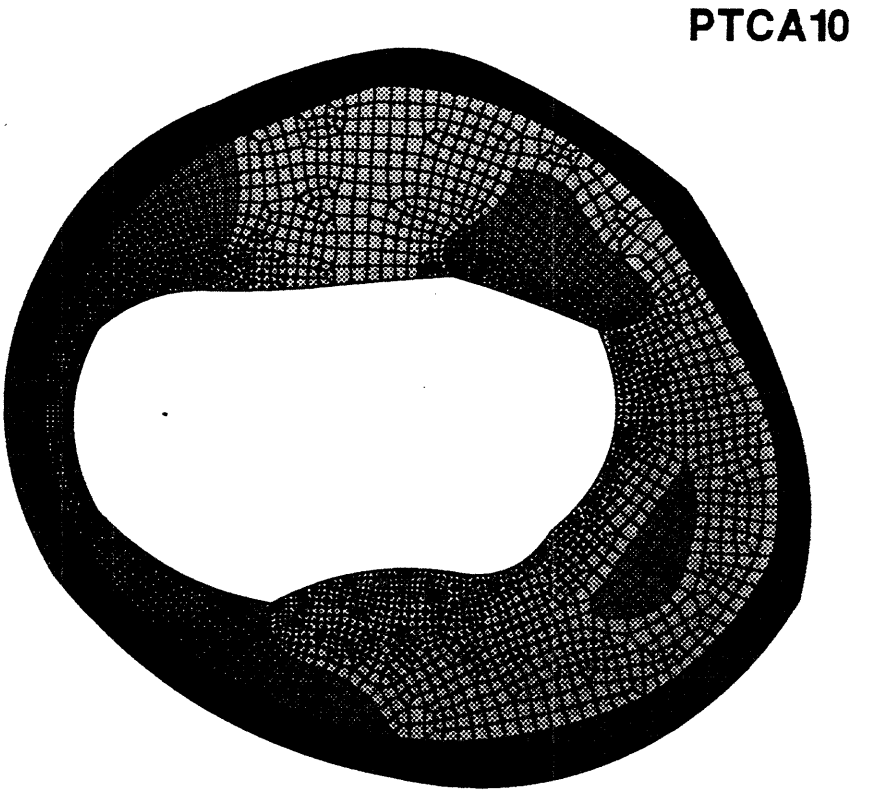

Fig. A.14 Iliac artery Model 10: a.) FEA mesh and b.) contour map of circumferential stress, and c.) deformed mesh.

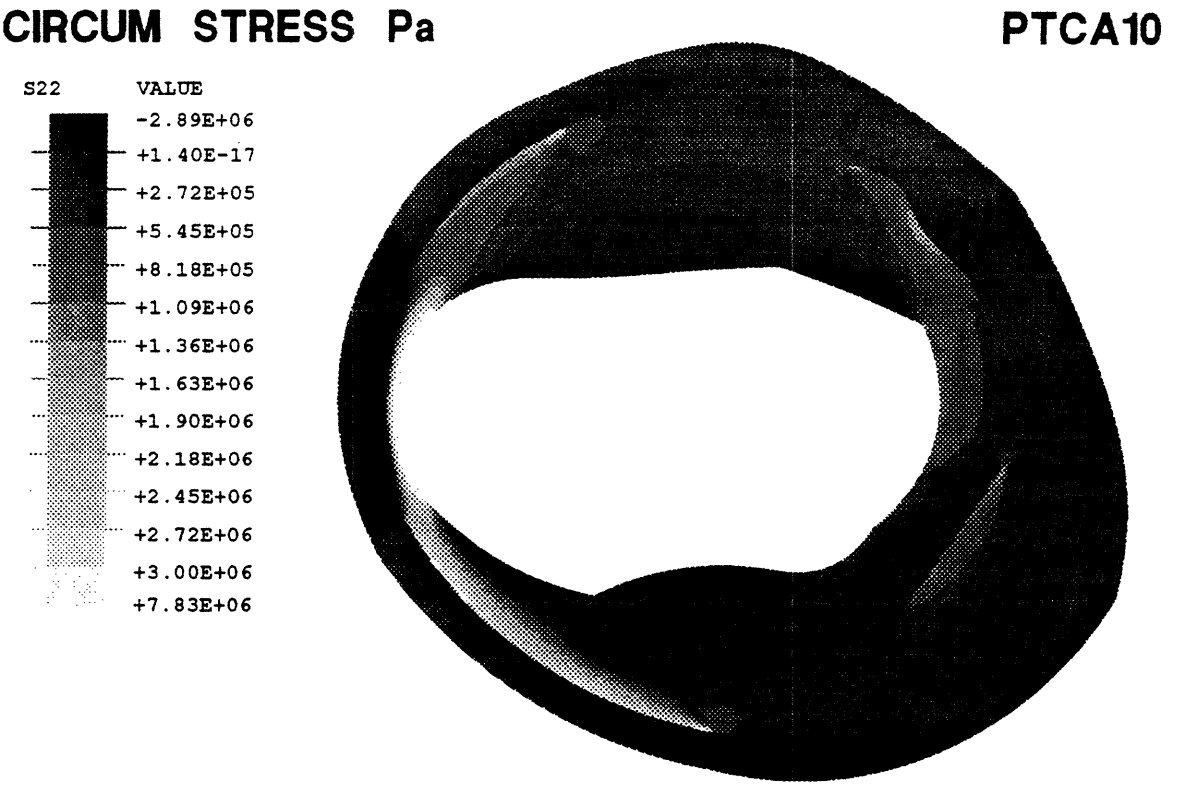

Fig. A.14b Contour map of circumferential stress (Model 10).

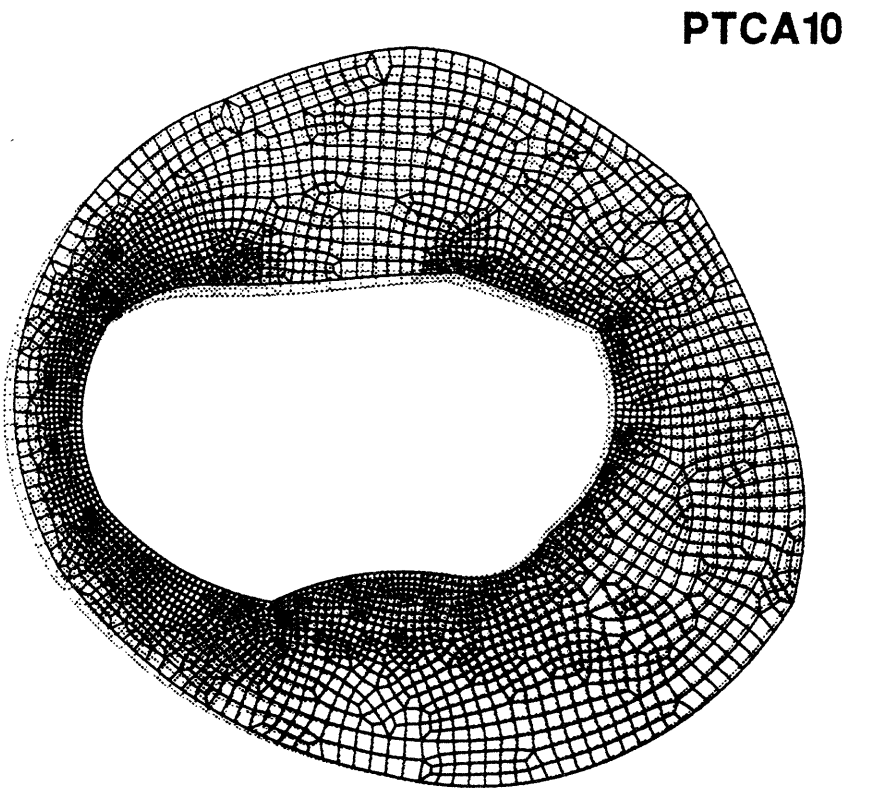

Fig. A.14c Deformed mesh (Model 10).

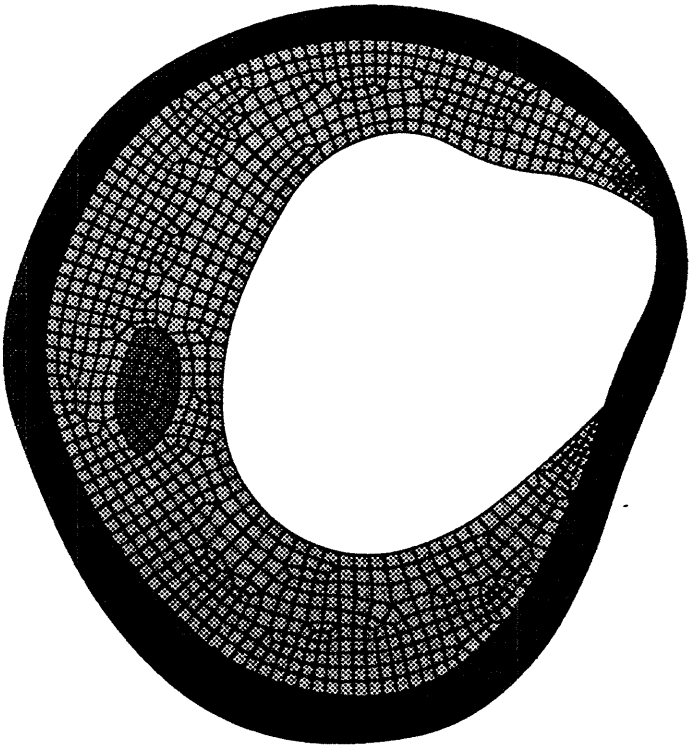

Fig. A.15 Iliac artery Model 11: a.) FEA mesh and b.) contour map of circumferential stress, and c.) deformed mesh.

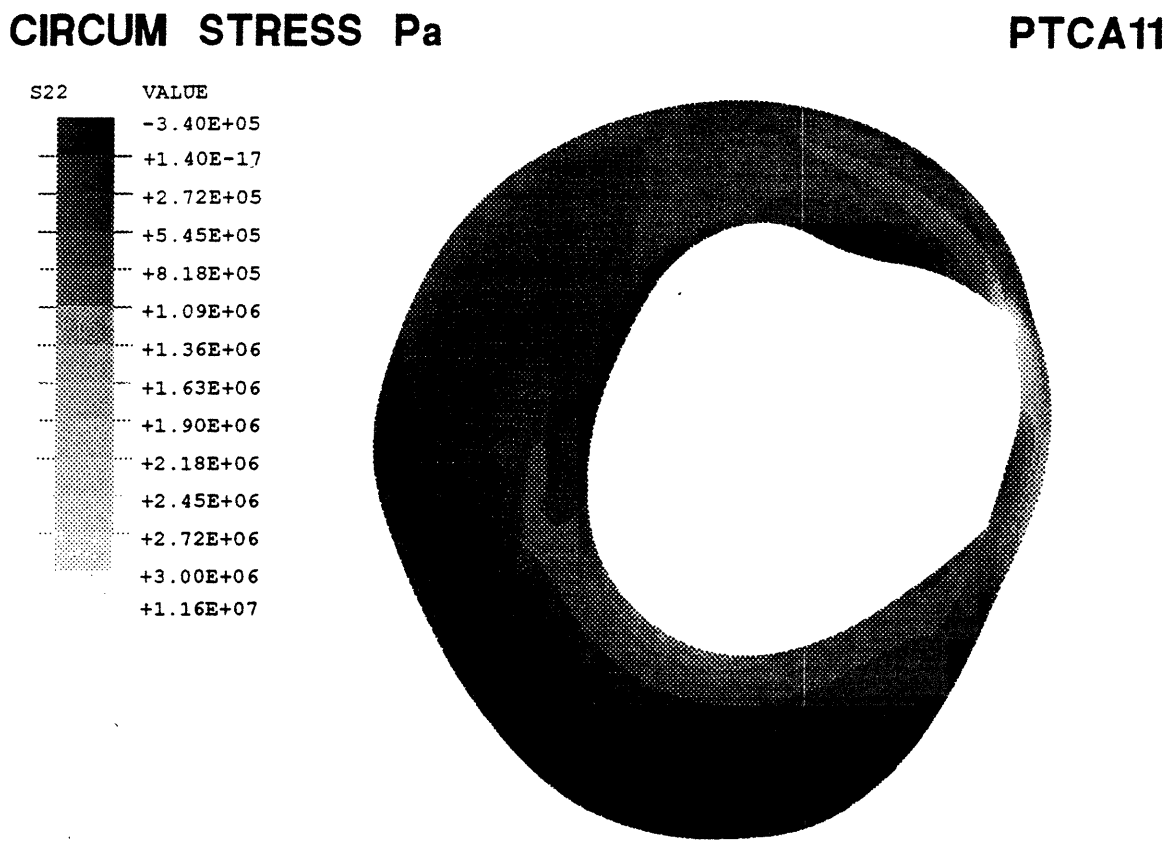

Fig. A.15b Contour map of circumferential stress (Model 11).

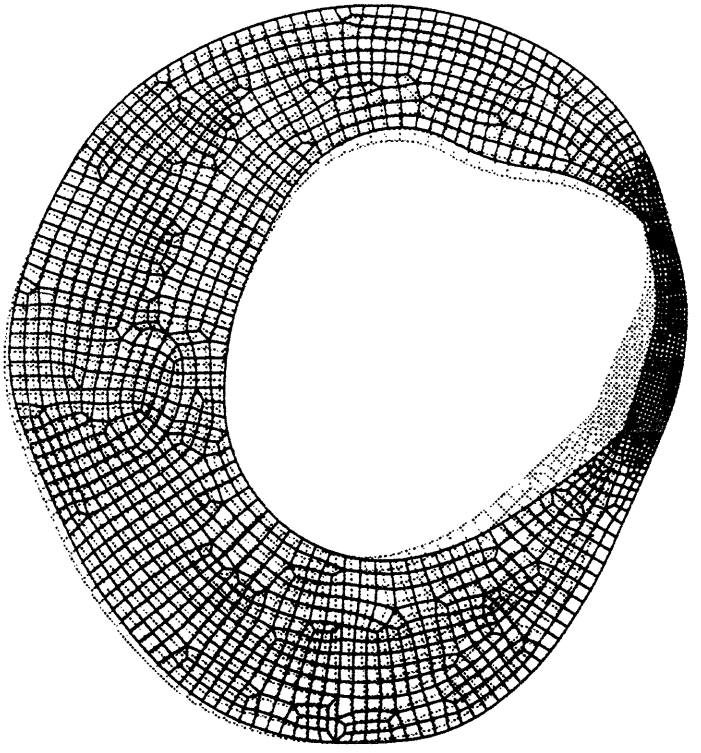

Fig. A.15c Deformed mesh (Model 11).

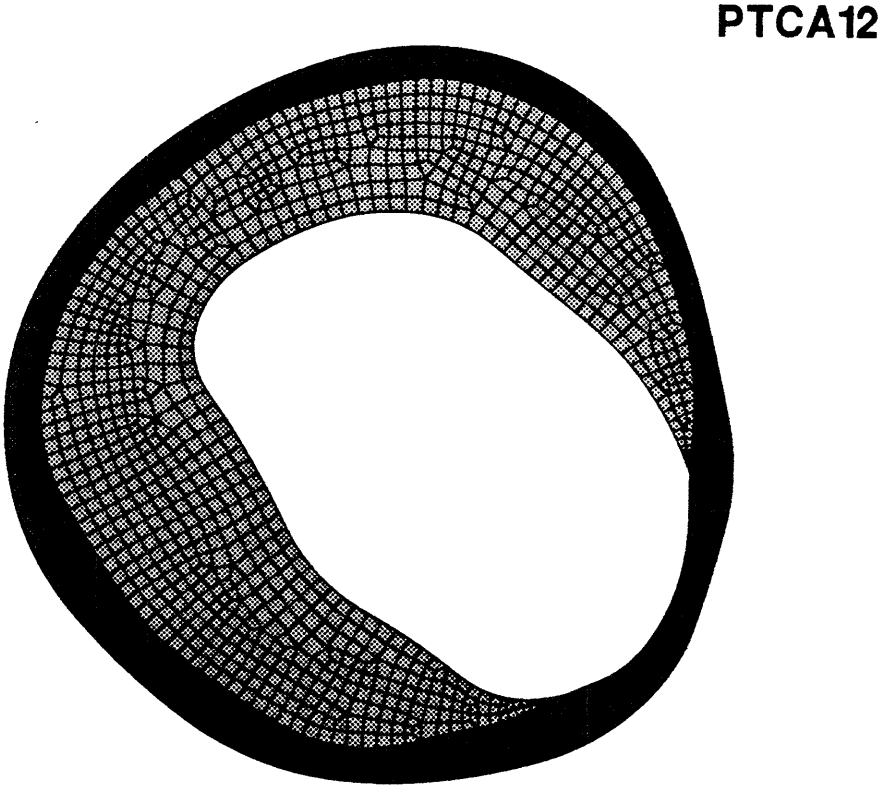

Fig. A.16 Iliac artery Model 12: a.) FEA mesh and b.) contour map of circumferential stress, and c.) deformed mesh.

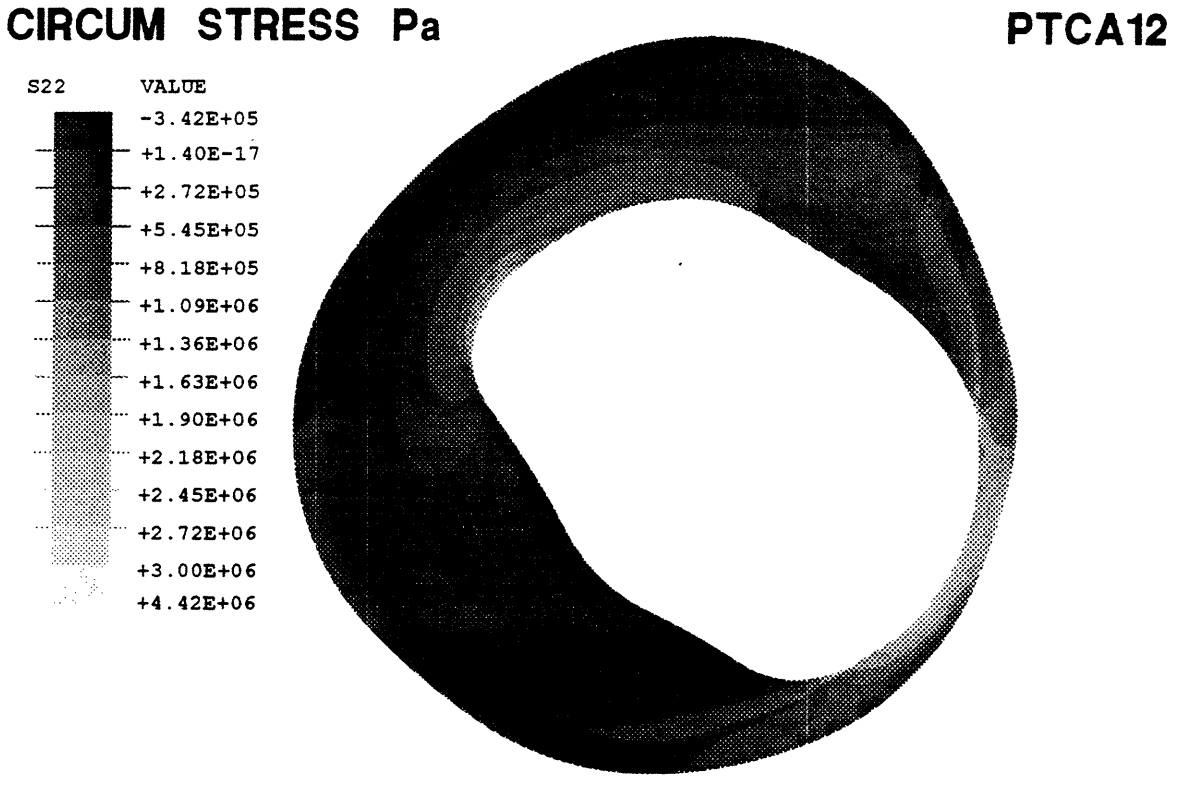

Fig. A.16b Contour map of circumferential stress (Model 12).

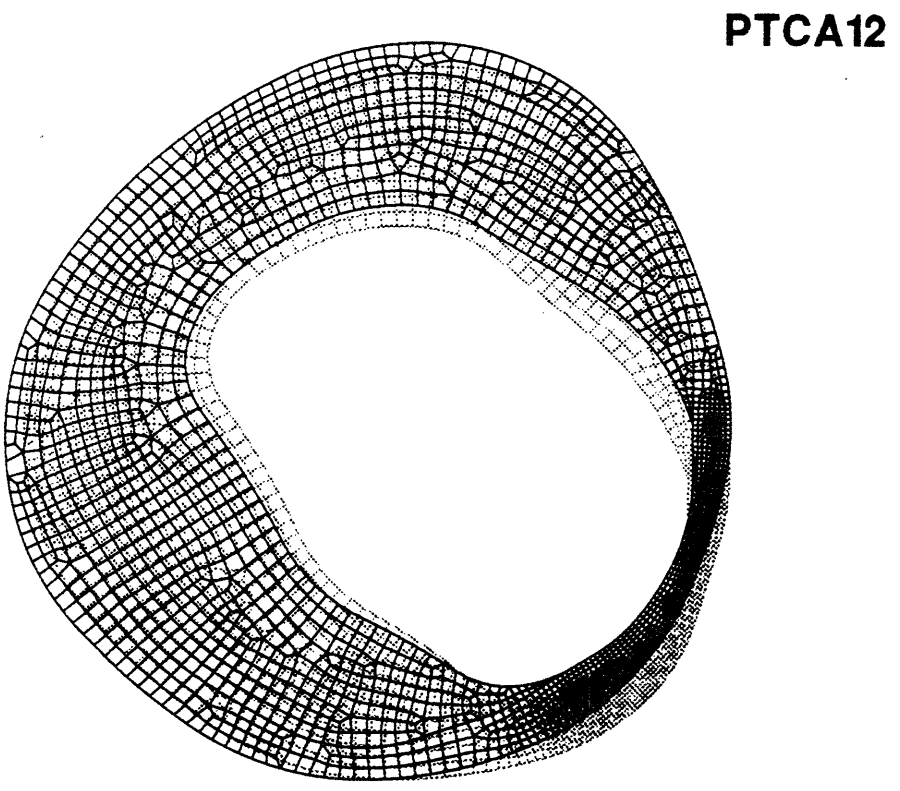

Fig. A.16c Deformed mesh (Model 12).

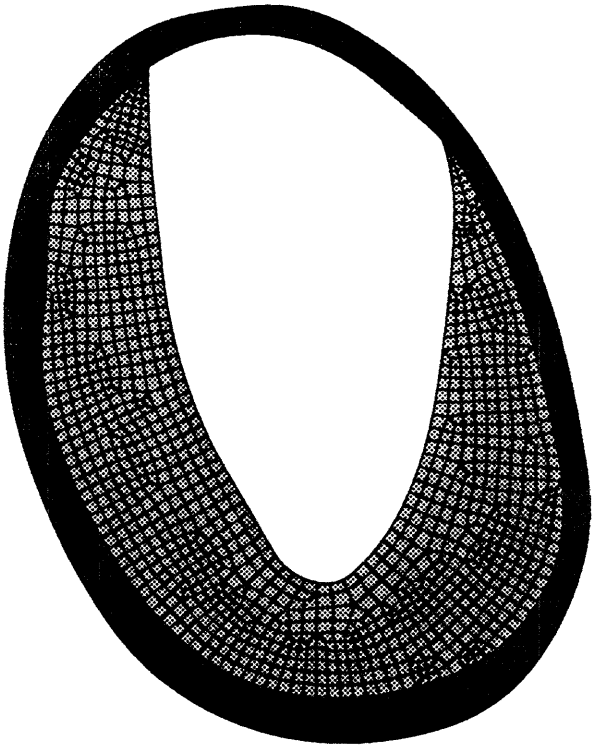

Fig. A.17 Iliac artery Model 14: a.) FEA mesh and b.) contour map of circumferential stress, and c.) deformed mesh.

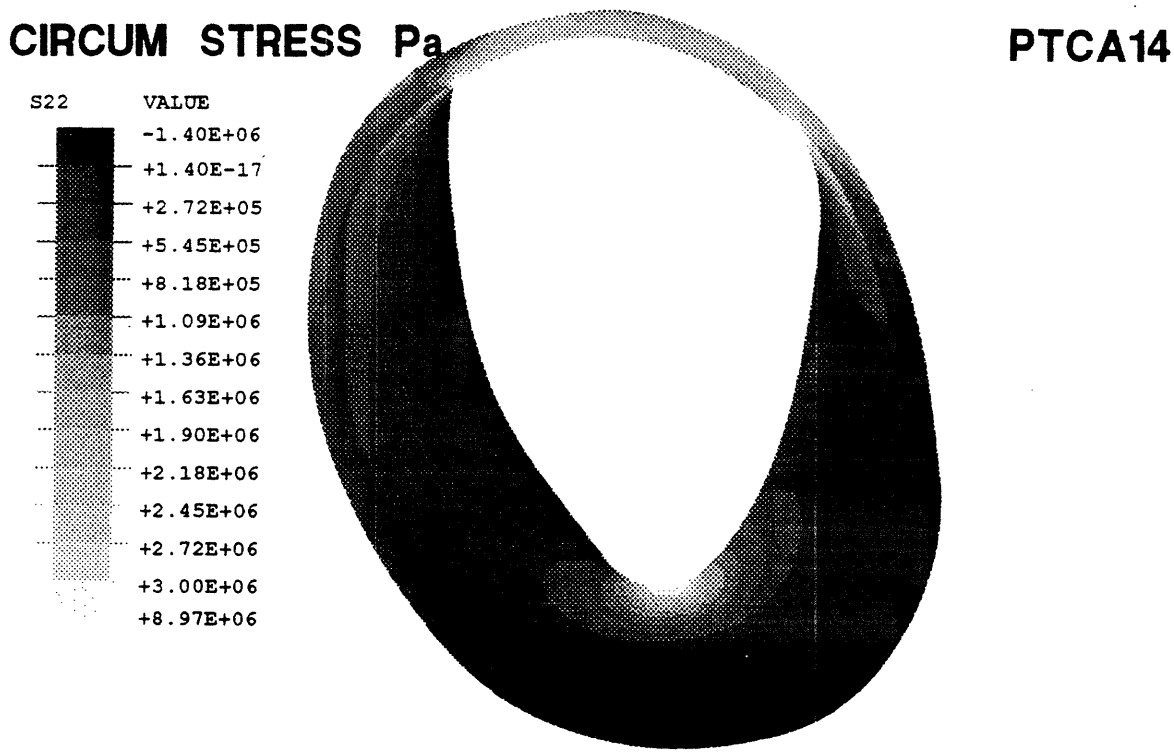

Fig. A.17b Contour map of circumferential stress (Model 14).

Fig. A.17c Deformed mesh (Model 14).

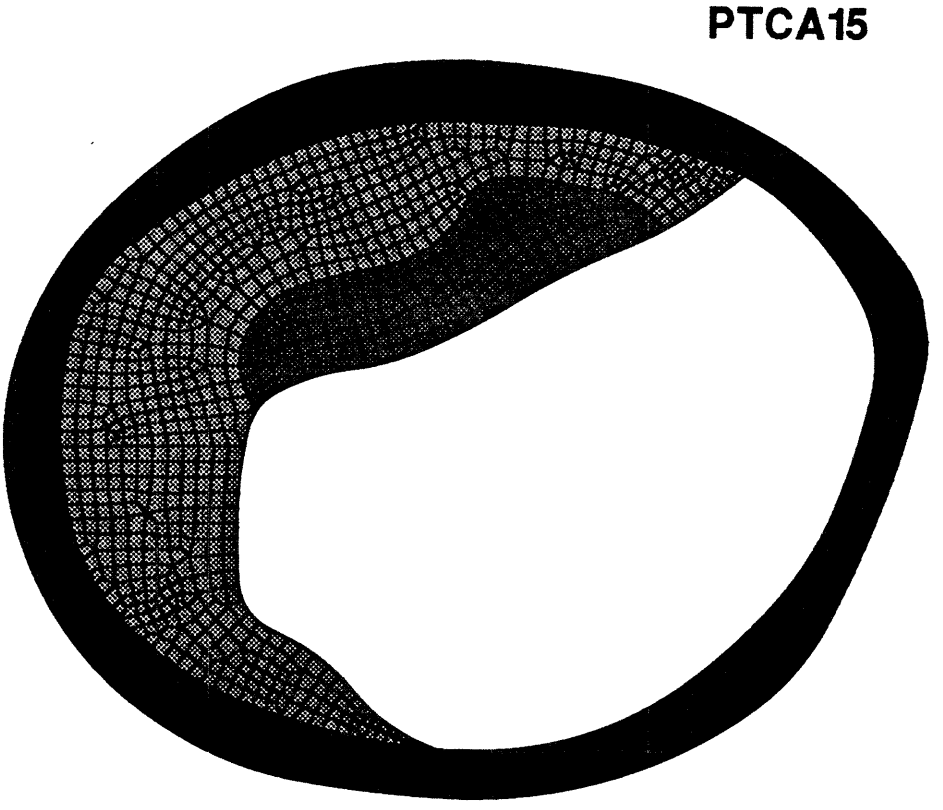

Fig. A.18 Iliac artery Model 15: a.) FEA mesh and b.) contour map of circumferential stress, and c.) deformed mesh.

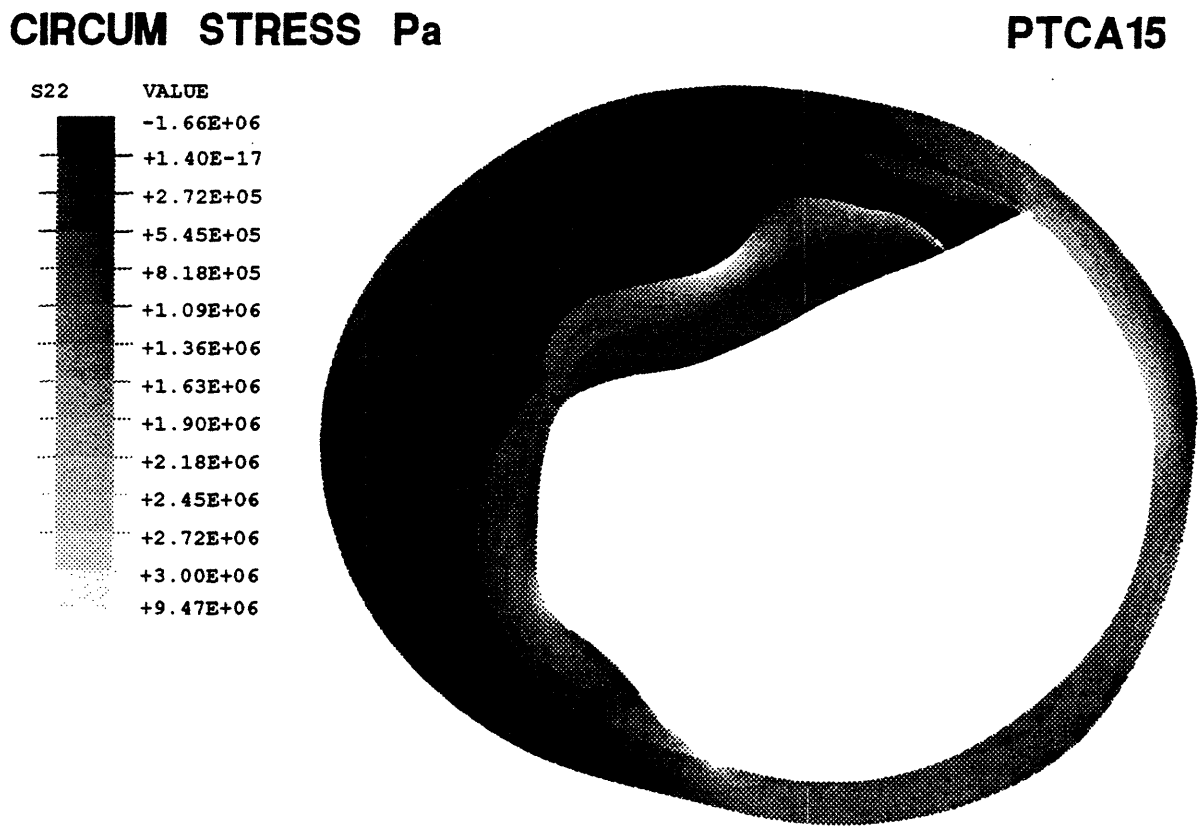

Fig. A.18b Contour map of circumferential stress (Model 15).

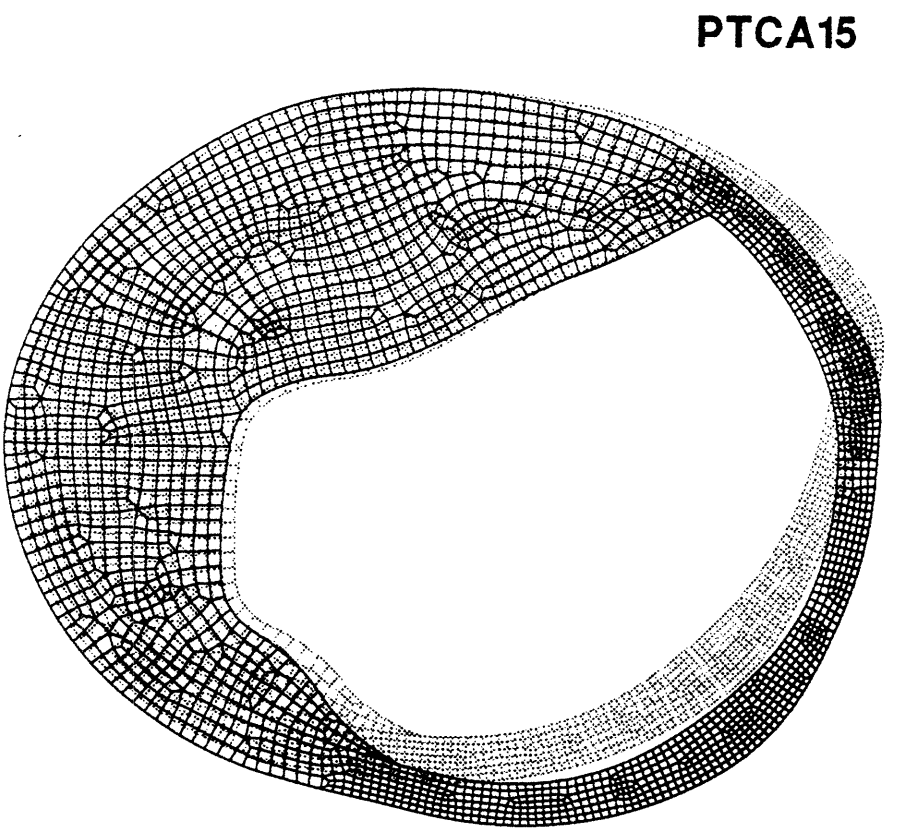

Fig. A.18c Deformed mesh (Model 15).

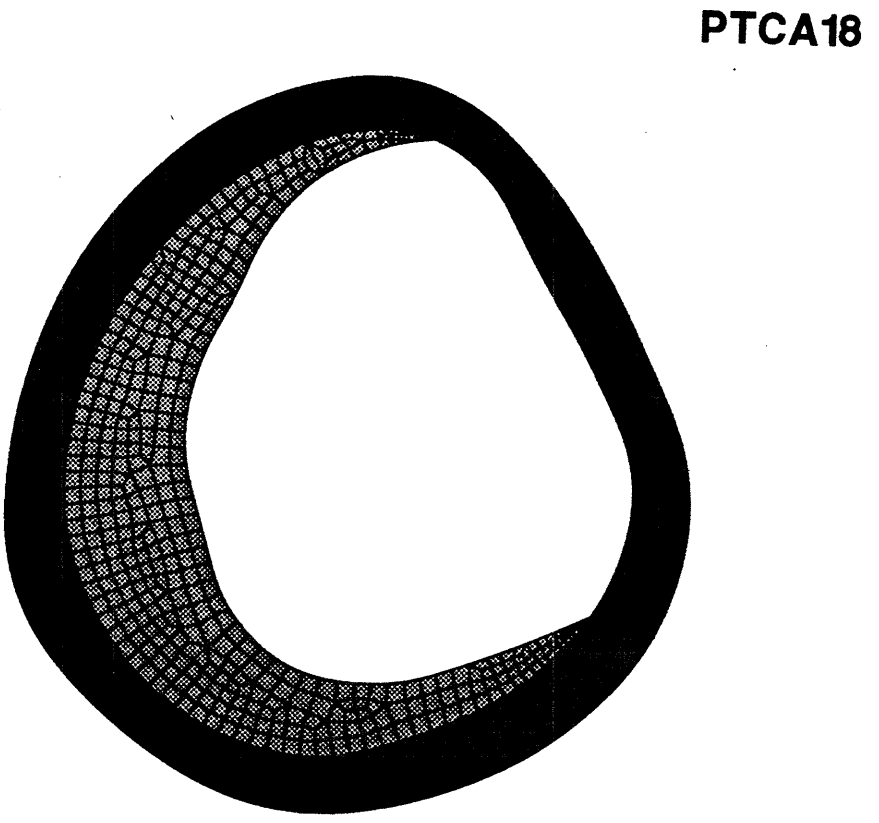

Fig. A.19 Iliac artery Model 18: a.) FEA mesh and b.) contour map of circumferential stress, and c.) deformed mesh.

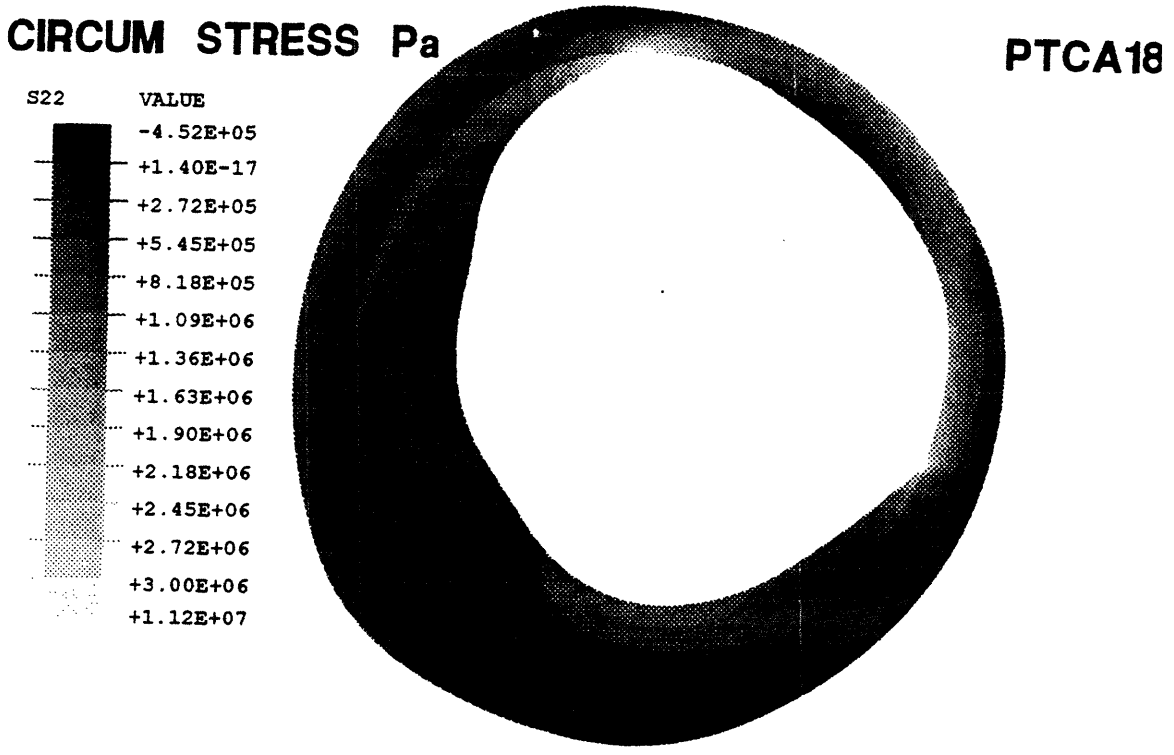

Fig. A.19b Contour map of circumferential stress (Model 18).

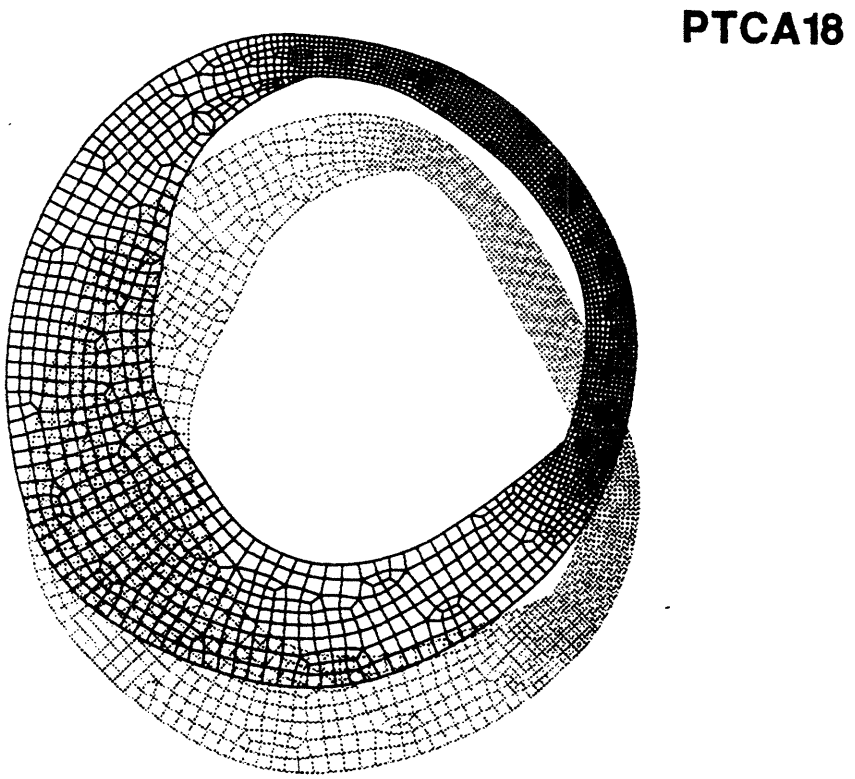

Fig. A.19c Deformed mesh (Model 18).

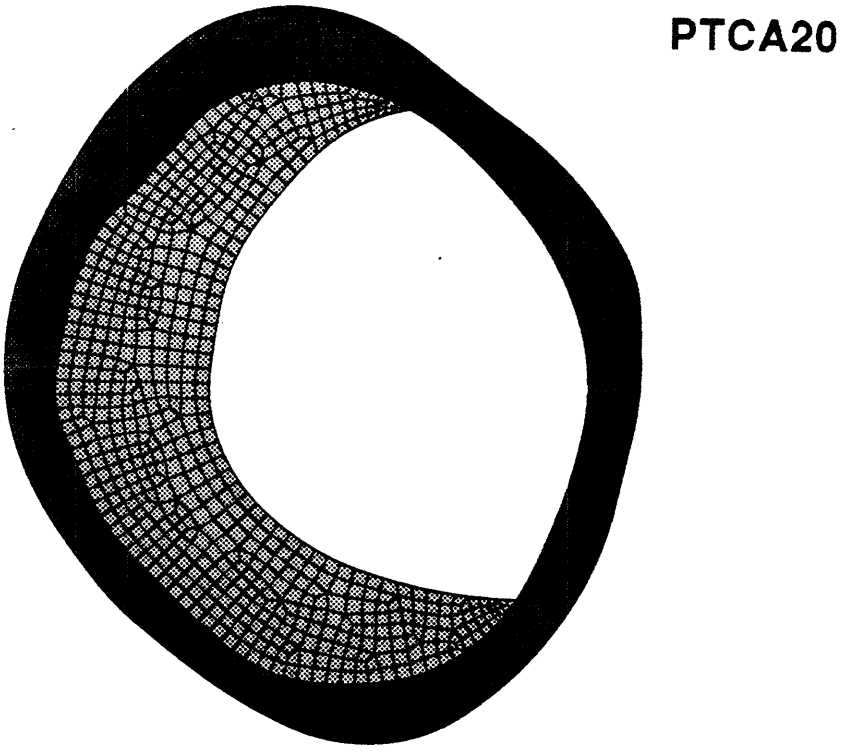

Fig. A.20 Iliac artery Model 20: a.) FEA mesh and b.) contour map of circumferential stress, and c.) deformed mesh.

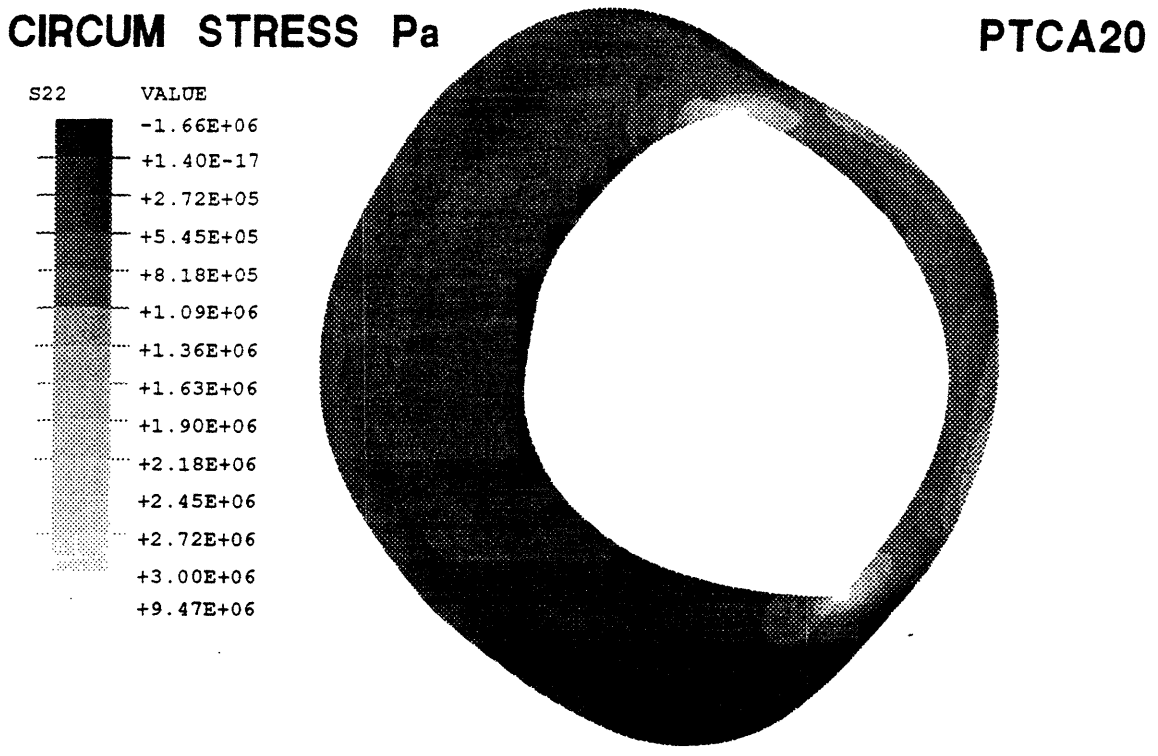

Fig. A.20b Contour map of circumferential stress (Model 20).

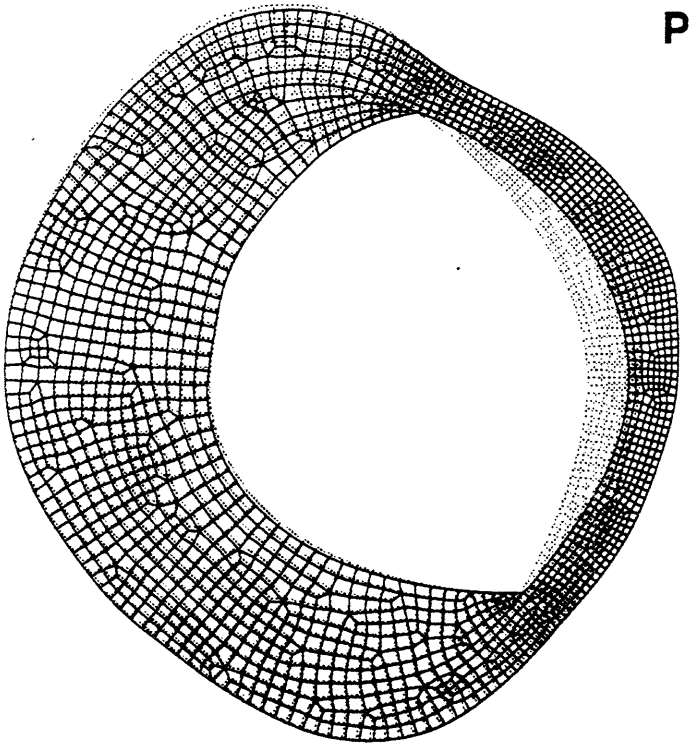

Fig. A.20c Deformed mesh (Model 20).

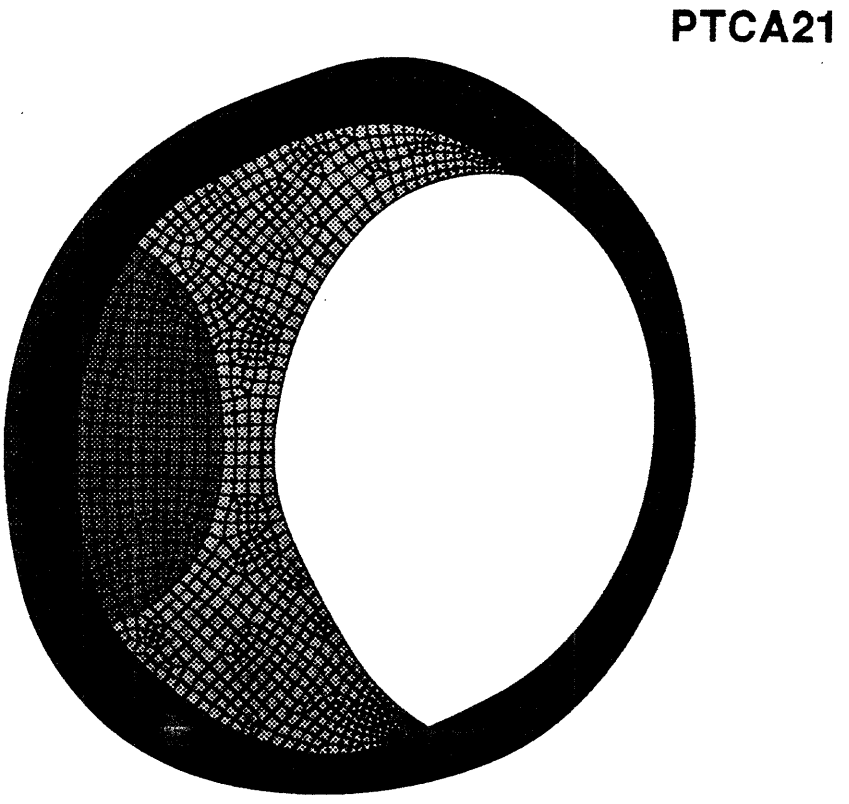

Fig. A.21 Iliac artery Model 21: a.) FEA mesh and b.) contour map of circumferential stress, and c.) deformed mesh.

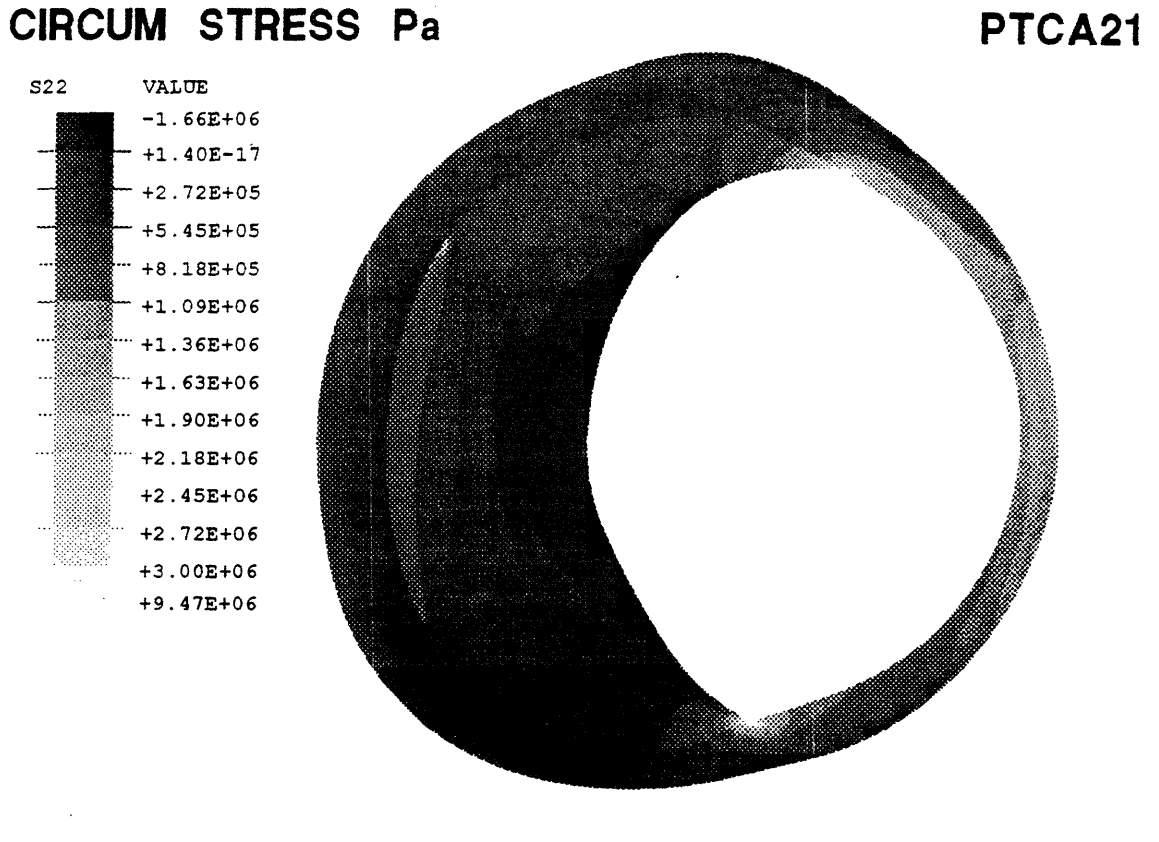

Fig. A.21b Contour map of circumferential stress (Model 21).

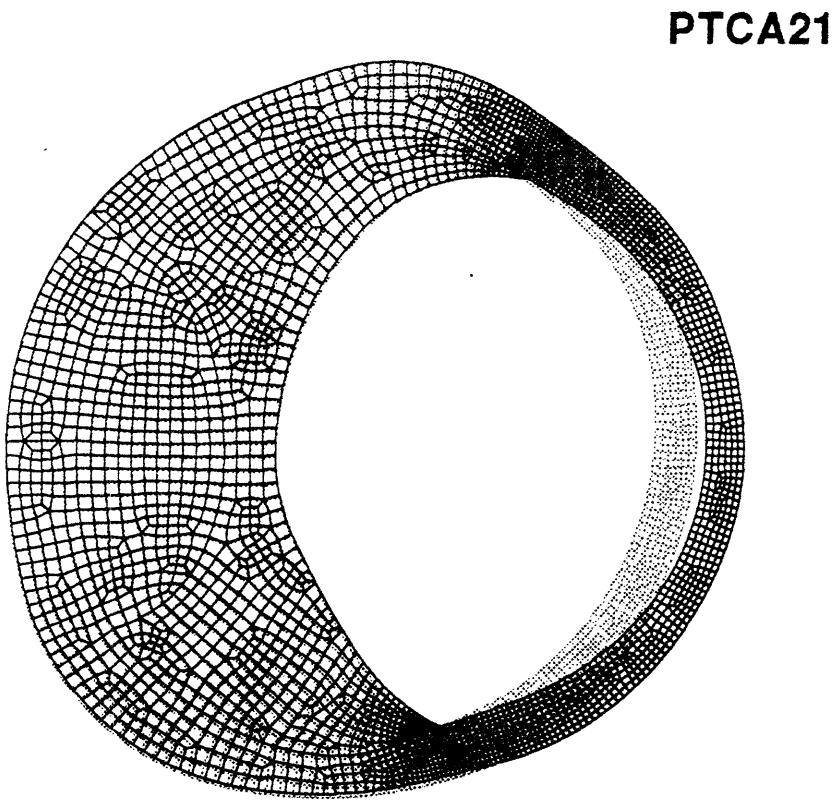

Fig. A.21c Deformed mesh (Model 21).

APPENDIX B

PROTOCOL FOR RADIAL COMPRESSION PLAQUE TESTING
Revised 2/25/92

Introduction: A complete run will take about 12 hours per specimen, during which time the experiment must be closely supervised. A maximum of two specimens should be taken from one patient. Autopsies start at 11 AM and end by 4 PM. Before collecting the specimens, reserve Dynastat time for the next two days. On both days of testing, start a run early in the morning and you will be done by dinner time. This plan allows you to finish testing the specimens before they are 72 hours post-mortem. Plan to analyze data as it is generated throughout the run. IMPORTANT: ALWAYS WEAR LATEX GLOVES WHEN HANDLING SPECIMENS.

Steps in the plaque testing protocol:

1. Plaque collection
2. Equipment setup
3. Static unconfirmed compression
4. Dynamic unconfined compression
5. Thickness measurement
6. Cleanup

Plaque Collection

1. Collect specimen as a circumferential strip from the abdominal aorta between the renal arteries and the bifurcation. Take a maximum of two specimens per patient. The specimens should have the geometry shown in Fig. B.1.

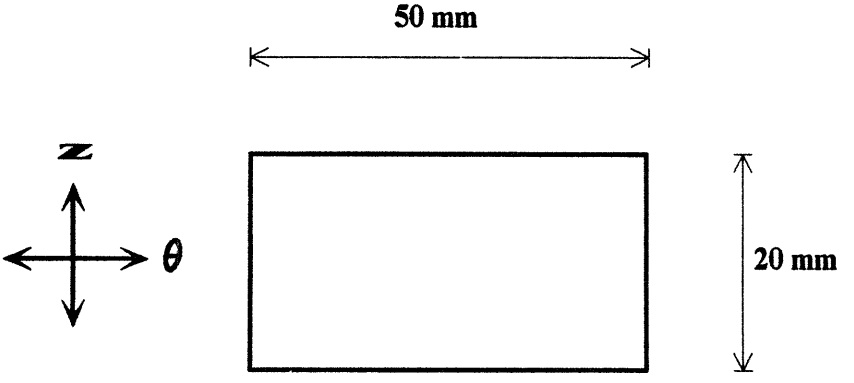

Fig. B.1 Geometry of plaque specimen for testing in radial compression.

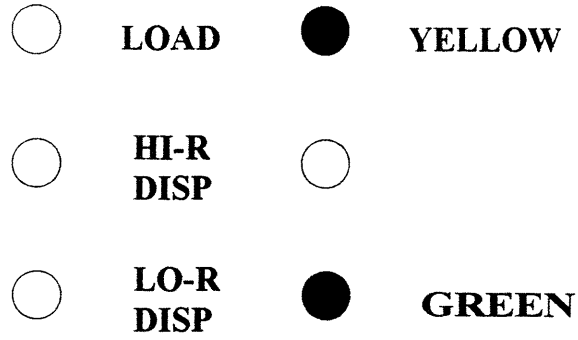

Fig. B.2 IMASS Dynastat back panel connections for compression test.

Plaques must be at least 5 mm from any vessel ostii and be visibly uncomplicated, with no surface fracture or overlying thrombus, and be at least 9 mm in diameter. Dissect the plaque free from adventitia, media, plaque components, and any adjacent normal aortic tissue.

2. Take a 10 mm section from the end of the strip. Place it in a small jar of formalin for histology study. Label and refrigerate.

3. Put the remaining section of the strip in a small jar of normal saline for mechanical testing. Label and refrigerate.

Equipment Setup. Equipment setup involves adjusting the controls on the room air conditioner, Dynastat, Rockland filter, Rockland frequency generator, Gould chart recorder, and NOVAS personal computer.

1. Set the room air conditioner on low cool.

2. Dynastat adjustments:

   Set the rear connections as shown in Fig. B.2

   Set the servo controls as shown below:

Servo:	Servo 2
Gain 2:	0.1
Damp:	7.5
Comp1:	1
Comp2:	10

Set the upper panel controls as shown below:

Displacement Read:	LO-R
Dyn/Ext:	ON, 002, scale 0
Load/Disp. Control:	Load Control

3. Set the Rockland filter as shown below:

	Channel 1	Channel 2
Cutoff	4.50 Hz	4.50 Hz
Mult	10	10
Gain	0 dB	20 dB
Function	Low Pass	Low Pass
	RC	RC

The back panel of the filter should have the connections shown in Fig. B.3.

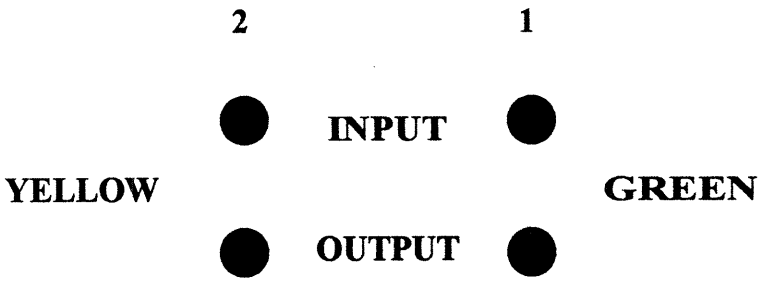

Fig. B.3 Rockland filter back panel connections.

4. Set the Rockland frequency generator so that all attenuation switches are out and all dials read zero.

5. Set the Gould chart recorder controls as shown below:

	Upper Channel	Lower Channel
	Load (Yellow)	Disp (Green)
Full Scale	1 V	1 V
Zero Suppress	off	+10
Cutoff	low DC	low DC
	high 10	high 10

Turn power ON, with chart speed set to STOP. Note: the chart paper will change color when it is close to running out. Remember to record all changes in Dynastat load settings or chart recorder voltage scales on the strip chart

during the run.

6. Enter the following keyboard commands at the computer:

    Login: rich
    % dynssp
    Enter "o" to name output file
    Enter "specimenname.data"

Static unconfined compression. This procedure allows measurement of static unconfined radial compressive stiffness between loads of 4 and 17 KPa.

1. Place the 1 cm platen in the upper spindle. Place the unconfined compression chamber in the lower spindle. Tighten both spindles.

2. Zero the load voltage with the attached screwdriver, using C (coarse) and then (F) fine BAL adjustments.

3. Place 1 Kg mass on top of the knurled knob. Adjust the gain so that the load voltage reads -1.000. Remove the mass.

4. Turn the knurled knob in the down direction until the platen just touches the sample. Lock the top fitting located just below the load cell.

5. On the Dynastat front panel, set Static A and B to ON, COMP, and 000.

6. Apply slight downward pressure to the lower spindle while turning control mode to CLOSED and program to ON.

7. Adjust Static A and B dials to give a load voltage of -.030. If it is not possible to get the voltage this low in COMP, then switch to TENS.

8. Adjust the low range displacement sensor height (knob located on top of Dynastat servo box) so that the displacement voltage reads 3.000.

9. Set recorder speed to .05 mm/sec. Set both pens to the far left of their ranges using the position and vernier dials.

10. Begin recording the displacement voltage every 5 minutes. (Use a timer!) When the displacement pen reaches the extreme right side of its range, use the vernier dial to reset it to the extreme left. Allow the specimen to creep until the displacement voltage changes 2% over a five minute period, as illustrated in Fig. B.4. Record the "equilibrium" displacement voltage.

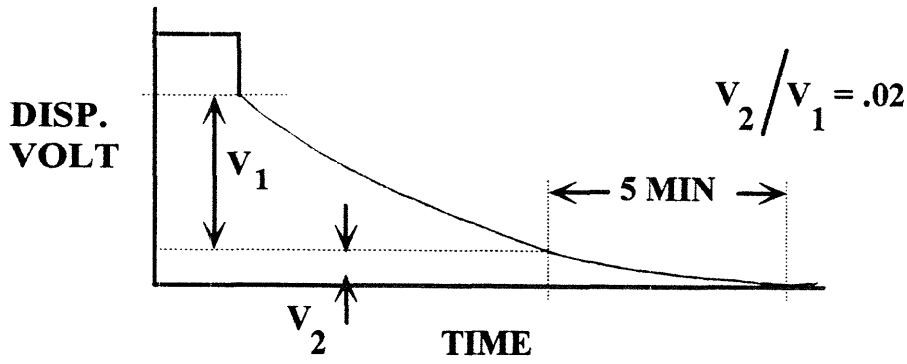

Figure B.4. Definition of equilibrium displacement voltage.

11. Set Static A or B to give a load voltage of -.100. This will require the COMP setting. Set the displacement pen to the extreme left. Repeat step 10.

Dynamic unconfined compression. This procedure allows measurement of dynamic unconfined radial compressive stiffness at a mean load of 17 KPa.

1. Set the displacement recorder channel full scale voltage to .25. Center the displacement recorder pen using the vernier and position.

2. Enter "g" to dynssp to start the dynamic test. Make sure that the two recorder pens are moving roughly in phase. Relax and take a 20 minute break while the test runs.

3. When the test is complete, immediately check the data:

    Insert floppy disk in drive.
    Enter "q" to quit dynssp.
    % tar cvn specimenname.data.
    Take floppy to RIF.
    login:rich.
    % tar xvn.
    % lprep specimenname.data.
    After printing % rem *.list to remove printer files.

Thickness measurement. Specimen thickness is measured at a static radial compressive load of 17 KPa, under equilibrium conditions.

1. STOP the chart recorder.

2. Change displacement read to HI-R.

3. Read displacement voltage with specimen.

4. Change control mode to OPEN to release specimen.

5. Use forceps to remove specimen from under platen. Place it in a saline filled container.

6. Applying light downward on the lower spindle, switch control mode to CLOSED and program to ON. This will allow the compression chamber to move up and contact the platen.

7. Record the displacement voltage without the specimen. Switch control mode to OPEN to release jaws.

Cleanup. It is very important to clean the apparatus and tools carefully to prevent contamination of other students' experiments and to limit the risk of human infection by blood-borne agents.

1. Remove the compression apparatus from the Dynastat.

2. Put the specimen in a small container of formalin for ultrasound study. Label and refrigerate.

3. Place all compression apparatus. Dynastat wrenches, and instruments in the sink and flood with a half gallon of activated Cidex solution. Allow to stand for ten minutes, then rinse and dry.

4. Turn recorder power OFF. Set the Dynastat static A and B controls to COMP and 000. Turn off the room air conditioner.

5. Reset the servo control as shown below:

Servo:	Servo 2
Gain 2:	2.0
Damp:	5.75
Comp1:	8.3
Comp2:	7.0

6. It is a good idea to occasionally drain the water in the air line supplying the Dynastat servo. The filter cartridges are simply rolls of toilet paper sawed off with a hacksaw.

APPENDIX C

PROTOCOL FOR CIRCUMFERENTIAL TENSION PLAQUE TESTING
Revised 2/25/92

Introduction. A complete run will take about 18 hours per specimen, during which time the experiment must be closely supervised. A maximum of two specimens should be taken from one patient. Autopsies start at 11 AM and end by 4 PM. Before collecting the specimens, reserve Dynastat time for the next two days. On both days of testing, start a run early in the morning. This plan allows you to finish testing the specimens before they are 72 hours post-mortem. Plan to analyze data as it is generated throughout the run. IMPORTANT: ALWAYS WEAR LATEX GLOVES WHEN HANDLING SPECIMENS.

Steps in the plaque testing protocol:

1. Plaque collection
2. Equipment setup
3. Static tension
4. Static tension to fracture
5. Cleanup

Plaque collection

1. Collect specimens as 2 cm wide circumferential strips from the abdominal aorta between the renal arteries and the bifurcation. Take a maximum of two specimens per patient. The specimens should have the geometry shown in Fig. B.1.

   Plaques must be at least 5 mm from any vessel ostii and be visibly uncomplicated, with no surface fracture or overlying thrombus, and be at least 9 mm in diameter. Dissect the plaque free from adventitis, media, necrotic plaque components, and any adjacent normal aortic tissue.

2. Take a 5 mm section from the end of the strip. Place it in a small jar of formalin for histology study. Label and refrigerate.

3. Put the remaining section of the strip in a small jar of normal saline for mechanical testing. Label and refrigerate.

4. For each specimen collected, fill a jar with formalin. These will be used to store the specimens after mechanical testing.

Equipment setup. Equipment setup involves adjusting the controls on the room air conditioner, Dynastat, Rockland filter, and Gould chart recorder.

1. Set the room air conditioner on low cool.

2. Dynastat adjustments: Set the rear connections as shown in Fig. C.1.

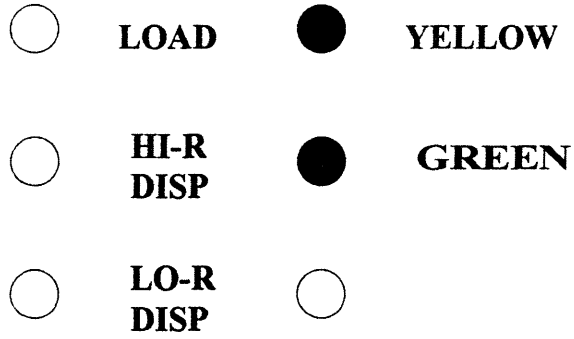

Fig. C.1 IMASS Dynastat back panel connections for tension test.

Set the servo controls as shown below (Each may need adjustments to prevent the servo from ringing or overshooting):

Servo:	Servo 2
Gain 2:	0.1
Damp:	10
Comp1:	1
Comp2:	6.0

Set the upper panel controls as shown below:

Displacement Read:	HI-R
Dyn/Ext:	OFF
Load/Disp. Control:	Load Control

3. Set the Rockland filter as shown below:

	Channel 1	Channel 2
Cutoff	1.50 Hz	4.50 Hz
Mult	1	1
Gain	0 dB	20 dB
Function	Low Pass RC	Low Pass RC

The back panel of the filter should have the connections shown in Fig. B.3.

4. Turn power ON, with chart speed set to STOP. Note: the chart paper will change color when it is close to running out. Remember to record all changes in Dynastat load settings or chart recorder voltage scales on the strip chart during the run.

5. Switch the green cable to HI-R DISP on the back panel of the Dynastat.

6. Install the hook in the upper spindle and the tensile chamber in the lower spindle.

7. Cut the specimen with ribbon die to the dimensions shown in Fig. 3.1.C. (47).

8. Measure the thickness of the specimen with the compliant material micrometer in three locations across the width of the center of the gage section.

9. Using dissecting microscope, apply cyanoacrylate adhesive with a pin to the four corners of gage section. Position one 300 μm fluorescent microsphere on each glue drop.

10. Fit the specimen in the upper clamp to 5 mm depth. Tighten screws. Hang the upper clamp on the hook, adjusting the knurled knob so that the specimen hangs straight into the lower clamp to a depth of 5 mm.

11. Set up perfusion pump to drip on specimen from top clamp, recover from full basin. Set on 2.

12. Set up camera bracket, UV lamp, and camera alongside Dynastat chamber. Camera uses 27.5 mm extension, 60 mm micro lens, +2 magnifying lens, orange filter, UV filter, air shutter release, and Kodak Ektachrome 100HC slide film. Set the camera to manual mode with an aperture of 5.6 and an exposure time of 1 sec.

13. Zero the load voltage. Place the 1 kg mass on top of the knurled knob and adjust the gain so that the load voltage reads 1.000. Remove the mass from the knurled knob. Turn knurled knob until load voltage reads .025. Tighten the top fitting just below the load cell.

14. Set static A and B to TENS and 005. Switch control mode to CLOSED and program to ON. Adjust static A and B so that the load voltage reads 0.00. Adjust Gain 2 to 3.5. Adjust static A and B to return to a load voltage of 0.00. Take a photograph.

15. Set the Gould chart recorder controls as shown below:

	Upper Channel	Lower Channel
Full Scale	Load (Yellow)	Disp (Green)
Zero Suppress	+1	1 V
Cutoff	low DC	low DC
	high 10	high 10

Turn power to ON, with chart speed set to STOP. Note: the chart paper will change color when it is close to running out. Remember to record all changes in Dynastat load settings or chart recorder voltage scales on the strip chart during the run.

Static tension. This procedure allows measurement of static circumferential tensile stiffness between loads of about 30 and 50 KPa. A preconditioning cycle is included (46).

1. Start the recorder with speed .10 mm/sec and both pens at the extreme right limit of range.

2. Allow the specimen to creep. Record the displacement voltage every 5 minutes until the voltage changes by 2% over 5 minutes. (Fig. B.4.) Record the final voltage. Photograph.

3. Adjust static A and B to increase load voltage by .025 V. Reset both recorder pens to the extreme right with position and vernier controls.

4. Repeat steps 2 and 3 until the specimen fractures. Usually this occurs at a load of 200-700 grams. After 300 gr, increase by increments of 100 gr.

5. Note where the specimen fractured (at clamp edge or midlength) and the nature of the fracture (edge tear, formation of hole, or delamination).

Cleanup. It is very important to clean the apparatus and tools carefully to prevent contamination of other students' experiments and to limit the risk of human infection by blood-borne agents.

1. Remove the tensile apparatus from the Dynastat.

2. Put the fractured specimen in a small container of formalin for histology study. Label and refrigerate.

3. Place all tensile apparatus, Dynastat wrenches, and instruments in the sink and flood with a half gallon of activated Cidex solution. Allow to stand for

ten minutes, then rinse and dry.

4. Reset Dynastat servo controls to:

Gain2:	2
Damping:	5.75
Comp1:	8.3
Comp2:	7.0

5. Turn recorder power to OFF. Set the Dynastat static A and B controls to COMP and 000. Turn off the room air conditioner.

6. It is good to occasionally drain the water trap in the air line supplying the Dynastat servo. The filter cartridges are simply rolls of toilet paper sawed off with a hacksaw.

APPENDIX D

PROTOCOL FOR FINITE ELEMENT MODELING (I-DEAS V4, ABAQUS 4.9 SOFTWARE)

I. Creating a surface to attach to mesh areas.

This is essential if you plan to do adaptive meshing.

Starting from engineering analysis (EA) pre/post processing (P):

A. Create Surfaces:

GM	global menu
NM	new module
CF	change family
SM	subject modeling
OM	object modeling
C	create
B (1,1,1) <default>	block
OR	orient
TR (0,0,.5)	translate
STO object 1 <default>	store

Now have a cube where surface 2 is in the XY plane

B. Go back to EA, P:

GM	global menu
NM	new module
CF	change family
EA	eng. analysis
P	pre/post proc.
TA	task
G	geometry
MF	model file
T	tolerance
set all tolerances to 1E-06	
if not already set	
/	
DO	display option
EN	entity
G	geometry
SU -(on)	surface

C. Get surfaces:

```
/
 S                                          surface
  F                                         from object
   G                                        get object
    working set 1 <default>
      bin         1 <default>
      curve tol     (1E-06)
```

D. Attach surface 2 to mesh areas:

```
/
TA                                          task
 ME                                         mesh generation
  MA                                        mesh area
   MO                                       modify
    *                                       (all)
     A                                      attached surface
      A                                     attach new
       L                                    label
        2                                   surface
         D                                  done
```

E. Delete extra surfaces, points, curves:

```
/
 TA                                         task
  G                                         geometry
   S                                        surface
    DEL                                     delete
     L                                      label
      /
       3,6
         D                                  done

/
 DE
  ATT                                       delete
    * (all curves, all points in block)     attribute

GM
 SAVE
```

II. Running I-DEAS Analysis.

This is a precursor to adaptive meshing. Note that the model must use supported elements (thin shell). The connectivity can be either CW or CCW.

Starting from EA, P:

A. Running an analysis:

GM	global menu
NM	new module
CF	change family
MS	model solutions
E	execution option
B or I (if you can tie up terminal and system)	batch or interactive
/	
C	case set
U (1)	use 1
/ ME	method
S	soln no restart
/	
0	output
SE	strain energies
S	store
/	
SO	solve linear statics
. run title <cr>	
. delete scratch <cr>	
. assign 4 letter jobname	

B. After running batch:
You will find yourself in the operating system. After the batch job is finished @ IDEAS (JOBNAME) gets you back into I-DEAS where you were before.

GM	
SAVE	stores analysis results in permanent I-DEAS files

III. Adaptive remeshing

. only for freemeshed mesh areas
. must first have filename.fil containing strain energies from I-DEAS analysis.
. must have attached mesh areas to a surface.

Starting from EA, P:

A. Set up adaptive remeshing:

TA	task
AD	adaptive meshing
S	settings
B	basis
AR	anal. results
AD	anal. data select
CU	current
(1)	
/	
S	settings
M	methods
E	element split
SP	splitting default
Q	quadrilateral
FQ	4 quadrilateral
/	
S	

Can leave SM (smoothing factors) and R (remeshing %) at default values

ST	status

Look over the settings...

B. Executing adaptive remeshing:

/	
EX	execute
(shells) <default>	
* (all mesh areas)	
...wait...	
B	begin adaptive meshing
...wait...	
S	save if all is well
K (model 2)	keep

C. Saving results:

I would suggest saving the adaptively meshed model twice: once in filename.mf and a second time in filenameb.mf. That way you can adaptively remesh it again if necessary.

GM	global menu
SAVE	save
MA	manage FE models
A	active
2	FE model 2
GM	global menu
SAVE	save
O.K. to save in filename? (n)	
new in f name: filenameb	
MF	model file
NF	new file
filenameb	
MAN	manage FE models
DEL	delete
1	FE model 1
TA	task
ME	mesh generation
E	elements
MO	modify
. Set all elements with mat'l prop 1,2,3,4 to appropriate color	
. Set all elements to plane strain PST family.	
. Reassign mat'l properties to elements by color.	
TA	task
AN	analysis cases
. Establish restraints, edge pressures, and case set.	
GM	global menu
SAVE	save

IV. Creating ABAQUS inp file from I-DEAS model.

Starting from EA, P:

A. Preparing model:

```
DO                                        display options
  L                                       line
    E                                     element 1st edge sw
/
  GM                                      global menu
    REDI                                  redisplay
```

Make sure element connectivity is CCW
Make sure case set is defined

B. Creating .inp file from Pearl database:

```
TA                                        task
  PT                                      pearl data transfer
    O                                     open
     filename.pdb
     create new Y <default>
     L                                    load
       MO                                 model
        ...wait...
       MA                                 manage FE models
         W                                write
           AB                             ABAQUS
        Enter pearl database name filename <def>
        Enter ABAQUS filename filename <def>
        Write new file? Y <def>
        Problem type structural <def>
        Hybrid elements ? No <def>
        Reduced integration ? No <def>
        Case set  1
        Start JCL  No <def>
        End JCL    No <def>
   ...wait...
        Do not save (no need to keep Pearl database)
GM
  Exit
```

In operating system:

. Append tricks.inp to filename.inp.
. Edit filename.inp to prepare file for ABAQUS.
. Purge extra files.

V. Procedure for running ABAQUS job on CRAY

From VAX:

A. Analysis on CRAY:

```
% Cray
(login)

% cd  /tmp/hloree                    Go to temporary dir
% ftp ted (login)                    Get .inp file from VAX
  > cd  dirname
  > get  filename.inp
  > quit

% Abaqus                             run job
  (start job on "s" que)             let batch job run
% abaqus - abares1                   convert .res to .rnb
  (enter job name)

% ftp  herman                        put .rnb and .dat on VAX
  (login)
  > cd  dirname
  > put  filename.dat
  > binary
  > put  filename.rnb
  > quit
% logout (may also rm files)
```

B. Post processing on VAX:

```
% set def  dirname
% abares                            convert .rnb to .rst
  (enter name of .rnb file)          batch job started
Delete .rnb after batchjob completed
```

VI Procedure for sending ABAQUS-POST results to Athena Postscript printer.

A. Run ABAQUS POST on VAX:
% post
start with * set, hardcopy = on (or run journal file: input, file=filename.jnl)
Produce only 1 plot per session!
After * end, POST will create filename.mpl.

B. Put .mpl file into postscript form and print on Athena:

% abaplotp
(enter filename)
will produce postscript file for009.dat.
% rn for009.dat filename.ps
% athena
(log into hmloree)
% attach bitbucket
% cd /mit/bitbucket
% mkdir howard
% cd howard
% ftp ted

(log into hml)
> get filename.ps
> quit

% lpr -P thesis filename.ps To dispatch bldg 11 - 2nd floor

lpq -P printername to check que
When printing completed:
% rm filename.ps

% logout

Back on VAX:
del filename.ps;*
del filename.mpl;*

VII Photography

Settings for black background:
100 HC film
exp 1/2 sec
Ap 11, 8, 5.6 (bracket) (8 works best)

Use tripod, lights out, cable release

A. ABAQUS POST plots:
* contour, v=s22, range gives min and max values for scale.
* set, dialog color = black hides the dialog text.

B. I-DEAS meshes:
From EA, P:

Do	display options
V	viewpoint
T <cr>	triad sw
OR <cr>	origin sw
OV <cr>	outline sw
LA <cr>	label sw
GM	global menu
CL	clear

Sample ABAQUS input for simple concentric, orthotropic FEA model:

```
*HEADING
**UNITS M,PA
SIMPLE ELASTIC: 1/4 ARTERY WITH PLAQUE
*RESTART,WRITE,FREQUENCY=1
*NODE,SYSTEM=R
1,0.001,0.0
41,0.002,0.0
411,0.,0.001
451,0.,0.002
*NGEN,NSET=INNER,LINE=C
1,411,41
*NGEN,NSET=OUTER,LINE=C
41,451,41
*NFILL
INNER,OUTER,40,1
*NSET,NSET=NALL,GENERATE
1,451,1
*NSET,NSET=XSYM,GENERATE
1,41,1
*NSET,NSET=YSYM,GENERATE
411,451,1
*ELEMENT,TYPE=CPE8
1,1,3,85,83,2,44,84,42
*ELGEN,ELSET=PLAQUE
1,10,2,1,5,82,20
*ELEMENT,TYPE=CPE8
11,21,23,105,103,22,64,104,62
*ELGEN,ELSET=ARTERY
11,10,2,1,5,82,20
*ELSET,ELSET=ELINNER,GENERATE
1,81,20
*ORIENTATION,SYSTEM=CYLINDRICAL,NAME=PLOR
0.0,0.0,0.0,0.0,0.0,1.0
3,0.0
**PLAQUE
*SOLID SECTION,ELSET=PLAQUE,MATERIAL=M0000001,ORIENTATION=PLOR
*MATERIAL,NAME=M0000001
*ELASTIC,TYPE=ORTHOTROPIC
50275.48, 13774.10, 1082406., 13774.1, 295004.4, 1082406., 500000., 500000.,
393700.8
**ARTERY
*SOLID SECTION,ELSET=ARTERY,MATERIAL=M0000002,ORIENTATION=PLOR
*MATERIAL,NAME=M0000002
*ELASTIC,TYPE=ORTHOTROPIC
10027.47, 1373.626, 108051.4, 1373.626, 29311.24, 108051.4, 50000., 50000.,
39370.08
*TRANSFORM,NSET=NALL,TYPE=C
0.0,0.0,0.0,0.0,0.0,1.0
*BOUNDARY
XSYM,2
YSYM,2
*STEP
*STATIC
*DLOAD,OP=NEW
ELINNER,P4,1.46E+04
*EL PRINT,POSITION=AVERAGED AT NODES
S,E
*END STEP
```

Sample ABAQUS input for FEA models in Chapters 4 and 5:

```
*HEADING
CEDAR2 12-OCT-91   16:29:18
*RESTART,WRITE
*NODE, SYSTEM=R
          1, 1.0066E-04, 2.7781E-03, 0.0000E+00
                  ******
       3111,-3.7894E-04, 2.3020E-03, 0.0000E+00
*NSET,NSET=NALL,GENERATE
1,3111,1
*ELEMENT,TYPE=CPE8   ,ELSET=E0000001
 1110  864   16  881 2406  865  882 2481 1488
                  ******
 1325 2165  735   14  776 1194  734  777 2195
*ELEMENT,TYPE=CPE8   ,ELSET=E0000002
  509 1893 1894 1831 1832 2394 2461 2366 2450
                  ******
  866 2165 2164 2119 2168 2330 2331 2332 2328
*ELEMENT,TYPE=CPE8   ,ELSET=E0000003
  510 1836 1837 1886 1887 2296 2462 2411 2457
                  ******
    1  920   49   51  910 1153   50 1154 1155
*ELEMENT,TYPE=CPE8   ,ELSET=E0000004
  410 836 837 886 887 296 462 411 457
                  ******
    5  820   149   151  810 1053 150 1054 1055
*ORIENTATION,SYSTEM=CYLINDRICAL,NAME=PLOR
0.0,0.0,0.0,0.0,0.0,0.0,1.0
3,0.0
**PLAQUE
*SOLID SECTION,ELSET=E0000001,MATERIAL=M0000001,ORIENTATION=PLOR
*MATERIAL,NAME=M0000001
*ELASTIC,TYPE=ORTHOTROPIC
50275.48, 13774.10, 1082406., 13774.1, 295004.4, 1082406., 500000., 500000.,
393700.8
**ARTERY
*SOLID SECTION,ELSET=E0000002,MATERIAL=M0000002,ORIENTATION=PLOR
*MATERIAL,NAME=M0000002
*ELASTIC,TYPE=ORTHOTROPIC
10027.47, 1373.626, 108051.4, 1373.626, 29311.24, 108051.4, 50000., 50000.,
39370.08
**LIPID
*SOLID SECTION,ELSET=E0000003,MATERIAL=M0000003,ORIENTATION=PLOR
*MATERIAL,NAME=M0000003
*ELASTIC,TYPE=ISOTROPIC
 1.0E+03, 4.800E-01
**CALCIUM
*SOLID SECTION,ELSET=E0000004,MATERIAL=M0000004,ORIENTATION=PLOR
*MATERIAL,NAME=M0000004
*ELASTIC,TYPE=ISOTROPIC
 1.0E+07, 4.800E-01
*TRANSFORM,NSET=NALL,TYPE=C
0.0,0.0,0.0,0.0,0.0,1.0
*BOUNDARY
          7,    1,, 0.0000E+00
          7,    2,, 0.0000E+00
          7,    3,, 0.0000E+00
          7,    4,, 0.0000E+00
          7,    5,, 0.0000E+00
          7,    6,, 0.0000E+00
        458,    2,, 0.0000E+00
        458,    3,, 0.0000E+00
        458,    4,, 0.0000E+00
        458,    5,, 0.0000E+00
        458,    6,, 0.0000E+00
*STEP
*STATIC
*DLOAD,OP=NEW
         94,   P2, 2.0200E+05
                  ******
       1702,   P2, 2.0200E+05
*EL PRINT,POSITION=AVERAGED AT NODES
S
*END STEP
```

Sample ABAQUS input for FEA models in Chapter 6:

```
*HEADING
PTCA21 12-APR-92   16:29:18
*RESTART,WRITE,FREQUENCY=50
*NODE, SYSTEM=R
          1, 9.0066E-04, 2.7781E-03, 0.0000E+00
                          ******
       5496,-3.7894E-04, 2.3020E-03, 0.0000E+00
*NSET,NSET=NALL,GENERATE
1,5496,1
*ELEMENT,TYPE=CPE8H    ,ELSET=E0000001
 1732  864   16  881 5406  865  882 5481 5488
                          ******
 1225 4165  735   14  776 4194  734  777 4195
*ELEMENT,TYPE=CPE8H    ,ELSET=E0000002
  509 1893 1894 1831 1832 2394 2461 2366 2450
                          ******
  866 3165 3164 3119 3168 3330 3331 3332 3328
*ELEMENT,TYPE=CPE8H    ,ELSET=E0000003
  409 1793 1794 1731 1732 2294 2361 2266 2350
                          ******
  766 3065 3064 3019 3068 3230 3231 3232 3228
*ORIENTATION,SYSTEM=CYLINDRICAL,NAME=PLOR
0.0,0.0,0.0,0.0,0.0,1.0
3,0.0
**PLAQUE
*SOLID SECTION,ELSET=E0000001,MATERIAL=M0000001,ORIENTATION=PLOR
*MATERIAL,NAME=M0000001
*HYPERELASTIC,N=1,TEST INPUT DATA
*UNIAXIAL TEST DATA
0.0,0.0
3.00E+04,.001
3.00E+05,.01
3.00E+06,.10
**ARTERY
*SOLID SECTION,ELSET=E0000002,MATERIAL=M0000002,ORIENTATION=PLOR
*MATERIAL,NAME=M0000002
*HYPERELASTIC,N=1,TEST INPUT DATA
*UNIAXIAL TEST DATA
0.0,0.0
1.50E+04,.001
1.50E+05,.01
1.50E+06,.10
**CALCIUM
*SOLID SECTION,ELSET=E0000003,MATERIAL=M0000003,ORIENTATION=PLOR
*MATERIAL,NAME=M0000003
*HYPERELASTIC,N=1,TEST INPUT DATA
*UNIAXIAL TEST DATA
0.0,0.0
1.00E+06,.001
1.00E+07,.01
1.00E+08,.10
*TRANSFORM,NSET=NALL,TYPE=C
0.0,0.0,0.0,0.0,0.0,1.0
*BOUNDARY
         10,    1,, 0.0000E+00
         10,    2,, 0.0000E+00
         10,    3,, 0.0000E+00
         10,    4,, 0.0000E+00
         10,    5,, 0.0000E+00
         10,    6,, 0.0000E+00
        558,    2,, 0.0000E+00
        558,    3,, 0.0000E+00
        558,    4,, 0.0000E+00
        558,    5,, 0.0000E+00
        558,    6,, 0.0000E+00
*STEP,NLGEOM,INC=50
*STATIC,PTOL=1.0E-01
*DLOAD,OP=NEW
          1,   P2, 2.0200E+05
                ******
       1732,   P2, 2.0200E+05
*EL PRINT,POSITION=AVERAGED AT NODES,FREQ=50
S,E
*NODE PRINT,FREQ=50
RF
*END STEP
```